Development of a Large scale simulation approach for deflagration

Bassam Gamal

To cite this version:

Bassam Gamal. Development of a Large scale simulation approach for deflagration. Chemical and Process Engineering. Université Paris-Saclay, 2022. English. NNT : 2022UPAST067 . tel-03704052

HAL Id: tel-03704052
https://theses.hal.science/tel-03704052v1

Submitted on 24 Jun 2022

Development of a Large Scale Simulation approach for deflagration

Développement d'une approche par simulation des grandes échelles pour la déflagration

Thèse de doctorat de l'Université Paris-Saclay

Ecole doctorale n◦ 579, Sciences mécaniques et Energétiques, matériaux et géosciences (SMEMAG).
Spécialité de doctorat: Combustion
Graduate School: Sciences de l'ingénierie et des systèmes
Référent : CentraleSupélec

Thèse préparée dans l'unité de recherche : Laboratoire EM2C (Université Paris-Saclay, CNRS, CentraleSupélec), sous la direction de **Denis Veynante**, directeur de recherche CNRS

Thèse soutenue à Paris-Saclay, le 17 mai 2022, par

Bassam Gamal

Composition du jury

qu **Christian Tenaud** Directeur de recherche CNRS, CentraleSupélec	Président du jury
Jean-Marc Hérard Expert HDR, EDF	Rapporteur & Examinateur
Luc Vervisch Professeur, INSA Rouen	Rapporteur & Examinateur
Éric Serre Directeur de recherche CNRS, université Aix-Marseille	Examinateur
Ahmed Bentaib Expert HDR, IRSN	Examinateur
Denis Veynante Directeur de recherche CNRS, CentrraleSupélec	Directeur de thèse

Thèse de doctorat

NNT: 2022UPAST067

universite PARIS-SACLAY

ÉCOLE DOCTORALE
Sciences mécaniques et
énergétiques, matériaux
et géosciences (SMEMAG)

Titre: Développement d'une approche par simulation des grandes Echelles pour la déflagration

Mots clés: Explosion, accélération de flamme, simulation des grandes échelles, modèle de flamme épaissie, modèle dynamique, schéma explicite

Résumé: Ce travail s'inscrit dans le cadre de la simulation des déflagrations turbulentes telles que celles rencontrées dans les études de sûreté pour les installations nucléaires ou civiles. Nous y développons une approche par simulation des grandes échelles permettant une description fine de l'écoulement. L'outil de simulation ainsi construit est utilisé dans l'étude de transitoires expérimentaux à petite et moyenne échelle. La première étape de la thèse a porté sur le développement et l'analyse d'un schéma numérique pour les équations de Navier-Stokes pour les écoulements compressibles non réactifs. Le schéma est explicite et basé sur une discrétisation en temps du second ordre (schéma d'Heun). La discrétisation enespace est de type mailles décalées. Elle se base sur une formulation en énergie interne. Une discrétisation des opérateurs de convection via une technique de montée en ordre de type MUSCL permet alors de garantir la positivité des variables scalaires (densité, énergie interne et pression) sous condition de CFL. De plus, le schéma est peu dissipatif numériquement, ce qui est primordial dans le contexte de la simulation des grandes échelles.

Ce schéma est étendu au cas réactif par une technique de pas fractionnaires. L'équation de conservation des espèces chimiques est résolue dans un premier temps par un algorithme de Strang découplant convection et réaction. L'énergie de réaction associée est introduite dans le bilan d'énergie des équations de Navier Stokes, traitées dans un second temps.

Nous développons ensuite un modèle de combustion et l'appliquons à l'étude d'écoulements d'intérêt. La combustion est traitée par un modèle de flamme artificiellement épaissie. Un modèle de sous-maille permet d'ajuster de façon dynamique le plissement de sous-maille, qui disparaît dans l'opération d'épaississement, à partir de la connaissance des champs résolus. Trois configurations expérimentales de déflagrations accélérées par des obstacles en chambre semi-confinée ont été étudiées. Ces configurations diffèrent par la disposition des obstacles qui génèrent la turbulence au passage de l'écoulement induit par l'expansion thermique et promeuvent l'accélération de la flamme. Ces cas ont permis d'analyser le comportement du modèle de combustion et valider ses résultats à partir des données expérimentales. L'étude a également mis en évidence la supériorité de la formulation dynamique du modèle par rapport à l'utilisation d'un paramètre de plissement constant. Des simulations de type RANS (résolution des équations de Navier-Stokes moyennées) où la combustion est décrite par une formulation de type « G-equation » ont également été réalisées et confortent l'utilisation de la simulation aux grandes échelles.

Title: Development of a Large Scale Simulation approach for deflagration

Keywords: Explosion, flame acceleration, large eddy simulation, thickened flame model, dynamic modeling, explicit scheme

Abstract: This work is part of the simulation of turbulent deflagrations encountered in safety studies for nuclear power plants or industrial plants. Large Eddy Simulation approach is developed allowing a thin description of the flow. The simulation tool developed is used for the study of experimental transients at small and medium scales.

In the first part of this thesis, a numerical scheme for the Navier-Stokes equations for compressible non-reactive flows is developed and analysed. The scheme is explicit and based on a second order time discretization (Heun scheme). Staggered discretization is used in space. The scheme is based on the internal energy formulation. High order methods of MUSCL type used in the discrete convective operators allow then to guarantee the positivity of scalar unknowns (density, internal energy and pressure) under CFL condition. Moreover, the scheme is numerically low dissipative, which is essential in the context of large eddy simulation.

This scheme is extended to the reactive case with a fractional step technique. The chemical species mass balances are solved with the Strang algorithm decoupling convection and reaction. The associated reaction energy is introduced into the energy balance of Navier-Stokes equations, solved in a second time.

Then, a combustion model is developed and used for the study of flows of interest. The combustion is modelled using a virtually thickened flame formalism. A subgrid scale model allow a dynamical determination of the subgrid scale flame wrinkling factors to handle unresolved contributions. Three experimental configurations of accelerated deflagrations in an obstructed semi-confined chamber are investigated. Each configuration differs from the other by the obstacles location. The flame is progressively wrinkled by turbulent motions generated by thermal expansion around obstacles and accelerates. These test cases allow to analyse the combustion model behavior and compare the numerical results to experimental data. The superiority of the wrinkling factor dynamical formulation with respect to the constant one is highlighted. RANS simulations (averaged Navier-Stokes resolution) combined with a combustion description with the so called "G-equation" have also been performed and support the use of large eddy simulation.

Remerciements

Je voudrais tout d'abord commencer ces quelques lignes en remerciant les deux rapporteurs: Jean-Marc Hérard et Luc Vervich pour avoir lu mon manuscrit et apporté leurs points de vue à ce dernier à l'aide de leurs rapports. Je remercie également les membres du jury qui ont permis un échange enrichissant lors des questions après la soutenance de thèse. Je remercie bien évidemMent Denis Veynante, mon directeur de thèse qui s'est toujours rendu disponible afin de répondre à mes questions. Cette thèse n'aurait pas été possible sans l'aide de l'équipe du LIE et tout particulièrement de mon encadrante Laura Gastaldo. Malgré mon manque de connaissance dans le domaine, Laura a su être patiente et m'a appris les rudiments du métier en dépit des confinements rendant la tache bien compliquée. Le LIE m'a permis de travailler dans une ambiance bienveillante grâce au soutien de Jean-Claude Latché et Fabrice Babik qui m'ont aidé à plusieurs reprises. Sans oublier Aubin Brunel et Jérémie Janin qui ont été des collègues et des amis surtout lors des longues journées de télétravail : Cafew !

En ce qui concerne ma vie à l'extérieur du labo, je tiens à remercier mon premier colocataire Jean-Christophe (JC pour les intimes), avec qui cette aventure a débuté, de la descente en voiture de Paris au premier appartement à Aix. Merci pour toutes ces soirées à discuter après le boulot et à bien vouloir parler code et physique dans des endroits douteux comme la terrasse du Shannon.

La colocation a été une occasion parfaite pour rencontrer des personnes avec qui j'ai partagé la majeure partie de ces trois années dans le sud de la France. Tout particulièrement, Delphine et Irene qui ont été géniales du début à la fin. Merci les filles pour tous ces moments de rires, de sorties, et de confinements ! J'ai partagé plusieurs années de cohabitations avec vous deux et c'était juste génial (B2D) !

J'ai fait de nombreuses rencontres durant cette vie aixoise mais je souhaite particulièrement remercier Cardo et Flo pour tous ces moments sur Marseille !

Même si il y a plus de 700 km entre Paris et Aix, j'ai pu compter sur l'appui de mes amis de Paris (#VM). Merci mes poètes préférés car malgré la distance, j'ai pu compter sur votre soutien sans faille et merci d'être venu me voir aussi souvent.

J'ai eu la chance d'avoir croisé la route d'Adrien, Théo et Thibaud il y a plusieurs années maintenant. Je pourrais écrire des pages de remerciements pour être devenu mes amis les plus proches et sur qui j'ai pu compter... Au final, je dirai juste ceci : ne changez rien les gars.

Bien entendu, je remercie profondément ma famille qui m'a écouté raler au téléphone tellement de fois. Plus de 4000 km entre nous et pourtant je ne me suis jamais senti aussi proche. Merci de vous être inquiété de ma santé physique et mentale et de toujours vouloir le mieux pour moi.

Last but not least, Je ne pourrais jamais assez te remercier Agathe. Tu as été un vrai soutien pendant toutes ces années. Tu as vécu cette thèse autant, si ce n'est plus que moi. Tu as toujours su trouver les mots pour me remonter le moral. Même s'il suffisait de te voir pour aller mieux. Tu as été essentiel durant toute cette période. Je n'arrive pas à trouver les mots pour te remercier comme il se doit, autant tu as été chaleureuse, présente, réconfortante, apaisante, encourageante, aimante... en bref, merci d'avoir été là.

Contents

List of Tables

List of Figures

Nomenclature

Greek characters:

β	Wrinkling factor exponent
Δ	Combustion filter size
Δ_x	Characteristic cell size
$\widehat{\Delta}$	Test-filter size
δ	Diffusive flame thickness
δ_c	Inner cut-off length scale
δ_r	Reaction zone thickness
δ_t	Total flame thickness
δ_L^0	Thermal flame thickness
$\mathcal{E}$	Set of faces
ϵ_v	Subgrid scale viscous dissipation
ε	Dissipation rate
Γ	Efficiency function
λ	Heat conduction coefficient
μ	Laminar viscosity
ν	Kinematic viscosity
ν'_{kj}	Molar stoichiometric coefficient of the reactant k for reaction j
ν''_{kj}	Molar stoichiometric coefficient of the product k for reaction j
ν_{SGS}	Turbulent viscosity
Ω	Computable domain
$\dot{\omega}_k$	Mass reaction rate of species k
$\dot{\omega}_T$	Heat release
$\check{\boldsymbol{\Phi}}$	Filtered computable viscous dissipation
ϕ	Equivalence ratio
ρ	Density of the mixture
ρ_k	Density of the species k
σ	Specific face of a cell
$\boldsymbol{\tau}$	Shear-stress tensor
τ_c	Chemical time scale
τ_k	Kolmogorov time scale
$\boldsymbol{\tau}_{SGS}$	Unresolved Reynolds stress tensor
$\overline{\boldsymbol{\tau}}$	Laminar stress tensor
Ξ	Wrinkling factor

Latin characters

A_{fj}	Pre-exponential factor of reaction j
c	Progress variable
c_p	Specific heat
c_s	Smagorinski constant
c_v	Heat capacity at a constant volume
D_σ	Dual cell associated to σ
D_k	Diffusion coefficient of species k
D_f	Test-filter diffusivity coefficient
D_{th}	Diffusivity coefficient
E	Total energy
e	Sensible energy
e_c	Sensible + Chemical energy
E_{aj}	Activation energy of reaction j
$\boldsymbol{f}$	External forces
$\mathcal{F}$	Thickening Factor

$F_{K,\sigma}$	Mass flux through $\mathcal{E}$ outward K cell
H	Total mass enthalpy
h	Mass enthalpy of species k
$\boldsymbol{j}$	Species mass diffusion flux
$\boldsymbol{j}^{SGS}$	Unresolved transport species flux
$\overline{\boldsymbol{j}}$	Laminar diffuse species flux
K	Cell of the primal grid
K_{eq}^{j}	Equilibrium constant of reaction j
K_{fj}	Forward rate of reaction j
K_{rj}	Reverse rate of reaction j
L	A cell next to the K cell
l_k	Kolmogorov length scale
L_t	Integral length scale
$\mathcal{M}$	Primal grid
m	Mass of the mixture
$\mathcal{M}_k$	Chemical species symbol
m_k	Mass of species k
n	Number of mesh grid in the front
N_s	Number of species
p	Pressure
$\boldsymbol{q}$	Heat flux
$\boldsymbol{q}^{SGS}$	Subgrid scale Heat flux
$\overline{\boldsymbol{q}}$	Computable Heat flux
R	Perfect gas constant
S	Entropy
s	Mass stoichiometric ratio
s_a	Absolute flame speed
s_c	Consumption flame speed
s_d	Displacement flame speed
s_L	Laminar flame speed
T	Temperature
t	Time
$\boldsymbol{v}$	Velocity vector
$\boldsymbol{v}'(r)$	Characteristic velocity of the motion of size r
W	Mean molar mass
W_k	Molar mass of species k
Y_k	Mass fraction of species k
z	Mixture fraction

Non-dimensional numbers:

Da	Damköhler number
Ka	Karlovitz number
Le	Lewis number
Pr	Prandtl number
Pr_t	Turbulent Prandtl number
Re	Reynolds number
Re_f	Flame Reynolds number
Re_T	Turbulent Reynolds number
Sc	Schmidt number
Sc_t	Turbulent Schmidt number

Introduction

General context

The explosion of gases and more especially of hydrogen is a major hazard in industrial plants, and more specifically in nuclear power plants.

In a nuclear power plant, hydrogen can be produced during a severe accident, from oxidation of fuel cladding or fuel assembly canisters and other hot metallic components. In case of failure of in-vessel corium retention, a large amount of carbon monoxide in addition to hydrogen and other gases may be produced during molten core concrete interaction in the reactor pit. As a consequence, local concentrations of inflammable gases can exceed the flammability limit of the mixture. In case of high pressure or external energy supply such as hot spots or sparks, the mixture ignites. Subsequent deflagration would develop and propagates until transiting to detonation inducing high dynamic pressure loads which could threaten the containment structures and technical equipment. A recent reminder of the potential consequences of the release and ignition of hydrogen during severe accident conditions in a nuclear power plant is the Fukushima Daiichi accident in 2011 (Bentaib et al., 2017). During this accident, chemical reactions between the fuel cladding, in this case the zirconium alloy and water generated large quantities of hydrogen, which from the containment escaped into reactor's primary containment vessel and then further into the reactor building where it mixed with air. This subsequently raised a combustion hazard and ultimately led to a series of explosions (shown in Fig. 1a), damaging the reactor containment and leading to the release of radioactive materials into the reactor building and eventually to the environment, forcing to evacuate in a 20 km radius the 154 000 persons living there (Braun, 2017).

Explosion may also occur in a nuclear power plant, inside or outside the reactor building due to loss of sealing of pipes containing hydrogen. This situation may lead to delayed explosions of hydrogen high pressure releases (as shown in Fig. 1b, where an experiment of Daubech et al. (2015) is illustrated).

In some areas of the fuel cycle, the potential for the creation of an explosive atmosphere exists through the production of hydrogen by radiolysis or the use of this gas in the process, and by chemical or corrosion reactions through the presence of finely divided oxidisable dusts or pyrophoric materials, and through certain nitric acid/heavy metal/organic-matter reactions (OECD, 2005). An explosion may cause either physical damage such as breach of containment or system pressurisation resulting in an unplanned discharge of radioactive material.


(a) Explosion of Fukushima reactor 3 (b) Hydrogen jet deflagration

Figure 1: Explosions inside and outside a reactor building.

A major example of an explosion incident in an industrial plant is the 1983 Stockholm hydrogen accident (Venetsanos et al., 2003) in central Stockholm, Sweden. The accidental release of approximately 13.5 kg of hydrogen from a rack of 18 interconnected industrial pressure vessels being transported by a delivery truck led to an explosion. More recently, an explosion occurred at a hydrogen filling station in Norway in 2019 near Oslo. A leak at the high-pressure hydrogen storage unit leaded to the mixing of the leaked hydrogen with air forming an inflammable mixture and causing the explosion.

The energetic worldwide demand is growing as seen in Fig.2. As a consequence, the number of industrial facilities is increasing. Oil, coal and natural gas are the main energy sources worldwide, they are based on the consumption of highly inflammable fuel. Therefore, explosion hazards remain important. For all theses reasons, explosion phenomena have to be investigated in order to prevent them.

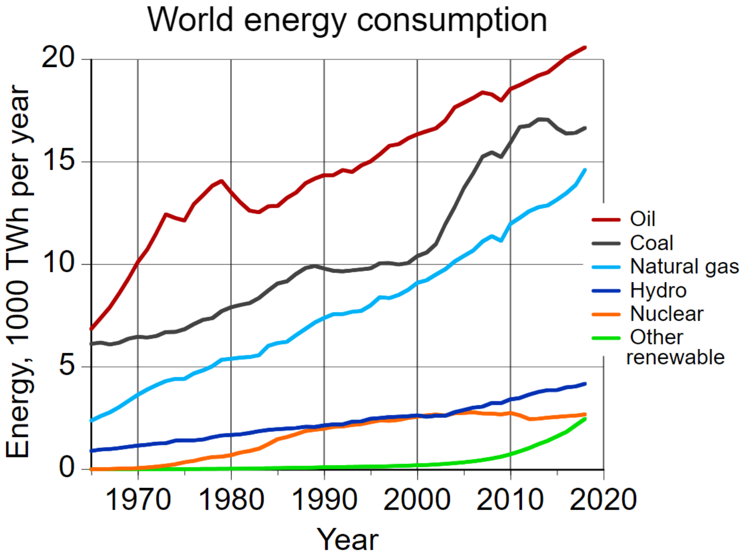

Figure 2: Energy consumption by source until 2018. BP Statistical Review of world energy, BP, 11 juin 2019.

One role of IRSN (Institut de Radioprotection et de Sûreté Nucléaire) is to carefully analyze and understand the risk of explosion in nuclear facilities as it poses a potential threat to the reactor (breakdown of safety equipments, failure of containment) and the environment (diffusion of radioactive materials in the environment) which can be catastrophic. Fukushima Daiichi nuclear disaster also led to complementary research and development projects (Bentaib et al., 2015, 2017) to better understand the phenomena associated with the combustion hazard and to address issues such as explosion hazard in the venting system, dispersion of radioactive particles beyond the primary containment and motivated further work to develop and validate Computational Fluid Dynamics (CFD) tools (Bentaib et al., 2011), which are growing into useful analysis tools for supporting safety management. The safety issues related to the explosion hazards are usually segregated into three linked yet separate phases:

(i) The first phase corresponds to the release and dispersion of the explosive gases leading to a partially premixed (*i.e.* in-homogeneous is space) explosive atmosphere from the turbulent mixing of the gases,

(ii) A possible chemical reaction between the gases or an external energy source (spark, hot spot...) could lead to the mixture ignition and thus to an explosion, regarded as the second phase. The challenges posed here constitute the understanding of the rate of combustion and of the flame-front structure along with turbulence coupling,

(iii) The final phase involve the propagation of the blast wave and its effects on the structural integrity of the reactor facility.

The P^{2}REMICS (Partially PREMixed Combustion Solver) is an in-house CFD software developed at IRSN dedicated to the computation of the three phases listed above, the formation of explosive atmospheres (i), their deflagration or detonation (ii) and the subsequent propagation of blast waves (iii). Phase two addressing the deflagration of the explosive gases is focused in this work where turbulence modeling plays a central role in the flame front propagation.

Motivation of the thesis

Because of the large number of degrees of freedom involved in a deflagration, a full Direct Numerical Simulation (DNS) of a practical system cannot be performed. Instead, two techniques less expensive than DNS were developed and are used in industries nowadays. The first one is the less expensive and the most spread technique in industrial codes. It consists in solving the averaged flow governing equations; it is the so-called Reynolds Averaged Navier-Stokes (RANS) approach. The averaging operations introduce unresolved terms that require specific closures. Basically, a turbulence model to deal with the flow dynamics and a combustion model to describe chemical species conversion and heat release are needed.

This approach is available in CALIF^{3}S -P^{2}REMICS and is the one used for safety studies on large scale domains. The turbulence is modeled with two-equations models, mainly, the models k-ε or k-ω models with or without usual wall laws (low-Reynolds extension or elliptical relaxation) (Menter et al., 2003). The combustion model is based on the *turbulent flame-speed closure* approach. The location of the flame brush is explicitly tracked by a phase-field-like technique, the flame front passage being followed by an instantaneous combustion, thanks to an ad-hoc modification of the reactive term in the species mass balance equations. These latter deal with transport and turbulent diffusion of the chemical species, which allows addressing non-perfectly (*i.e.* non homogeneous) premixed situations. The model is closed with a turbulent flame speed correlation which depends on the properties of the unburnt mixture of fresh gases (laminar flame speed) as well as on the turbulent characteristics of the flow (integral length scale, turbulent kinetic energy).

The experimental characterization of the velocity field during a deflagration is difficult, especially in medium and large-scale configurations. The turbulence flame speed is controlled by the turbulence generated by the thermal expansion ahead the flame front. Moreover, turbulent flame speed correlations in literature assume an equilibrium between turbulence motions and flame surface wrinkling, generally not verified in unsteady flames, and display a large scatter (Gastaldo et al., 2017).

The second approach called Large Eddy Simulation (LES) has gained a great success in simulating turbulent flows. In such a method, the large scale fluid motions are computed explicitly from the filtered instantaneous equations while small-scale effects are modeled. LES determines the instantaneous position of a large scale resolved flame front but a subgrid model, as in RANS, is still required to take into account the effect of small turbulent scales on combustion.

This latest approach is reliable and efficient, but is also extremely costly in term of computer resources for domain with large dimension and remains prohibitive for industrial purpose, even with the rapid increase of supercomputer power (Pope, 2004; Choi and Moin, 2012). However, LES approach can be used in order to perform in indepth the interpretation of experiments and to support RANS model validation. To develop, implement and validate a LES approach for turbulent deflagrations motivates the work performed during this thesis.

Manuscript organisation

This manuscript is organized in three parts. In Part I, general features on turbulent combustion are discussed. In Part II, a second order numerical MAC scheme is developed for large-eddy simulation of compressible reactive flows. In Part III, the developed approach is validated and tested on different cases.

Part I - General concepts

Chapter 1 presents the governing equations for turbulent reactive compressible flows. The three main numerical approaches for turbulence description are introduced and a particular focus is granted to LES approach. The filtered governing equations are then stated. Premixed laminar and turbulent flames are discussed in Chapter 2 and different combustion regimes are identified. Different combustion models used in the LES framework are described. A particular focus on the Thickened Flame model for Large Eddy Simulation (TFLES) used in this work is made. Afterwards, several subgrid wrinkling factor closures available in literature are proposed.

Part II - A second order numerical scheme for large-eddy simulation of compressible reactive flows

- In Chapter 3, a formally second order scheme is proposed, with as low kinetic energy dissipation as possible, dedicated to the numerical simulation of the filtered Navier-Stokes equations for compressible non reactive flows.

  The space discretization is staggered, and works on structured grids using the so-called Marker-And-Cell (MAC) scheme (Harlow and Amsden, 1971; Harlow and Welch, 1965). Time-stepping is segregated, in the sense that balance equations are solved successively, and each step is explicit. Time discretization is performed with a Strong Stability Preserving (SSP) scheme, namely the Heun scheme.

  The scheme is shown to preserve the stability properties of the continuous problem under CFL condition (*i.e.* the positivity of the density and of the internal energy, at least when no numerical corrective terms are added). A kinetic energy conservation identity, essential requirement for a numerical scheme in the context of large eddy simulation of turbulent flows, is proved at discrete level. Finally, a total energy balance for the scheme is established, which may be made conservative by adding corrective terms to the sensible energy balance, for instance if one wants to compute shock solutions.

- In Chapter 4 a numerical scheme for the computation of turbulent deflagrations occurring in a premixed atmosphere is developed. The flow under consideration is governed by the compositional Navier-Stokes equations and the flame propagation is represented by a virtually thickened flame formalism (Butler and O'Rourke, 1977) combined with a dynamical determination of the subgrid scale flame wrinkling factor to handle unresolved contributions (Veynante and Moureau, 2015).

  The numerical scheme developed in this chapter extends the one presented in Chapter 3 to reactive flows. The chemical species mass balances are solved with the Strang algorithm decoupling convection and reaction. The associated reaction energy is introduced into the Navier-Stokes energy balance equation, solved in a second time. A positivity-preserving discretization of the convective operators allow to guarantee the positivity of scalar unknowns (density, internal energy, pressure and chemical species), under CFL condition. Moreover, with a suitable choice of the coefficients involved in the discretization of the chemical species convection terms, the chemical species are also shown to be bounded by 1 at discrete level. Finally, the approximate solutions satisfy a conservative weakly-consistent discrete total energy balance equation in the inviscid case.

Part III - Thickened flame model for large eddy simulation: calibration and application on an accelerated deflagration

Accelerated turbulent deflagrations, potentially transiting to detonation, are a major hazard in industrial plants, and more specifically in nuclear power plants. The pressure increase is governed by a complex unsteady interaction between flame propagation, turbulence and geometry. This overpressure is often considered as the key parameter, since it controls the severity of the explosion and corresponding damages. This complex phenomenon is very challenging for computational fluid dynamics problems since it involves a large spectrum of spatial and time scales and involves a large range of flow and combustion regimes.

- In Chapter 5 the second order scheme developed previously is validated on laminar one-dimensional steady flames. The aim is to assess the laminar behavior of the combustion model and its capacity to reproduce the early stages of a deflagration. This test case may be considered as a prerequisite before applications to turbulent reactive problems in two or three dimensions. Physical features such as flame front velocity are investigated alongside numerical one such as the minimum number of grid points needed for the description of the flame front.

- In Chapter 6, a case of interest for IRSN is simulated. Accelerated turbulent deflagrations in a semi-confined chamber with different obstacle configurations are investigated (Wen et al., 2013). Two-dimensional simulations are first performed. The purpose of these simulations is twofold: first, the model parameters are adjusted for the three-dimensional computations more expensive in terms of CPU time, second they allow at a moderate cost to investigate several parameters such as the impact of the obstacle location, the thickening factor, the dynamic computation of the wrinkling factor, ... Afterward, three-dimensional simulations have been carried out on the most penalizing configuration security wise (most important pressure peak).

  The LES approach is then compared to a RANS turbulence description complemented with a turbulent flame speed closure combustion model already available in the CALIF^{3}S -P^{2}REMICSsoftware. The results computed with different turbulent flame speed closures are compared.

At last, a global conclusion on the work made during this thesis is drawn, evidencing some perspectives.

Part I

General concepts

Chapter 1

A compressible model for turbulent reactive flows

This chapter is devoted to a brief description of turbulent compressible and reactive flows. First, the governing equations are presented. This is followed by an introduction to the various approaches present in the literature for turbulence description. The underlying principle of DNS, RANS, and LES methods along with their advantages and weaknesses are briefly discussed. Focus is then made on LES methods which are used in this work. We conclude with the filtered equations for compressible turbulent and reactive flows.

1.1 Governing equations

Hydrodynamics

The hydrodynamics of the flow is governed by the mass balance and momentum balance equations, which read in the conservative form (Garnier et al., 2009; Poinsot and Veynante, 2012):

$$\partial_t \rho + \operatorname{div}(\rho \boldsymbol{v}) = 0, \tag{1.1a}$$

$$\partial_t(\rho\, \boldsymbol{v}) + \operatorname{div}(\rho \boldsymbol{v} \otimes \boldsymbol{v}) + \boldsymbol{\nabla} p - \operatorname{div}(\boldsymbol{\tau}(\boldsymbol{v})) = \boldsymbol{f}, \tag{1.1b}$$

where t stands for the time, ρ, $\boldsymbol{v}$, p, $\boldsymbol{\tau}$ and $\boldsymbol{f}$ are respectively the density, the velocity, the pressure, the shear-stress tensor and an external force. The computational domain of dimension d is denoted by $\Omega \subset \mathbb{R}^d$, $d = 1,\ 2,\ 3$ and the computational time interval is denoted by $[0, T]$. We only consider Newtonian fluids in this work, therefore the viscous stress tensor is given by:

$$\boldsymbol{\tau}(\boldsymbol{v}) = \mu(\boldsymbol{\nabla}\boldsymbol{v} + \boldsymbol{\nabla}^t\boldsymbol{v}) - \frac{1}{3}\mu \operatorname{Tr}(\boldsymbol{\nabla}\boldsymbol{v} + \boldsymbol{\nabla}^t\boldsymbol{v}) \tag{1.2}$$

where $\operatorname{Tr}(X)$ denotes the sum of the diagonal terms of the matrix X and $\mu \geq 0$ stands for the dynamic viscosity.

Transport of chemical species

Let suppose that N_s species are present in the flow reacting through M reactions:

$$\sum_{k=1}^{N_s} \nu'_{kj} \mathcal{M}_k \rightleftharpoons \sum_{k=1}^{N_s} \nu''_{kj} \mathcal{M}_k \tag{1.3}$$

where $\mathcal{M}_k$ is the chemical species symbol, ν'_{kj} and ν''_{kj} are respectively the molar stoichiometric coefficient of the reacting and product species in reaction j.
Let now define the mass fraction given by:

$$Y_k = m_k/m \qquad \text{for } 1 \leq k \leq N_s, \tag{1.4}$$

with m the total mass in a given volume V and m_k the k-species mass in this same volume V. The density of a species k is defined as:

$$\rho_k = m_k/V = \rho Y_k \qquad \text{for } 1 \leq k \leq N_s, \tag{1.5}$$

where the global mixture density ρ is also defined in function of the species density as:

$$\rho = \sum_{k=1}^{N_s} \rho_k. \tag{1.6}$$

Analogously, the molar concentration of the species k is written as:

$$[X_k] = \rho \frac{Y_k}{W_k} = \rho \frac{X_k}{W} \qquad \text{for } 1 \leq k \leq N_s, \tag{1.7}$$

where X_k is the molar fraction, W_k the molar mass of the species k and W the mean molar mass of the mixture given by:

$$\frac{1}{W} = \sum_{k=1}^{N_s} \frac{Y_k}{W_k}, \qquad W = \sum_{k=1}^{N_s} W_k X_k. \tag{1.8}$$

The system of the mass balance equations for the chemical species reads (Poinsot and Veynante, 2012):

$$\partial_t(\rho Y_k) + \operatorname{div}(\rho Y_k \boldsymbol{v}) + \operatorname{div}(\boldsymbol{j}_k) = \dot{\omega}_k, \qquad \text{for } 1 \leq k \leq N_s, \tag{1.9}$$

where $\boldsymbol{j}_k$ and $\dot{\omega}_k$ stand respectively for the mass diffusion flux and the reaction rate of the species k.

The reaction rate of each chemical species may be written as:

$$\dot{\omega}_k = \sum_{j=1}^{M} \dot{\omega}_{kj} = W_k \sum_{j=1}^{M} \nu_{kj}\, \mathcal{Q}_j \qquad \text{for } 1 \leq k \leq N_s,$$

where $\dot{\omega}_j$ is the reaction rate of reaction j and $\nu_{kj} = \nu''_{kj} - \nu'_{kj}$. Due to mass conservation the following property holds:

$$\sum_{k=1}^{N_s} \nu_{kj} W_k = 0 \qquad \text{for } 1 \leq j \leq M. \tag{1.10}$$

Then, we also have:

$$\sum_{k=1}^{N_s} \dot{\omega}_k = 0. \tag{1.11}$$

The reaction rate of the reaction j is given by (Poinsot and Veynante, 2012):

$$\mathcal{Q}_j = K_{fj} \prod_{k=1}^{N_s} [X_k]^{\nu'_{kj}} - K_{rj} \prod_{k=1}^{N_s} [X_k]^{\nu''_{kj}} \qquad \text{for } 1 \leq j \leq M,$$

where K_{fj} and K_{rj} are the forward and reverse rates of reaction j. The previous relation could be rewritten using mass fractions as:

$$\mathcal{Q}_j = K_{fj} \prod_{k=1}^{N_s} \Big(\frac{\rho\, Y_k}{W_k}\Big)^{\nu'_{kj}} - K_{rj} \prod_{k=1}^{N_s} \Big(\frac{\rho\, Y_k}{W_k}\Big)^{\nu''_{kj}} \qquad \text{for } 1 \leq j \leq M.$$

The forward rates K_{fj} are usually modeled throughout the empirical Arrhenius law (Poinsot and Veynante, 2012):

$$K_{fj} = A_{fj} T^{\beta_j} \exp\left[-\frac{E_{aj}}{RT}\right] \qquad \text{for } 1 \leq j \leq M, \tag{1.12}$$

where E_{aj} A_{fj} and β_j are respectively the activation energy, the pre-exponential constant and the temperature exponent of the reaction j. The reverse rates K_{rj} are computed from the forward rates:

$$K_{rj} = \frac{K_{fj}}{K^j_{eq}} \qquad \text{for } 1 \leq j \leq M,$$

and the equilibrium constants K^j_{eq} are given by (Kuo, 1986):

$$K^j_{eq} = \left[\frac{p_{atm}}{RT}\right]^{\sum_{k=1}^{N_s} \nu_{kj}} \exp\left(\frac{\Delta S^0_j}{R} - \frac{\Delta H^0_j}{RT}\right) \qquad \text{for } 1 \leq j \leq M$$

with p_{atm}, ΔS^0_j and ΔH^0_j denote respectively the atmospheric pressure, enthalpy and entropy changes for reaction j.

Let us now define the species mass diffusion fluxes $\boldsymbol{j}_k$, $1 \leq k \leq N_s$. Diffusion processes involve binary diffusion coefficients, which are complex functions of collision integrals and thermodynamic variables, obtained from kinetic theory (Hirschfelder and Curtiss, 1954; Bird et al., 1960) and require the resolution of a system giving diffusion velocities (Ern and Giovangigli, 1994). Simplified diffusion laws are thus used in a majority of combustion codes. Here, we assume that the mass diffusion fluxes of chemical species obey to the Fick's law, thus they are given by:

$$\text{for } 1 \leq k \leq N_s, \quad \boldsymbol{j}_k = -\rho\, D_k\, \boldsymbol{\nabla} Y_k. \tag{1.13}$$

where D_k stands for the diffusion coefficient of the species k. The Soret effect, that is the molecular species diffusion due to temperature gradients (Giovangigli, 1999) is neglected in this thesis. Let the variable Σ stand for $\Sigma = \sum_{k=1}^{N_s} Y_k$. In order to guarantee the global mass conservation (*i.e.* $\Sigma = 1$) everywhere in Ω, we must have:

$$\sum_{k=1}^{N_s} \boldsymbol{j}_k = 0. \tag{1.14}$$

Two methods can be applied in order to guarantee the global mass conservation.

- The first and simplest method is to solve the species mass balance equation only for $N_s - 1$ species instead of the N_s species and to write the mass fraction for the last species as:
$$Y_{N_s} = 1 - \sum_{k=1}^{N_s-1} Y_k. \tag{1.15}$$
This method may not be the most accurate technique but it has the advantage to be easy to implement.

- The second method consists on adding a correctional term in the species mass balance equation in order to ensure the global mass conservation (Hilbert et al., 2004; Poinsot and Veynante, 2012). The species diffusion fluxes are then rewritten as:
$$\text{for } 1 \leq k \leq N_s, \quad \boldsymbol{j}_k = -\rho\, D_k \boldsymbol{\nabla} Y_k + Y_k\, \boldsymbol{J}, \tag{1.16}$$
where $\boldsymbol{J}$ is a correction term added to ensure that $\sum_{k=1}^{N_s} \boldsymbol{j}_k = 0$ when $\Sigma = 1$:
$$\boldsymbol{J} = \rho \sum_{k=1}^{N_s} D_k\, \boldsymbol{\nabla} Y_k.$$
This solution is often chosen in laminar flame codes where diffusion coefficients can be very different.

In this work, the diffusion coefficients D_k are assumed to be identical for all chemical species k, denoted by D:
$$D_k = D, \quad 1 \leq k \leq N. \tag{1.17}$$
With this last assumption, the global mass conservation is ensured:
$$\sum_{k=1}^{N_s} \boldsymbol{j}_k = -\rho \sum_{k=1}^{N_s} D\, \boldsymbol{\nabla} Y_k = 0. \tag{1.18}$$

Therefore, the mass balance equation for the chemical species is written:
$$\partial_t(\rho\, Y_k) + \operatorname{div}(\rho\, Y_k\, \boldsymbol{v}) - \operatorname{div}(\rho\, D\, \boldsymbol{\nabla} Y_k) = \dot{\omega}_k, \qquad \text{for } 1 \leq k \leq N_s. \tag{1.19}$$

Energy balance

Multiple forms of the conservation equation energy exist in literature. In this section we will present the two forms involved in the present work, that is the total energy balance equation and the sensible energy balance equation. Before getting into the details let define the different forms of energy thanks to table 1.1. Here, all enthalpies and energies are mass quantities.

Form	Energy	Enthalpy
Sensible	$e = h - \dfrac{p}{\rho} = \displaystyle\int_{T_0}^{T} c_{\mathrm{v}}\, dT - \dfrac{R\,T_0}{W}$	$h = \displaystyle\int_{T_0}^{T} c_{\mathrm{p}}\, dT$
Sensible + Chemical	$e_c = h_c - \dfrac{p}{\rho} = e + \displaystyle\sum_{k=1}^{N_s} \Delta h_{f,k}^0 Y_k$	$h_c = h + \displaystyle\sum_{k=1}^{N_s} \Delta h_{f,k}^0 Y_k$
Total	$E = H - \dfrac{p}{\rho} = e_c + \dfrac{1}{2}\lvert\boldsymbol{v}\rvert^2$	$H = h_c + \dfrac{1}{2}\lvert\boldsymbol{v}\rvert^2$

Table 1.1: Enthalpy and energy forms (Poinsot and Veynante, 2012).

The total energy balance reads:

$$\partial_t(\rho\, E) + \mathrm{div}(\rho\, E\, \boldsymbol{v}) + \mathrm{div}(p\, \boldsymbol{v}) + \mathrm{div}(\boldsymbol{q}) = \mathrm{div}(\boldsymbol{\tau}(\boldsymbol{v})\ \cdot \boldsymbol{v}), \tag{1.20}$$

where $E = e_k + e_c$ with $e_k = \frac{1}{2}\ \lvert\boldsymbol{v}\rvert^2$ the kinetic energy. The so-called sensible+chemical energy e_c (see Table 1.1) is defined as:

$$e_c = \sum_{k=1}^{N_s} e_{c,k}\, Y_k = e + \sum_{k=1}^{N_s} \Delta h_{f,k}^0 Y_k, \tag{1.21}$$

where $\Delta h_{f,k}^0$ stands for the formation enthalpy of the species k at the reference temperature T_0, that is the enthalpy released while the formation of products occurs. As the enthalpy of formation is obtained thanks to experimental data, the reference temperature T_0 is usually taken at atmospheric condition (approximately $T_0 = 300\,\mathrm{K}$). The sensible+chemical energy of the species k, denoted $e_{c,k}$, is the sum of the energy associated to the variation of temperature of the species k, called sensible energy of this latest and denoted e_k, and of the chemical energy, that is the energy needed to form the species k. The sensible energy of the mixture e, introduced in (1.21), is given by:

$$e = \sum_{k=1}^{N_s} e_k\, Y_k = \int_{T_0}^{T} c_{\mathrm{v}}\, dT - \frac{R\,T_0}{W}, \tag{1.22}$$

with c_{v} the heat capacity at constant volume of the mixture and $R = 8.31451\,\mathrm{JK^{-1}mol^{-1}}$ the perfect gases constant. The energy flux $\boldsymbol{q}$ is expressed thanks to the Fourier's law of thermal conduction as:

$$\boldsymbol{q} = -\lambda \boldsymbol{\nabla} T + \sum_{k=1}^{N_s} h_{c,k}\, \boldsymbol{j}_k, \tag{1.23}$$

where λ is the thermal conductivity and $h_{c,k}$ the sensible+chemical enthalpy for the species k, defined by:

$$h_{c,k} = \int_{T_0}^{T} c_{\mathrm{p}k}\, dT + \Delta h_{f,k}^0, \qquad \text{for } 1 \le k \le N_s,$$

with $c_{\mathrm{p},k}$ the heat capacity at constant pressure for the species k. Let notice that the Dufour effect which takes into account the energy flux due to mass fraction gradients (Giovangigli, 1999) is omitted in this work.

Replacing the total energy E by its expression in (1.20) and developing some terms, we obtain:

$$\begin{aligned}&\partial_t(\rho\, e_c) + \mathrm{div}(\rho\, e_c\, \boldsymbol{v}) + p\, \mathrm{div}\boldsymbol{v} + \mathrm{div}\boldsymbol{q}\\ &\qquad + \frac{1}{2}\partial_t(\rho\, |\boldsymbol{v}|^2) + \frac{1}{2}\mathrm{div}(\rho\, |\boldsymbol{v}|^2\, \boldsymbol{v}) + \boldsymbol{v}\cdot\boldsymbol{\nabla} p - \mathrm{div}(\boldsymbol{\tau}(\boldsymbol{v}))\cdot\boldsymbol{v} = \boldsymbol{\tau}(\boldsymbol{v}) : \boldsymbol{\nabla}\boldsymbol{v}.\end{aligned} \tag{1.24}$$

Thanks to the mass balance equation (1.1a), we get formally, for any function ψ:

$$\partial_t(\rho\, \psi) + \mathrm{div}(\rho\, \psi\, \boldsymbol{v}) = \rho\, \partial_t \psi + \rho\, \boldsymbol{v}\cdot\boldsymbol{\nabla}\psi.$$

Using twice the previous identity and then the momentum balance equation (1.1b), we have for $1 \le i \le d$:

$$\begin{aligned}\frac{1}{2}\partial_t(\rho\, v_i^2) + \frac{1}{2}\mathrm{div}(\rho\, v_i^2\, \boldsymbol{v}) &= \rho\, v_i\, \partial_t v_i + \rho\, v_i\, \boldsymbol{u}\cdot\boldsymbol{\nabla} v_i\\ &= v_i\left[\rho\, \partial_t v_i + \rho\, \boldsymbol{v}\cdot\boldsymbol{\nabla} v_i\right] = v_i\left[\partial_t(\rho\, v_i) + \mathrm{div}(\rho\, v_i\, \boldsymbol{v})\right] = -v_i\, \partial_i p + v_i\, \mathrm{div}(\boldsymbol{\tau}(\boldsymbol{v}))_i,\end{aligned}$$

so, summing for $i = 1$ to d:

$$\frac{1}{2}\partial_t(\rho\, |\boldsymbol{v}|^2) + \frac{1}{2}\mathrm{div}(\rho\, |\boldsymbol{v}|^2\, \boldsymbol{v}) = \boldsymbol{v}\cdot\left[\partial_t(\rho\, \boldsymbol{v}) + \mathrm{div}(\rho\, \boldsymbol{v}\otimes\boldsymbol{v})\right] = -\boldsymbol{v}\cdot\boldsymbol{\nabla} p + \mathrm{div}(\boldsymbol{\tau}(\boldsymbol{v}))\cdot\boldsymbol{v}.$$

Using this last relation in the total energy equation (1.24) yields the chemical+sensible energy balance:

$$\partial_t(\rho\, e_c) + \mathrm{div}(\rho\, e_c\, \boldsymbol{v}) + p\, \mathrm{div}\boldsymbol{v} = \boldsymbol{\tau}(\boldsymbol{v}) : \boldsymbol{\nabla}\boldsymbol{v} - \mathrm{div}\boldsymbol{q}. \tag{1.25}$$

Replacing e_c by its definition (1.21) (or Table 1.1) and using the species mass balances (1.9) yields the sensible energy balance:

$$\partial_t(\rho\, e) + \mathrm{div}(\rho\, e\, \boldsymbol{v}) + \mathrm{div}\boldsymbol{q} - \sum_{k=1}^{N_s} \mathrm{div}(\Delta h^0_{f,k}\, \boldsymbol{j}_k) + p\, \mathrm{div}\boldsymbol{v} = \boldsymbol{\tau}(\boldsymbol{v}) : \boldsymbol{\nabla}\boldsymbol{v} - \sum_{k=1}^{N_s} \Delta h^0_{f,k}\, \dot{\omega}_k.$$

Using expression (1.23) and denoting $\dot{\omega}_T$ the heat production rate due to the chemical reactions:

$$\dot{\omega}_T = -\sum_{k=1}^{N_s} \Delta h^0_{f,k}\, \dot{\omega}_k, \tag{1.26}$$

we have:

$$\partial_t(\rho\, e) + \mathrm{div}(\rho\, e\, \boldsymbol{v}) + \sum_{k=1}^{N_s} \mathrm{div}(h_k\, \boldsymbol{j}_k) + p\, \mathrm{div}\boldsymbol{v} - \mathrm{div}(\lambda\boldsymbol{\nabla} T) = \dot{\omega}_T + \boldsymbol{\tau}(\boldsymbol{v}) : \boldsymbol{\nabla}\boldsymbol{v}, \tag{1.27}$$

where h_k is the sensible enthalpy of species k obtained using the following expression:

$$h_k = h_{c,k} - \Delta h^0_{f,k}, \qquad \text{for } 1 \le k \le N_s.$$

Redefining the heat flux as:

$$\boldsymbol{q} = -\lambda\boldsymbol{\nabla} T + \sum_{k=1}^{N_s} h_k\, \boldsymbol{j}_k, \tag{1.28}$$

we finally have the sensible energy balance equation:

$$\partial_t(\rho\, e) + \mathrm{div}(\rho\, e\, \boldsymbol{v}) + \mathrm{div}(\boldsymbol{q}) + p\, \mathrm{div}\boldsymbol{v} = \dot{\omega}_T + \boldsymbol{\tau}(\boldsymbol{v}) : \boldsymbol{\nabla v}. \tag{1.29}$$

The heat diffusivity coefficient defined by

$$D_{th} = \frac{\lambda}{\rho\, c_{\mathrm{p}}}, \tag{1.30}$$

is usually linked to the diffusion coefficient D_k, $1 \le k \le N_s$ through the Lewis number of the species k, which compares the diffusion speeds of heat and species k, given by:

$$\mathrm{Le}_k = \frac{\lambda}{\rho\, c_{\mathrm{p}}\, D_k} = \frac{D_{th}}{D_k}. \tag{1.31}$$

This latest non-dimensional number can also be rewritten in the following way:

$$\mathrm{Le}_k = \frac{\mathrm{Sc}_k}{\mathrm{Pr}}, \tag{1.32}$$

where the Prandtl number Pr, which characterize the ratio between momentum diffusivity and thermal diffusivity is given by:

$$\mathrm{Pr} = \frac{\mu\, c_{\mathrm{p}}}{\lambda}, \tag{1.33}$$

and the Schmidt number Sc_k, which is a dimensionless number given by the ratio of momentum diffusivity (viscosity) and mass diffusivity of the species k reads:

$$\mathrm{Sc}_k = \frac{\mu}{D_k\, \rho}.$$

In the framework of turbulent flows modelling, it is often assumed that the Prandtl number Pr is constant and takes a value of the order of unity, and that the Lewis number Le is also constant and equal to unity (see Hilbert et al. (2004) for a detailed review). These assumptions are often made in industrial softwares, since they considerably simplify the heat balance formulation. This choice is made here (let notice, moreover, that assumption (1.17) corresponds to a constant Lewis number). The Prandtl number being constant, according to (1.33), the thermal conductivity reads:

$$\lambda(\boldsymbol{x}, t) = \frac{\mu\, c_{\mathrm{p}}}{\mathrm{Pr}} = \frac{\mu}{\mathrm{Pr}} \sum_{k=1}^{N_s} c_{\mathrm{p},k}\, Y_k(\boldsymbol{x}, t). \tag{1.34}$$

Assuming a unity Lewis number, then according to (1.31) $\lambda = \rho c_p D$, thus the mass diffusion fluxes of chemical species are written as:

$$\text{for } 1 \le k \le N_s, \quad \boldsymbol{j}_k = -\frac{\mu}{\mathrm{Pr}}\, \boldsymbol{\nabla} Y_k. \tag{1.35}$$

Moreover, the assumption that Le = 1 allows to write:

$$-\frac{\mu}{\mathrm{Pr}} \boldsymbol{\nabla} h = -\frac{\mu}{\mathrm{Pr}}\, c_{\mathrm{p}} \boldsymbol{\nabla} T - \frac{\mu}{\mathrm{Pr}}\, T\, \boldsymbol{\nabla} c_{\mathrm{p}} = -\underbrace{\frac{\mu}{\mathrm{Pr}}\, c_{\mathrm{p}}}_{\lambda}\, \boldsymbol{\nabla} T + \sum_{k=1}^{N_s} c_{\mathrm{p},k}\, T\, \underbrace{(\mu/\mathrm{Pr}) \boldsymbol{\nabla} Y_k}_{\boldsymbol{j}_k}. \tag{1.36}$$

Hence, the sensible energy balance (1.29) may be recast as:

$$\partial_t(\rho\, e) + \mathrm{div}(\rho\, e\, \boldsymbol{v}) - \mathrm{div}[(\mu/\mathrm{Pr})\, \boldsymbol{\nabla} h] + p\, \mathrm{div}\boldsymbol{v} = \dot{\omega}_T + \boldsymbol{\tau}(\boldsymbol{v}) : \boldsymbol{\nabla v}. \tag{1.37}$$

Remark. (Constant specific molar heat capacity) For specific multi-component mixtures, the molar specific heat of the chemical species may be supposed to be independent of the species, which may be written:

$$\text{for } 1 \le k \le N_s, \qquad c_{\mathrm{p},k}\, W_k = cst = R\,\frac{\gamma}{\gamma - 1}, \tag{1.38}$$

where γ is the ratio $c_{\mathrm{p},k}/c_{\mathrm{v},k}$, thus supposed to be constant. In this case, the sensible energy balance (1.37) may be rewritten as:

$$\partial_t(\rho\, e) + \operatorname{div}(\rho\, e\, \boldsymbol{v}) - \operatorname{div}\left[\frac{\mu\,\gamma}{\mathrm{Pr}}\,\boldsymbol{\nabla} e\right] + p\,\operatorname{div}\boldsymbol{v} = \dot{\omega}_T + \boldsymbol{\tau}(\boldsymbol{v}) : \boldsymbol{\nabla}\boldsymbol{v}. \tag{1.39}$$

State law

Finally, an equation of state is required to close the system, assuming a mixture of perfect gases:

$$p = \rho\,\frac{R}{W}\,T. \tag{1.40}$$

Note that, this relation has to be complemented by the following equation linking e and T:

$$e = \sum_{k=1}^{N_s} Y_k\, e_k = \sum_{k=1}^{N_s} Y_k\, c_{\mathrm{v},k}\, T = \sum_{k=1}^{N_s}\left(c_{\mathrm{p},k} - \frac{R}{W_k}\right) Y_k\, T, \tag{1.41}$$

with $c_{\mathrm{v},k}$ the heat capacity at constant volume of the species k.

The set of conservation equations used in this work are summarized-up in Table 1.2.

Name	Conservation equation
Mass	$\partial_t\rho + \operatorname{div}(\rho\boldsymbol{v}) = 0$
Chemical species	$\partial_t(\rho\, Y_k) + \operatorname{div}(\rho\, Y_k\, \boldsymbol{v}) - \operatorname{div}\Big(\frac{\mu}{\mathrm{Pr}}\,\boldsymbol{\nabla} Y_k\Big) = \dot{\omega}_k, \qquad \text{for } 1 \le k \le N_s$
Momentum	$\partial_t(\rho\, \boldsymbol{v}) + \operatorname{div}(\rho\boldsymbol{v} \otimes \boldsymbol{v}) + \boldsymbol{\nabla} p - \operatorname{div}(\boldsymbol{\tau}(\boldsymbol{v})) = \boldsymbol{f}$
Sensible energy	$\partial_t(\rho\, e) + \operatorname{div}(\rho\, e\, \boldsymbol{v}) - \operatorname{div}\left[\frac{\mu}{\mathrm{Pr}}\,\boldsymbol{\nabla} h\right] + p\,\operatorname{div}\boldsymbol{v} = \dot{\omega}_T + \boldsymbol{\tau}(\boldsymbol{v}) : \boldsymbol{\nabla}\boldsymbol{v}$
State law	$p = \rho\,\frac{R}{W}\,T$

Table 1.2: Conservation equations with unitary Lewis assumption and an identical diffusion coefficient for all species. The viscous stress tensor is given by (1.2) and the heat production rate by (1.26). Relation (1.41) closes the system.

1.2 Turbulence approaches

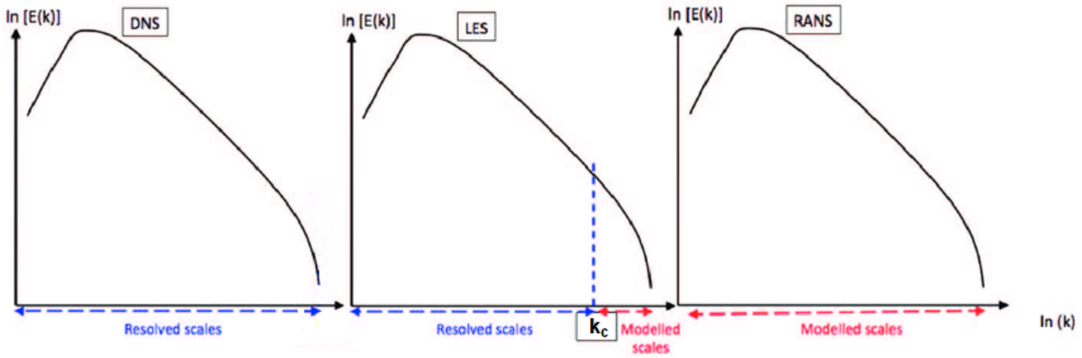

Figure 1.1: Energy spectra repartition of resolved and modeled scales for DNS, LES and RANS approaches.

Most of the time, an analytical solution does not exist to properly deal with such complex phenomena as turbulent reactive flows. Hence, for most of the cases, to predict the evolution of turbulent reactive flows and the phenomenon attributed to it, one uses CFD tools consisting of turbulence and combustion models. These models are simplified constitutive equations that predict the evolution (depending on the modeling technique) of certain quantities of turbulent flows. The three main approaches to simulate turbulent flows are:

- Direct Numerical Simulation (DNS)

The DNS approach is the most accurate technique. It resolves the set of equations of motions with initial and boundary conditions appropriate to the flow considered without any use of a turbulence model. The whole range of turbulent scales is solved explicitly. The turbulent energy spectrum is completely resolved as shown on the left in Fig. 1.1. However, a DNS approach is too expensive to be applied outside academic purposes. Therefore the amount of information needs to be reduced.

- Reynolds Averaged Navier Stokes (RANS)

Statistical approaches are used in an attempt to reduce the complexity and cost of the numerical simulation. Any instantaneous unknown φ is decomposed into a mean/averaged part $\bar{\varphi}$ and a fluctuating part φ': $\varphi = \bar{\varphi} + \varphi'$. This procedure is called the Reynolds averaging, initially introduced by Reynolds (1895). The averaging operation corresponds to a statistical average over a certain number of realizations of the same physical event. With this approach, only averaged quantities $\bar{\varphi}$ are resolved. The averaging operations introduce unresolved terms, containing the information on fluctuations. Such terms require specific closures. The whole energy spectrum is modeled as shown at the right side of Fig. 1.1. Solving mean quantities allows a relatively coarse grid which reduces the numerical cost. In addition, assumptions such as symmetry, two dimensional domains may be applied. RANS approach is the most spread technique in industrial codes because it allows to simulate reactive flows in large scale domains at a low computational cost.

- Large Eddy Simulation (LES)

Large Eddy Simulation approach is an intermediate approach between DNS and RANS in terms of precision and numerical cost. The large scales of the flow are resolved explicitly, as in DNS, while the small scales dissipation are modeled. The spectrum with the large resolved scales and the small modeled scales distribution is shown in the middle part of Fig. 1.1. Large eddies are the most effective transporters of conserved quantities (mass, momentum and energy). Small eddies are weaker and a well established hypothesis is that they show a universal behavior. They are assumed to be isotropic irrespective of the Reynolds number and geometry of the flow. In LES, the instantaneous equations are filtered. The separation between the large scales and the small scales is achieved with the help of spatial filters (detailed in Section 1.3.1). The size of the smallest resolved eddies is related to the filter width. When the filter size tends to 0, the resolution of the LES approaches tends to the DNS resolution. The filtering procedure brings unresolved terms containing information at the unresolved scales and information relative to energy transfer between resolved and unresolved scales. These unresolved terms are closed using subgrid models (see Section 1.3.3).

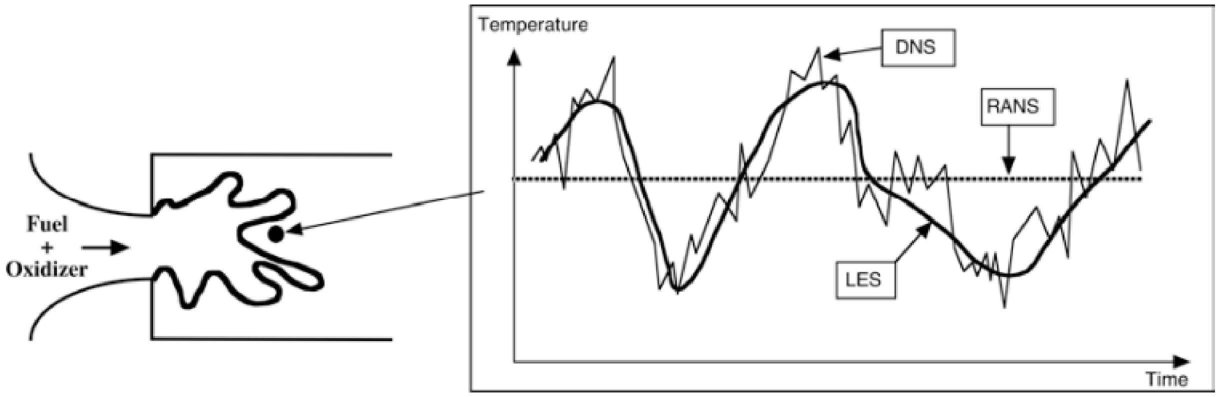

Figure 1.2: Representation of the expected temporal evolution of a temperature for DNS, LES and RANS approaches (Poinsot and Veynante, 2012).

Figure 1.2 shows an example of the local temperature variation computed with each approach. DNS approach predicts turbulence and recovers well the instantaneous fields like a high-resolution sensor would measure them in an experiment. LES delivers less information than the DNS approach for simulating turbulent motions, but it would capture the temperature low-frequency fluctuations and recover quite well the instantaneous fields. As the whole spectra is modeled for the RANS approach, the temperature predicted is a constant corresponding to the mean temperature.

The LES approach is chosen for the investigations made in this work and is detailed in the following Section.

1.3 The Large Eddy Simulation approach

In this section the LES approach is detailed and the filtered equations are established.

1.3.1 Filtering operator

Large and small scales are separated using a low-pass filter in frequency. The energy spectrum is thus partitioned into two parts: $[0, k_c]$ and $[k_c, +\infty]$ with k_c the cutoff wave number. The first part is the turbulent large scales energy spectrum contribution and the second part is the small scales energy spectrum contribution (see Fig. 1.3).

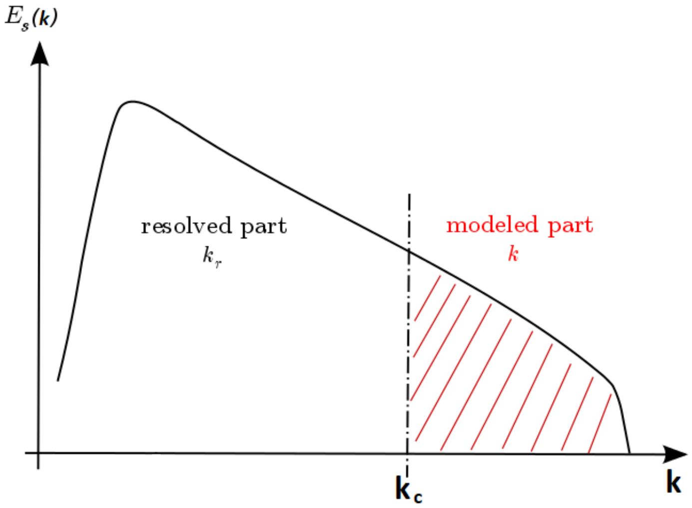

Figure 1.3: Turbulence energy spectrum plotted as a function of the wave number. k_c being the cutoff wave number used in LES.

Filtering is represented mathematically in the physical space as a convolution product. The resolved part $\overline{\phi}(\boldsymbol{x}, t)$ of a space-time variable $\phi(\boldsymbol{x}, t)$ is defined by (Garnier et al., 2009):

$$\overline{\phi}(\boldsymbol{x}) = \frac{1}{\boldsymbol{\Delta}^d} \int_{\mathbb{R}^d} G\left(\frac{\boldsymbol{x} - \boldsymbol{\xi}}{\boldsymbol{\Delta}}\right) \phi(\boldsymbol{\xi}) \mathrm{d}\boldsymbol{\xi}. \tag{1.42}$$

where the convolution kernel G is characteristic of the filter used and is associated with the cutoff scale in space $\boldsymbol{\Delta}$. We assume that the space convolution kernel is obtained by tensorial extension of the one-dimensional kernel, *i.e.*:

$$G(\boldsymbol{\xi}) = \prod_{i=1}^{d} G_i(\xi_i).$$

The filtering operator respects the three properties given below. The first one is satisfied by the convolution form of the filtering, while the latter ones depend on the filtering function G.

- Linearity,

$$\overline{\phi + \psi} = \overline{\phi} + \overline{\psi}. \tag{1.43}$$

- Consistency,

$$\overline{\phi} = \phi \iff \int_{\mathbb{R}^d} G\left(\boldsymbol{\xi}\right) \mathrm{d}^3\boldsymbol{\xi} = 1, \qquad \text{if } \phi = \mathit{constant}. \tag{1.44}$$

- Commutation with derivation,

$$\overline{\partial_s \phi} = \partial_s \overline{\phi} \qquad s = \boldsymbol{x}, t. \tag{1.45}$$

This latter property is needed in order to establish the balance equations for the filtered variables. But, for an inhomogeneous or anisotropic filter, the commutation of derivative and filtering operators is generally not verified. Thus, spatial commutation errors may occur when the filter varies with time and/or space, especially when the domain is bounded by walls or when the mesh size is not uniform. Previous studies (Ghosal and Moin, 1995; Ghosal, 2004; Moureau et al., 2005) have characterized commutativity errors. In general, uncertainties due to this operator exchange are neglected and their effects are assumed to be incorporated in the subgrid scale model.

The most common filters are given in the following.

- **Sharp cut-off filter** – The spectral expression of the sharp cut-off filter is given by:

  $$\hat{G}(\kappa) = \begin{cases} 1 & \text{if } \kappa \leq \kappa_c \\ \\ 0 & \text{otherwise.} \end{cases} \tag{1.46}$$

  The sharp cut-off filter is represented by its kernel in physical space:

  $$G(\boldsymbol{x} - \boldsymbol{\xi}) = \frac{\sin\left(\frac{\pi}{\Delta}(\boldsymbol{x} - \boldsymbol{\xi})\right)}{\left(\frac{\pi}{\Delta}(\boldsymbol{x} - \boldsymbol{\xi})\right)}. \tag{1.47}$$

- **Box filter** – The physical expression of the box filter is given by:

  $$G(\boldsymbol{x} - \boldsymbol{\xi}) = \begin{cases} \dfrac{1}{\Delta^d} & \text{if } |x_i - \xi_i| \leq \Delta/2,\ 1 \leq i \leq d \\ \\ 0 & \text{otherwise} \end{cases} \tag{1.48}$$

  This filter corresponds to an averaging over a cubic box of size Δ. The spectral expression of the box filter is:

  $$\hat{G}(\kappa) = \frac{\sin(\kappa\Delta/2)}{\kappa\Delta/2}, \tag{1.49}$$

  where κ is the spatial wave number.

- **Gaussian filter** – Another well known filter is the Gaussian filter defined as:

  $$G(\boldsymbol{x} - \boldsymbol{\xi}) = \left(\frac{6}{\pi\Delta^2}\right)^{3/2} \exp\left[-\frac{6}{\Delta^2}\sum_{i=1}^{d}(x_i - \xi_i)^2\right], \tag{1.50}$$

  for the physical expression with d the computable domain dimension. Its kernel in spectral space is given by:

  $$\hat{G}(\kappa) = \exp\left(-\frac{\Delta^2\kappa^2}{24}\right). \tag{1.51}$$

As stated before, applying one of the operators introduced above to a space-time variable $\phi(\boldsymbol{x},t)$ leads to the filtered quantity $\overline{\phi}(\boldsymbol{x},t)$ which represent the resolved turbulent structures. The small (non-resolved) structures (*i.e.* the structures smaller than the filter width) are defined by (Garnier et al., 2009):

$$\phi'(\boldsymbol{x},t) = \phi(\boldsymbol{x},t) - \overline{\phi}(\boldsymbol{x},t).$$

This decomposition is formally analogous to the Reynolds decomposition but it should be pointed out here that in general:

$$\overline{\overline{\phi}} \neq \overline{\phi} \qquad \overline{\phi'} \neq 0. \tag{1.52}$$

The classical LES filtering in compressible flows has been employed by some authors (Yoshizawa, 1986; Bodony and Lele, 2005), but most authors dealing with LES of compressible flows have used a change of variable in which filtered variables are weighted by the density (Garnier et al., 2009). This operation is the Favre filtering and is written:

$$\overline{\rho\phi} = \overline{\rho}\,\frac{\overline{\rho\phi}}{\overline{\rho}} = \overline{\rho}\widetilde{\phi} \tag{1.53}$$

where $\widetilde{\phi}$ is the so called Favre filtered quantity. The quantity ϕ may be decomposed into mean and fluctuating components such as:

$$\phi = \widetilde{\phi} + \phi''. \tag{1.54}$$

The motivation of using such filtering operator is double. First, filtering the balance equations with the classical LES filter defined previously would lead to additional subgrid terms which are avoided by using the Favre filtering. Second, the Favre-filtered equations are structurally similar to their corresponding non filtered equations (with the exception of the subgrid terms). One should keep in mind that the Favre filtering is a mathematical formalism and should be taken into account when the results are compared to DNS or experimental data (Sagaut and Grohens, 1999).

1.3.2 Filtered governing equations

The filtering operator is applied to the instantaneous system of equations introduced in Section 1.1. For each balance equation, the large scales terms (resolved terms) and the modeled small scales terms (unresolved terms) are presented. The small structures have an impact on the resolved structures. This effect is included through the subgrid scale (SGS) models (presented in Section1.3.3).

Hydrodynamics

Filtering the instantaneous mass balance (1.1a) and the momentum balance (1.1b) leads to:

$$\partial_t\overline{\rho} + \mathrm{div}(\overline{\rho}\,\widetilde{\boldsymbol{v}}) = 0, \tag{1.55}$$

$$\partial_t(\overline{\rho}\,\widetilde{\boldsymbol{v}}) + \mathrm{div}(\overline{\rho}\,\widetilde{\boldsymbol{v}} \otimes \widetilde{\boldsymbol{v}}) + \mathrm{div}\left[\overline{\rho}\,(\widetilde{\boldsymbol{v} \otimes \boldsymbol{v}} - \widetilde{\boldsymbol{v}} \otimes \widetilde{\boldsymbol{v}})\right] + \boldsymbol{\nabla}\overline{p} - \mathrm{div}\overline{\boldsymbol{\tau}} = \overline{\rho\,\boldsymbol{f}}. \tag{1.56}$$

The filtered laminar fluxes and unresolved terms introduced in the filtered momentum balance must be closed:

- The laminar filtered stress tensor for a Newtonian fluid $\overline{\boldsymbol{\tau}}$ is given by:

$$\overline{\boldsymbol{\tau}} = \overline{2\mu\left(\mathbf{S} - \frac{1}{3}\mathrm{Tr}(\mathbf{S})\boldsymbol{I}\right)} \approx 2\overline{\mu}\left(\widetilde{\mathbf{S}} - \frac{1}{3}\mathrm{Tr}(\widetilde{\mathbf{S}})\boldsymbol{I}\right), \tag{1.57}$$

  where $\overline{\mu}$ is the filtered laminar viscosity (with the assumption: $\overline{\mu} \approx \mu$), $\boldsymbol{I}$ stands for the $\mathbb{R}^{d\times d}$ identity matrix and $\widetilde{\mathbf{S}}$ is the rate-of-strain tensor of the resolved structures given by:

$$\widetilde{\mathbf{S}} = \frac{1}{2}\left(\boldsymbol{\nabla}\widetilde{\boldsymbol{v}} + \boldsymbol{\nabla}^t\widetilde{\boldsymbol{v}}\right). \tag{1.58}$$

- The Boussinesq (1877) hypothesis is essentially valid within the cascade theory of turbulence of Kolmogorov (1941) leading to the following model for the unresolved Reynolds stress tensor:

$$\boldsymbol{\tau}^{SGS} = \overline{\rho}\,(\widetilde{\boldsymbol{v}\otimes\boldsymbol{v}} - \widetilde{\boldsymbol{v}}\otimes\widetilde{\boldsymbol{v}}) \approx -2\mu_{SGS}\left(\widetilde{\mathbf{S}} - \frac{1}{3}\mathrm{Tr}(\widetilde{\mathbf{S}})\boldsymbol{I}\right) \tag{1.59}$$

  where the subgrid scale viscosity μ_{SGS} is computed by a subgrid scale turbulence model (see Section 1.3.3).

Transport of chemical species

Filtering the system of mass balance equations for the chemical species (1.9) yields:

$$\partial_t(\overline{\rho}\,\widetilde{Y}_k) + \mathrm{div}(\overline{\rho}\,\widetilde{Y}_k\,\widetilde{\boldsymbol{v}}) + \mathrm{div}\left[\overline{\rho}\,(\widetilde{\boldsymbol{v}\,Y_k} - \widetilde{\boldsymbol{v}}\,\widetilde{Y}_k)\right] + \mathrm{div}(\overline{\boldsymbol{j}_k}) = \overline{\dot{\omega}_k}, \qquad \text{for } 1 \leq k \leq N_s \tag{1.60}$$

The filtered laminar fluxes and unresolved terms introduced are closed by:

- Using the assumptions stated earlier (Fick's law, unitary Lewis number, same diffusion coefficient for all chemical species), the laminar diffusive species fluxes read:

$$\overline{\boldsymbol{j}_k} = -\overline{\rho D\boldsymbol{\nabla}Y_k} \approx -\overline{\rho}\overline{D}\boldsymbol{\nabla}\widetilde{Y}_k = -\frac{\overline{\mu}}{\mathrm{Sc}}\boldsymbol{\nabla}\widetilde{Y}_k, \qquad \text{for } 1 \leq k \leq N_s \tag{1.61}$$

  where Sc stands for the laminar Schmidt number (replaced now on by the laminar Prandtl number Pr thanks to the unitary Lewis number assumption).

- The unresolved transport species fluxes is expressed using a diffusion-like model:

$$\boldsymbol{j}_k^{SGS} = \overline{\rho}\,(\widetilde{\boldsymbol{v}\,Y_k} - \widetilde{\boldsymbol{v}}\,\widetilde{Y}_k) \approx -\overline{\rho}\,D_{SGS}\boldsymbol{\nabla}\widetilde{Y}_k = -\frac{\mu_{SGS}}{\mathrm{Sc}_t}\boldsymbol{\nabla}\widetilde{Y}_k, \qquad \text{for } 1 \leq k \leq N_s \tag{1.62}$$

  where D_{SGS} is the SGS diffusion coefficient and Sc_t is the turbulent Schmidt number (replaced now on by the turbulent Prandtl number Pr_t by assuming the same subgrid scale thermal and species diffusion).

- Different models exist for the filtered reaction rate $\overline{\dot{\omega}_k}$. They are discussed in Chapter 2 together with combustion regimes.

Energy balance

Filtering the sensible energy balance (1.29) equation leads to:

$$\begin{aligned}\partial_t(\overline{\rho}\,\widetilde{e}) + \mathrm{div}(\overline{\rho}\,\widetilde{\boldsymbol{v}}\,\widetilde{e}) + \mathrm{div}(\overline{\boldsymbol{q}}) + \overline{p}\,\mathrm{div}(\widetilde{\boldsymbol{v}}) - \check{\boldsymbol{\Phi}} - \overline{\dot{\omega}_T} \\ = -\mathrm{div}\left[\overline{\rho}\,(\widetilde{\boldsymbol{v}\,e} - \widetilde{\boldsymbol{v}}\,\widetilde{e})\right] - \left[\overline{p\,\mathrm{div}(v)} - \overline{p}\,\mathrm{div}(\widetilde{\boldsymbol{v}})\right] + \left[\overline{\boldsymbol{\Phi}} - \check{\boldsymbol{\Phi}}\right] \qquad (1.63)\end{aligned}$$

The filtered computable and unresolved terms are the following:

- The filtered computable viscous dissipation is given by:

  $$\check{\boldsymbol{\Phi}} = \overline{\boldsymbol{\tau}}(\widetilde{\boldsymbol{v}}) : \boldsymbol{\nabla}\widetilde{\boldsymbol{v}} \qquad (1.64)$$

  where the filtered computable stress tensor $\overline{\boldsymbol{\tau}}$ is given by (1.57).

- The computable heat flux $\overline{\boldsymbol{q}}$ is expressed as:

  $$\overline{\boldsymbol{q}} \approx -\overline{\lambda}\boldsymbol{\nabla}\widetilde{T} + \sum_{k=1}^{N_s} \widetilde{h}_k\,\overline{\boldsymbol{j}_k}. \qquad (1.65)$$

  Using the assumptions stated earlier (Fick's law, unitary Lewis number, same diffusion coefficient for all chemical species), analogously to (1.36), the heat flux can be expressed as:

  $$\overline{\boldsymbol{q}} \approx -\frac{\overline{\mu}}{\mathrm{Pr}}\boldsymbol{\nabla}\widetilde{h}. \qquad (1.66)$$

- The computable heat production rate is written as:

  $$\overline{\dot{\omega}_T} = -\sum_{k=1}^{N_s} \Delta h^0_{f,k}\,\overline{\dot{\omega}_k}. \qquad (1.67)$$

- The SGS heat flux is modelled by:

  $$\boldsymbol{q}^{SGS} = \overline{\rho}\,(\widetilde{\boldsymbol{v}e} - \widetilde{\boldsymbol{v}}\widetilde{e}) \approx -\lambda_{SGS}\boldsymbol{\nabla}\widetilde{T} + \sum_{k=1}^{N_s} \widetilde{h}_k\,\boldsymbol{j}_k^{SGS}, \qquad (1.68)$$

  with $\lambda_{SGS} = \mu_{SGS}\,c_p/\mathrm{Pr}_t$ the subgrid scale conductivity. Analogously to the resolved heat flux, the subgrid heat flux could be written as:

  $$\boldsymbol{q}^{SGS} \approx -\frac{\mu_{SGS}}{\mathrm{Pr}_t}\boldsymbol{\nabla}\widetilde{h}. \qquad (1.69)$$

- The SGS pressure-dilatation term can be written as:

  $$\Pi^{dil} = \overline{p\,\mathrm{div}(v)} - \overline{p}\,\mathrm{div}(\widetilde{\boldsymbol{v}}). \qquad (1.70)$$

  It will be neglected in this work (Martin et al., 2000; Garnier et al., 2009).

- The SGS viscous dissipation is expressed as:

$$\epsilon_v = \overline{\boldsymbol{\Phi}} - \check{\boldsymbol{\Phi}} = \overline{\boldsymbol{\tau}(\boldsymbol{v}) : \boldsymbol{\nabla}\boldsymbol{v}} - \overline{\boldsymbol{\tau}}(\widetilde{\boldsymbol{v}}) : \boldsymbol{\nabla}\widetilde{\boldsymbol{v}}. \tag{1.71}$$

  Various models exist for the SGS viscous dissipation term (Yoshizawa, 1986; Vreman et al., 1995; Martin et al., 2000). In this work, we choose to model ϵ_v in order to recover a conservative form of the total energy balance. First, let us obtain the filtered kinetic energy balance equation by the inner product of the filtered momentum balance equation with the filtered velocity:

$$\frac{1}{2}\,\partial_t(\overline{\rho}\,|\widetilde{\boldsymbol{v}}|^2) + \frac{1}{2}\,\mathrm{div}\left(\overline{\rho}\,|\widetilde{\boldsymbol{v}}|^2\,\widetilde{\boldsymbol{v}}\right) + \boldsymbol{\nabla}\overline{p}\cdot\widetilde{\boldsymbol{v}} - \mathrm{div}\overline{\boldsymbol{\tau}}(\widetilde{\boldsymbol{v}})\cdot\widetilde{\boldsymbol{v}} = -\mathrm{div}\boldsymbol{\tau}^{SGS}(\widetilde{\boldsymbol{v}})\cdot\widetilde{\boldsymbol{v}} \tag{1.72}$$

  Summing equations (1.63) and (1.72) gives rise to the filtered total energy balance equation:

$$\begin{aligned}\partial_t(\overline{\rho}\,\widetilde{E}) + \mathrm{div}(\overline{\rho}\,\widetilde{\boldsymbol{v}}\,\widetilde{E}) + \mathrm{div}(\overline{p}\,\widetilde{\boldsymbol{v}}) - \mathrm{div}\left(\overline{\boldsymbol{\tau}}(\widetilde{\boldsymbol{v}})\cdot\widetilde{\boldsymbol{v}}\right) - \overline{\dot{\omega}_T}&\\ = -\mathrm{div}(\overline{\boldsymbol{q}} - \boldsymbol{q}^{SGS}) - \mathrm{div}\left(\boldsymbol{\tau}^{SGS}(\widetilde{\boldsymbol{v}})\cdot\widetilde{\boldsymbol{v}}\right) + \boldsymbol{\tau}^{SGS}(\widetilde{\boldsymbol{v}}) : \boldsymbol{\nabla}\widetilde{\boldsymbol{v}} + \epsilon_v.&\end{aligned} \tag{1.73}$$

  In order to obtain a conservative form of the previous equation, the SGS viscous dissipation is modelled by:

$$\epsilon_v = -\boldsymbol{\tau}^{SGS}(\widetilde{\boldsymbol{v}}) : \boldsymbol{\nabla}\widetilde{\boldsymbol{v}} \tag{1.74}$$

  Therefore the filtered internal energy balance equation reads:

$$\partial_t(\overline{\rho}\,\widetilde{e}) + \mathrm{div}(\overline{\rho}\,\widetilde{\boldsymbol{v}}\,\widetilde{e}) + \overline{p}\,\mathrm{div}(\widetilde{\boldsymbol{v}}) = \overline{\dot{\omega}_T} - \mathrm{div}(\overline{\boldsymbol{q}} - \boldsymbol{q}^{SGS}) + \check{\boldsymbol{\tau}}(\widetilde{\boldsymbol{v}}) : \boldsymbol{\nabla}\widetilde{\boldsymbol{v}} \tag{1.75}$$

  where $\check{\boldsymbol{\tau}}(\widetilde{\boldsymbol{v}}) = \overline{\boldsymbol{\tau}}(\widetilde{\boldsymbol{v}}) - \boldsymbol{\tau}^{SGS}(\widetilde{\boldsymbol{v}})$.

1.3.3 Subgrid scale viscosity models

In this section, some models for the subgrid scale viscosity are introduced.

Smagorinsky model

The Smagorinsky model is the most popular and simplest model to obtain the subgrid scale viscosity (Smagorinsky, 1963). The eddy viscosity is expressed as follows:

$$\mu_{SGS} = \overline{\rho}\,c_s^2\Delta^2|\widetilde{\mathbf{S}}|, \tag{1.76}$$

with $|\widetilde{\mathbf{S}}|$ the resolved rate-of-stain magnitude given by:

$$|\widetilde{\mathbf{S}}| = \left(2\sum_{i=1}^{d}\sum_{j=1}^{d}\widetilde{S}_{ij}\widetilde{S}_{ij}\right)^{1/2}, \tag{1.77}$$

c_s a constant and Δ the characteristic filter length. The constant parameter c_s is usually taken in the range $0.1 - 0.2$.

WALE (Wall-Adapting Local Eddy-viscosity) model

The Smagorinsky model being too dissipitave especially near walls, Nicoud and Ducros (1999) introduce the WALE model in order to take recover the scaling laws at the walls. The eddy viscosity is modeled by:

$$\mu_{SGS} = \overline{\rho}\, c_W^2 \Delta^2 \frac{\left(\sum_{i,j} \widetilde{s}^d_{ij}\widetilde{s}^d_{ij}\right)^{3/2}}{\left(\sum_{i,j} \widetilde{S}_{ij}\widetilde{S}_{ij}\right)^{5/2} + \left(\sum_{i,j} \widetilde{s}^d_{ij}\widetilde{s}^d_{ij}\right)^{5/4}}, \tag{1.78}$$

where c_W is the model constant, set at 0.5, and s^d_{ij} is the traceless symmetric part of the square of the resolved velocity gradiant defined as:

$$\widetilde{s}^d_{ij} = \frac{1}{2}\left(\boldsymbol{\nabla}\widetilde{\boldsymbol{v}}^2 + (\boldsymbol{\nabla}\widetilde{\boldsymbol{v}}^2)^t\right) - \frac{1}{3}\mathrm{Tr}(\boldsymbol{\nabla}\widetilde{\boldsymbol{v}}^2)\boldsymbol{I}. \tag{1.79}$$

Dynamic Smagorinsky model

An alternative method for calculating the Reynolds stresses is to use a second filter of a size larger than that of the LES filter and to estimate the small scale dissipation from the knowledge of the resolved eddies. This procedure was originally proposed by Germano et al. (1991). The dynamic procedure is usually combined with a subgrid scale viscosity model, but it is very general and can be applied to any model that makes explicit use of an arbitrary model constant.

Here, the dynamic procedure is described for the Smagorinsky model. A test filter of width $\widehat{\Delta}$ larger than the LES filter size, $\widehat{\Delta} > \Delta$, is introduced. Thanks to this second filtering, the model constant c_s, which is strongly affected by the configuration of flows, is no more a constant but dynamically adjusted at each point in space and at each time step. The constant becomes then time and space-dependent: $c_s(\boldsymbol{x}, t)$.

The subgrid stress tensor at the test filtering level reads:

$$T_{ij} = \widehat{\overline{\rho\, v_i\, v_j}} - \frac{1}{\widehat{\overline{\rho}}}\,\widehat{\overline{\rho\, v_i}}\,\widehat{\overline{\rho\, v_j}} \tag{1.80}$$

where $\widehat{\cdot}$ stands for the filtering at the test level and $1 \leq i, j \leq d$. Subtracting the SGS Reynolds stress tensor after filtering with the test filter yields the Germano identity:

$$\boldsymbol{\mathcal{L}}_{ij} = T_{ij} - \widehat{\tau^{SGS}_{ij}} \tag{1.81}$$

with

$$\boldsymbol{\mathcal{L}}_{ij} = \widehat{\overline{\rho}\,\widetilde{v}_i\,\widetilde{v}_j} - \frac{1}{\widehat{\overline{\rho}}}\,\widehat{\overline{\rho}\,\widetilde{v}_i}\,\widehat{\overline{\rho}\,\widetilde{v}_j} \tag{1.82}$$

Let notice that all quantities in the Germano identity (1.81) are known (left hand side from the resolved flow field, right hand side through the model). Applying the Smagorinsky model, the two subgrid stress tensors T and τ^{SGS} are written as:

$$\tau^{SGS}_{ij} - \frac{\delta_{ij}}{3}\,\tau^{SGS}_{kk} = -2\,\overline{\rho}\,c_s\,\Delta^2\,|\widetilde{\mathbf{S}}|\left(\widetilde{S}_{ij} - \frac{\delta_{ij}}{3}\widetilde{S}_{kk}\right) = c_s\;\beta_{ij} \tag{1.83}$$

$$T_{ij} - \frac{\delta_{ij}}{3}\,T_{kk} = -2\,\widehat{\overline{\rho}}\,c_s\,\widehat{\Delta}^2\,|\widehat{\widetilde{\mathbf{S}}}|\left(\widehat{\widetilde{S}}_{ij} - \frac{\delta_{ij}}{3}\widehat{\widetilde{S}}_{kk}\right) = c_s\;\alpha_{ij} \tag{1.84}$$

where we assume that the same constant c_s for both filtering levels can be used. The constant c_s is thus the dynamical parameter to determine, α_{ij} and β_{ij}, $1 \leq i, j \leq d$ are lightening notations. Introducing relations (1.83) and (1.84) in (1.81) leads to:

$$\mathcal{L}^d_{ij} = \mathcal{L}_{ij} - \frac{\delta_{ij}}{3}\,\mathcal{L}_{kk} = c_s\,\alpha_{ij} - \widehat{c_s\,\beta_{ij}}. \tag{1.85}$$

This relation gives a set of equations, where the only unknown term is the model constant c_s. The model parameter c_s may be determined by minimizing the following error:

$$E_{ij} = \mathcal{L}^d_{ij} - c_s\,\alpha_{ij} + c_s\widehat{\beta_{ij}}, \tag{1.86}$$

where c_s is supposed to be constant over an interval at least equal to the test filter cutoff length, *i.e.* $\widehat{c_s\,\beta_{ij}} = c_s\widehat{\beta_{ij}}$. The definition (1.86) consists of six independent relations (if $d = 3$, or four if $d = 2$), which in theory makes it possible to compute six values (if $d = 3$, or four if $d = 2$) of the constant (Garnier et al., 2009). In order to maintain a single relation and thereby determine a single value of the constant, Germano et al. (1991) propose to contract the relation (1.86) with the resolved strain rate tensor. c_s is thus found by solving:

$$\frac{\partial(E_{ij}\,\widetilde{S}_{ij})}{\partial c_s} = 0. \tag{1.87}$$

This problem is however indeterminate when the tensor S_{ij} cancels out (Garnier et al., 2009). To remedy this problem, Lilly (1992) proposes to calculate the constant c_s by a least-squares method. The model constant becomes then a solution of:

$$\frac{\partial(E_{ij}\,E_{ij})}{\partial c_s} = 0, \tag{1.88}$$

or more explicitly:

$$c_s = \frac{M_{ij}\,\mathcal{L}^d_{ij}}{M_{kl}\,M_{kl}}, \tag{1.89}$$

with $M_{ij} = \alpha_{ij} - \widehat{\beta_{ij}}$. In practical applications, to avoid negative values leading to numerical difficulties, c_s is not determined locally but averaged in homogeneous directions or along streamlines following a Lagrangian procedure (Meneveau et al., 1996).

Chapter 2

Premixed combustion: general notions and LES combustion models

Flames are usually classified in terms of chemical mixture (i.e. *fuel is perfectly premixed with oxidizer or not) and fluid state (* i.e. *the flow is laminar or turbulent). Then, four ideal regimes are identified, laminar premixed, laminar non-premixed (also called laminar diffusion flames), turbulent premixed and turbulent non-premixed flames (also called turbulent diffusion flames). In our framework, we consider explosions in the premixed flames regime. Balance equations described in Chapter 1 can be applied to each regime.*

In this chapter, we focus on laminar and turbulent premixed flames. After a description of the mean features of both kind of flames, the main combustion models used in the framework of large eddy simulations are introduced, thus allowing to close the combustion terms of the governing system of equations presented in Chapter 1.

2.1 Laminar premixed flames

2.1.1 Combustion regime

The equivalence ratio characterizes the combustion regime of a laminar premixed flame. It is defined by the ratio between the fuel mass fraction (Y_F) and the oxidizer mass fraction (Y_O) in the mixture divided by the same ratio at stoichiometric conditions:

$$\phi = \left(\frac{Y_F}{Y_O}\right) / \left(\frac{Y_F}{Y_O}\right)_{st} = s\left(\frac{Y_F}{Y_O}\right) \tag{2.1}$$

with s the mass stoichiometric ratio. Let assume that the species react through the following chemical reaction:

$$\nu'_F F + \nu'_O O \rightarrow \nu''_P P$$

the mass stoichiometric ratio reads:

$$s = \frac{\nu'_O W_O}{\nu'_F W_F}. \tag{2.2}$$

Combustion is considered lean when $\phi < 1$ (oxidizer in excess) or rich when $\phi > 1$ (fuel in excess). In a complete lean combustion, the fuel is entirely burnt and an amount of oxidant remains in the burnt mixture. In a complete rich combustion, theoretically, the oxidant is entirely consumed and an amount of fuel remains in the burnt mixture.

2.1.2 Flame structure

The structure of a stationary laminar premixed flame is shown in Fig. 2.1. This flame propagates like a wave from the burnt gases (on the right part of Fig. 2.1) to fresh gases (on the left part of Fig. 2.1) at a flame speed s_L with respect to the unburnt gases and perpendicular to the flame brush surface.

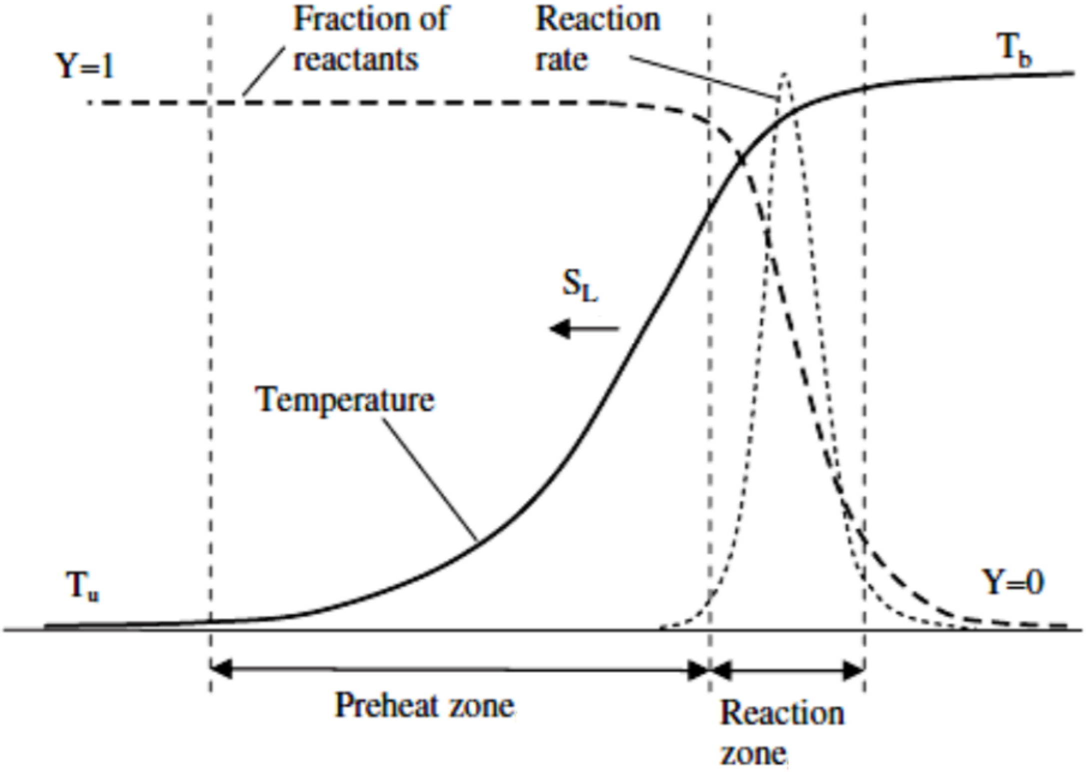

Figure 2.1: One-dimensional laminar premixed flame structure from Zeldovich et al. (1985).

The fresh gases are composed by fuel and oxidizer premixed at a given equivalence ratio with stable thermodynamic conditions. No reaction occurs in the unburnt zone. Ignition occurs when a threshold amount of energy called the activation energy is reached.

The flame front is usually decomposed into two zones: the preheated zone and the reaction zone. The preheated zone is characterized by strong temperature and concentration gradients. In this zone, the reactive terms are negligible compared to the diffusion terms and the temperature gradually rises until the ignition temperature of the mixture is reached. The chemical reaction occurs in the reaction zone. Usually, in the reaction zone, the temperature gradient is neglected and the temperature is assumed to have almost reached its maximum value. These assumptions are made by Zeldovich and Frank-Kamenetskii (1938) in most of their theories on flame propagation. The reactive zone is thinner than the preheat zone which makes it more difficult to numerically reproduce.

The burnt gases zone is on the right side of Fig. 2.1, it is the final state, where all reactants are transformed into products in case of complete chemical reaction. By making a low Mach number assumption combined with adiabatic boundaries conditions, the burnt gases temperature is equal to the adiabatic flame temperature.

2.1.3 Laminar flame features

Flame speeds

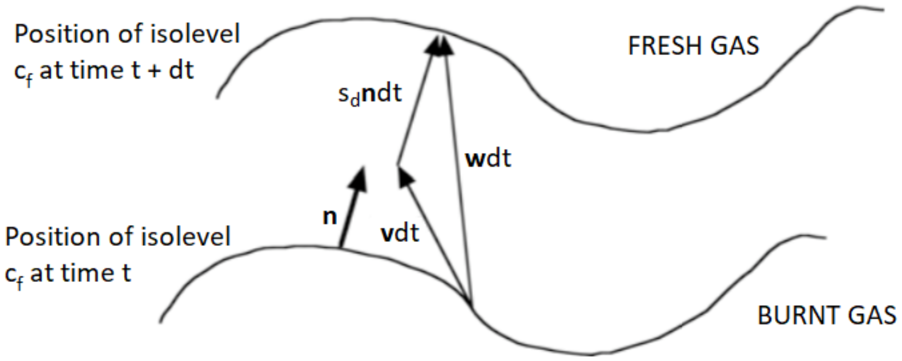

Figure 2.2: Notations for flame speed definitions (Poinsot and Veynante, 2012).

In a laminar flame, the combustion process results in a thin reaction surface travelling in the flow. We will consider that the flame front is infinitely thin and located at the isovalue surface $c = c_f$ (see Fig. 2.2) of a scalar function c going from zero (in the fresh gases) to one (in the burnt gases) and defined by:

$$c = \frac{Y_F - Y_F^u}{Y_F^b - Y_F^u} \quad \text{or} \quad c = \frac{T - T_u}{T_b - T_u} \tag{2.3}$$

where u and b are used as exponents or subscripts to denote quantities in the fresh (u) and in the burnt gas (b). The normal to the flame front pointing towards fresh gases is defined with the local gradient of c:

$$\mathbf{n} = -\frac{\nabla c}{|\nabla c|}. \tag{2.4}$$

The flame speed definition is a central point in combustion theory. Many definitions of local and global flame speeds exist in the literature (Poinsot and Veynante, 2012). The most commonly used are the following:

- The absolute flame speed is the flame front speed relative to a fixed reference frame located at the isovalue surface $c = c_f$. Its magnitude is given by:

$$s_a = \mathbf{w} \cdot \mathbf{n}, \tag{2.5}$$

  where $\mathbf{w}$ is the velocity of the isosurface and $\mathbf{n}$ the normal to the flame front represented on Fig. 2.2.

- The displacement speed is the flame front speed in the fluid reference that is the difference between the flow velocity $\boldsymbol{v}$ and the absolute flame speed (see Fig. 2.2). Its magnitude is given by:

$$s_d = (\mathbf{w} - \boldsymbol{v}) \cdot \mathbf{n} = s_a - \boldsymbol{v} \cdot \mathbf{n}. \tag{2.6}$$

- The consumption speed is the speed of reactant consumption. It is based on the flame chemical properties while the previous definitions are based on the kinematic properties of the flame. Its magnitude is defined with the fuel reaction rate:

$$s_c = -\frac{1}{\rho_u \left(Y_F^u - Y_F^b\right)} \int_{-\infty}^{+\infty} \dot{\omega}_F \, d\mathbf{n}, \tag{2.7}$$

  with ρ_u the density of the unburnt mixture. For planar laminar premixed flames, consumption speed and displacement speed are the same ($s_d = s_c$). This definition of s_L is used as the reference speed in order to compute the laminar flame speed in all studies in combustion.

Flame thickness

An other important feature of the laminar flame is the flame thickness. This thickness is also used as a reference length for numerical modeling. The flame thickness can be defined in different ways (Poinsot and Veynante, 2012). The most used are stated in the following.

- The diffusive thickness δ is given by:

$$\delta = \frac{\lambda_u}{\rho_u \, c_{p,u} \, s_L}, \tag{2.8}$$

  with λ_u and $c_{p,u}$ the thermal conductivity and the heat capacity of the fresh mixture respectively. Knowing the laminar flame speed, the flame thickness can be evaluated easily with the previous relation. Laminar flames propagates due to diffusion and chemical reactions, this thickness is therefore used in many approaches.

- An other definition is obtained using the temperature profile:

$$\delta_L^0 = \frac{T_b - T_u}{\max\left(|\nabla T|\right)}, \tag{2.9}$$

  where T_b and T_u are respectively the burnt and unburnt gases temperature.

- The total thickness δ_t corresponds to the temperature jump of 98% of the temperature difference between fresh and burnt gas. It is always larger than δ_L^0 and it is not used for computations.

- The thickness of the reaction zone δ_r is the thinnest thickness where chemical reaction occurs.

The time for the flame to cover a distance equal its own thickness is a characteristic time scale called the chemical time scale τ_c and is defined as:

$$\tau_c = \frac{\delta_L^0}{s_L}. \tag{2.10}$$

Flame stretch

In non-uniform flows, the flame may be stretched due to flow shear stress and the domain geometry. The flame stretch κ impacts its own velocity (Williams, 1985). It is defined by the fractional rate of change of a flame surface element A (Matalon and Matkowsky, 1982; Candel and Poinsot, 1990):

$$\kappa = \frac{1}{A}\frac{dA}{dt} \tag{2.11}$$

which can be expressed in a more global way using the shear stress and the curvature definitions:

$$\kappa = \nabla_t \cdot \boldsymbol{v} + s_d \nabla_t \cdot \mathbf{n}, \tag{2.12}$$

where ∇_t is the gradient velocity tangential component (Chung and Law, 1984). In expression (2.12), the term $\nabla_t \cdot \boldsymbol{v}$ is the flow shear stress due to the flow non-uniformity called strain rate and $s_d \nabla_t \cdot \mathbf{n}$ is due to the flame front curvature.

The flame front speed depends on its stretch. Asymptotic theories have shown under some conditions that the displacement speed s_d and consumption speed s_c are linear function of the stretch κ (Poinsot and Veynante, 2012; Quillatre, 2014):

$$\frac{s_d}{s_L} = 1 - \mathcal{L}_a^d \frac{\kappa}{s_L} \qquad \text{and} \qquad \frac{s_c}{s_L} = 1 - \mathcal{L}_a^c \frac{\kappa}{s_L} \tag{2.13}$$

with $\mathcal{L}_a^d$ and $\mathcal{L}_a^c$ the Markstein lengths for the displacement speed and consumption speed. Many expressions can be found in the literature for both lengths, for example see Clavin and Joulin (1983) expressions. However, expression (2.13) is correct only if the stretch is relatively low, the dynamic viscosity is constant, the Lewis number is close to unity, the Prandtl number is constant and the activation temperature is high.

2.2 Turbulent premixed flames

The turbulent combustion regimes have to be defined upstream as the developed models are based on physical analysis of the various length scales and characteristic times involved in combustion. The diagram of combustion regimes is presented in this section allowing to characterize the turbulent combustion. To do so, some definitions on characteristic quantities for turbulence and chemistry are first given. Then, a presentation of relevant models for turbulent combustion is given before ending this chapter with a brief description of the chemical models used in literature.

2.2.1 Turbulent combustion regimes

Chemistry is described mainly by one characteristic length scale δ_L^0 and the time needed to travel its own thickness (τ_c defined by (2.10)). Actually it is a very reducing assumption to considerate complex chemistry with only one space and time scale. Turbulence is described by different characteristic lengths and times ranging from the largest, the integral scale L_t and its time scale τ_t to the smallest one, the Kolmogorov length scale l_k and its time scale τ_k . To apprehend the wide range of scales at stake, some dimensionless numbers are defined here after:

- The flame Reynolds number Re_f is defined thanks to the Zeldovitch / Franck-Kamenetski (ZFK) theory (Zeldovich and Frank-Kamenetskii, 1938):

$$\mathrm{Re}_f = \frac{\delta_L^0 \, s_L}{\nu} \approx 1, \tag{2.14}$$

  with $\nu = \mu/\rho$ the flow kinematic viscosity.

- The Damköhler number Da quantifies the large scale turbulence effect on flames and is defined as the ratio of the turbulence integral time to the chemical time:

$$\mathrm{Da} = \frac{\tau_t}{\tau_c} = \frac{L_t/v'(L_t)}{\delta_L^0/s_L}, \tag{2.15}$$

  where $v'(L_t)$ is the velocity associated to an eddy of size L_t.

- The Karlovitz number Ka quantifies the Kolmogorov's scale turbulence effect on flames and is defined as the ratio of the chemical time scale to the Kolmogorov time:

$$\mathrm{Ka} = \frac{\tau_c}{\tau_k} = \frac{\delta_L^0/s_L}{l_k/v'(l_k)}, \tag{2.16}$$

  where $v'(l_k)$ is the velocity of a the motion of size l_k.

  For homogeneous isotropic turbulence (Hinze, 1975), the turbulent energy goes from the large scales to the smaller scales. The energy transfer from one scale to another is constant through the different scales and given by the dissipation of the kinetic energy. This latest is estimated as:

$$\varepsilon = \frac{v'(r)^3}{r}, \tag{2.17}$$

  where $v'(r)$ is the characteristic velocity of the motion of size r. The smallest scale, where the inertial and viscous forces compensate leading to a unitary Reynolds number is the Kolmogorov scale. Its length scale l_k arise from expression (2.17) and is given by (Kolmogorov, 1941):

$$l_k = \left(\frac{\nu^3}{\varepsilon}\right)^{1/4}. \tag{2.18}$$

  Introducing expression (2.17) and relation (2.18) into (2.16) and thanks to the flame Reynolds number (expression (2.14)), the Karlovitz number may also be recast as (Poinsot and Veynante, 2012):

$$\mathrm{Ka} = \left(\frac{l_k}{\delta_L^0}\right)^{-1/2} \left(\frac{v'(l_k)}{s_L}\right)^{3/2} = \left(\frac{\delta_L^0}{l_k}\right)^2. \tag{2.19}$$

  Therefore, the Karlovitz number compares the flame characteristic length scale to the size of the smallest turbulent structure.

- The Reynolds number Re is introduced for each turbulent scale. The Reynolds number represents the ratio of inertia to viscous forces. This number is essential to characterize the turbulent regime and reads:

$$\mathrm{Re}(r) = \frac{v'(r)r}{\nu}, \tag{2.20}$$

with $v'(r)$ the characteristic velocity of the motion of size r. When r corresponds to the integral length scale, $v'(L_t)$ is the velocity associated to an eddy of size L_t. The corresponding Reynolds number is the integral (or turbulent) Reynolds number:

$$\mathrm{Re}_T = \mathrm{Re}(L_t) = \frac{v'(L_t)\, L_t}{\nu}. \tag{2.21}$$

The largest scales in a turbulent flow are mainly controlled by inertia and are not affected by viscous dissipation when $\mathrm{Re}(L_t) >> 1$. In such case, the turbulent Reynolds number can be related to the Damköhler and Karlovitz numbers in the following way:

$$\mathrm{Re}_T = \mathrm{Da}^2\, \mathrm{Ka}^2. \tag{2.22}$$

These dimensionless numbers allow to distinguish various possible turbulent combustion regimes (Borghi, 1985; Borghi and Destriau, 1998; Peters, 1986, 1999): laminar combustion, wrinkled flamelets, corrugated flamelets... The purpose is to better understand the physical phenomenon at stake behind each regime and thus be able to correctly choose or develop numerical combustion models for turbulent premixed combustion.

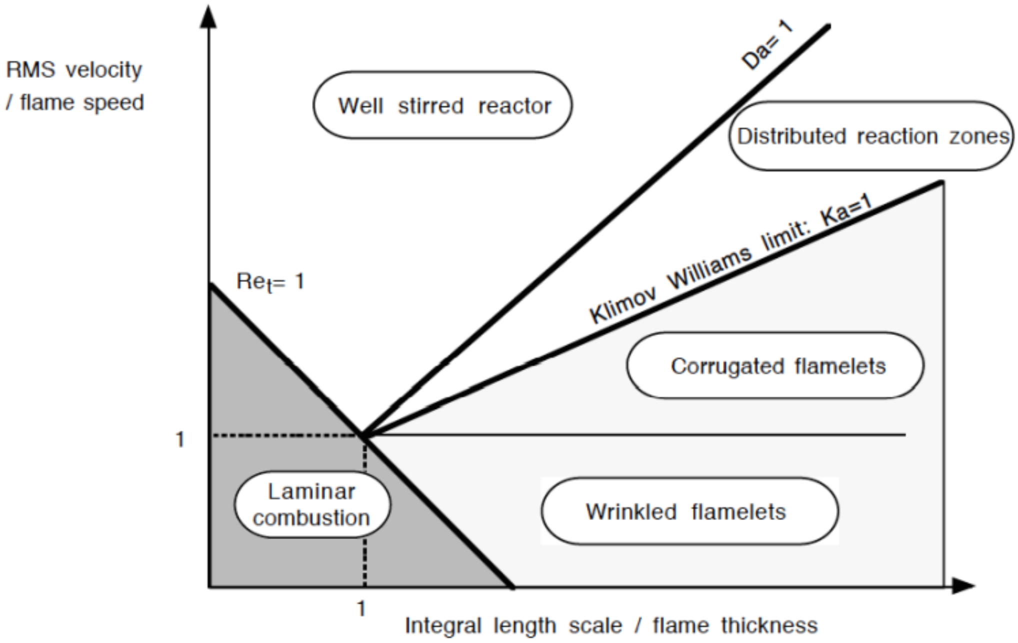

Figure 2.3: Turbulent premixed combustion diagram (Poinsot and Veynante, 2012).

The turbulent premixed combustion diagram made by Peters (1986) summarized up the different combustion regimes. This diagram is reported in Fig. 2.3 showing in ordinate the ratio between the fluctuating velocity and the laminar flame velocity, $v'(L_t)/s_L$, and in abscissa the ratio between the integral length scale and the laminar front thickness, L_t/δ_L^0. The different combustion regimes are separated using the Damköhler number Da, the Karlovitz number Ka, and the turbulent Reynolds number Re_T, but one has to keep in mind that these limits are only qualitative. The line Ka = 1 corresponds to the Klimov-Williams limit.

Peters (1999) suggests the following repartition for the combustion regimes:

- $\mathbf{Re}_{\boldsymbol{T}} < \mathbf{1}$ - *Laminar flame regime*: the flow is laminar and the flame front is not wrinkled. During a deflagration, this regime corresponds to the first moments after ignition when the flame surface expands without any turbulence.
- $\mathbf{Re}_{\boldsymbol{T}} > \mathbf{1}$ - *Turbulent flame regime*: the flow is turbulent and the flame is described such as:
  - $\mathbf{Ka} < \mathbf{1}$ - *Flamelet regime or thin flame regime*: all flames in this zone are thinner than the smallest turbulent scales. Their inner structure are close to the laminar flame structure. Two regimes can be distinguished depending on of the ratio $(v'(L_t)/s_L)$ value:
    - $\boldsymbol{(v'(L_t)/s_L) < 1}$ - *Wrinkled flamelet regime*: turbulence wrinkles weakly the flame as turbulence characteristic velocity $(v'(L_t))$ is smaller than the combustion characteristic velocity (s_L). This regime is the closest regime to the laminar regime.
    - $\boldsymbol{(v'(L_t)/s_L) > 1}$ - *Corrugated flamelet regime*: turbulent motion velocities become larger than laminar flame speed. Then, the largest eddies become able to wrinkle the flame front up to flame front interactions and may head to the stretching of the front until rupture leading to flame pockets.
  - $\mathbf{Ka} > \mathbf{1}$ and $\mathbf{Da} > \mathbf{1}$ - *Thickened wrinkled flame regime or distributed reaction zones*: the smallest turbulent eddies are smaller than the laminar flame thickness and can interact with the preheated zone enhancing heat and mass transfers. Therefore, the preheated zone is thickened but the reaction zone remains unchanged and keeps its laminar structure.
  - $\mathbf{Da} < \mathbf{1}$ - *Well stirred reactor regime*: here, turbulent motions have shorter characteristic times than the chemical time scale τ_c. The preheated zone and the reaction zone are strongly impacted by turbulence which leads to the loss of all laminar structures.

In our frame work, the turbulent flames of interest (like the accelerated deflagrations studied in Chapter 6) are most of the time in the flamelet regime or in the distributed reaction zone regime (Quillatre, 2014; Goulier, 2015). However, the flames are laminar at the early stages of a deflagration when the flow is at rest during the ignition. Thus, the combustion model chosen must be able to reproduce the transition from laminar to turbulent regimes.

For laminar flames, the front speed was described using only diffusive and chemical properties of the flame. For turbulent flames, quantifying the front speed is more complex as not only the diffusive and chemical aspects have to be taken into account but also turbulence and its interaction with the inner structure of the flame. The turbulent speed is then expressed in function of the combustion regime. In the flamelet regime, for instance, Damköhler expressed that the front can be modeled locally as a laminar flame which has been stretched and wrinkled by large turbulent structures leading to an increase of the total flame surface

A_T (Damköhler, 1940). As the flame surface increases, the reactant consumption rate also increases, raising the propagation speed of the mean flame front. Thus, in the flamelet regime, the turbulent flame speed s_T reads:

$$s_T = s_L \frac{A_T}{A}, \tag{2.23}$$

where A is the mean flame surface and A_T the total wrinkled flame surface (both surfaces are represented in Fig. 2.4). Many expressions have been proposed in the literature for the turbulent flame speed s_T (Bradley et al., 1992a; Zimont, 2000; Driscoll, 2008). The debate around models for turbulent flame speed is still on going.

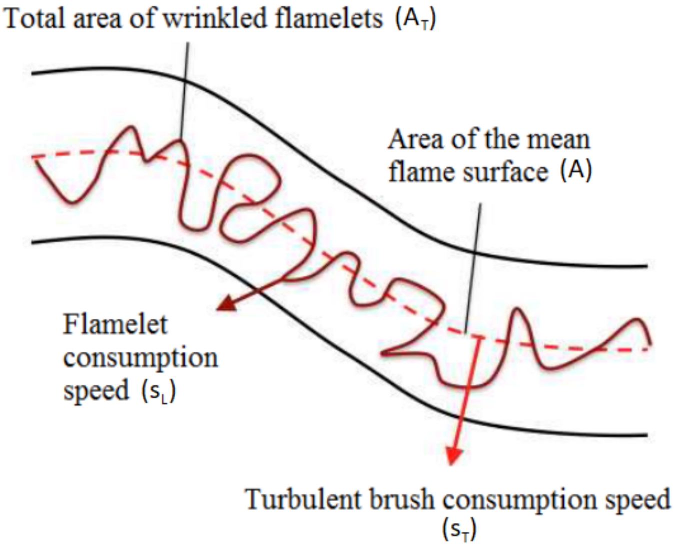

Figure 2.4: Sketch of the total wrinkled area A_T and the mean flame surface A with the flamelet turbulent speed S_T and the flamelet consumption speed s_L (Driscoll, 2008).

2.3 Chemistry modeling in LES

In this section the different methods used for chemistry modeling are stated.

Detailed chemical kinetic mechanisms

Detailed chemical kinetic mechanisms are employed to describe the transformation of reactants into products at the molecular level, involving numerous intermediate species. For example, the GRI mechanism developed by Smith et al. (2012) for methane/air mixture induces 325 reactions and 53 transported species. The number of reactions and the number of species are higher for larger hydrocarbons chains (Dagaut et al., 1994). This kind of method is prohibitive for simulation of industrial configurations for several reasons. First, a high number of grid points in the flame front (about 100 in most of cases) is required to capture all intermediate and radicals species presenting very stiff profiles. Second, a transport equation for each species must be solved. Moreover, it is still unclear how to couple detailed kinetic mechanisms with turbulent combustion models to run large eddy simulations: the models for closing transport and reactive terms can be different from a species to another and may depend of the characteristic time and size scale. To simplify this problem, various strategies are used to describe chemistry: (i) to consider a global single-step reaction as done in this work, (ii) to use tabulated chemistry from a reduced number of species, (iii) to use reduced kinetic schemes. The different types of strategies are shortly described in the following.

Simplified schemes

The number of species and reactions are radically reduced (Peters, 1985; Jones and Lindstedt, 1988; Franzelli et al., 2010). Global reactions are taken into account with Arrhenius-like law calibrated in order to reproduce some basic features of the flame (usually the laminar flame speed and the burnt gas state) in a given range of operating conditions (fresh gas temperature, pressure, equivalence ratio). To extend the validity range of these schemes, on-the fly adjustment methods of the kinetic parameters (like the activation energy and the pre-exponential constant) can be used (Franzelli et al., 2010, 2013). The CPU cost being lower than the detailed chemical mechanism, simplified schemes are widely used in LES for industrial codes (Granet et al., 2012).

Skeletal schemes

Skeletal schemes are based on detailed mechanisms with the assumption that some reactions and species are more relevant than others allowing to remove the less impacting reactions. This method allows to keep details on the phenomena of interest. In order to choose the less impacting species, a set of targets is chosen. These targets are associated to chemical features that the chemical mechanism needs to accurately reproduce over a predefined range of physical conditions. Several methods exist to determine which species have a negligible contribution to these targets (Turanyi, 1990; Tomlin et al., 1997; Massias et al., 1999; Lu and Law, 2005; Pepiot-Desjardins and Pitsch, 2008). The CPU costs are lower than detailed mechanisms but stays too high for industrial purposes as the number of species may remain high. Moreover, some of the species kept by the skeletal scheme may have extremely short life span, resulting in very stiff profiles which cannot be resolved on the LES grid. This last issue leads to the development of analytical schemes.

Analytical schemes

Analytical schemes are based on the skeletal mechanisms with the purpose to avoid species with very short time span. The Quasi Stationnary State Assumption (QSSA) is applied. The quasi stationary state (QSS) species reaction rates are removed from the set of species transported. In order to spot the QSS species, Lovas et al. (2002) developed an algorithm using the same target method as the skeletal mechanisms. The number of reactions are reduced with the partial equilibrium assumption (Li et al., 1999; Sànchez et al., 2000; Boivin et al., 2011). The automation of the reduction processes is performed using mathematical methods more or less sophisticated. Examples of analytical schemes are PETERS (Peters, 1985; Chen et al., 1996; Seshadri et al., 2001) and LU (Lu and Law, 2008). Analytical schemes are still quite new but have already showed some promising results in industrial configurations (Bauerheim et al., 2015).

Tabulated chemistries

Tabulated chemistries are an alternative to reduced kinetic mechanisms (Pitsch and Steiner, 2000; Fiorina et al., 2005; Galpin et al., 2008; Michel et al., 2008). The combustion process is described as a set of flame prototypes, each corresponding to a particular characteristic: a mixture composition, an initial temperature, an initial pressure, ... A lookup table is then built from a flamelets library obtained from one-dimensional flame simulations performed using detailed or skeletal schemes. This database then directly allows to estimate all thermo-chemical variables in function of the various parameters considered (pressure, temperature, fresh gas composition, ...). Among these tabulation techniques, we can mention the Intrinsic Low Dimensional Manifold (IDLM) (Maas and Pope, 1992), the Flame prolongation of ILDM (FPI) (Gicquel et al., 2000; Fiorina et al., 2005), the Flamelet generated manifold (FGM) (Van Oijen and De Goey, 2000; Van Oijen et al., 2016), the REDIM (Bykov and Maas, 2007) or the ICE-PIC (Ren et al., 2006) methods. A major issue associated to tabulation techniques is their extension to cases where the number of controlling variables is drastically increased. Generating and handling a lookup table can be difficult and can lead to memory problems on massively parallel machines, where the table must be stored on each core. Additionally, determining the most adequate flame prototype can be a complicated task when the combustion regime is unknown.

In this work, a global single-step reaction is chosen to model chemistry but simplified schemes or even the recently developed analytical mechanisms could also be retained.

2.4 LES models for turbulent premixed combustion

In the following, numerical models for combustion available in the literature and the ones implemented in CALIF^{3}S - P^{2}REMICS are presented. For the chemistry modeling, Appendix 2.3 presents the available models in the literature and the approach chosen for the chemical reaction.

Usually a laminar flame thickness is about 0.1 mm to 1 mm and need several grid points in order to be correctly resolved. Moreover, the reaction rate has important values variations in a thin zone which makes it even harder to compute, thus, most of the reaction rate contribution takes place at the subgrid scale and require modelling.

In Section 1.3.2, the filtered Navier-Stokes equations for compressible reactive flows are presented, but the SGS terms modelling related to combustion is not discussed. The aim of this section is to present the different combustion subgrid models available in the literature.

2.4.1 EBU model

The Eddy-Break-Up (EBU) model (Spalding, 1971, 1976) has been developed for RANS approaches before being extended to LES (Düsing et al., 2006; Fureby, 2006). This model is based on the simple idea that chemistry does not play any explicit role while turbulent mixing controls the reaction rate.

This model is devoted to perfectly premixed combustion. By considering a simple one step, irreversible reaction with adiabatic, constant pressure conditions and unitary Lewis number, the mass balance equations for chemical species are replaced by a progress variable transport equation :

$$\partial_t(\overline{\rho}\,\widetilde{c}) + \mathrm{div}(\overline{\rho}\,\widetilde{c}\,\widetilde{\boldsymbol{v}}) + \mathrm{div}\left[\overline{\rho}\,(\widetilde{\boldsymbol{v}\,c} - \widetilde{\boldsymbol{v}}\,\widetilde{c})\right] + \mathrm{div}(\overline{\boldsymbol{j}_c}) = \overline{\dot{\omega}_c}, \tag{2.24}$$

where the progress variable c is defined by equation (2.3), $\boldsymbol{j}_c$ and $\dot{\omega}_c$ stand respectively for the diffusive flux and the reaction rate. The species diffusion rates are supposed to be the same for each species.

The EBU model is based on a phenomenological analysis of turbulent combustion assuming high Reynolds and Damköhler numbers. The reaction rate is expressed with the following relation (Spalding, 1976, 1971):

$$\overline{\dot{\omega}_c} = c_{EBU}\,\frac{\overline{\rho}}{\tau^{SGS}}\,\widetilde{c}(1-\widetilde{c}). \tag{2.25}$$

with c_{EBU} a constant defined by the user.

The EBU has the same known deficiencies observed in the RANS context: reaction rate independent of chemical reaction, overestimation of the reaction rate in zones with strong shears... Moreover, the model constants seem to be strongly dependent on various parameters (flow conditions, mesh size). Finally, this model is not able to reproduce the laminar to turbulent transition, as encountered in the early stages of accelerated deflagrations (studied in this work).

2.4.2 Probability density function models

The probability density function (PDF) methods are based on the statistical properties of the intermediate states of the flame front. A probability density function $P(\Psi^*, \boldsymbol{x}, t)$ is the probability that an unknown Ψ (for example, the progress variable or the fuel mass fraction) takes values in the range of $[\Psi^* - \Delta\Psi^*/2; \Psi^* + \Delta\Psi^*/2]$ at a given position and time.

The information contained in a PDF allows to describe the combustion phenomenon. The reaction rates can be found with the same approach. For instance, in LES, for the case of a global one step reaction and a unitary Lewis number, the filtered reaction rate is given by:

$$\overline{\dot{\omega}_\Psi} = \int_0^1 \dot{\omega}_\Psi(\Psi^*) P(\Psi^*, \boldsymbol{x}, t)\, d\Psi^*. \tag{2.26}$$

This stochastic description can thus contain all the required information to describe unsteady reacting flow fields. The difficulty lays in the PDF computation. Two main methods exist (Pope, 1990): solve a balance (transport) equation for the PDF of presume the PDF shape. Elements about the physics, mathematics, numerical details and applications of the transported PDF method may be found in the review of Haworth (2010). This is a complex approach using statistical tools, thus, the method can require long CPU run times. In addition, these models for transported PDF seem to be more efficient for turbulent diffusion flames than for premixed flames such as our cases of interest. The second method, the presumed PDF approach is the most common approach. Many presumed PDF shapes have been developed in the literature (Borghi and Destriau, 1998; Bray et al., 1989; Janicka and Sadiki, 2004). The most spread PDF used is the β-PDF function (O'Brien, 1980; Pope, 1985; Cook and Riley, 1994). However, as shown by Fiorina et al. (2010), the β-PDF formulation method does not ensure the conservation of the laminar flame speed in the absence of turbulence, and therefore is unsuitable when the flame wrinkling is totally resolved, as in the early stages of accelerated deflagrations.

2.4.3 Turbulent Flame-speed Closure (TFC) models

In the subgrid scale turbulent flame speed closure models, the combustion process is described as a thin reaction surface travelling in the flow, picking a closure law for the flame front velocity, and computing its position by solving an ad-hoc equation, which may be obtained by a level-set approach (G-equation) or by solving a progress variable transport equation (2.24) (Flohr and Pitsch, 2000; Pitsch, 2006; Knudsen and Pitsch, 2008). In the level-set approach, the flame front is supposed to be located at the isovalue surface $G = G^*$ of a scalar function G obeying the following equation (Kerstein et al., 1988; Kim et al., 1999):

$$\partial_t(\overline{\rho}\,\widetilde{G}) + \mathrm{div}(\overline{\rho}\,\widetilde{\boldsymbol{v}}\,\widetilde{G}) = \overline{\dot{\omega}_G}. \tag{2.27}$$

In both cases (progress variable formulation (2.24) or G-equation (2.27)), the term $\overline{\dot{\omega}_\Psi}$, with $\Psi = G$ or $\Psi = c$ according to the formulation used, is modelled as a convection term and reads:

$$\overline{\dot{\omega}_\Psi} = \rho_u\, s_T |\nabla \widetilde{\Psi}| \tag{2.28}$$

with ρ_u is the density of fresh gas and s_T the turbulent flame speed. The main difficulty in this approach is to model the turbulent flame speed s_T. Many correlations exists in the literature based on experimental measurements (Bradley et al., 1992a; Bray, 1990; Lipatnikov and Chomiak, 2002) or obtained from theoretical analysis based on the assumption that combustion is in the “thickened flamelet” regime (Flohr and Pitsch, 2000; Pitsch, 2006; Knudsen and Pitsch, 2008). These correlations depend on the laminar flame speed and on the subgrid scale turbulent intensity $v'(L_t)$.

TFC approach is a popular method with LES for premixed combustion, because of its simplicity. The drawback is that this approach is sensitive to the turbulent flame speed correlation used. Most of these latest, used usually in RANS, turbulent flame speed correlation are directly used in LES by replacing the root mean square velocity by the subgrid scale turbulent intensity without further justifications. In addition, the results display a large scatter according to the correlation.

2.4.4 Flame surface density (FSD) models

The FSD approach is based on the filtered progress variable balance equation (2.24). However, the reaction rate term summed with the diffusion term are rewritten using a cinematic approach:

$$\partial_t(\overline{\rho}\,\widetilde{c}) + \mathrm{div}(\overline{\rho}\,\widetilde{c}\,\widetilde{\boldsymbol{v}}) + \mathrm{div}\left[\overline{\rho}\,(\widetilde{\boldsymbol{v}\,c} - \widetilde{\boldsymbol{v}}\,\widetilde{c})\right] = -\mathrm{div}(\overline{\boldsymbol{j}_c}) + \overline{\dot{\omega}_c} = \overline{\rho\, s_d |\nabla c|}, \tag{2.29}$$

with s_d the local displacement speed and the term $\overline{\rho\, s_d |\nabla c|}$ the flame front displacement. By taking the assumption of flamelet regime, this latter may be written as:

$$\overline{\rho s_d |\nabla c|} \approx \rho_u s_L \overline{\Sigma}, \tag{2.30}$$

with Σ the subgrid scale flame surface density (the flame surface density per unit volume at the subgrid scale level). Various closing models are available in literature for Σ. Some models are based on algebraic expressions (Boger et al., 1998; Boger and Veynante, 2000), similarity models (Knikker et al., 2004) or by the resolution of a balance equation (Boger et al., 1998; Hawkes and Cant, 2000; Richard et al., 2007). Several closures for the wrinkling factor Ξ_Δ have been developed for the past two decades. In Section 2.4.6 some of the main models developed are stated.

Even though the balance equation involved in the FSD method seems close to the G-equation balance equation, the FSD method has the advantage to transport physical scalars (c and Σ) which can be recovered with DNS or experimental measurements.

2.4.5 Artificially thickened flames: TFLES

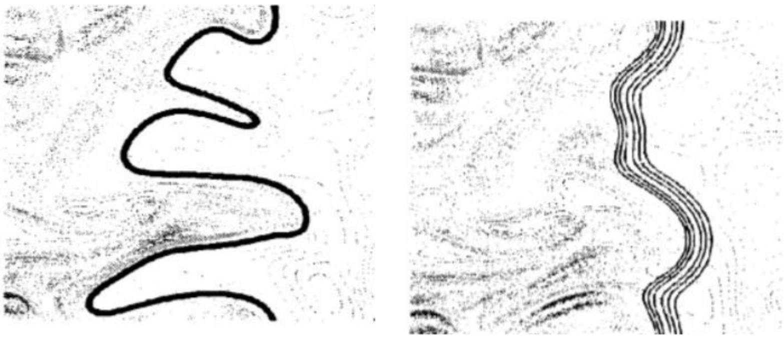

Figure 2.5: DNS of flame turbulence interactions. Reaction rate and vorticity fields are superimposed. (left-side) reference flame; (right-side) flame artificially thickened by a factor $\mathcal{F} = 5$. Because of the change in the length scale ratio L_t/δ_L^0, combustion/turbulence interaction is changed and the thickened flame is less wrinkled by turbulence motions. This effect can be parametrized using a subgrid scale model (Poinsot and Veynante, 2012).

The thickened flame model for large eddy simulation (TFLES) was originally proposed by Butler and O'Rourke (1977). The flame front is artificially thickened in order to be resolved on the numerical mesh while keeping the same laminar speed s_L. Simple theories of laminar premixed flame (Williams, 1985) allow to express the laminar flame speed s_L and the laminar flame thickness δ_L^0 as:

$$s_L \propto \sqrt{D\dot{\omega}}, \qquad \delta_L^0 \propto \frac{D}{s_L} \propto \sqrt{\frac{D}{\dot{\omega}}}, \tag{2.31}$$

with D the diffusivity and $\dot{\omega}$ the reaction rate. Then, in order to increase the flame thickness by a factor $\mathcal{F}$ while keeping the same laminar flame speed, the diffusion coefficient must become $\mathcal{F}D$ and the reaction rate $\dot{\omega}/\mathcal{F}$. This is a property of the equations governing the steady propagation of a planar premixed laminar flame. A simple change of variable shows that multiplying the diffusion and dividing the reaction rate by a factor $\mathcal{F}$ increases the flame thickness of $\mathcal{F}$ while s_L stays the same.

The thickening factor $\mathcal{F}$ is a model parameter adjusted to ensure that the grid is sufficient to resolve the thickened flame front. Typically $\mathcal{F}$ is calculated as a function of the laminar flame thickness δ_L^0 and of the characteristic cell size Δ_x such as $\mathcal{F} = n\Delta_x/\delta_L^0$, with n the number of cells needed to resolve the flame front.

Unfortunately, when a flame is thickened the interactions between chemistry and turbulence are changed (Colin et al., 2000). Indeed, the Damköhler number Da, given by equation

(2.15), is decreased by a factor $\mathcal{F}$ and becomes $\mathrm{Da}/\mathcal{F}$ changing the turbulent and chemical time scales ratio. In addition, eddies of size smaller than $\mathcal{F}\,\delta_L^0$ cannot wrinkle the thickened flame front. The other eddies affect the thickened flame front, but in a different way compared to the non-thickened flame. As a result, the thickened flame is less wrinkled than the real flame; the flame surface and the reaction rate are thus underestimated. A wrinkling factor Ξ_Δ, is introduced to compensate the corresponding reduction of flame surface (Angelberger et al., 1998; Colin et al., 2000). The filtered species balance equations become:

$$\partial_t \overline{\rho}\widetilde{Y_k} + \mathrm{div}(\overline{\rho}\widetilde{Y_k}\widetilde{\boldsymbol{v}}) + \mathrm{div}\left(\Xi_\Delta\, \mathcal{F}\,\overline{\boldsymbol{j}_k}\right) = \Xi_\Delta\, \frac{\overline{\dot{\omega}_k}}{\mathcal{F}}, \tag{2.32}$$

Analogously, the filtered sensible energy balance reads:

$$\partial_t(\overline{\rho}\,\widetilde{e}) + \mathrm{div}(\overline{\rho}\,\widetilde{\boldsymbol{v}}\,\widetilde{e}) + \overline{p}\,\mathrm{div}(\widetilde{\boldsymbol{v}}) + \mathrm{div}(\Xi_\Delta\, \mathcal{F}\,\overline{\boldsymbol{q}}) = \Xi_\Delta\, \frac{\overline{\dot{\omega}_T}}{\mathcal{F}} + \overline{\boldsymbol{\tau}}(\widetilde{\boldsymbol{v}}) : \boldsymbol{\nabla}\widetilde{\boldsymbol{v}} + \epsilon_v. \tag{2.33}$$

where the SGS viscous dissipation ϵ_v is expressed as (Garnier et al., 2009):

$$\epsilon_v = \overline{\boldsymbol{\tau}(\boldsymbol{v}) : \boldsymbol{\nabla}\boldsymbol{v}} - \overline{\boldsymbol{\tau}}(\widetilde{\boldsymbol{v}}) : \boldsymbol{\nabla}\widetilde{\boldsymbol{v}}. \tag{2.34}$$

This model compensates the subgrid flame surface lost by increasing the flame speed: equation (2.32) transports a flame front of thickness $\mathcal{F}\delta_L^0$ at a subgrid scale turbulent velocity of $\Xi_\Delta\, s_L$. Let notice that the species diffusive fluxes in (2.32) (and analogously the heat diffusive flux in (2.33)) can be rewritten as:

$$\mathrm{div}\left(\Xi_\Delta\, \mathcal{F}\,\overline{\boldsymbol{j}_k}\right) = \mathrm{div}(\mathcal{F}\,\overline{\boldsymbol{j}_k}) + \mathrm{div}\left[(\Xi_\Delta - 1)\,\mathcal{F}\,\overline{\boldsymbol{j}_k}\right]$$

where the first term at the right hand side is the laminar diffusive term and the second one models the unresolved transport diffusive term. Several closures for Ξ_Δ have been developed for the past two decades (see Section 2.4.6).

The TFLES method is easy to implement. The model correctly degenerates towards laminar combustion in the absence of turbulence where $\Xi_\Delta = 1$, which is an essential characteristic for the simulations of the flows of interest in this work. Moreover, the transport of each species is solved, which allows a certain flexibility of the model. For example, as future prospects, it would be possible to extend it to mixtures with non-unit Lewis number as well as to more complex chemistry under some assumptions (Avdić et al., 2017; Filho et al., 2018). For these reasons, the TFLES model has been retained for this work.

2.4.6 Subgrid wrinkling closures

The subgrid wrinkling factor being present in various models, this section presents some of the main closures.

Colin et al. (2000) wrinkling factor

Inspired by the work of Meneveau and Poinsot (1991) on the stretching of flames in the flamelets regime, Colin et al. (2000) have developed a wrinkling factor model thanks to direct numerical results of flame-vortex interactions combined with a spectral analysis. The wrinkling factor is derived by assuming an equilibrium between turbulence and subgrid flame surface and is written:

$$\Xi_\Delta = 1 + \alpha \frac{\Delta}{s_L} \Gamma \left(\frac{\Delta}{\delta_L^0}, \frac{v'_\Delta}{s_L} \right) \frac{v'_\Delta}{s_L} \tag{2.35}$$

with Δ the combustion filter size, v'_Δ the subgrid scale turbulent velocity and α a model parameter. The efficiency function Γ describes the ability of vortices to wrinkle the flame front at scale Δ. The following expression for Γ is given by Colin et al. (2000):

$$\Gamma \left(\frac{\Delta}{\delta_L^0}, \frac{v'_\Delta}{s_L} \right) = 0.75 \, \exp \left[- \frac{1.2}{(v'_\Delta/s_L)^{0.3}} \right] \left(\frac{\Delta}{\delta_L^0} \right)^{\frac{2}{3}} . \tag{2.36}$$

The model constant α is estimated in order to recover the Damköhler theory (*i.e.* $\Xi \approx 1 + v'/s_L$) when the flame front is wrinkled by all the turbulent motions, from l_k to L_t. It reads:

$$\alpha = \beta \frac{2 \ln(2)}{3 \, c_{ms} \, [\mathrm{Re}_T^{1/2} - 1]} \tag{2.37}$$

where β is a model constant of the order of unity, $c_{ms} = 0.28$ and the turbulent Reynolds number Re_T is given by (2.22).

The wrinkling factor is highly dependent on the subgrid scale turbulent intensity, which is difficult to quantify. Different approaches exist in order to evaluate v'_Δ. Here, two methods are presented:

- A first approach would be to estimate v'_Δ from the subgrid scale turbulent viscosity provided by the LES model. From the Smagorinsky's model it can be written:

  $$v'_\Delta = \frac{\mu_{SGS}}{\overline{\rho} \, c_s \Delta} = c_s \, \Delta |\widetilde{\mathbf{S}}|. \tag{2.38}$$

  This approach has two major drawbacks. First, the Smagorinsky's model is derived to recover the right amount of kinetic energy dissipation and is not designed to estimate velocity fluctuation. Second, in absence of turbulence, the laminar flame speed is not recovered because the strain $|\widetilde{\mathbf{S}}|$ is dominated by the thermal expansion. This approach is thus not suitable, leading to the second method for quantifying v'_Δ.

- The second method, introduced by Colin et al. (2000), is an alternative approach based on the rotational part of the local average resolved velocity field $\overline{\boldsymbol{v}}$:

  $$v'_\Delta = c_2 \, \Delta_x^3 \, |\nabla^2 (\nabla \times \overline{\boldsymbol{v}})| \tag{2.39}$$

  where Δ_x stands for the mesh step and the model constant estimated to $c_s = 2$.

Charlette et al. (2002a) wrinkling factor

Charlette's wrinkling factor computation is based on the same assumptions as Colin et al. (2000). Actually Charlette et al. (2002a) have used the flame-vortex DNS of Colin et al. (2000) but with a different integration method for the efficiency function Γ in order to avoid the prescription of the turbulent Reynolds number and correct some nonphysical behaviors at the limits. Charlette's model retains a fractal power law (Klimenko, 1998) for the he wrinkling factor:

$$\Xi_\Delta = \left(1 + \min\left[\frac{\Delta}{\delta_L^0}, \Gamma\left(\frac{\Delta}{\delta_L^0}, \frac{v'_\Delta}{s_L}, \mathrm{Re}_\Delta\right)\frac{v'_\Delta}{s_L}\right]\right)^\beta \tag{2.40}$$

where Δ is the combustion filter size, Γ an efficiency function and $\mathrm{Re}_\Delta = v'_\Delta\,\Delta/\nu$ the SGS Reynolds number. The exponent β is an a priori unknown parameter. It is related to the fractal dimension of the flame $\mathcal{D}$ when $\beta \leq 1$ such as $\beta = \mathcal{D} - 2$. Thus, if $\beta = 0$, $\mathcal{D} = 2$, therefore the flame is not wrinkled by turbulent motions, *i.e.* the flame is laminar and $\Xi_\Delta = 1$. The subgrid scale velocity v'_Δ is calculated the same way as for the Colin et al. (2000) model.

Charlette et al. (2002a) propose the fitted expression for Γ:

$$\Gamma\left(\frac{\Delta}{\delta_L^0}, \frac{v'_\Delta}{s_L}, \mathrm{Re}_\Delta\right) = \left[((f_u^{-a} + f_\Delta^{-a})^{-1/a})^{-b} + f_{\mathrm{Re}_\Delta}^{-b}\right]^{-1/b}, \tag{2.41}$$

with

$$f_u = 4\left(\frac{27\,C_k}{110}\right)^{1/2}\left(\frac{18\,C_k}{55}\right)\left(\frac{\boldsymbol{v}'_\Delta}{s_L}\right)^2, \tag{2.42}$$

$$f_\Delta = \left[\frac{27\,C_k\,\pi^{4/3}}{110} \times \left(\left(\frac{\Delta}{\delta_L^0}\right)^{4/3} - 1\right)\right]^{1/2}, \tag{2.43}$$

$$f_{\mathrm{Re}_\Delta} = \left[\frac{9}{55}\exp\left(-\frac{3}{2}\,C_k\,\pi^{4/3}\,\mathrm{Re}_\Delta^{-1}\right)\right]^{1/2}\mathrm{Re}_\Delta^{1/2}, \tag{2.44}$$

and $C_k = 1.5$ the universal Kolmogorov constant. The exponents a and b control the stiffness of the transitions between the two asymptotic behaviors and are expressed as:

$$a = 0.60 + 0.20\,\exp\left[-0.1\left(\frac{v'_\Delta}{s_L}\right)\right] - 0.20\,\exp\left[-0.01\left(\frac{\Delta}{\delta_L^0}\right)\right] \quad \text{and} \quad b = 1.4. \tag{2.45}$$

Other efficiency functions have been developed more recently (Bougrine et al., 2014; Thiesset et al., 2017) based on the same approach as Charlette et al. (2002a).

When the turbulent intensity is weak (*i.e.* $\Delta < \delta_L^0$) expression (2.40) is recast:

$$\Xi_\Delta = \left(1 + \frac{\Delta}{\delta_L^0}\right)^\beta. \tag{2.46}$$

Wang et al. (2011) have proposed a correction to expression (2.40) in order to the recover the fractal expression:

$$\Xi_\Delta = \left(\frac{\Delta}{\delta_L^0}\right)^\beta, \tag{2.47}$$

in case of weak turbulent intensity. Details of Wang et al. (2011) wrinkling factor expression are given later in this section.

Charlette et al. (2002b) dynamic wrinkling factor

As shown in the previous section the constant model β is related to the fractal dimension of the flame. Then, it can depend on various parameters such as turbulent intensity, Reynolds number, thermodiffusive property of the flame, filter size... Considering a constant value for all the configurations seems too restrictive for a parameter which depends on the physics of the flame. Moreover, the wrinkling factor developed by Charlette et al. (2002a) is based on the assumption of an equilibrium between turbulence and flame surface which might be no longer true for transiting phenomena as explosions. Therefore, Charlette et al. (2002b) developed an extension of the Germano-like procedure (Germano et al., 1991) to turbulent combustion in order to compute the model parameter β in function of time and space. This approach allows an adaptive model to take into account the turbulence increase or transient phenomena.

Following Charlette et al. (2002b), the generic form of the filtered reaction rate for all the combustion models involving a subgrid wrinkling factor presented in Section 2.4 reads:

$$\overline{\dot{\omega}} = \frac{\Xi_\Delta}{\Delta} W_\Delta(\widetilde{Q}) \tag{2.48}$$

where $W_\Delta(\widetilde{Q})/\Delta$ is the resolved reaction rate, estimated from filtered quantities $\widetilde{Q}$ (for example the filtered species mass fractions, the filtered temperature, the filtered progress variable) and Δ the combustion filter size. A test filter of width $\widehat{\Delta}$ larger than the combustion filter size Δ is introduced. The principle of the dynamic method is to compare the test filtered resolved reaction rate to the reaction rate estimated at the test-filter level:

$$\widehat{\frac{\Xi_\Delta}{\Delta} W_\Delta(\widetilde{Q})} = \frac{\Xi_{\hat{\Delta}}}{\hat{\Delta}} W_{\hat{\Delta}}(\widehat{\widetilde{Q}}) \tag{2.49}$$

where $\hat{\Delta}$ is the size of the effective filter obtained by convoluting two filters of size Δ and $\widehat{\Delta}$. Assuming that these two filters are Gaussian filter operators, the effective filter size is given by $\hat{\Delta} = \gamma\Delta$ with

$$\gamma = \left[1 + (\widehat{\Delta}/\Delta)^2\right]^{1/2}. \tag{2.50}$$

Charlette et al. (2002b) proposed a weak formulation of (2.49) by averaging over a domain large enough to eliminate nonphysical fluctuations ($\langle . \rangle$ operator):

$$\left\langle \widehat{\frac{\Xi_\Delta}{\Delta} W_\Delta(\widetilde{Q})} \right\rangle = \left\langle \frac{\Xi_{\hat{\Delta}}}{\hat{\Delta}} W_{\hat{\Delta}}(\widehat{\widetilde{Q}}) \right\rangle. \tag{2.51}$$

The meaning of relation (2.51) is that the total reaction rate averaged on a given domain should be the same when estimated from resolved and test-filtered scales. This last equality is schematized in Fig. 2.6 where the subgrid scales represented by the red part corresponds to the terms in the left side of equation (2.51) and the scales represented by the test-filters size represented by the green + red part correspond to the scales in the right side of equation (2.51). The green part is directly resolved on the mesh grid and is used to model the red part (subgrid scales).

Introducing the wrinkling factor expression (2.40) in (2.51), yields:

$$\left\langle \overbrace{\left(1+\min\left[\frac{\Delta}{\delta_L^0},\Gamma\left(\frac{\Delta}{\delta_L^0},\frac{v'_\Delta}{s_L},\mathrm{Re}_\Delta\right)\frac{v'_\Delta}{s_L}\right]\right)^\beta \frac{W_\Delta(\widetilde{Q})}{\Delta}} \right\rangle$$

$$= \left\langle \left(1+\min\left[\frac{\gamma\Delta}{\delta_L^0},\Gamma\left(\frac{\gamma\Delta}{\delta_L^0},\frac{v'_{\gamma\Delta}}{s_L},\mathrm{Re}_{\gamma\Delta}\right)\frac{v'_{\gamma\Delta}}{s_L}\right]\right)^\beta \frac{W_{\gamma\Delta}(\widehat{\widetilde{Q}})}{\gamma\Delta} \right\rangle.$$

Assuming that the wrinkling factors Ξ_Δ and $\Xi_{\gamma\Delta}$ are uniform within the averaging volume and that v'_Δ and $W_\Delta(\widetilde{Q})$ are uncorrelated, β is given by:

$$\beta = \frac{\log\left(\gamma\,\langle\overbrace{W_\Delta(\widetilde{Q})}\rangle / \langle W_{\gamma\Delta}(\widehat{\widetilde{Q}})\rangle\right)}{\log\left(\dfrac{1+\min\left[\dfrac{\gamma\Delta}{\delta_L^0},\Gamma\left(\dfrac{\gamma\Delta}{\delta_L^0},\dfrac{v'_{\gamma\Delta}}{s_L},\mathrm{Re}_{\gamma\Delta}\right)\dfrac{\langle v'_{\gamma\Delta}\rangle}{s_L}\right]}{1+\min\left[\dfrac{\Delta}{\delta_L^0},\Gamma\left(\dfrac{\Delta}{\delta_L^0},\dfrac{v'_\Delta}{s_L},\mathrm{Re}_\Delta\right)\dfrac{\langle v'_\Delta\rangle}{s_L}\right]}\right)} \tag{2.52}$$

The exponent β obtained with the previous relation is then injected in expression (2.40).

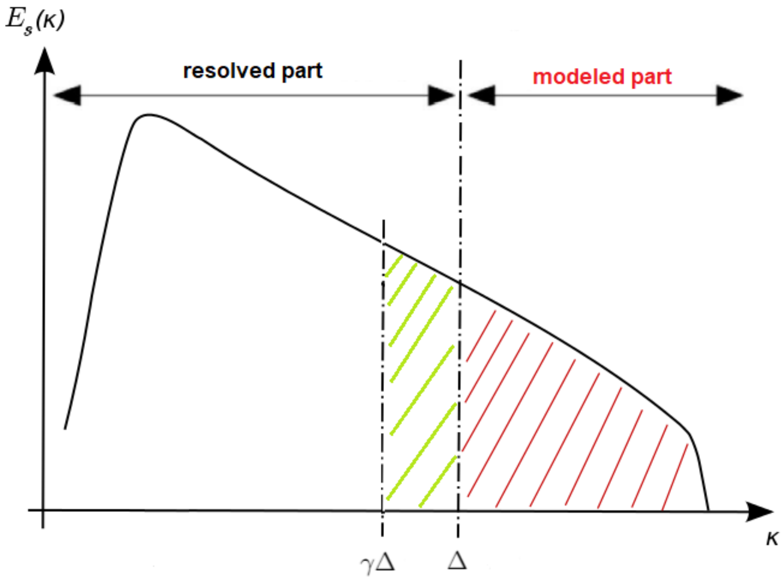

Figure 2.6: Germano-like procedure: resolved scales are used to model subgrid scales.

Wang et al. (2011) dynamic wrinkling factor

Wang et al. (2011) slightly modified Charlette et al. (2002a) expression (2.40) according to:

$$\Xi_\Delta = \left(1+\min\left[\max\left(\frac{\Delta}{\delta_L^0}-1,0\right),\Gamma\left(\frac{\Delta}{\delta_L^0},\frac{v'_\Delta}{s_L},\mathrm{Re}_\Delta\right)\frac{v'_\Delta}{s_L}\right]\right)^\beta \tag{2.53}$$

with $\Delta \geq \delta_L^0$. This modification enables to maximize the wrinkling factor Ξ_Δ for large turbulence intensities by the following fractal formulation:

$$\Xi_\Delta = \left(\frac{\Delta}{\delta_L^0}\right)^\beta ,$$

and to recover:

$$\Xi_\Delta = 1 \quad \text{when } \Delta < \delta_L^0 .$$

This formulation is found to be valid most of the time as shown by Veynante and Moureau (2015) using direct numerical simulations. In this case, Charlette et al. (2002a) expression is said saturated.

Finally, Wang et al. (2011) propose to compute the parameter β dynamically by solving the following expression, avoiding thus the estimation of turbulence intensities at both, combustion filter scale v'_Δ and test filter scale $v'_{\gamma\Delta}$:

$$\left\langle \widehat{\left(\frac{\Delta}{\delta_L^0}\right)^\beta \frac{W_\Delta(\widetilde{Q})}{\Delta}} \right\rangle = \left\langle \left(\frac{\gamma\Delta}{\delta_L^0}\right)^\beta \frac{W_{\gamma\Delta}(\widehat{\widetilde{Q}})}{\gamma\,\Delta} \right\rangle, \tag{2.54}$$

leading to the following expression for β:

$$\beta = 1 + \frac{\log\left(\langle \widehat{W_\Delta(\widetilde{Q})} \rangle / \langle W_{\gamma\Delta}(\widehat{\widetilde{Q}}) \rangle\right)}{\log\gamma}. \tag{2.55}$$

Wang et al. (2012) dynamic wrinkling factor

Wang et al. (2012) applied the previous dynamic model in the context of the Flame Surface Density model writing:

$$\left\langle \widehat{\left(\frac{\Delta}{\delta_c}\right)^\beta |\nabla\overline{c}|} \right\rangle = \left\langle \left(\frac{\gamma\Delta}{\delta_c}\right)^\beta |\nabla \widehat{\overline{c}}\,| \right\rangle, \tag{2.56}$$

where $|\nabla\overline{c}|$, $\Xi_\Delta\,|\nabla\overline{c}|$, $|\,\widehat{\nabla\overline{c}}\,|$ and $\Xi_{\gamma\Delta}\,|\nabla\,\widehat{\overline{c}}\,|$ measure the resolved and total flame surfaces at combustion and test filter scales respectively and δ_c is the inner cut-off scale (Charlette et al. (2002a) related the inner cut-off scale to the laminar flame thickness).

Hence, solving (2.56) leads to the following expression for β:

$$\beta = \frac{\log\left(\langle\, \widehat{|\nabla\overline{c}|}\, \rangle / \langle\, |\nabla\, \widehat{\overline{c}}\, |\, \rangle\right)}{\log(\gamma)}. \tag{2.57}$$

The relation (2.57) involves unweighted quantities instead of Favre (or mass-weighted) ones. Veynante and Moureau (2015), using a priori analysis and DNS results of Moureau et al. (2011) on the lean-premixed PRECCINSTA burner, show that expression (2.57) can be approximated by:

$$\beta \approx \frac{\log\left(\langle\, \widehat{|\nabla\widetilde{c}|}\, \rangle \,/\, \langle\, |\nabla\, \widehat{\widetilde{c}}\, |\, \rangle\right)}{\log(\gamma)}, \tag{2.58}$$

and propose to use Gaussian filters for the average operator $\langle . \rangle$ because it is easier to implement in case of unstructured grids and parallel solver utilisation. This Gaussian operator has a filter size denoted by Δ^{avg} with $\Delta^{avg} > \overbrace{\Delta}$.

Mouriaux et al. (2016) dynamic wrinkling factor correction

In order to lighten the notation, expression (2.58) is rewritten:

$$\beta \approx \frac{\log\left(\Sigma_1/\Sigma_2\right)}{\log(\gamma)}, \tag{2.59}$$

with $\Sigma_1 = \langle\ \overbrace{|\nabla \tilde{c}|}\ \rangle$ and $\Sigma_2 = \langle\ |\nabla\ \overbrace{\tilde{c}}\ |\ \rangle$.

Mouriaux et al. (2016) validated and improved the dynamic model studied by Veynante and Moureau (2015). They show that interactions of flame fronts and interaction with solid boundaries can be problematic, inducing large nonphysical values of the β parameter.

Indeed, when the resolved flame front is close to the computational domain boundary (*i.e.* at a distance $d < \hat{\Delta}$), the stencil of the test-filtering operator is truncated. Then, the gradient operator does not commute anymore with the filtering operator leading to $\beta \neq 0$ for laminar flame near the domain boundary. Therefore, the subgrid model is slightly modified by replacing Σ_2 in (2.59) by $\Sigma_{2,new} = \langle\ |\ \overbrace{\nabla \tilde{c}}\ |\ \rangle$ in the entire domain. With this formulation, $\Sigma_1 = \Sigma_{2,new}$ near the boundary, because operators norm and test-filter commute in the 1D planar case (Mouriaux et al., 2016). Therefore $\beta = 0$ leading to a unitary wrinkling factor close to the computational domain boundaries. Far to the boundary (*i.e.* at a distance $d > \hat{\Delta}$), when the mesh is regular, $\Sigma_2 = \Sigma_{2,new}$ and the wrinkling factor Ξ_Δ is unchanged. For non-regular mesh, however, practical tests made by Mouriaux (2016) evidenced that $\Sigma_2 \approx \Sigma_{2,new}$. That far, the wrinkling factor exponent is rewritten:

$$\beta \approx \frac{\log\left(\Sigma_1/\Sigma_{2,new}\right)}{\log(\gamma)} = \frac{\log\left(\langle\ \overbrace{|\nabla \tilde{c}|}\ \rangle\ /\ \langle\ |\ \overbrace{\nabla \tilde{c}}\ |\ \rangle\right)}{\log(\gamma)}, \tag{2.60}$$

The second improvement of the Mouriaux et al. (2016) dynamic model is developed to fix nonphysical values in case of front interactions (Mouriaux et al., 2016; Mouriaux, 2016). This usually happens when the flame is fully turbulent and wrinkled leading to front interactions. More specifically, when several flame fronts interact at a scale lower than $\hat{\Delta}$, $\overbrace{\tilde{c}}$ may reach a local minimum, leading to $|\nabla\ \overbrace{\tilde{c}}\ | = 0$ (even if $\tilde{c}$ is not null nor equal to unity). This leads to an ill-posed formulation of the SGS wrinkling factor at the effective scale $\hat{\Delta}$:

$$\Xi_{\hat{\Delta}} = \frac{|\overbrace{\nabla \tilde{c}}|}{|\nabla\ \overbrace{\tilde{c}}\ |}.$$

Moreover, as pointed by Mouriaux et al. (2016), $\Sigma_1 >> \Sigma_2$, leading to abnormal high values of Ξ_Δ. To overcome this difficulty, a sensor denoted by ζ is introduced in order to detect flame front interactions and defined as:

$$\zeta = \left|\ \begin{array}{ll} 1 & \text{if } \boldsymbol{n}.\boldsymbol{N} < 1 - \varepsilon \\ 0 & \text{elsewhere} \end{array}\right.$$

where $\boldsymbol{n} = -\nabla\tilde{c}/|\nabla\tilde{c}|$ and $\boldsymbol{N} = -\widehat{\nabla\tilde{c}}/|\widehat{\nabla\tilde{c}}|$ are the normal vectors to the resolved flame front at scale Δ and $\hat{\Delta}$ respectively and ε is a model parameter (usually set to 0.1). As shown in Fig. 2.7-(a), fronts do not interact at scale $\hat{\Delta}$ when both normal are collinear. However, when the fronts interact at scale $\hat{\Delta}$ the blue zone (test-filtering zone) in Fig. 2.7-(b) contains more than one front separated by a distance inferior than $\hat{\Delta}$. Therefore, $\boldsymbol{n}$ and $\boldsymbol{N}$ are not collinear anymore leading to a unitary value for the sensor ζ.

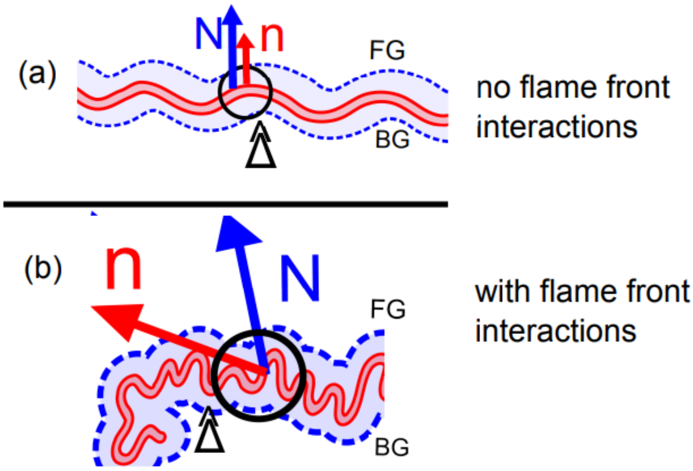

Figure 2.7: Sketch of flame fronts. Red surface: surface estimated at the combustion filter Δ scale; Blue surface: surface estimated at the effective filter $\hat{\Delta}$ scale; Black circle: effective filter $\hat{\Delta}$. (a) Situation without front interactions at scale $\hat{\Delta}$; (b): Situation with flame front interactions (Mouriaux et al., 2016).

The flag ζ is then test-filtered as flame front interactions induce high values of Ξ_Δ over a zone of characteristic length $\hat{\Delta}$. The subgrid model is then corrected by replacing $\Sigma_2 = \langle\, |\widehat{\nabla\tilde{c}}|\, \rangle$ in (2.59) by:

$$\Sigma_{2,corr} = \left\langle (1-\hat{\zeta})\, |\widehat{\nabla\tilde{c}}| + \hat{\zeta}\, \Sigma_3 \right\rangle . \tag{2.61}$$

with $\Sigma_3 = \widehat{|\nabla\tilde{c}|\, \boldsymbol{n}.\boldsymbol{N}}$. This expression shows that in case of front interactions, *i.e.* when $\hat{\zeta} \geq 0$, $\Sigma_{2,corr}$ tends toward Σ_3, but Σ_3 does not approach 0 unlike Σ_2. When there is no front interactions, $\Sigma_{2,corr}$ tends toward $|\widehat{\nabla\tilde{c}}|$ allowing to recover expression (2.59). Therefore the wrinkling factor exponent is finally written:

$$\beta \approx \frac{\log\left(\Sigma_1/\Sigma_{2,corr}\right)}{\log(\gamma)} = \frac{\log\left(\left\langle \widehat{|\nabla\tilde{c}|} \right\rangle / \left\langle (1-\hat{\zeta})\, |\widehat{\nabla\tilde{c}}| + \hat{\zeta}\, \widehat{|\nabla\tilde{c}|\, \boldsymbol{n}.\boldsymbol{N}} \right\rangle\right)}{\log(\gamma)}, \tag{2.62}$$

Mouriaux et al. (2016) have shown for a 1D laminar flame, that with this improvement, $\Sigma_{2,corr}$ profile does not tend toward zero and stays close to the profile of $\Sigma_3 = \Sigma_1$ even in case of front interactions. Therefore, the wrinkling factor values have been significantly lowered in case of fronts interactions allowing to avoid nonphysical values of the β parameter. The same conclusions are obtained in more complex cases.

Because of its simplicity and its good behavior in case of transiting regimes, the Veynante and Moureau (2015) wrinkling factor expression combined to Mouriaux et al. (2016) correction was chosen for this work and implemented in the CALIF^{3}S - P^{2}REMICS software.

Inner cut-off length scale

An inner cut-off scale was already introduced in the Charlette et al. (2002b) and in the Wang et al. (2011) formulations and modelled as the laminar flame thickness δ_L^0. In practice, this parameter is difficult to estimate and modeling the inner cut-off length scale remains an open question. The inner cut-off scale has been first estimated to $\delta_c = 3\delta_L^0$ by Knikker et al. (2002). In practical simulations of the growth of a flame kernel, Wang et al. (2012) found that reducing the inner cut-off scale to $\delta_c = 2\delta_L^0$ modifies β and Ξ_Δ values but not the total flame surface, which is the quantity of physical interest. Refined models for δ_c may be found in literature (Gülder and Smallwood, 1995). More recently, Proch et al. (2017) has developed a model for estimating the inner cut-off scale. In practical simulations, an overestimation (respectively underestimation) of δ_c would induce an underestimation (overestimation) of the wrinkling factor for a given β, leading to a lower (higher) subgrid scale turbulent flame speed, a larger (lower) resolved flame front wrinkling and a higher (lower) β and wrinkling factor values (Veynante and Moureau, 2015). This self-adjusting mechanism has been investigated by Volpiani (2017) and more recently by Veynante (2021). Furthermore,

In practice, it is commonly assumed to be proportional to the laminar flame thickness δ_L^0. This choice is made in this work with δ_L^0 the thermal thickness of the flame front.

2.5 Conclusion

An overview of premixed laminar flames has been first presented in order to define essential parameters such as characteristic flame thickness, speed and stretch. In a second time, turbulence characteristic features have been introduced alongside fundamental dimensionless numbers for turbulent combustion. All these definitions served at setting the Peters (1999) repartition of the combustion regimes. This study allowed to frame the deflagration phenomena in the repartition combustion regimes. Here, the numerical combustion model has to be able to reproduce transiting phenomena from laminar to turbulent flame in the flamelet or distributed reaction zone regimes.

In this work, turbulent premixed flames are modelled with the LES approach. Among the different models described in this chapter, the numerical choices made here are summarized in Table 2.1.

Chemistry	Global one-step reaction
Combustion	Artificially thickened flame model (Butler and O'Rourke, 1977)
Subgrid wrinkling closure	Veynante and Moureau (2015) dynamic formalism with Mouriaux et al. (2016) correction

Table 2.1: Modeling choices for turbulent premixed combustion used in this work.

Part II

A second order numerical scheme for large-eddy simulation of compressible reactive flows

Chapter 3

A quasi non-dissipative second-order explicit MAC scheme for the compressible Navier-Stokes equations

*In the context of large eddy simulation of turbulent flows, the control of kinetic energy seems to be an essential requirement for a numerical scheme. We propose in this chapter a formally second order non-dissipative scheme dedicated to the numerical simulation of the filtered Navier-Stokes equations for compressible flows. The spatial discretization is staggered and based on the so-called Marker-And-Cell (MAC) scheme. Time discretization is performed with the Heun scheme. For the energy balance equation, the scheme uses a discrete form of the conservation of the sensible energy; this relation includes a numerical corrective term, to allow the scheme to compute correct shock solutions in the Euler limit. A MUSCL-like technique is used for convection operators of the mass and the sensible energy balance equations. The scheme is shown to preserve the stability properties of the continuous problem under CFL condition (*i.e.* the positivity of the density and of the internal energy, at least when no numerical corrective terms are added). A kinetic energy conservation identity at discrete level is proved (up to remainder terms, which are shown to be of second order in time). Finally, a total energy balance for the scheme is established, which may be made conservative by adding corrective terms to the sensible energy balance, for instance if one wants to compute shock solutions. The good behaviour of the scheme is assessed on some numerical tests.*

3.1 Introduction

Large-eddy simulation (LES) has gained a great success in simulating practical flows where the Reynolds numbers are usually very high. In such a method, the large scale fluid motions are computed explicitly from the filtered Navier-Stokes equations while small-scale effects are modeled. The aim of this chapter is to propose a formally second order scheme, with as low kinetic energy dissipation as possible, dedicated to the numerical simulation of the filtered Navier-Stokes equations for compressible non reactive flows.

The space discretization is staggered, and works on structured grids using the so-called Marker-And-Cell (MAC) scheme (Harlow and Amsden, 1971; Harlow and Welch, 1965): the scalar variables are approximated at the cell centers and the normal velocity at the face centers. Time-stepping is segregated, in the sense that balance equations are solved successively, and each step is explicit: apart from the time derivative, all terms involve only known quantities and no linear system solution is required. The staggered arrangement of the unknowns makes difficult the definition of the fluxes through the solution of a Riemann problem: indeed, if the unknowns may be considered as piecewise functions, they are not associated to the same partition of the computational domain (*i.e.*scalars and normal velocity are computed separately). To preserve the positivity of the density and the sensible energy, we thus rely on another technique, which consists in: (*i*) solving the sensible energy balance instead of the total energy balance and (*ii*) deriving discretizations of the mass and sensible energy balance which preserve by construction the positiveness of the unknowns. In fact, it turns out that this may be reached by a simple upwinding (here, second order, *i.e.* with a MUSCL-like technique) of the convection terms with respect to the material velocity. As a by-product, we also obtain a very simple expression of the fluxes, well suited to high-performance computing. In addition, this choice avoids building an approximation of the total energy which, for staggered discretizations, is a "composite" variable combining quantities discretized on the cells and at the faces. Of course, a raw discretization of the (non-conservative) sensible energy balance can lead to non-consistent solutions in the inviscid case (precisely speaking, predictions of shocks which do not satisfy the correct Rankine-Hugoniot jump conditions); this difficulty may be overstepped by adding, a corrective term in the discrete sensible energy balance equation (Herbin et al., 2014, 2018, 2021), which may be seen as the counterpart of the dissipation generated by the momentum balance numerical diffusion. A class of schemes combining these ingredients is implemented in the open-source software platform CALIF^{3}S (2021) developed at the French Institut de Radioprotection et de Sûreté Nucléaire (IRSN). In this context, such staggered schemes present another major advantage, namely the possibility to build unconditionally stable variants through a pressure correction technique and a partial implicitation of the fluxes (Herbin et al., 2014; Grapsas et al., 2016) (by opposition with Riemann solvers, where the high nonlinearity of the fluxes makes difficult the development of an implicitation preserving the positiveness properties). In addition, since the staggered discretization satisfies a discrete *inf-sup* stability conditions, these schemes naturally boil down to usual algorithms for incompressible flows when the Mach number tends to zero; a rigorous proof of this asymptotic preserving property for barotropic flows is given in Herbin et al. (2017) (see Appendix 3.C for more details). For turbulent flows modelling, such semi-implicit variants may be useful to implement a solver building a bridge from Large Eddy Simulation models to statistical models, by hybrid (DES for example) approaches.

First-order explicit schemes based on the above described arguments have been built (Herbin et al., 2014, 2018), then extended to higher orders in space by a MUSCL-like technique in Gastaldo et al. (2018). The task undertaken here is to build a second-order time scheme, by embedding the latter scheme (extended to Navier-Stokes equations by adding an explicit-in-time discretization of the diffusion terms) in a Strong Stability Preserving (SSP) scheme, namely the Heun scheme. By construction, we hope the resulting algorithm to enjoy the same positivity preservation properties for the density and the sensible energy. Indeed, the density is shown to be non-negative at the discrete level under a CFL condition by an easy adaptation of the technique developed in Gastaldo et al. (2018). To obtain the positivity of the internal energy, we must combine two arguments:

- first, to extend the proof of Gastaldo et al. (2018) to cope with a heat diffusion term (with an adaptation of the CFL condition),
- second, to implement a discretization of the momentum diffusion which yields a positive

dissipation term. To this purpose, we use an idea proposed in Grapsas et al. (2016), which consists in recasting the MAC scheme under a weak form, so that we may closely mimick the continuous expression of the dissipation: *in fine*, the cell dissipation is computed as the integral over the considered cell of the inner product of the stress and strain tensors, linked *a.e.* by the usual (continuous) relation (hence the non-negativity). Then we turn to the kinetic energy preservation property. Considering the Heun scheme as a three-steps scheme, with two prediction steps and a final average, we show that the solution of the first two steps obeys a kinetic energy balance with numerical production terms (*i.e.* non-negative residual terms when put at the right-hand side), while the last step is dissipative; finally, we are able to derive a local kinetic energy balance for the algorithm with remainder terms, which we show to be of second order in time. Numerical experiments show that these remainder terms take in fact very low values: the compensation operated by the final averaging is almost exact, in the sense that the final residual is more than one thousand times smaller than the residuals associated to the first two steps of the algorithm (which are nothing more than the first-order Euler forward scheme). Finally, we establish a total energy balance for the scheme, which may be made conservative by adding corrective terms to the sensible energy balance, for instance if one wants to compute shock solutions. Since we address here essentially viscous flows, we do not follow this line; however, we numerically check that the scheme correctly captures the viscous perturbation of mild shocks (similar for instance to the strongest ones which may be generated by deflagrations) even with coarse meshes. On the opposite, for strong shocks (typical of detonations), correcting the discrete sensible energy balance seems to be preferable.

This chapter is organized as follows. We first present the continuous model as well as its stability properties (Section 3.2). After a description of the space discretization (Section 3.3), the scheme is introduced in Section 3.4.1. Positivity results, at the discrete level, and then kinetic and total energy conservation are discussed in Section 3.4.2. Finally, Section 3.5 presents some numerical tests, addressing either the scheme properties on model problems or test cases inspired by real world large eddy simulations. In Appendix 3.A, we first recall, for the sake of completeness, the discretization of the diffusion term in the momentum balance equation; then, in a second step, we derive a discretization of the dissipation term which, if used in the internal energy balance, would made the scheme fully conservative. This expression shows that the (simpler) implemented discretization of the dissipation term yields a consistent scheme, in the sense that, if both the "conservative" and the implemented dissipation terms are controlled in L^1, their difference tends to zero in a distributional sense. The MUSCL algorithm used in the mass and energy balance equations, presented in Gastaldo et al. (2018), is recalled in Appendix 3.B.

3.2 Physical model

The mathematical model, based on the Navier-Stokes equations for compressible flows reads:

$$\partial_t \rho + \operatorname{div}(\rho \boldsymbol{v}) = 0 \tag{3.1a}$$

$$\partial_t (\rho \boldsymbol{v}) + \operatorname{div}(\rho \boldsymbol{v} \otimes \boldsymbol{v}) = -\nabla p + \operatorname{div}(\boldsymbol{\tau}(\boldsymbol{v})) \tag{3.1b}$$

$$\partial_t (\rho E) + \operatorname{div}(\rho \boldsymbol{v} E) + \operatorname{div}(p\, \boldsymbol{v}) = \operatorname{div}(\boldsymbol{\tau}(\boldsymbol{v}) \cdot \boldsymbol{v}) + \operatorname{div}\boldsymbol{q} \tag{3.1c}$$

$$E = \frac{1}{2}\, |\boldsymbol{v}|^2 + e \tag{3.1d}$$

$$p = (\gamma - 1)\, \rho\, e \tag{3.1e}$$

where t stands for the time, ρ, $\boldsymbol{v}$, p, E and e are the density, velocity, pressure, total energy and sensible energy, $\boldsymbol{\tau}$ stands for the shear stress tensor, $\boldsymbol{q}$ stands for the heat diffusion flux and $\gamma > 1$ is a coefficient specific to the considered fluid.

The problem is supposed to be posed over $\Omega \times (0, T)$, where Ω is an open bounded connected subset of $\mathbb{R}^d$ with $1 \leq d \leq 3$ and $(0, T)$ is a finite time interval.

In order to describe turbulence, the system of equations (3.1) is filtered in the sense of large eddy simulations: the large, non-universal, energy containing scales of the flow are computed explicitly, while the small scales are modeled. Each flow variable ϕ is thus decomposed into computable (large-scale structures) and residual (small structures) terms, $\phi = \bar{\phi} + \phi'$, by means of a filtering operation represented mathematically in the physical space as a convolution product. The resolved part $\bar{\phi}$ reads

$$\bar{\phi}(\mathbf{x}, t) \equiv \int_\Omega G(\mathbf{r}, \mathbf{x}) \phi(\mathbf{x} - \mathbf{r}, t)\, d\mathbf{r} \tag{3.2}$$

where G is the filter function that determines the scale of the resolved structures (we refer to Chapter 1 for more details). In order to account for density fluctuations, the density-weighted (Favre) filtering is also used for compressible flows:

$$\widetilde{\phi} = (\overline{\rho\phi}) / \overline{\rho}$$

for a flow variable ϕ, with $\overline{\rho}$ the filtered density.

Filtering the mass balance (3.1a) and the momentum balance (3.1b) leads to:

$$\partial_t \overline{\rho} + \operatorname{div}(\overline{\rho} \widetilde{\boldsymbol{v}}) = 0 \tag{3.3a}$$

$$\partial_t (\overline{\rho} \widetilde{\boldsymbol{v}}) + \operatorname{div}(\overline{\rho} \widetilde{\boldsymbol{v}} \otimes \widetilde{\boldsymbol{v}}) = -\nabla \overline{p} + \operatorname{div}(\breve{\boldsymbol{\tau}}(\widetilde{\boldsymbol{v}})). \tag{3.3b}$$

The effective momentum diffusion tensor can be seen as composed by a computable and an unresolved or subgrid-scale (SGS) part $\breve{\boldsymbol{\tau}} = \overline{\boldsymbol{\tau}} - \boldsymbol{\tau}^{SGS}$. The computable part $\overline{\boldsymbol{\tau}}$ is modelled as :

$$\overline{\boldsymbol{\tau}}(\widetilde{\boldsymbol{v}}) = 2 \overline{\mu} \left(\widetilde{\mathbf{S}} - \frac{1}{3} \operatorname{Tr}(\widetilde{\mathbf{S}}) \boldsymbol{I} \right) \tag{3.4}$$

where $\overline{\mu}$ is the "computable" turbulent viscosity, $\widetilde{\mathbf{S}}$ is the mean rate-of-strain tensor defined as $\widetilde{\mathbf{S}} = 1/2 \left(\nabla \widetilde{\boldsymbol{v}} + \nabla^t \widetilde{\boldsymbol{v}} \right)$ and $\boldsymbol{I}$ stands for the $\mathbb{R}^{d \times d}$ identity matrix. We assume that $\overline{\mu} \in L^\infty(\Omega)$

and that it exists $\mu' > 0$ such as $\mu \geq \mu'$ *a.e.*. Thus, the computable shear stress tensor satisfies:

$$\overline{\boldsymbol{\tau}}(\widetilde{\boldsymbol{v}}) : \boldsymbol{\nabla}\widetilde{\boldsymbol{v}} \geq 0, \quad \forall \widetilde{\boldsymbol{v}} \in \mathbb{R}^d. \tag{3.5}$$

The SGS turbulent shear stress $\boldsymbol{\tau}^{SGS}$ can not be calculated directly and therefore is modelled in terms of resolved quantities by the Boussinesq's eddy viscosity model:

$$\boldsymbol{\tau}^{SGS}(\widetilde{\boldsymbol{v}}) = \overline{\rho}\,(\widetilde{\boldsymbol{v} \otimes \boldsymbol{v}} - \widetilde{\boldsymbol{v}} \otimes \widetilde{\boldsymbol{v}}) \approx -2\mu_{SGS}\left(\widetilde{\mathbf{S}} - \frac{1}{3}\mathrm{Tr}(\widetilde{\mathbf{S}})\boldsymbol{I}\right). \tag{3.6}$$

where μ_{SGS} is the SGS turbulent viscosity.

The spatially filtered sensible energy balance reads:

$$\partial_t(\overline{\rho}\widetilde{e}) + \mathrm{div}(\overline{\rho}\widetilde{\boldsymbol{v}}\widetilde{e}) + \overline{p}\,\mathrm{div}\widetilde{\boldsymbol{v}} = \overline{\boldsymbol{\tau}}(\widetilde{\boldsymbol{v}}) : \nabla\widetilde{\boldsymbol{v}} + \mathrm{div}(\check{\boldsymbol{q}}) + \epsilon_v. \tag{3.7}$$

The heat flux, $\check{\boldsymbol{q}} = \overline{\boldsymbol{q}} + \boldsymbol{q}^{SGS}$, is decomposed into a computable part $\overline{\boldsymbol{q}}$:

$$\overline{\boldsymbol{q}} = -\overline{\lambda}\,\boldsymbol{\nabla}\widetilde{e} \tag{3.8}$$

and a SGS part $\boldsymbol{q}^{SGS}$:

$$\boldsymbol{q}^{SGS} = \overline{\rho}\,(\widetilde{\boldsymbol{v}e} - \widetilde{\boldsymbol{v}}\widetilde{e}) \approx -\lambda_{SGS}\,\boldsymbol{\nabla}\widetilde{e} \tag{3.9}$$

where $\overline{\lambda}$ and λ_{SGS} are respectively the "computable" and the subgrid scale heat diffusion coefficients. The thermal conductivity may be expressed by $\overline{\lambda} = \overline{\mu}c_{\mathrm{p}}/\mathrm{Pr}$, where the specific heat constant at constant pressure c_{p} and the laminar Prandtl number Pr are assumed to be constant and positive. Thus, $\overline{\lambda} \in L^\infty(\Omega)$ and there exists $\lambda' > 0$ such as $\overline{\lambda} \geq \lambda'$ *a.e.*. Analogously, the SGS heat diffusion coefficient λ_{SGS} is modelled by $\lambda_{SGS} = \mu_{SGS}\,c_{\mathrm{p}}/\mathrm{Pr}_t$, where the turbulent Prandtl number Pr_t is assumed to be constant and positive.

The SGS viscous dissipation term is modelled by:

$$\epsilon_v = -\boldsymbol{\tau}^{SGS}(\widetilde{\boldsymbol{v}}) : \boldsymbol{\nabla}\widetilde{\boldsymbol{v}}. \tag{3.10}$$

The filtered kinetic energy balance equation is obtained by the inner product of the filtered momentum balance equation with the filtered velocity:

$$\frac{1}{2}\,\partial_t(\overline{\rho}\,|\widetilde{\boldsymbol{v}}|^2) + \frac{1}{2}\,\mathrm{div}\left(\overline{\rho}\,|\widetilde{\boldsymbol{v}}|^2\,\widetilde{\boldsymbol{v}}\right) + \boldsymbol{\nabla}\overline{p}\cdot\widetilde{\boldsymbol{v}} - \mathrm{div}\overline{\boldsymbol{\tau}}(\widetilde{\boldsymbol{v}})\cdot\widetilde{\boldsymbol{v}} = -\mathrm{div}\boldsymbol{\tau}^{SGS}(\widetilde{\boldsymbol{v}})\cdot\widetilde{\boldsymbol{v}}. \tag{3.11}$$

Summing equations (3.7) and (3.11), and thanks to (3.10), gives rise to the following conservative form of the filtered total energy balance equation:

$$\partial_t(\overline{\rho}\,\widetilde{E}) + \mathrm{div}(\overline{\rho}\,\widetilde{\boldsymbol{v}}\,\widetilde{E}) + \mathrm{div}(\overline{p}\,\widetilde{\boldsymbol{v}}) = \mathrm{div}(\check{\boldsymbol{q}}) + \mathrm{div}\left(\check{\boldsymbol{\tau}}(\widetilde{\boldsymbol{v}})\cdot\widetilde{\boldsymbol{v}}\right), \tag{3.12}$$

where the filtered total energy is defined by: $\widetilde{E} = \widetilde{e} + \dfrac{1}{2}\,|\widetilde{\boldsymbol{v}}|^2$.

The system is closed with a model for the SGS turbulent viscosity computation. Here, the Smagorinsky model (Smagorinsky, 1963) is used:

$$\mu_{SGS} = \overline{\rho}(C_s\Delta)^2|\bar{\mathbf{S}}|, \tag{3.13}$$

where $C_s > 0$ is a model parameter and Δ is the cut-off scale which corresponds here to the the computational cell volume. Then, thanks to (3.5), the shear stress tensor satisfies:

$$\breve{\boldsymbol{\tau}}(\widetilde{\boldsymbol{v}}) : \boldsymbol{\nabla}\widetilde{\boldsymbol{v}} \geq 0, \quad \forall \widetilde{\boldsymbol{v}} \in \mathbb{R}^d. \tag{3.14}$$

Finally, the filtered equation of state reads:

$$\overline{p} = (\gamma - 1)\, \overline{\rho}\widetilde{e}. \tag{3.15}$$

This system composed by equations (3.3), (3.7) and (3.15), must be supplemented by suitable boundary conditions and initial conditions. For the sake of simplicity, only impermeability conditions are imposed and that the system is supposed to be adiabatic:

$$\widetilde{\boldsymbol{v}} \cdot \mathbf{n} = 0, \quad \breve{\boldsymbol{q}} \cdot \mathbf{n} = 0 \text{ on } \partial\Omega$$

where $\mathbf{n}$ stands for the normal vector to the boundary. An initial condition must be given for $\overline{\rho}$, $\widetilde{e}$ and $\widetilde{\boldsymbol{v}}$ which is written:

$$\overline{\rho}(x, 0) = \overline{\rho}_0(x),\, \widetilde{e}(x, 0) = \widetilde{e}_0(x),\, \widetilde{\boldsymbol{v}}(x, 0) = \widetilde{\boldsymbol{v}}_0(x),\ \forall \boldsymbol{x} \in \Omega,$$

with $\overline{\rho}_0 > 0$ and $\widetilde{e}_0 \geq 0$.

Since we assume that the initial condition for $\overline{\rho}$ is positive, the mass balance (3.3a) implies that the density $\overline{\rho}$ remains non-negative. Equation (3.7) then implies, thanks to (3.14), that the filtered sensible energy $\widetilde{e}$ remains non-negative. We also have, by the equation of state, $\overline{p} \geq 0$.

To alleviate the notations, we drop in the remainder of this chapter the overbar and the tilde symbols to denote the filtered fields.

3.3 Meshes and unknowns

A discretization $(\mathcal{M}, \mathcal{E})$ of Ω with a staggered rectangular grid or MAC grid (Harlow and Amsden, 1971; Harlow and Welch, 1965), involves a primal grid $\mathcal{M}$ which consists in a conforming structured partition of Ω in rectangles ($d = 2$) or rectangular parallelepipeds ($d = 3$), possibly non uniform.

By $\mathcal{E}$ and $\mathcal{E}(K)$ we denote the set of all (d - 1)-faces σ of the mesh and of the element $K \in \mathcal{M}$ respectively. The set of faces included in the boundary of Ω is denoted by $\mathcal{E}_{ext}$ and the set of internal faces (i.e. $\mathcal{E}\backslash\mathcal{E}_{ext}$) is denoted by $\mathcal{E}_{int}$; a face $\sigma \in \mathcal{E}_{int}$ separating the cells K and L is denoted by $\sigma = K|L$. The set of the edges (resp. the internal and boundary edges) that are orthogonal to the i^{th} vector of the orthonormal basis of $\mathbb{R}^d$, $\boldsymbol{e}^{(i)}$, is denoted by $\mathcal{E}^{(i)}$ (resp. $\mathcal{E}^{(i)}_{\text{int}}$ and $\mathcal{E}^{(i)}_{\text{ext}}$), for $1 \leq i \leq d$. The outward normal vector to a face σ of K is denoted by $\mathbf{n}_{K,\sigma}$. For $K \in \mathcal{M}$ and $\sigma \in \mathcal{E}$, $|K|$ denotes the measure of K and $|\sigma|$ the (d - 1)-measure of the face σ. For $K \in \mathcal{M}$ (resp. $\sigma \in \mathcal{E}_{\text{int}}$), $\boldsymbol{x}_K$ (resp. $\boldsymbol{x}_\sigma$) denotes the mass center of K (resp. σ). We denote by $d_{K,\sigma}$, $\forall K \in \mathcal{M}$ and $\forall \sigma \in \mathcal{E}$, the Euclidean distance between the center $\boldsymbol{x}_K$ of the cell and the edge σ. We define $d_\sigma = d_{K,\sigma} + d_{L,\sigma}$ if $\sigma \in \mathcal{E}_{\text{int}}$ and $d_\sigma = d_{K,\sigma}$ if $\sigma \in \mathcal{E}_{\text{ext}}$.

The degrees of freedom for the pressure, the density and the sensible energy (*i.e.* the discrete pressure, density and sensible energy unknowns) are associated to the cells of the mesh $\mathcal{M}$, and are denoted by:

$$\{p_K, \rho_K, e_K,\ K \in \mathcal{M}\}\,.$$

Let us then turn to the degrees of freedom for the velocity. The degrees of freedom for the i-th component of the velocity are located at the centre of the faces $\sigma \in \mathcal{E}^{(i)}$, so the whole set of discrete velocity unknowns reads:

$$\Big\{v_{\sigma,i},\ \sigma \in \mathcal{E}^{(i)}_{\rm int},\ 1 \leq i \leq d\Big\}\,.$$

We now introduce a dual mesh, for the finite volume approximation of the time derivative and convection terms in the momentum balance equation. A dual cell D_σ associated to an edge $\sigma \in \mathcal{E}$ is defined as follows:

- if $\sigma = K|L \in \mathcal{E}_{\rm int}$ then $D_\sigma = D_{K,\sigma} \cup D_{L,\sigma}$, where $D_{K,\sigma}$ (resp. $D_{L,\sigma}$) is the rectangle or rectangular parallelepiped of basis σ and of measure $|D_{K,\sigma}| = |K|/2$ (respectively $|D_{L,\sigma}| = |L|/2$) adjacent to σ (see Fig. 3.1);
- if $\sigma \in \mathcal{E}_{\rm ext}$ is adjacent to the cell K, then $D_\sigma = D_{K,\sigma}$.

We denote by $|D_\sigma|$ the measure (area of volume) of the dual cell D_σ, and by $\epsilon = D_\sigma|D'_\sigma$ the face separating two diamond cells D_σ and $D_{\sigma'}$. The set of the (dual) faces of D_σ is denoted by $\tilde{\mathcal{E}}(D_\sigma)$ (see Fig. 3.1). For each velocity component i, the domain Ω is thus partitioned in dual cells: $\Omega = \cup_{\sigma\in\mathcal{E}^{(i)}} D_\sigma$. The i^{th} partition is referred to as the i^{th} dual mesh, associated to the i^{th} velocity component. The set of the edges of the i^{th} dual mesh is denoted by $\tilde{\mathcal{E}}^{(i)}$.

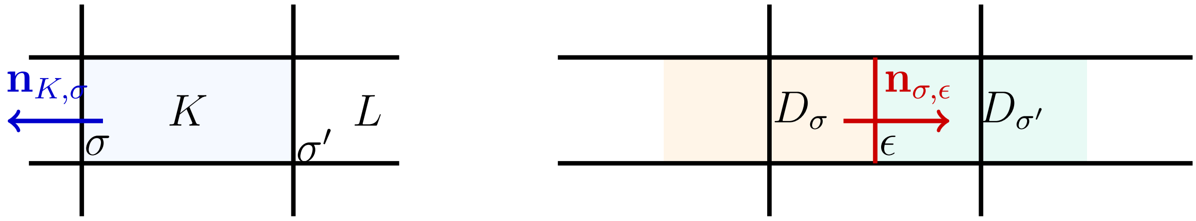

Figure 3.1: Notations for control volumes and edges - left: primal mesh, right: dual mesh for the first component of the velocity.

We need, now, to deal with the impermeability boundary condition, i.e. $\boldsymbol{v}\cdot\mathbf{n} = 0$. Since the velocity unknowns lie on the boundary (and not inside the cells), this condition is taken into account in the definition of the discrete spaces. Given the assumption that the boundary is normal to a coordinate axis, we simply set:

$$v_{\sigma,i} = 0, \quad \forall\sigma \in \mathcal{E}^{(i)}_{ext},\ 1 \leq i \leq d$$

Therefore, there are no degrees of freedom for the velocity on the boundary.

3.4 The numerical scheme

3.4.1 The algorithm

Let us consider a partition $0 = t_0 < t_1 < \cdots < t_N = T$ of the time interval $(0, T)$, which we suppose uniform, and let $\delta t = t_{n+1} - t_n$ for $n = 0, 1, \cdots, N-1$ be the (constant) time step.

The time integration is performed by the second order Heun scheme (which falls in the class of Runge-Kutta schemes), the step n of which may be described throughout three fractional steps described hereafter. The first step reads:

$$\mathbf{W}^n = (\rho^n,\, e^n,\, p^n,\, \boldsymbol{v}^n) \text{ being known,}$$

$$\textbf{First step} \text{ – Compute } \mathbf{W}^{(1)} = (\rho^{(1)},\, e^{(1)},\, p^{(1)},\, \boldsymbol{v}^{(1)}), \text{ by :}$$

$$\mathbf{W}^{(1)} = \mathcal{S}(\mathbf{W}^n) \tag{3.16a}$$

where the relation $\mathbf{W}^{(1)} = \mathcal{S}(\mathbf{W}^n)$ means that the left-hand side is obtained by applying the standard first-order in time explicit scheme to an initial data given by $\mathbf{W}^n$, which reads:

$$\frac{\rho_K^{(1)} - \rho_K^n}{\delta t} + \mathrm{div}_K(\rho^n\, \boldsymbol{v}^n) = 0, \quad \forall K \in \mathcal{M} \tag{3.17a}$$

$$\begin{aligned} \frac{\rho_K^{(1)} e_K^{(1)} - \rho_K^n e_K^n}{\delta t} &+ \mathrm{div}_K(\rho^n\, e^n\, \boldsymbol{v}^n) + p_K^n\, \mathrm{div}_K(\boldsymbol{v}^n) \\ &= (\breve{\boldsymbol{\tau}}(\boldsymbol{v}^n) : \boldsymbol{\nabla} \boldsymbol{v}^n)_K + \mathrm{div}(\breve{\boldsymbol{q}}^n)_K, \quad \forall K \in \mathcal{M} \end{aligned} \tag{3.17b}$$

$$\frac{\rho_{D_\sigma}^{(1)} v_{\sigma,i}^{(1)} - \rho_{D_\sigma}^n v_{\sigma,i}^n}{\delta t} + \mathrm{div}_\sigma(\rho^n \boldsymbol{v}^n v_i^n) + (\boldsymbol{\nabla} p^n)_{\sigma,i} = \mathrm{div}(\breve{\boldsymbol{\tau}}(\boldsymbol{v}^n))_{\sigma,i},\ \forall \sigma \in \mathcal{E}_{\mathrm{int}}^{(i)},\ 1 \le i \le d \tag{3.17c}$$

$$p_K^{(1)} = (\gamma - 1)\, \rho_K^{(1)}\, e_K^{(1)}, \quad \forall K \in \mathcal{M} \tag{3.17d}$$

The terms introduced for each discrete equation will be defined in the following. Note that, to cope with impermeability conditions, the momentum balance equation is not written on the boundary dual cells, and the velocity (in fact, the normal velocity, due to the arrangement of the unknowns) on the boundary edges is just set to zero. The second step of the numerical scheme is analogous to the first one:

$$\textbf{Second step} \text{ – Compute } \mathbf{W}^{(2)} = (\rho^{(2)},\, e^{(2)},\, p^{(2)},\, \boldsymbol{v}^{(2)}), \text{ by :} \tag{3.18a}$$

$$\mathbf{W}^{(2)} = \mathcal{S}(\mathbf{W}^{(1)})$$

Finally, the last step of the algorithm allows to write the $n+1$ unknowns as a linear combination of the n and (2) unknowns:

$$\textbf{Last step} \text{ – Compute } \rho^{n+1},\, e^{n+1},\, p^{n+1} \text{ and } v_i^{n+1},\ 1 \le i \le d \text{ by:}$$

$$\rho_K^{n+1} = \frac{1}{2}\,(\rho_K^n + \rho_K^{(2)}), \quad \forall K \in \mathcal{M} \tag{3.19a}$$

$$\rho_K^{n+1}\, e_K^{n+1} = \frac{1}{2}\big(\rho_K^n\, e_K^n + \rho_K^{(2)}\, e_K^{(2)}\big), \quad \forall K \in \mathcal{M} \tag{3.19b}$$

$$\rho_{D_\sigma}^{n+1}\, v_{\sigma,i}^{n+1} = \frac{1}{2}\big(\rho_{D_\sigma}^n v_{\sigma,i}^n + \rho_{D_\sigma}^{(2)}\, v_{\sigma,i}^{(2)}\big), \quad \forall \sigma \in \mathcal{E}_{\mathrm{int}}^{(i)} \tag{3.19c}$$

$$p_K^{n+1} = (\gamma - 1)\, \rho_K^{n+1}\, e_K^{n+1} \quad \forall K \in \mathcal{M} \tag{3.19d}$$

Remark (A more compact formulation of the time-marching scheme)**.** The Runge Kutta scheme under consideration may be written under the following equivalent form:

$$\tilde{\boldsymbol{W}}^{n+1/2} = \tilde{\boldsymbol{W}}^n - \delta t\ \mathcal{F}(\tilde{\boldsymbol{W}}^n), \tag{3.20}$$

$$\tilde{\boldsymbol{W}}^{n+1} = \tilde{\boldsymbol{W}}^n - \frac{\delta t}{2}\ \big[\mathcal{F}(\tilde{\boldsymbol{W}}^n) + \mathcal{F}(\tilde{\boldsymbol{W}}^{n+1/2})\big], \tag{3.21}$$

where $\tilde{\boldsymbol{W}}$ stands for the vector of conservative variables and $\mathcal{F}$ is a function which gathers the divergence of the fluxes complemented, in the internal energy balance, with the non-conservative terms. In the time semi-discrete stetting, $\tilde{\boldsymbol{W}} = (\rho, \rho\boldsymbol{v}, \rho e)^t$ and

$$\mathcal{F}(\tilde{\boldsymbol{W}}) = \left(\begin{array}{c} \mathrm{div}(\rho\boldsymbol{v}) \\ \mathrm{div}(\rho\boldsymbol{v} \otimes \boldsymbol{v}) + \boldsymbol{\nabla} p - \mathrm{div}(\breve{\boldsymbol{\tau}}(\boldsymbol{v})) \\ \mathrm{div}(\rho e\boldsymbol{v}) + p \ \mathrm{div}\boldsymbol{v} - \mathrm{div}(\breve{\boldsymbol{q}}) - \breve{\boldsymbol{\tau}}(\boldsymbol{v}) : \boldsymbol{\nabla}\boldsymbol{v} \end{array} \right).$$

The first step (3.20) is strictly the same as Step (3.17), so $\tilde{\boldsymbol{W}}^{n+1/2}$ and $\mathbf{W}^{(1)}$ coincide (in the sense that they corresponds to the same primitive functions ρ, $\boldsymbol{u}$, p and e). For conservative equations, the form (3.21) stresses the fact that the scheme is conservative. For instance, considering the mass balance equation, we obtain, in the fully discrete setting,

$$|K| \ \rho_K^{n+1} = |K| \ \rho_K^n + \frac{\delta t}{2} \left(|K| \ \mathrm{div}_K(\rho^n \, \boldsymbol{v}^n) + |K| \ \mathrm{div}_K(\rho^{n+1/2} \, \boldsymbol{v}^{n+1/2}) \right), \quad \forall K \in \mathcal{M},$$

and the last two terms will be defined in the following (see Equation (3.22)) as a sum of mass fluxes over the primal faces of the cell K (so their sum takes itself the same form). Conversely, writing the scheme as a three steps procedure (3.17)-(3.18)-(3.19) facilitates the derivation of some stabilities properties: for instance, if an Euler step (*i.e.* Step (3.17) or (3.18)) preserves the positivity of the density and the internal energy, so does the whole algorithm.

Let us now detail the discrete balance equations involved in (3.17) (or in (3.18)). For the sake of clarity, we omit in the following all the superscripts relative to the time step number.

Discrete mass balance

The convection term of equation (3.17a) reads:

$$\mathrm{div}_K(\rho \, \boldsymbol{v}) = \frac{1}{|K|} \sum_{\sigma \in \mathcal{E}(K)} F_{K,\sigma} \tag{3.22}$$

where $F_{K,\sigma}$ stands for the mass flux across σ outward K. By the impermeability boundary conditions, it vanishes on external faces and is given on internal faces by:

$$F_{K,\sigma} = |\sigma| \ \rho_\sigma \ v_{K,\sigma}, \quad \forall \mathcal{E} \in \mathcal{E}_{\mathrm{int}} \tag{3.23}$$

where $v_{K,\sigma}$ is an approximation of the normal velocity to the face σ outward K defined by:

$$v_{K,\sigma} = v_{\sigma,i} \ \boldsymbol{e}^{(i)} \cdot \mathbf{n}_{K,\sigma}, \quad \forall \mathcal{E} \in \mathcal{E}^{(i)}. \tag{3.24}$$

The density at the face $\sigma = K|L$, ρ_σ, is approximated by a second order MUSCL-like interpolation detailed in Appendix 3.B. The algebraic condition required for this reconstruction is that $\forall K \in \mathcal{M}$ and $\forall \sigma \in \mathcal{E}(K) \cap \mathcal{E}_{\mathrm{int}}$, there exists $\beta^\rho_{K,\sigma} \in [0,1]$ and $M^\rho_{K,\sigma} \in \mathcal{M}$ such that:

$$\rho_\sigma - \rho_K = \left| \begin{array}{ll} \beta^\rho_{K,\sigma}(\rho_K - \rho_{M^\rho_{K,\sigma}}) & \text{if } \boldsymbol{v}_{K,\sigma} \geq 0, \\ \beta^\rho_{K,\sigma}(\rho_{M^\rho_{K,\sigma}} - \rho_K) & \text{otherwise.} \end{array} \right. \tag{3.25}$$

This condition allows, under CFL condition, to guarantee the positivity of the density (see Section 3.4.2). It is, of course, satisfied by the upwind scheme which corresponds to $\beta^\rho_{K,\sigma} = 0$ if $\boldsymbol{v}_{K,\sigma} \geq 0$ and $\beta^\rho_{K,\sigma} = 1$, $M^\rho_{K,\sigma} = L$ if $\boldsymbol{v}_{K,\sigma} \leq 0$.

Discrete sensible energy balance

Equation (3.17b) is an approximation of the sensible energy balance over the primal cell K. The convection operator is defined as follows:

$$|K|\,\mathrm{div}_K(\rho\,\boldsymbol{v}\,e) = \sum_{\sigma\in\mathcal{E}(K)} F_{K,\sigma}\,e_\sigma \tag{3.26}$$

where the discretization of the sensible energy at the primal faces uses the same MUSCL technique as for the density (detailed in Appendix 3.B) to ensure the positivity of the convection operator (see Section 3.4.2). Then, $\forall K \in \mathcal{M}$ and $\forall \sigma \in \mathcal{E}(K) \cap \mathcal{E}_{\mathrm{int}}$, there exists $\beta^{e}_{K,\sigma} \in [0,1]$ and $M^{e}_{K,\sigma} \in \mathcal{M}$ such that:

$$e_\sigma - e_K = \left|\begin{array}{ll} \beta^{e}_{K,\sigma}(e_K - e_{M^{e}_{K,\sigma}}) & \text{if } F_{K,\sigma} \geq 0, \\ \beta^{e}_{K,\sigma}(e_{M^{e}_{K,\sigma}} - e_K) & \text{otherwise.} \end{array}\right. \tag{3.27}$$

Let notice that in the Euler case, this allows also to keep the velocity and pressure constant across (1D) contact discontinuities (Gastaldo et al., 2018).

The discrete divergence of the velocity $\mathrm{div}_K(\boldsymbol{v})$ is simply defined by setting $\rho = 1$ in the $\mathrm{div}_K\,(\rho\boldsymbol{v})$ operator defined by (3.22):

$$\mathrm{div}_K(\boldsymbol{v}) = \frac{1}{|K|}\sum_{\sigma\in\mathcal{E}(K)} |\sigma|\; v_{K,\sigma} \tag{3.28}$$

The viscous dissipation term $(\breve{\boldsymbol{\tau}}(\boldsymbol{v}) : \boldsymbol{\nabla v})_K$ and the viscous diffusion term $\mathrm{div}(\breve{\boldsymbol{\tau}}(\boldsymbol{v}))_{\sigma,i}$ of the momentum balance equation are defined so that they satisfy the following two constraints (see Grapsas (2017) for more details):

- non-negativity of the dissipation : $(\breve{\boldsymbol{\tau}}(\boldsymbol{v}) : \boldsymbol{\nabla v})_K \geq 0$, $\forall K \in \mathcal{M}$;
- consistency of the diffusion and the dissipation, in the following sense:

$$-\sum_{i=1}^{d}\sum_{\sigma\in\mathcal{E}^{(i)}_{\mathrm{int}}} |D_\sigma|\;\mathrm{div}(\breve{\boldsymbol{\tau}}(\boldsymbol{v}))_{\sigma,i}\; v_{\sigma,i} = \sum_{K\in\mathcal{M}} |K|(\breve{\boldsymbol{\tau}}(\boldsymbol{v}) : \boldsymbol{\nabla v})_K \tag{3.29}$$

i.e. the discrete analogue of the identity $\displaystyle\int_\Omega \mathrm{div}(\breve{\boldsymbol{\tau}}(\boldsymbol{v})\cdot\boldsymbol{v}) = -\int_\Omega \breve{\boldsymbol{\tau}}(\boldsymbol{v}) : \boldsymbol{\nabla v}$.

For the heat diffusion term, the usual finite volume scheme based on a two-point approximation of the fluxes is used (Eymard et al., 2000), $\forall K \in \mathcal{M}$:

$$\mathrm{div}(\breve{\boldsymbol{q}})_K = \mathrm{div}\big((\lambda + (\lambda_{SGS})\;\boldsymbol{\nabla} e\big)_K = -\sum_{\sigma\in\mathcal{E}(K),\;\sigma=K|L} (\lambda + (\lambda_{SGS})_\sigma)\;\frac{|\sigma|}{d_\sigma}\;(e_K - e_L), \tag{3.30}$$

with, for $\sigma = K|L$, $(\lambda_{SGS})_\sigma$, the harmonic value of the subgrid heat diffusion coefficient approximation on K and L, weighted by the distances $|\boldsymbol{x}_K - \boldsymbol{x}_\sigma|$ and $|\boldsymbol{x}_K - \boldsymbol{x}_\sigma|$ respectively ($\boldsymbol{x}_K$, $\boldsymbol{x}_L$ and $\boldsymbol{x}_\sigma$ being the mass centers of K, L and σ, respectively). Note that, in this relation, no flux is computed on the external faces, which is consistent with homogeneous Neumann boundary conditions. The SGS heat diffusion coefficient is approximated on the cell K by $(\lambda_{SGS})_K = (\mu_{SGS})_K\,(c_{\mathrm{p}}/\mathrm{Pr}_t)$, the discrete SGS turbulent viscosity $(\mu_{SGS})_K$ being defined hereafter.

Remark. (Dirichlet boundary conditions). In case of Dirichlet boundary conditions, the definition (3.30) of the heat diffusion term must be changed to:

$$\begin{aligned}\operatorname{div}\big((\lambda + (\lambda_{SGS})\ \boldsymbol{\nabla} e)_K \ &= \ -\sum_{\sigma=K|L,\sigma\in\mathcal{E}(K)} \frac{|\sigma|}{d_\sigma}\ (\lambda + (\lambda_{SGS})_\sigma)\ (e_K - e_L)\\ &\quad -\sum_{\sigma\in\mathcal{E}(K)\mathcal{E}(K)\cap\mathcal{E}_{\text{ext}}} \frac{|\sigma|}{d_\sigma}\ (\lambda + (\lambda_{SGS})_\sigma)\ (e_K - e_{\sigma,D})\end{aligned}$$

with $e_{\sigma,D}$ the prescribed value for e on the face σ.

Discrete momentum balance

We now turn to the discrete momentum balance (3.17c). Following Herbin et al. (2018), the density on the dual cells is given by the following weighted average:

$$\left|\begin{array}{l} |D_\sigma|\ \rho_{D_\sigma} = |D_{K,\sigma}|\ \rho_K + |D_{L,\sigma}|\ \rho_L, \quad \text{for } \sigma\in\mathcal{E}_{\text{int}}, \sigma = K|L,\\ \rho_{D_\sigma} = \rho_K, \quad \text{for } \sigma\in\mathcal{E}_{\text{ext}}\end{array}\right. \tag{3.31}$$

The discrete divergence operator on the dual mesh is given by:

$$\operatorname{div}_{D_\sigma}(\rho\,\boldsymbol{v}\,v_i) = \frac{1}{|D_\sigma|}\sum_{\epsilon\in\tilde{\mathcal{E}}^{(i)}(D_\sigma)} F_{\sigma,\epsilon} v_{\epsilon,i} \tag{3.32}$$

where $F_{\sigma,\epsilon}$ is the mass flux through the dual face ϵ outward D_σ and the centered choice is made for the approximation of the i-th component of the velocity on ϵ, $v_{\epsilon,i}$. The discrete mass flux $F_{\sigma,\epsilon}$ is evaluated as linear combination, with constant coefficients, of the primal mass fluxes at the neighboring faces, in such a way that a discrete mass balance over the dual cells holds (Herbin et al., 2018; Gastaldo et al., 2018):

$$\frac{|D_\sigma|}{\delta t}(\rho_{D_\sigma} - \rho^*_{D_\sigma}) + \sum_{\epsilon\in\tilde{\mathcal{E}}^{(i)}(D_\sigma)} F^*_{\sigma,\epsilon} = 0,$$

where the superscript $*$ stands for n for the first step (respectively (1) for the second step) of the Heun scheme. This latest relation allows to derive discrete balance equations for convex functions of the velocity, as a discrete kinetic energy balance (see Section 3.4.2).

The term $(\boldsymbol{\nabla} p)_{\sigma,i}$ stands for the i^{th} component of the discrete pressure gradient at the face σ. The gradient operator is built as the transpose of the discrete operator for the divergence of the velocity on the primal mesh (3.28):

$$(\boldsymbol{\nabla} p)_{\sigma,i} = \frac{|\sigma|}{|D_\sigma|}\ (p_L - p_K)\ \mathbf{n}_{K,\sigma}\cdot\boldsymbol{e}^{(i)}, \text{ for } \sigma = K|L,\ 1\le i\le d \tag{3.33}$$

This pressure gradient is only defined at internal faces since, thanks to the impermeability boundary conditions, no momentum balance equation is written at the external faces. Let notice that definitions (3.33) and (3.28) imply that the discrete gradient and divergence operators are dual with respect to the L^2 inner product:

$$\sum_{K\in\mathcal{M}} |K|\,p_K\operatorname{div}_K(\boldsymbol{v}) + \sum_{i=1}^{d}\sum_{\sigma\in\mathcal{E}^{(i)}_{\text{int}}} |D_\sigma|\,(\boldsymbol{\nabla} p)_{\sigma,i}\,v_{\sigma,i} = 0.$$

Remark. (Outflow or Neumann boundary conditions) When the normal velocity is not prescribed to zero at the boundary face $\sigma \in \mathcal{E}(K)$, we suppose that the flow leaves the domain (*i.e.* $v_{K,\sigma} \geq 0$). The definition (3.23) of $F_{K,\sigma}$ remains unchanged with $\rho_\sigma = \rho_K$. The face σ is also an external dual face of the diamond cell D_σ, and the above mentioned construction procedure of the dual mass fluxes yields $F_{\sigma,\epsilon} = F_{K,\sigma}$; that is $v_{\epsilon,i} = v_{\sigma,i}$, $1 \leq i \leq d$. The expression (3.28) of the discrete divergence of the velocity still holds, but now takes into account a (possibly) non-zero normal velocity $v_{K,\sigma}$ at the external face σ. Therefore, the gradient-divergence duality property becomes:

$$\sum_{K\in\mathcal{M}} |K|\, p_K \operatorname{div}_K(\boldsymbol{v}) + \sum_{i=1}^{d} \sum_{\sigma\in\mathcal{E}^{(i)}_{\text{int}}} |D_\sigma|\, (\boldsymbol{\nabla} p)_{\sigma,i}\, v_{\sigma,i} = \sum_{\sigma\in\mathcal{E}_{\text{ext}}} -|\sigma|\, p_{ext},$$

where p_{ext} stands for the external pressure involved in the outlet boundary condition (applied here on the whole boundary). We thus obtain the following definition of the gradient on the external face σ adjacent to the cell K:

$$(\boldsymbol{\nabla} p)_{\sigma,i} = \frac{|\sigma|}{|D_\sigma|}\, (p_{ext} - p_K)\; \mathbf{n}_{K,\sigma} \cdot \boldsymbol{e}^{(i)}.$$

The definition of the internal energy flux (3.26) remains unchanged (and $e_\sigma = e_K$).

Expression of the discrete subgrid scale viscosity

The mean value of the velocity gradient over K is computed and used in the definition of $\mathbf{S}$:

$$\begin{aligned}\overline{\mathbf{S}_{ij}}^{K} &= \frac{1}{2}\left(\overline{\boldsymbol{\nabla}_j v_i}^{K} + \overline{\boldsymbol{\nabla}_i v_j}^{K}\right) \\ &= \frac{1}{2}\left[\frac{1}{|K|}\int_K \partial_j v_i \, dx + \frac{1}{|K|}\int_K \partial_i v_j \, dx\right],\ 1 \leq i,j \leq d \qquad (3.34)\end{aligned}$$

The SGS viscosity on the cell K is then written as (Boyer et al., 2011):

$$(\mu_{SGS})_K = \rho_K (C_s \Delta)^2 \left[2 \sum_{i=1}^{d} \sum_{j=1}^{d} \overline{\mathbf{S}_{ij}}^{K}\, \overline{\mathbf{S}_{ij}}^{K}\right]^{1/2}. \qquad (3.35)$$

Finally, the initial approximations for ρ, e and $\boldsymbol{v}$ are given by the average of the initial conditions ρ_0 and e_0 on the primal cells and of $\boldsymbol{v}_0$ on the dual cells:

$$\begin{aligned}&\forall K \in \mathcal{M}, \quad \rho^0_K = \frac{1}{|K|}\int_K \rho_0(\boldsymbol{x})\, d\boldsymbol{x}, \qquad \text{and } e^0_K = \frac{1}{|K|}\int_K e_0(\boldsymbol{x})\, d\boldsymbol{x}, \\ &\text{for } 1 \leq i \leq d,\ \forall \sigma \in \mathcal{E}^{(i)}_{\text{int}}, \quad v^0_{\sigma,i} = \frac{1}{|D_\sigma|}\int_{D_\sigma} (\boldsymbol{v}_0(\boldsymbol{x}))_i\, d\boldsymbol{x}.\end{aligned}$$

These average values may be obtained by a quadrature formula if need be.

3.4.2 Properties of the scheme

We first show that the scheme preserves the positivity of the density and of the sensible energy (which, thanks to the equation of state, also implies the positivity of the pressure). Then we discuss the energy preservation properties of the scheme: first, a discrete kinetic energy balance is derived, featuring numerical residual terms which are been shown to be formally of second order in time; then, we obtain that, up to these remainder terms, the scheme conserves the total energy.

Positivity of the density and the sensible energy

The following positivity result is an easy extension of (Gastaldo et al., 2018, Lemma 3.2) to the second order Heun scheme.

LEMMA 3.4.1 (Positivity of the density). *Let* $0 \leq n \leq N-1$, *and let assume that* $\rho^n > 0$ *(*i.e. *for all* $K \in \mathcal{M}$, $\rho_K^n > 0$*) and that the time step satisfies the following condition,* $\forall K \in \mathcal{M}$*:*

$$\delta t \leq \min \left[\frac{|K|}{\displaystyle\sum_{\sigma \in \mathcal{E}(K)} |\sigma| \, (1+\beta^{\rho}_{K,\sigma})(\boldsymbol{v}^n_{K,\sigma})^+}, \frac{|K|}{\displaystyle\sum_{\sigma \in \mathcal{E}(K)} |\sigma| \, (1+\beta^{\rho}_{K,\sigma})(\boldsymbol{v}^{(1)}_{K,\sigma})^+} \right] \tag{3.37}$$

where, for $a \in \mathbb{R}$, $a^+ \geq 0$ *is defined by* $a^+ = \max(a,0)$ *and* $\beta^{\rho}_{K,\sigma}$ *is introduced in* (3.25). *Then a solution to the scheme* (3.16)-(3.19) *satisfies* $\rho^{n+1} > 0$.

The MUSCL interpolation of sensible energy at the face in the discretization of the convection term together with the positivity of the diffusion scheme allows to prove the positivity of the internal energy under a CFL-condition.

LEMMA 3.4.2 (Positivity of the sensible energy). *Let assume that* $e^n > 0$ *(*i.e. $e_K^n > 0$, $\forall K \in \mathcal{M}$*),* $0 \leq n \leq N-1$, *that* $\rho^n > 0$ *and that the CFL condition* (3.37) *holds. In addition, let the time step satisfy the following condition* $\forall K \in \mathcal{M}$*:*

$$\delta t \leq \min \left[\frac{|K| \; \rho_K^n}{(\gamma-1)\, \rho_K^n \displaystyle\sum_{\sigma \in \mathcal{E}(K)} |\sigma| \, (v^n_{K,\sigma})^+ + \displaystyle\sum_{\sigma \in \mathcal{E}(K)} (1+\beta^{e}_{K,\sigma})\, (F^n_{K,\sigma})^+ + |K| \displaystyle\sum_{\sigma \in \mathcal{E}(K)} \frac{|\sigma|}{d_\sigma} \, \breve{\lambda}^n_\sigma}, \right.$$
$$\left. \frac{|K| \; \rho_K^{(1)}}{(\gamma-1)\, \rho_K^{(1)} \displaystyle\sum_{\sigma \in \mathcal{E}(K)} |\sigma| \, (v^{(1)}_{K,\sigma})^+ + \displaystyle\sum_{\sigma \in \mathcal{E}(K)} (1+\beta^{e}_{K,\sigma})\, (F^{(1)}_{K,\sigma})^+ + |K| \displaystyle\sum_{\sigma \in \mathcal{E}(K)} \frac{|\sigma|}{d_\sigma} \, \breve{\lambda}^{(1)}_\sigma} \right] \tag{3.38}$$

with $\breve{\lambda}_\sigma = \lambda + (\lambda_{SGS})_\sigma$, $\sigma = K|L$. *Then the solution to the scheme* (3.17)-(3.19) *satisfies* $e^{n+1} > 0$.

Proof. Let first consider the discrete sensible energy at the first step of the numerical scheme (3.17b). Because $\rho^n > 0$ and (3.37) holds, we have $\rho^{(1)} > 0$ (thanks to (Gastaldo et al., 2018, Lemma 3.2)).

Using the internal energy discretization at the face $\sigma \in \mathcal{E}(K)$, (3.27), there exists $\beta^e_{K,\sigma} \in [0,1]$ and $M^e_{K,\sigma} \in \mathcal{M}$ such that the convection term of (3.17b) reads:

$$\begin{aligned}
|K| \operatorname{div}_K(\rho^n \boldsymbol{v}^n e^n) &= \sum_{\sigma \in \mathcal{E}(K)} F^n_{K,\sigma}\, e^n_\sigma \\
&= \sum_{\sigma \in \mathcal{E}(K)} \left(F^n_{K,\sigma}\right)^+ \left[(\beta^e_{K,\sigma} + 1) e^n_k - \beta^e_{K,\sigma} e^n_{M^e_{K,\sigma}}\right] \\
&- \sum_{\sigma \in \mathcal{E}(K)} \left(F^n_{K,\sigma}\right)^- \left[(1 - \beta^e_{K,\sigma}) e^n_k + \beta^e_{K,\sigma} e^n_{M^e_{K,\sigma}}\right] \qquad (3.39)
\end{aligned}$$

where, for $a \in \mathbb{R}$, $a^- \geq 0$ is defined by $a^- = -\min(a, 0)$. Moreover, expressing the pressure thanks to the equation of state (3.17d) leads to:

$$\begin{aligned}
|K|\, p^n_K \operatorname{div}_K(\boldsymbol{v}^n) &= p^n_K \sum_{\sigma \in \mathcal{E}(K)} |\sigma| \boldsymbol{v}^n_{K,\sigma} \\
&= (\gamma - 1)\, \rho^n_K\, e^n_K \sum_{\sigma \in \mathcal{E}(K)} |\sigma| (\boldsymbol{v}^n_{K,\sigma})^+ \\
&- (\gamma - 1)\, \rho^n_K\, e^n_K \sum_{\sigma \in \mathcal{E}(K)} |\sigma| (\boldsymbol{v}^n_{K,\sigma})^- \qquad (3.40)
\end{aligned}$$

Thus, using (3.39), (3.40) and (3.30), the energy balance (3.17b) can be rewritten as:

$$\begin{aligned}
\frac{|K|}{\delta t} \rho^{(1)}_K\, e^{(1)}_K &= \Bigg[\frac{|K|}{\delta t} \rho^n_K - \sum_{\sigma \in \mathcal{E}(K)} (\beta^e_{K,\sigma} + 1) \left(F^n_{K,\sigma}\right)^+ \\
&- (\gamma - 1)\, \rho^n_K \sum_{\sigma \in \mathcal{E}(K)} |\sigma| \left(\boldsymbol{v}^n_{K,\sigma}\right)^+ - |K| \sum_{\sigma \in \mathcal{E}(K)} \frac{|\sigma|}{d_\sigma} \breve{\lambda}^n_\sigma \Bigg]\, e^n_K \\
&+ \sum_{\sigma \in \mathcal{E}(K)} \beta^e_{K,\sigma}\, |F^n_{K,\sigma}|\, e^n_{M^e_{K,\sigma}} + \sum_{\sigma \in \mathcal{E}(K)} (1 - \beta^e_{K,\sigma}) e^n_K \left(F^n_{K,\sigma}\right)^- \\
&+ (\gamma - 1)\, \rho^n_K\, e^n_K \sum_{\sigma \in \mathcal{E}(K)} |\sigma| \left(\boldsymbol{v}^n_{K,\sigma}\right)^- \\
&+ |K| \sum_{\sigma \in \mathcal{E}(K)} \frac{|\sigma|}{d_\sigma} \breve{\lambda}^n_\sigma\, e^n_L + |K|\, (\boldsymbol{\tau}(\boldsymbol{v}^n) : \boldsymbol{\nabla} \boldsymbol{v}^n)_K \qquad (3.41)
\end{aligned}$$

Thus, using to the non-negativity of the viscous dissipation term and the fact that by construction $\breve{\lambda}^n_\sigma > 0$, we get $e^{(1)} > 0$ under the following CFL condition:

$$\delta t \leq \left[\frac{|K|\, \rho^n_K}{(\gamma - 1)\, \rho^n_K \displaystyle\sum_{\sigma \in \mathcal{E}(K)} |\sigma|\, (v^n_{K,\sigma})^+ + \sum_{\sigma \in \mathcal{E}(K)} (1 + \beta^e_{K,\sigma})\, (F^n_{K,\sigma})^+ + |K| \sum_{\sigma \in \mathcal{E}(K)} \frac{|\sigma|}{d_\sigma} \breve{\lambda}^n_\sigma}\right]$$

Using the same methodology, we prove that $e^{(2)} > 0$ under the CFL condition (3.38). Finally, because $\rho^n > 0$ and (3.37) is satisfied, $\rho^{n+1} > 0$. The definition of e^{n+1} (3.19b) ends the proof. $\square$

Energy balances

At the continuous level, the kinetic energy balance is obtained by taking the inner product of the momentum balance equation by the velocity and using the mass balance equation. At the discrete level, the computation is essentially the same for the convection term, provided that a momentum balance and a mass balance hold on the same cell, which is ensured by construction of the dual densities and mass fluxes (Relations (3.31) and (3.32)). The conservative term is left at the left-hand side of the equation, while the dissipation term is considered as a residual.

Theorem 3.4.1 (Discrete kinetic energy balance for the second order time discretization) A solution to the system (3.17) satisfies the following equality, for $1 \leq i \leq d$, $\sigma \in \mathcal{E}_{\text{int}}^{(i)}$ and $0 \leq n \leq N-1$:

$$\begin{aligned}
&\frac{1}{2}\,\frac{|D_\sigma|}{\delta t}\left[\rho_{D_\sigma}^{n+1}(v_{\sigma,i}^{n+1})^2 - \rho_{D_\sigma}^{n}(v_{\sigma,i}^{n})^2\right] \\
&+\frac{1}{4}\sum_{\substack{\epsilon\in\tilde{\mathcal{E}}^{(i)}(D_\sigma),\\ \epsilon=D_\sigma|D_{\sigma'}}} F_{\sigma,\epsilon}^{n} v_{\sigma,i}^{n} v_{\sigma',i}^{n} + \frac{1}{2}\,|D_\sigma|\,(\boldsymbol{\nabla} p)_{\sigma,i}^{n}\; v_{\sigma,i}^{n} - \frac{1}{2}\,|D_\sigma|\,\mathrm{div}\boldsymbol{\tau}(\boldsymbol{v}^n)_{\sigma,i}\; v_{\sigma,i}^{n} \\
&+\frac{1}{4}\sum_{\substack{\epsilon\in\tilde{\mathcal{E}}^{(i)}(D_\sigma),\\ \epsilon=D_\sigma|D_{\sigma'}}} F_{\sigma,\epsilon}^{(1)} v_{\sigma,i}^{(1)} v_{\sigma',i}^{(1)} + \frac{1}{2}\,|D_\sigma|\,(\boldsymbol{\nabla} p)_{\sigma,i}^{(1)}\; v_{\sigma,i}^{(1)} - \frac{1}{2}\,|D_\sigma|\,\mathrm{div}\boldsymbol{\tau}(\boldsymbol{v}^{(1)})_{\sigma,i}\; v_{\sigma,i}^{(1)} = -R_{\sigma,i}^{n+1}
\end{aligned} \tag{3.43}$$

with

$$R_{\sigma,i}^{n+1} = \frac{1}{4}\frac{|D_\sigma|}{\delta t}\rho_{D_\sigma}^{n}\,\left(v_{\sigma,i}^{n+1} - v_{\sigma,i}^{n}\right)^2 + \frac{1}{4}\frac{|D_\sigma|}{\delta t}\rho_{D_\sigma}^{(2)}\left(v_{\sigma,i}^{n+1} - v_{\sigma,i}^{(2)}\right)^2 + \frac{1}{2}\,R_{\sigma,i}^{(1)} + \frac{1}{2}\,R_{\sigma,i}^{(2)} \tag{3.44}$$

and

$$R_{\sigma,i}^{(1)} = -\frac{1}{2}\,\frac{|D_\sigma|}{\delta t}\rho_{D_\sigma}^{(1)}\left(v_{\sigma,i}^{n} - v_{\sigma,i}^{(1)}\right)^2, \quad R_{\sigma,i}^{(2)} = -\frac{1}{2}\,\frac{|D_\sigma|}{\delta t}\rho_{D_\sigma}^{(2)}\left(v_{\sigma,i}^{(1)} - v_{\sigma,i}^{(2)}\right)^2 \tag{3.45}$$

Proof. Multiplying (3.19c) by $v_{\sigma,i}^{n+1}$, $\forall\sigma \in \mathcal{E}_{\text{int}}^{(i)}$, $1 \leq i \leq d$ yields:

$$\begin{aligned}
2\,\rho_{D_\sigma}^{n+1}\;(v_{\sigma,i}^{n+1})^2 &= \left(\rho_{D_\sigma}^{n} v_{\sigma,i}^{n} + \rho_{D_\sigma}^{(2)}\; v_{\sigma,i}^{(2)}\right)\; v_{\sigma,i}^{n+1} \\
&= \rho_{D_\sigma}^{n}\;\left(v_{\sigma,i}^{n} - v_{\sigma,i}^{n+1}\right)\; v_{\sigma,i}^{n+1} + \rho_{D_\sigma}^{n}\;(v_{\sigma,i}^{n+1})^2 \\
&+\; \rho_{D_\sigma}^{(2)}\;\left(v_{\sigma,i}^{(2)} - v_{\sigma,i}^{n+1}\right)\; v_{\sigma,i}^{n+1} + \rho_{D_\sigma}^{(2)}\;(v_{\sigma,i}^{n+1})^2
\end{aligned}$$

Using the identity $2a(a-b) = a^2 - b^2 + (a-b)^2$, we get:

$$\begin{aligned}
2\,\rho_{D_\sigma}^{n+1}\;(v_{\sigma,i}^{n+1})^2 &= \frac{1}{2}\rho_{D_\sigma}^{n}(v_{\sigma,i}^{n+1})^2 + \frac{1}{2}\rho_{D_\sigma}^{n}\;(v_{\sigma,i}^{n})^2 - \frac{1}{2}\rho_{D_\sigma}^{n}\;\left(v_{\sigma,i}^{n+1} - v_{\sigma,i}^{n}\right)^2 \\
&+\; \frac{1}{2}\rho_{D_\sigma}^{(2)}(v_{\sigma,i}^{n+1})^2 + \frac{1}{2}\rho_{D_\sigma}^{(2)}(v_{\sigma,i}^{(2)})^2 - \frac{1}{2}\rho_{D_\sigma}^{(2)}\left(v_{\sigma,i}^{n+1} - v_{\sigma,i}^{(2)}\right)^2
\end{aligned} \tag{3.46}$$

Thanks to (3.19a) and to (3.31), $\rho^{n+1}_{D_\sigma} = 1/2\big(\rho^n_{D_\sigma} + \rho^{(2)}_{D_\sigma}\big)$, thus:

$$\begin{aligned}\rho^{n+1}_{D_\sigma}\,(v^{n+1}_{\sigma,i})^2 &= \frac{1}{2}\rho^n_{D_\sigma}\,(v^n_{\sigma,i})^2 - \frac{1}{2}\rho^n_{D_\sigma}\,\big(v^{n+1}_{\sigma,i} - v^n_{\sigma,i}\big)^2 \\ &+ \frac{1}{2}\rho^{(2)}_{D_\sigma}(v^{(2)}_{\sigma,i})^2 - \frac{1}{2}\rho^{(2)}_{D_\sigma}\big(v^{n+1}_{\sigma,i} - v^{(2)}_{\sigma,i}\big)^2\end{aligned} \tag{3.47}$$

Subtracting $\rho^n_{D_\sigma}\,(v^n_{\sigma,i})^2$ and multiplying by $\dfrac{1}{2}\,\dfrac{|D_\sigma|}{\delta t}$ leads to:

$$\begin{aligned}\frac{1}{2}\,\frac{|D_\sigma|}{\delta t}\,\big[\rho^{n+1}_{D_\sigma}\,(v^{n+1}_{\sigma,i})^2 - \rho^n_{D_\sigma}\,(v^n_{\sigma,i})^2\big] &= \underbrace{\frac{1}{4}\frac{|D_\sigma|}{\delta t}\,\Big[\rho^{(1)}_{D_\sigma}\,(v^{(1)}_{\sigma,i})^2 - \rho^n_{D_\sigma}\,(v^n_{\sigma,i})^2\Big]}_{T_1} \\ &+ \underbrace{\frac{1}{4}\frac{|D_\sigma|}{\delta t}\,\Big[\rho^{(2)}_{D_\sigma}(v^{(2)}_{\sigma,i})^2 - \rho^{(1)}_{D_\sigma}\,(v^{(1)}_{\sigma,i})^2\Big]}_{T_2} \\ &- \frac{1}{4}\frac{|D_\sigma|}{\delta t}\rho^n_{D_\sigma}\,\big(v^{n+1}_{\sigma,i} - v^n_{\sigma,i}\big)^2 \\ &- \frac{1}{4}\frac{|D_\sigma|}{\delta t}\rho^{(2)}_{D_\sigma}\big(v^{n+1}_{\sigma,i} - v^{(2)}_{\sigma,i}\big)^2\end{aligned} \tag{3.48}$$

In order to recover T_1, let multiply the momentum balance of the first step of the Heun scheme by $v^n_{\sigma,i}$, $\forall \sigma \in \mathcal{E}^{(i)}_{\text{int}}$, $1 \le i \le d$:

$$\begin{aligned}&\underbrace{\left[\frac{|D_\sigma|}{\delta t}\,\big(\rho^{(1)}_{D_\sigma} v^{(1)}_{\sigma,i} - \rho^n_{D_\sigma} v^n_{\sigma,i}\big) + \sum_\epsilon F^n_{\sigma,\epsilon} v^n_{\epsilon,i}\right]\,v^n_{\sigma,i}}_{T_3} \\ &\qquad + \big[|D_\sigma|\,(\boldsymbol{\nabla} p^n)_{\sigma,i} - |D_\sigma|\,\mathrm{div}(\boldsymbol{\tau}(\boldsymbol{v}^n))_{\sigma,i}\big]\;v^n_{\sigma,i} = 0\end{aligned} \tag{3.49}$$

where $\displaystyle\sum_\epsilon$ denotes the sum over the internal faces of D_σ, the neighboring diamond cell being $D_{\sigma'}$ (*i.e.* $\epsilon = D_\sigma|D_{\sigma'}$). Let remark that thanks to the mass balance equation (3.17a), for any families (z^n_σ) and (z^n_ϵ), $\sigma \in \mathcal{E}^{(i)}_{\text{int}}$, $\epsilon \in \tilde{\mathcal{E}}^{(i)}(D_\sigma)$, $0 \le n \le N-1$, we have:

$$\frac{|D_\sigma|}{\delta t}(\rho^{(1)}_{D_\sigma} z^{(1)}_\sigma\; - \;\rho^n_{D_\sigma} z^n_\sigma) + \sum_\epsilon F^n_{\sigma,\epsilon} z^n_\epsilon \;=\; \frac{|D_\sigma|}{\delta t}\rho^{(1)}_{D_\sigma}(z^{(1)}_\sigma\; - \;z^n_\sigma) + \sum_\epsilon F^n_{\sigma,\epsilon}\;\,(z^n_\epsilon\; - \;z^n_\sigma). \tag{3.50}$$

If (z^n_σ) and (z^n_ϵ) are approximations of a continuous variable z, the left and right hand sides may be seen as a discretization of $\partial_t(\rho\,z) + \mathrm{div}(\rho\,z\,\boldsymbol{v})$ and $\rho\,\partial_t z + \rho\,\boldsymbol{v}\cdot\boldsymbol{\nabla} z$, respectively. This computation is thus the discrete analogue of the passage from the conservative form to the non-conservative form of a balance equation. Then, T_3 can be rewritten as:

$$T_3 \;=\; \left[\frac{|D_\sigma|}{\delta t}\rho^{(1)}_{D_\sigma}(v^{(1)}_{\sigma,i} - v^n_{\sigma,i}) + \sum_\epsilon F^n_{\sigma,\epsilon}\frac{v^n_{\sigma',i} - v^n_{\sigma,i}}{2}\right]\,v^n_{\sigma,i} \tag{3.51}$$

Using twice the identity $2a(a-b) = a^2 - b^2 + (a-b)^2$, we get:

$$\begin{aligned}T_3 \;=\; &\frac{1}{2}\,\frac{|D_\sigma|}{\delta t}\rho^{(1)}_{D_\sigma}\Big[(v^{(1)}_{\sigma,i})^2 - (v^n_{\sigma,i})^2\Big] + \frac{1}{4}\sum_\epsilon F^n_{\sigma,\epsilon}\,\big[(v^n_{\sigma',i})^2 - (v^n_{\sigma,i})^2\big] \\ - \;&\frac{1}{2}\,\frac{|D_\sigma|}{\delta t}\rho^{(1)}_{D_\sigma}\big(v^n_{\sigma,i} - v^{(1)}_{\sigma,i}\big)^2 - \frac{1}{4}\sum_\epsilon F^n_{\sigma,\epsilon}\big(v^n_{\sigma,i} - v^n_{\sigma',i}\big)^2\end{aligned} \tag{3.52}$$

Turning to the conservative form with (3.50) yields:

$$\begin{aligned}
T_3 \;=\;& \frac{1}{2}\,\frac{|D_\sigma|}{\delta t}\Big[\rho^{(1)}_{D_\sigma}(v^{(1)}_{\sigma,i})^2 - \rho^{n}_{D_\sigma}(v^{n}_{\sigma,i})^2\Big] + \frac{1}{4}\sum_{\epsilon} F^{n}_{\sigma,\epsilon}\,\big[(v^{n}_{\sigma',i})^2 + (v^{n}_{\sigma,i})^2\big] \\
-\;& \frac{1}{2}\,\frac{|D_\sigma|}{\delta t}\rho^{(1)}_{D_\sigma}\big(v^{n}_{\sigma,i} - v^{(1)}_{\sigma,i}\big)^2 - \frac{1}{4}\sum_{\epsilon} F^{n}_{\sigma,\epsilon}\big(v^{n}_{\sigma,i} - v^{n}_{\sigma',i}\big)^2 \\
=\;& \frac{1}{2}\,\frac{|D_\sigma|}{\delta t}\Big[\rho^{(1)}_{D_\sigma}(v^{(1)}_{\sigma,i})^2 - \rho^{n}_{D_\sigma}(v^{n}_{\sigma,i})^2\Big] + \frac{1}{2}\sum_{\epsilon} F^{n}_{\sigma,\epsilon}\,v^{n}_{\sigma,i}\,v^{n}_{\sigma',i} \\
-\;& \frac{1}{2}\,\frac{|D_\sigma|}{\delta t}\rho^{(1)}_{D_\sigma}\big(v^{n}_{\sigma,i} - v^{(1)}_{\sigma,i}\big)^2
\end{aligned} \tag{3.53}$$

where the second term is conservative. Introducing the previous relation in (3.49), we obtain the following discrete kinetic energy balance equation for the first step of the Heun scheme:

$$\begin{aligned}
&\frac{1}{2}\,\frac{|D_\sigma|}{\delta t}\Big[\rho^{(1)}_{D_\sigma}(v^{(1)}_{\sigma,i})^2 - \rho^{n}_{D_\sigma}(v^{n}_{\sigma,i})^2\Big] + \frac{1}{2}\sum_{\epsilon} F^{n}_{\sigma,\epsilon}\,v^{n}_{\sigma,i}\,v^{n}_{\sigma',i} \\
&\qquad + \big[|D_\sigma|\,(\boldsymbol{\nabla} p^{n})_{\sigma,i} - |D_\sigma|\,\mathrm{div}(\boldsymbol{\tau}(\boldsymbol{v}^{n}))_{\sigma,i}\big]\;v^{n}_{\sigma,i} = -R^{(1)}_{\sigma,i}
\end{aligned} \tag{3.54}$$

with

$$R^{(1)}_{\sigma,i} = -\frac{1}{2}\,\frac{|D_\sigma|}{\delta t}\rho^{(1)}_{D_\sigma}\big(v^{n}_{\sigma,i} - v^{(1)}_{\sigma,i}\big)^2 \tag{3.55}$$

The term T_1 of (3.48) can thus be rewritten as:

$$T_1 = -\frac{1}{4}\sum_{\epsilon} F^{n}_{\sigma,\epsilon}\,v^{n}_{\sigma,i}\,v^{n}_{\sigma',i} - \frac{1}{2}\,\big[|D_\sigma|\,(\boldsymbol{\nabla} p^{n})_{\sigma,i} - |D_\sigma|\,\mathrm{div}(\boldsymbol{\tau}(\boldsymbol{v}^{n}))_{\sigma,i}\big]\;v^{n}_{\sigma,i} - \frac{1}{2}\,R^{(1)}_{\sigma,i}$$

Using the same procedure, the following discrete kinetic energy balance equation for the second step of the Heun scheme:

$$\begin{aligned}
&\frac{1}{2}\,\frac{|D_\sigma|}{\delta t}\Big[\rho^{(2)}_{D_\sigma}(v^{(2)}_{\sigma,i})^2 - \rho^{(1)}_{D_\sigma}(v^{(1)}_{\sigma,i})^2\Big] + \frac{1}{2}\sum_{\epsilon} F^{(1)}_{\sigma,\epsilon}\,v^{(1)}_{\sigma,i}\,v^{(1)}_{\sigma',i} \\
&\qquad + \Big[|D_\sigma|\,(\boldsymbol{\nabla} p^{(1)})_{\sigma,i} - |D_\sigma|\,\mathrm{div}(\boldsymbol{\tau}(\boldsymbol{v}^{(1)}))_{\sigma,i}\Big]\;v^{(1)}_{\sigma,i} = -R^{(2)}_{\sigma,i}
\end{aligned} \tag{3.56}$$

with

$$R^{(2)}_{\sigma,i} = -\frac{1}{2}\,\frac{|D_\sigma|}{\delta t}\rho^{(2)}_{D_\sigma}\big(v^{(1)}_{\sigma,i} - v^{(2)}_{\sigma,i}\big)^2$$

The term T_2 of (3.48) can thus be rewritten as:

$$T_2 = -\frac{1}{4}\sum_{\epsilon} F^{(1)}_{\sigma,\epsilon}\,v^{(1)}_{\sigma,i}\,v^{(1)}_{\sigma',i} - \frac{1}{2}\,\Big[|D_\sigma|\,(\boldsymbol{\nabla} p^{(1)})_{\sigma,i} - |D_\sigma|\,\mathrm{div}(\boldsymbol{\tau}(\boldsymbol{v}^{(1)}))_{\sigma,i}\Big]\;v^{(1)}_{\sigma,i} - \frac{1}{2}\,R^{(2)}_{\sigma,i}$$

Replacing in (3.56) and (3.57) in (3.48) leads to:

$$\begin{aligned}
&\frac{1}{2}\,\frac{|D_\sigma|}{\delta t}\,\big[\rho^{n+1}_{D_\sigma}(v^{n+1}_{\sigma,i})^2 - \rho^{n}_{D_\sigma}(v^{n}_{\sigma,i})^2\big] \\
&+\frac{1}{4}\sum_{\epsilon} F^{n}_{\sigma,\epsilon}\,v^{n}_{\sigma,i}\,v^{n}_{\sigma',i} + \frac{1}{2}|D_\sigma|\,(\boldsymbol{\nabla} p^{n})_{\sigma,i}\,v^{n}_{\sigma,i} - \frac{1}{2}|D_\sigma|\,\mathrm{div}(\boldsymbol{\tau}(\boldsymbol{v}^{n}))_{\sigma,i}\,v^{n}_{\sigma,i} \\
&+\frac{1}{4}\sum_{\epsilon} F^{(1)}_{\sigma,\epsilon}\,v^{(1)}_{\sigma,i}\,v^{(1)}_{\sigma',i} + \frac{1}{2}|D_\sigma|\,(\boldsymbol{\nabla} p^{(1)})_{\sigma,i}\,v^{(1)}_{\sigma,i} - \frac{1}{2}|D_\sigma|\,\mathrm{div}(\boldsymbol{\tau}(\boldsymbol{v}^{(1)}))_{\sigma,i}\,v^{(1)}_{\sigma,i} = -R^{n+1}_{\sigma,i}
\end{aligned} \tag{3.57}$$

with

$$R_{\sigma,i}^{n+1} = \frac{1}{4}\frac{|D_\sigma|}{\delta t}\rho_{D_\sigma}^{n}\ \big(v_{\sigma,i}^{n+1} - v_{\sigma,i}^{n}\big)^2 + \frac{1}{4}\frac{|D_\sigma|}{\delta t}\rho_{D_\sigma}^{(2)}\big(v_{\sigma,i}^{n+1} - v_{\sigma,i}^{(2)}\big)^2 + \frac{1}{2}\,R_{\sigma,i}^{(1)} + \frac{1}{2}\,R_{\sigma,i}^{(2)}$$

□

One of the essential features of the Heun scheme is that the remainder term of the kinetic energy balance is formally of second order with respect to the time step. This result is stated in the following lemma.

LEMMA 3.4.3. *The remainder term of the kinetic energy balance is of second order with respect to the time discretization in the following sense. For* $1 \leq i \leq d$, $0 \leq n \leq N$, $\sigma \in \mathcal{E}_{\rm int}^{(i)}$, *let* $(v')_{\sigma,i}^{n}$ *and* $C_{\sigma,i}^{n}$ *be two real numbers such that*

$$|v_{\sigma,i}^{n+1} - v_{\sigma,i}^{n} - \delta t\ (v')_{\sigma,i}^{n}| \leq C_{\sigma,i}^{n}\ \delta t^2, \quad |v_{\sigma,i}^{(1)} - v_{\sigma,i}^{n} - \delta t\ (v')_{\sigma,i}^{n}| \leq C_{\sigma,i}^{n}\ \delta t^2,$$
$$|v_{\sigma,i}^{(2)} - v_{\sigma,i}^{n} - 2\,\delta t\ (v')_{\sigma,i}^{n}| \leq C_{\sigma,i}^{n}\ \delta t^2. \tag{3.58}$$

Let us suppose in addition that the real numbers $\bar\rho_{D_\sigma}^{n}$, $(\rho')_{D_\sigma}^{n}$ *and* C_{D_σ} *are such that*

$$\rho_{D_\sigma}^{n} \leq \bar\rho_{D_\sigma}^{n}, \quad \rho_{D_\sigma}^{(2)} \leq \bar\rho_{D_\sigma}^{n} \quad \text{and } |\rho_{D_\sigma}^{(2)} - \rho_{D_\sigma}^{n} - \delta t\ (\rho')_{D_\sigma}^{n}| \leq C_{D_\sigma}\delta t^2. \tag{3.59}$$

Then:

$$|R_{\sigma,i}^{n+1}| \leq \mathcal{C}_{\sigma,i}^{n}\ |D_\sigma|\ \delta t^2 + h.o.t., \tag{3.60}$$

where $\mathcal{C}_{\sigma,i}^{n}$ *only depends on* $\bar\rho_{D_\sigma}^{n}$, $(\rho')_{D_\sigma}^{n}$, $(v')_{\sigma,i}^{n}$, C_{D_σ} *and* $C_{\sigma,i}^{n}$ *and h.o.t. stands for higher order terms,* i.e. *terms which take the form of a product of a function of these same coefficients and* δt *by* δt^3. *Consequently, if* $\mathcal{C}$ *is such that* $\mathcal{C}_{\sigma,i}^{n} \leq \mathcal{C}$ *for* $1 \leq i \leq d$, $0 \leq n \leq N-1$ *and* $\sigma \in \mathcal{E}_{\rm int}^{(i)}$, *the total residual of the kinetic energy balance and its integral over the time satisfies, up to higher order terms:*

$$\sum_{i=1}^{d}\sum_{\sigma\in\mathcal{E}_{\rm int}^{(i)}} |R_{\sigma,i}^{n+1}| \leq 2\ \mathcal{C}\ |\Omega|\ \delta t^2, \qquad \sum_{k=0}^{n}\delta t\sum_{i=1}^{d}\sum_{\sigma\in\mathcal{E}_{\rm int}^{(i)}} |R_{\sigma,i}^{k+1}| \leq 2\ \mathcal{C}\ |\Omega|\ T\ \delta t^2, \tag{3.61}$$

for $0 \leq n \leq N-1$.

Proof. Let us drop, for short, the face and component indexes, and the time indexes when they are not necessary. With such notations, we have

$$R = \frac{|D|}{4\,\delta t}\ (T_1 + T_2), \quad T_1 = \rho^{(2)}\ \big[(v^{n+1} - v^{(2)})^2 - (v^{(2)} - v^{(1)})^2\big],$$
$$T_2 = \rho^{n}(v^{n+1} - v^{n})^2 - \rho^{(1)}(v^{(1)} - v^{n})^2.$$

We write T_1 as

$$T_1 = \rho^{(2)}\ \big(v^{n+1} - 2\,v^{(2)} + v^{(1)}\big)\ \big(v^{n+1} - v^{(1)}\big),$$

and each velocity component is compared to its "Taylor-like development" featured in Inequalities (3.58):

$$T_1 = \rho^{(2)} \,\big[(v^{n+1} - v^n - v'\delta t) - 2\,(v^{(2)} - v^n - 2\,v'\delta t) + (v^{(1)} - v^n - v'\delta t) - 2\,v'\delta t\big] \\ \big[(v^{n+1} - v^n - v'\delta t) - (v^{(1)} - v^n - v'\delta t)\big],$$

Using the triangle inequalities and (3.58), we obtain that the leading order terms with respect to δt are of order δt in the second factor and of order δt^2 in the third one. Invoking the inequality (3.59), we obtain the desired bound for T_1. The term T_2 is decomposed as $T_2 = T_{2,1} + T_{2,2}$ with

$$T_{2,1} = (\rho^n - \rho^{(1)})(v^{(1)} - v^n)^2, \quad T_{2,2} = \rho^n \big[(v^{n+1} - v^n)^2 - (v^{(1)} - v^n)^2\big].$$

Thanks to (3.58) and (3.59), we obtain that the leading order terms in $T_{2,1}$ are of order δt for the first factor and of order δt^2 in the second one (taking into account the fact that the velocity difference is squared). The term $T_{2,2}$ is bounded by the same technique as T_1:

$$\begin{aligned} T_{2,2} &= \rho^n \big[v^{n+1} - 2\,v^n + v^{(1)}\big]\ \big[v^{n+1} - v^{(1)}\big] \\ &= \rho^n \big[v^{n+1} - 2\,v^n + v^{(1)}\big]\ \big[(v^{n+1} - v^n - v'\delta t) - (v^{(1)} - v^n - v'\delta t)\big], \end{aligned}$$

and the second factor is of order δt while the second factor is of order δt^2. This concludes the proof of Relation (3.60). The bounds (3.61) are obtained by summation first over the faces and then over the time steps. □

To obtain a conservation equation for the total energy, we first need to derive a discrete kinetic energy balance posed on the primal mesh. Then, this relation will be added to the internal energy balance, to obtain the desired discrete balance equation. This process fully applies when the viscosity is set to zero, and we restrict here the exposition to this case; the momentum diffusion terms are dealt with in the appendix 3.A. Let us recast the discrete kinetic energy balance in the inviscid case as follows:

$$\frac{|D_\sigma|}{\delta t} \big[(e_k)_{\sigma,i}^{n+1} - (e_k)_{\sigma,i}^n\big] + \sum_{\epsilon \in \tilde{\mathcal{E}}(D_\sigma)} G_{\sigma,\epsilon}^{n+1} + |D_\sigma|\ \big((\boldsymbol{\nabla} p)\ v\big)_{\sigma,i}^{n+1} = -R_{\sigma,i}^{n+1}, \tag{3.62}$$

where:

$$\begin{aligned} (e_k)_{\sigma,i}^\ell &= \frac{1}{2}\ \rho_{D_\sigma}^\ell (v_{\sigma,i}^\ell)^2, \quad \text{for } \ell = n \text{ and } \ell = n+1, \\ G_{\sigma,\epsilon}^{n+1} &= \frac{1}{4}\big(F_{\sigma,\epsilon}^n v_{\sigma,i}^n v_{\sigma',i}^n + F_{\sigma,\epsilon}^{(1)} v_{\sigma,i}^{(1)} v_{\sigma',i}^{(1)}\big), \quad \text{for } \epsilon = \sigma|\sigma', \\ |D_\sigma|\ \big((\boldsymbol{\nabla} p)\ v\big)_{\sigma,i}^{n+1} &= \frac{1}{2}\ |D_\sigma|\ \big((\boldsymbol{\nabla} p)_{\sigma,i}^n\ v_{\sigma,i}^n + (\boldsymbol{\nabla} p)_{\sigma,i}^{(1)}\ v_{\sigma,i}^{(1)}\big). \end{aligned}$$

Let $1 \le i \le d$, let $K \in \mathcal{M}$, let us denote by σ and σ' the two faces of $\mathcal{E}^{(i)}(K)$, and let us define:

$$(e_k)_{K,i}^\ell = \frac{1}{2\,|K|}\Big[|D_\sigma|\ (e_k)_{\sigma,i}^\ell + |D_{\sigma'}|\ (e_k)_{\sigma',i}^\ell\Big], \ \text{for } \ell = n \text{ or } \ell = n+1.$$

Case of primal faces parallel to the dual faces. Let $\tau = \sigma$ or $\tau = \sigma'$, let ϵ_1 and ϵ_2 be the two faces of D_τ perpendicular to $\boldsymbol{e}^{(i)}$, and let ϵ_2 be the one included in K (see Fig. 3.2). Then we define

$$G_{K,\tau,i}^{n+1} = \frac{1}{2}\big[G_{\tau,\epsilon_1}^{n+1} - G_{\tau,\epsilon_2}^{n+1}\big].$$

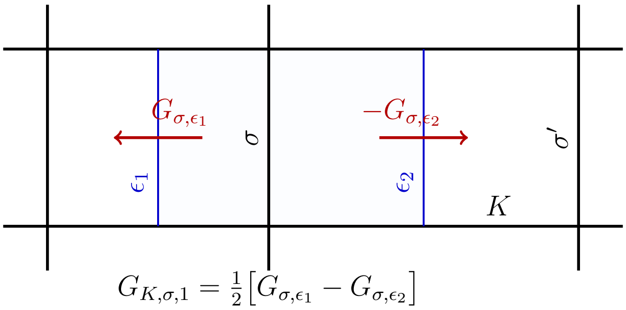

Figure 3.2: From fluxes at dual faces to fluxes at primal faces, for the MAC discretization, primal faces parallel to the dual edges, first component of the velocity.

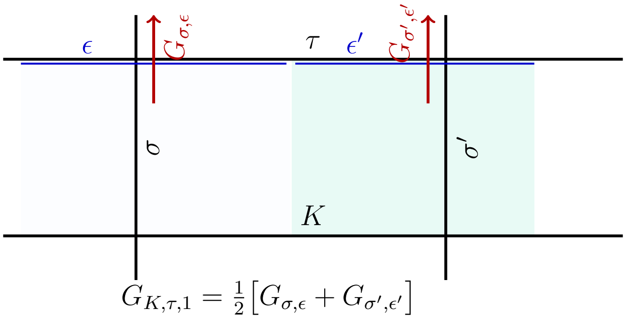

Figure 3.3: From fluxes at dual faces to fluxes at primal faces, for the MAC discretization, primal faces orthogonal to the dual edges, first component of the velocity.

Case of primal faces orthogonal to the dual faces. For $\tau \in \mathcal{E}(K) \setminus \{\sigma, \sigma'\}$, let ϵ and ϵ' be such that $\tau \subset (\bar\epsilon \cup \bar\epsilon')$ with ϵ a face of D_σ and ϵ' a face of $D_{\sigma'}$ (see Fig. 3.3).

Then we define

$$G^{n+1}_{K,\tau,i} = \frac{1}{2}\big[G^{n+1}_{\sigma,\epsilon} + G^{n+1}_{\sigma',\epsilon'}\big].$$

Summing Equation (3.62) written for σ and for σ' and dividing the result by 2 yields:

$$\frac{|K|}{\delta t}\big[(e_k)^{n+1}_{K,i} - (e_k)^{n}_{K,i}\big] + \sum_{\sigma\in\mathcal{E}(K)} G^{n+1}_{K,\sigma,i} \\ + \frac{1}{2} \sum_{\substack{\sigma\in\mathcal{E}^{(i)}(K) \\ \sigma=K|L}} |D_\sigma| \, \big((\boldsymbol{\nabla} p)\ v\big)^{n+1}_{\sigma,i} = -\frac{1}{2}\big(R^{n+1}_{\sigma,i} + R^{n+1}_{\sigma,i}\big). \quad (3.63)$$

Now let

$$(e_k)^\ell_K = \sum_{i=1}^d (e_k)^\ell_{K,i}, \text{ for } \ell = n \text{ or } \ell = n+1, \text{ and } G^{n+1}_{K,\sigma} = \sum_{i=1}^d G^{n+1}_{K,\sigma,i}, \text{ for } \sigma \in \mathcal{E}(K). \quad (3.64)$$

Summing Equation (3.63) over the space components, we finally get

$$\frac{|K|}{\delta t}\big[(e_k)_K^{n+1}-(e_k)_K^n\big]+\sum_{\sigma\in\mathcal{E}(K)} G_{K,\sigma}^{n+1}+\frac{1}{2}\sum_{i=1}^{d}\sum_{\substack{\sigma\in\mathcal{E}(K),\\ \sigma\in\mathcal{E}^{(i)}(K)}}|D_\sigma|\ \big((\boldsymbol{\nabla} p)\ v\big)_{\sigma,i}^{n+1}$$
$$=-R_K^{n+1},\ \text{with } R_K^{n+1}=\frac{1}{2}\sum_{i=1}^{d}\sum_{\substack{\sigma\in\mathcal{E}(K),\\ \sigma\in\mathcal{E}^{(i)}(K)}} R_{\sigma,i}^{n+1}. \qquad (3.65)$$

This equation is a discrete analogue of the kinetic energy balance, posed on the primal cells.

> **Remark** (On the definition of the cell kinetic energy)**.** Note that the cell kinetic energy is not a convex combination of the face kinetic energies, since, on a non-uniform mesh, the equality $|K|=\frac{1}{2}\sum_{\sigma\in\mathcal{E}^{(i)}(K)}|D_\sigma|$ generally does not hold. Consequently, the cell kinetic energy may oscillate from cell to cell while the face kinetic energy does not. Nevertheless, the discrete time derivative of the cell kinetic energy is consistent in the Lax-Wendroff sense, because, despite these oscillations, the cell kinetic energy still converges weakly if the velocity and the density converge, which would be sufficient to pass to the limit in the scheme.

Let us now apply the formulation (3.21) of the scheme to the internal energy balance, to obtain:

$$\frac{|K|}{\delta t}\ \big[\rho_K^{n+1}e_K^{n+1}-\rho_K^n e_K^n\big]+\sum_{\sigma\in\mathcal{E}(K)} H_{K,\sigma}^{n+1}+(p\,\mathrm{div}\boldsymbol{v})_K^{n+1}=0, \quad \forall K\in\mathcal{M}, \qquad (3.66)$$

with, thanks to Equation (3.26) for the internal energy convection flux and Equation (3.30) for the diffusion flux:

$$\begin{aligned} H_{K,\sigma}^{n+1} &= \frac{1}{2}\ \Big[F_{K,\sigma}^n\,e_\sigma^n+F_{K,\sigma}^{(1)}\,e_\sigma^{(1)} \\ &\qquad +(\lambda+(\lambda_{SGS})_\sigma^n)\ \frac{|\sigma|}{d_\sigma}\ (e_K^n-e_L^n)+(\lambda+(\lambda_{SGS})_\sigma^{(1)})\ \frac{|\sigma|}{d_\sigma}\ (e_K^{(1)}-e_L^{(1)})\Big], \qquad (3.67)\\ (p\,\mathrm{div}\boldsymbol{v})_K^{n+1} &= \frac{1}{2}\ \Big[p_K^n\,\mathrm{div}_K(\boldsymbol{v}^n)+p_K^{(1)}\,\mathrm{div}_K(\boldsymbol{v}^{(1)})\Big]. \end{aligned}$$

The next step is now to recast the sum

$$\big(\mathrm{div}(p\boldsymbol{v})\big)_K^{n+1}=\frac{1}{2}\sum_{\sigma=K|L}|D_\sigma|\ \big((\boldsymbol{\nabla} p)\ v\big)_{\sigma,i}^{n+1}+(p\,\mathrm{div}\boldsymbol{v})_K^{n+1}$$

as a conservative discretization of its continuous counterpart $\mathrm{div}(p\boldsymbol{v})$. We have $\mathrm{div}(p\boldsymbol{v})_K^{n+1}=\frac{1}{2}[\mathrm{div}(p\boldsymbol{v})_K^n+\mathrm{div}(p\boldsymbol{v})_K^{(1)}]$ with, for $\ell=n$ and $\ell=(1)$,

$$\mathrm{div}(p\boldsymbol{v})_K^\ell=\sum_{\substack{\sigma\in\mathcal{E}(K),\\ \sigma=K|L}}\frac{1}{2}\ |\sigma|\ (p_L^\ell-p_K^\ell)\ v_{K,\sigma}^\ell+p_K^\ell\sum_{\sigma\in\mathcal{E}(K)}|\sigma|\ v_{K,\sigma}^\ell,$$

which readily yields the following conservative expression:

$$\big(\mathrm{div}(p\boldsymbol{v})\big)_K^{n+1} = \sum_{\sigma\in\mathcal{E}(K)} I_{K,\sigma}^{n+1}, \quad I_{K,\sigma}^{n+1} = \frac{1}{2}\,\Big[|\sigma|\,\frac{p_K^n+p_L^n}{2}\,v_{K,\sigma}^n + |\sigma|\,\frac{p_K^{(1)}+p_L^{(1)}}{2}\,v_{K,\sigma}^{(1)}\Big]. \tag{3.68}$$

We are now in position to state that, in the inviscid case, the numerical solutions satisfy the following total energy balance.

Theorem 3.4.2 (Discrete total energy balance) In the inviscid case, the solutions to the scheme satisfy the following discrete total energy balance equation:

$$\frac{|K|}{\delta t}\,\big[\rho_K^{n+1}E_K^{n+1} - \rho_K^n E_K^n\big] + \sum_{\sigma\in\mathcal{E}(K)} \big(G_{K,\sigma}^{n+1} + H_{K,\sigma}^{n+1} + I_{K,\sigma}^{n+1}\big) = -R_K^{n+1}, \tag{3.69}$$

where $G_{K,\sigma}^{n+1}$ is the discrete kinetic energy convection flux given by (3.64), $H_{K,\sigma}^{n+1}$ gathers the discrete internal energy convection flux and the heat diffusion flux (see Equation (3.67)), $I_{K,\sigma}^{n+1}$ is the flux associated to the continuous counterpart $p\,\boldsymbol{v}$ and given by (3.68), $\rho_K^\ell E_K^\ell = \rho_K^\ell e_K^\ell + (e_k)_K^\ell$, $\ell = n$ and $\ell = n+1$, with the kinetic energy e_k given by (3.64), and R_K^{n+1} is given by (3.65).

Remark (Residual terms in the total energy balance)**.** The term $-R_K^{n+1}$ at the right-hand side of Equation (3.69) may be interpreted as the numerical dissipation due to the numerical diffusion associated to the time discretization in the momentum balance equation. It is the sum of an anti-diffusion due to the time-explicit discretization of the first and second substeps and a diffusion brought by the final averaging step. For shock solutions of Euler equations, it may be anticipated that this term does not tend to zero; the scheme consistency thus requires to compensate it in the internal energy balance (Herbin et al., 2021). This issue is discussed in Section 3.5.3.
Note that this compensation may be done in such a way that the scheme becomes fully conservative (Grapsas et al., 2021).

3.5 Numerical simulations

The scheme under consideration has been developed in the CALIF^{3}S open-source software (CALIF^{3}S, 2021), and several tests have been performed and are presented in this section. We begin with the computation of a regular solution, to check the scheme accuracy together with the conservation properties for the kinetic energy. Then we assess the ability of the scheme to transport a regular vortex in an homogeneous flow over long distances. We then turn to the computation of a shock wave. Finally, we address a benchmark which may be considered as a prerequisite before applications to turbulence problems, namely the simulation of the isotropic turbulence decay.

3.5.1 A regular solution

We first build a regular solution by the following tree-steps process: (a) first, derive a standing vortex solution to the Euler equations, (b) add a constant translation to the solution and (c) add diffusion terms and compensate them by source terms. For the first step, the expression of the velocity is chosen as:

$$\tilde{\boldsymbol{u}} = \alpha^{1/2}(1 - \hat{x}^2 - \hat{y}^2)^2 \begin{bmatrix} -\hat{y} \\ \hat{x} \end{bmatrix} \text{ if } \hat{x}^2 + \hat{y}^2 \leq 1, \ \tilde{\boldsymbol{u}} = 0 \text{ otherwise,}$$

with $\hat{x} = x/r$, $\hat{y} = y/r$, r and α being two scaling factors (see Section 3.5.2 for the utility of these coefficients and of the β coefficient introduced below). This velocity field meets two requirements: its is compactly supported (to avoid any time dependent, after step (b), boundary condition), and it belongs to $H^2(\Omega)^2$. For the same two reasons, the density is set to

$$\tilde{\rho} = 1 + \beta(1 - \hat{x}^2 - \hat{y}^2)^2 \text{ if } \hat{x}^2 + \hat{y}^2 \leq 1, \ \tilde{\rho} = 1 \text{ otherwise,}$$

with β another scaling factor. Finally, the pressure satisfies $\tilde{\rho}\, \tilde{\boldsymbol{u}} \cdot \boldsymbol{\nabla} \tilde{\boldsymbol{u}} + \boldsymbol{\nabla} \tilde{p} = 0$, which, since the velocity field is divergence free, ensures that the triplet $(\rho, \boldsymbol{u}, p)$ satisfies the steady Euler equations. This yields

$$\tilde{p} = \alpha^2 p_0 - \frac{\alpha}{10}\,(1 - \hat{x}^2 - \hat{y}^2)^5 - \frac{\alpha\beta}{14}\,(1 - \hat{x}^2 - \hat{y}^2)^7, \text{ if } \hat{x}^2 + \hat{y}^2 \leq 1, \ \tilde{p} = p_0 \text{ otherwise,}$$

where p_0 is a constant integration constant, to be chosen large enough for the pressure to remain positive. A solution to unsteady Euler equations is given by $\boldsymbol{u} = \boldsymbol{a} + \tilde{\boldsymbol{u}}(\hat{\boldsymbol{x}} - t\,\boldsymbol{a})$, with $\boldsymbol{a}$ a constant velocity vector, $\rho = \tilde{\rho}(\hat{\boldsymbol{x}} - t\,\boldsymbol{a})$ and $p = \tilde{p}(\hat{\boldsymbol{x}} - t\,\boldsymbol{a})$. We choose $r = 1$, $\boldsymbol{a} = (0.2, 0.2)^t$, and we set $\alpha = \beta = 1$. With this choice of α, the maximum norm of the velocity is close to 0.57. The equation of state is $p = (\gamma - 1)\,\rho e$, with $\gamma = 1.4$. The speed of sound is minimal at the center of the vortex, where it takes a value close to $c = 0.54$ and maximal outside the vortex, with c slightly greater than 0.9; the Mach number lies in the interval $(0, 0.9)$ (the maximum value of the velocity is obtained close to the exterior of the vortex, where the Mach number also is close to its maximum value). The center of the vortex is initialy located at the origin; the computation ends at $t = T = 4$, with a center of the vortex located at $(0.8, 0.8)^t$. The computational domain is $\Omega = (-1.2, 2)^2$.

Computations are performed with $n \times n$ square grids, with $n \in \{25, 50, 100, 200\}$. The time step is set at $\delta t = 1/n$, which corresponds to a CFL number with respect to the maximal waves speed in the range of 0.4. We measure the discrete L^1-norm of the error at $t = T$, defined by

$$|q_{n\times n} - q\|_{L^1} = \sum_{K \in \mathcal{M}} |K|\ |(q_{n\times n})_K^{N^n} - q(\boldsymbol{x}_K, T)|,$$

$$|\boldsymbol{u}_{n\times n} - \boldsymbol{u}\|_{L^1} = \sum_{i=1}^{d} \sum_{\sigma \in \mathcal{E}_{\rm int}^{(i)}} |K|\ |(u_{n\times n})_{i,\sigma}^{N^n} - u_i(\boldsymbol{x}_\sigma, T)|,$$

with $q = \rho$ or $q = p$, $(\rho_{n\times n}, \boldsymbol{u}_{n\times n}, p_{n\times n})$ the numerical solution obtained with the $n \times n$ grid, N^n the associated last time level. We recall that, for $K \in \mathcal{M}$ (resp. $\sigma \in \mathcal{E}_{\rm int}$), $\boldsymbol{x}_K$ (resp. $\boldsymbol{x}_\sigma$) stands for the mass center of K (resp. σ).

We first set the viscosity to $\mu = 0.004$, while the heat diffusion coefficient is kept to zero. The obtained numerical errors are reported in Table 3.1. We observe a second order

	$10^2\ \|\rho_{n\times n} - \rho\|_{L^1}$	$10^3\ \|p_{n\times n} - p\|_{L^1}$	$10^2\ \|\boldsymbol{u}_{n\times n} - \boldsymbol{u}\|_{L^1}$
$n = 25$	18.2	19.5	13.0
$n = 50$	6.83	5.21	3.34
$n = 100$	2.29	1.27	0.792
$n = 200$	0.666	0.315	0.186

Table 3.1: Navier-Stokes equations without heat diffusion – Numerical errors obtained with various $n \times n$ grids.

convergence for the velocity and the pressure, and a convergence rate which seems to tend to the same value, 2, for the density.

We then turn to the full Navier-Stokes equations, setting $\lambda = \mu$. The obtained results are gathered in Table 3.2. The accuracy falls down to approximately first order, which is probably due to the fact that, to keep the pressure constant accross contact discontinuities, we have chosen a MUSCL approximation of the scalar variables which is second order for the product ρe but not for e (only the groupment ρe - or p - appears in the equation except in the diffusion term).

	$10^2\ \|\rho_{n\times n} - \rho\|_{L^1}$	$10^3\ \|p_{n\times n} - p\|_{L^1}$	$10^2\ \|\boldsymbol{u}_{n\times n} - \boldsymbol{u}\|_{L^1}$
$n = 25$	14.4	20.5	13.3
$n = 50$	4.39	8.18	3.55
$n = 100$	1.17	4.35	1.04
$n = 200$	0.393	2.45	0.387

Table 3.2: Navier-Stokes equations – Numerical errors obtained with various $n \times n$ grids.

Finally, we check on the 50×50 grid the behaviour as a function of the time step of the residual term in the kinetic energy balance, defined by:

$$R(\boldsymbol{x}) = R_K(\boldsymbol{x}), \quad \forall \boldsymbol{x} \in K,\ \forall K \in \mathcal{M},$$

with R_K defined in Equation (3.65). An average of the values obtained in the last time steps for the L^1-norm and the integral of R are reported in Table 3.3. As expected, the L^1-norm of this remainder varies as δt with the Euler scheme and with δt^2 for the Heun scheme; in addition, values in this case are divided by 1000 when switching from Euler to Heun. Since the function R may take any sign, we also give its integral: the latter is about ten times smaller than the L^1-norm, and is divided by 10 each time the time step is divided by 2.

3.5.2 A travelling vortex test case

We now turn to a case closer to some practical applications of the scheme, namely the transport of "small spatial scale" perturbations in a compressible flow of moderate Mach number, with a variation of the velocity in the perturbations small with respect to the bulk

	Euler scheme	Heun scheme	
	L^1 norm $\times 10^4$	L^1-norm $\times 10^7$	integral over Ω $\times 10^8$
δt	11.	18.	50.
$\delta t/2$	5.0	3.7	5.
$\delta t/4$	2.5	0.88	0.5

Table 3.3: Navier-Stokes equations – Kinetic energy residual obtained with a 50×50 grid and various time steps ($\delta t = 0.02$).

velocity. To this purpose, we take once again the travelling vortex case of the previous section, and we set:

- $\alpha = 410$, so the uniform pressure $p_0 = 100860$ is now in the range of the atmospheric pressure; note that the velocity perturbation is scaled as $\alpha^{1/2}$, and a pre-factor α applies to the pressure variations in the vortex. With this choice, the maximum value of the velocity perturbation is close to 5.8.
- the factor β is set at $\beta = 0.2$ to avoid unrealistic variations of the density. With this value, the maximum value for ρ is close to 1.2 (while $\rho = 1$ outside the vortex). The conbined effects of α and β yield a depression of amplitude close to 50 in the vortex center.
- the translation velocity is set to $\boldsymbol{a} = (100, 0)^t$ (to be compared with the maximal speed of sound, equal to $c = 375$ outside the vortex).
- the radius r of the vortex is set to $r = 0.01$.

At the initial time, the vortex center is located at the origin. The computational domain is $\Omega = (-1.5\,r, 1.5\,r)^2$, perfect slip boundary conditions are applied to the bottom and top sides, and the left and right sides satisfy periodic boundary conditions. The final time is set to $T = 24\,r/\|\boldsymbol{a}\|$ so the vortex (more exactly speaking, an infinite row of vortices of centers distant from $3\,r$) is transported over the distance $24\,R$. For these computations, the viscosity and heat diffusion cefficients are set to $\mu = 0.0005$ and $\lambda = \mu/2$.

Computations are performed on $n \times n$ grids, for $n \in \{50, 100, 200, 400\}$, and $\delta t = 10^{-5}/n$, which corresponds to a CFL number (with respect to the fastest waves) close to 0.2. For larger time steps, spurious oscillations are observed on the pressure field, which we are unable to explain; note however that the convection field for the velocity is centered, to minimize the dissipation of kinetic energy, and that no oscillations appear for larger values of the viscosity. We show on Fig. 3.4 the density, second component of the velocity and pressure obtained at the final time along the line $y = 0$. The computation with $n = 400$ may be seen as a reference result, and an approximate convergence is obtained with $n = 200$. When decreasing n, we observe a (slight) decrease of the transport velocity, and an increase of the diffusion; at $n = 50$, the separation of the successive vortices begins to be lost (the plateau separating the vortices in the velocity curve begins to disappear).

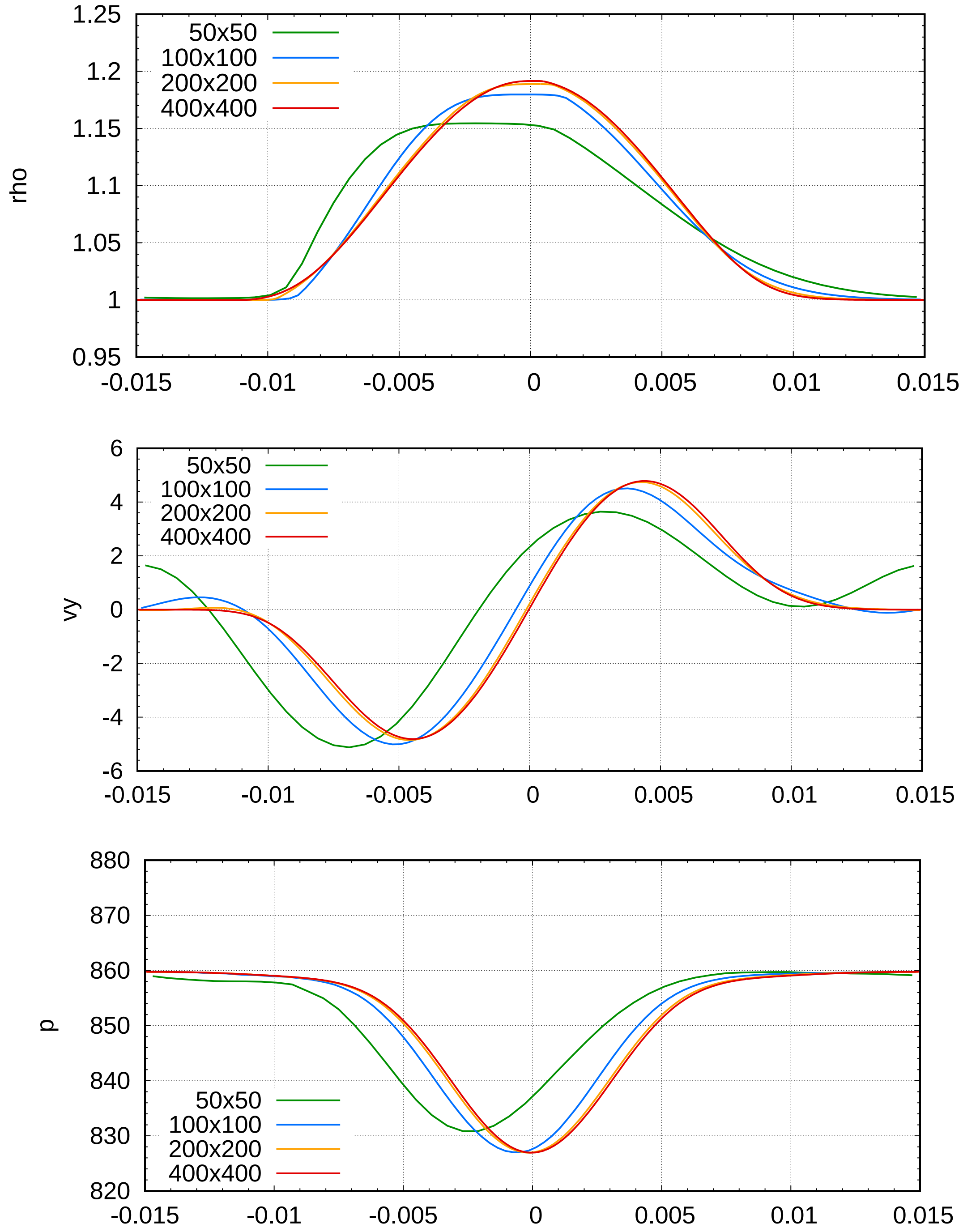

Figure 3.4: Travelling vortex – Density, second component of the velocity and pressure.

3.5.3 Shock solutions

The scheme proposed in this chapter is built to apply to Navier-Stokes equations, which excludes the occurence of shocks, so no specific adaptation of the scheme should be necessary. However, situations where the viscosity is low are in the domain of interest, and thus deserve some tests, presented in this section.

First, let us recall the expression of the numerical remainder terms in the native (*i.e.* posed on the dual cells) kinetic energy balance (3.43). For $1 \leq i \leq d$ and $\sigma \in \mathcal{E}^{(i)}_{\rm int}$, we have:

$$R^{n+1}_{\sigma,i} = \frac{1}{4}\frac{|D_\sigma|}{\delta t}\Big[\rho^n_{D_\sigma}\,\big(v^{n+1}_{\sigma,i} - v^n_{\sigma,i}\big)^2 + \rho^{(2)}_{D_\sigma}\big(v^{n+1}_{\sigma,i} - v^{(2)}_{\sigma,i}\big)^2 \\ - \rho^{(1)}_{D_\sigma}\big(v^n_{\sigma,i} - v^{(1)}_{\sigma,i}\big)^2, -\rho^{(2)}_{D_\sigma}\big(v^{(1)}_{\sigma,i} - v^{(2)}_{\sigma,i}\big)^2\Big]. \tag{3.70}$$

These terms in turn make a remainder term to appear in the total energy balance (on the primal cells), which reads:

$$R^{n+1}_K = \frac{1}{2}\sum_{i=1}^{d}\ \sum_{\sigma\in\mathcal{E}(K)\cap\mathcal{E}^{(i)}_{\rm int}} R^{n+1}_{\sigma,i}. \tag{3.71}$$

In (Grapsas et al., 2016, Remark 4.2), the following elementary analysis is performed. Let us suppose:

- that we address a one-dimensional problem and that the discrete solution features a smeared discontinuity, *i.e.* that a constant state is linked to another one by a narrow profile,
- that, on a sequence of more and more refined meshes, this profile spreads on a constant number of cells (so it converges to a discontinuity).

Then the piecewise constant function R defined by $(R^{n+1}_K)_{K\in\mathcal{M},\ 0\leq n\leq N}$ converges to a measure borne by this discontinuity. This is observed for shock solutions of Euler equations (Herbin et al., 2014; Grapsas et al., 2016), where the compressive nature of the convection flow allows to indeed capture the shock within a constant number of cells (by contrast with contact discontinuities, where the "numerical discontinuity" spreads over a zone of thickness varying as $h^{1/2}$, with h the space step, provided that the numerical scheme boils down to a first-order diffusive one at discontinuites, which is the case here). This spurious measure borne by the shock modifies the Rankine-Hugoniot jump conditions, and the consistency of the scheme is lost. By usual arguments, this analysis extends to multi-dimensional problems (roughly speaking, the one-dimensional situation is recovered in a coordinates system normal to the shock). On the contrary, for regular solutions, the remainder term R is supposed to tend to zero (precisely speaking, the remainders are formally of second order in time, as shown in Lemma 3.4.3).

We address, in this section, situations where the solution may be seen as a perturbation of a shock. The problem is one-dimensional, and initialized with the solution of a single shock wave. The right state is given by

$$\begin{bmatrix}\rho_L\\ p_L\\ v_L\end{bmatrix} = \begin{bmatrix}1\\ 10^5\\ 0\end{bmatrix},$$

and the left state is deduced from the Rankine-Hugoniot conditions for $\mathrm{Ma} = 1.2$ and $\mathrm{Ma} = 3$, with Ma the Mach number associated to the shock, defined as the ratio between the wave speed and the sound speed in the left state. The first case is typical of a strong deflagration (the pressure p_R in the left state is equal to $1.5\,10^5$) and the second one is representative of a weak detonation (p_R is slightly greater than 10^6). The viscosity and the heat diffusion coefficient are set $\mu = \lambda = 0.1$, which are reasonable values for a subgrid viscosity associated to usual meshes in such case. The shock is initially located at the origin, the computational domain is $\Omega = (-0.2, 1)$ and the final time is $T = 0.002$ for $\mathrm{Ma} = 1.2$ and $T = 0.0008$ for $\mathrm{Ma} = 3$.

The space step is $1.2/n$ for $n \in \{250,\ 500,\ 100,\ 5000\}$ and the time step is $\delta t = 0.001/n$ for $\mathrm{Ma} = 1.2$ and $\delta t = 0.0005/n$ for $\mathrm{Ma} = 3$ (which corresponds to a CFL number with respect of the fastest waves close to 0.5 for $\mathrm{Ma} = 1.2$ and 0.7 for $\mathrm{Ma} = 3$). We report on Fig. 3.5 the density obtained for $\mathrm{Ma} = 1.2$. The left and right states are correctly computed for any of the tested space steps; we observe oscillations at the shock for $n = 250$, and, to a much lesser extent for $n = 500$, which may be cured by adding a small numerical diffusion (with respect to the numerical diffusion associated to a first order scheme), see Herbin et al. (2018). The picture changes for $\mathrm{Ma} = 3$ (see Fig. 3.6): here, for coarse meshes, the leading phenomenon governing the solution is the (wrong) jump conditions, and we observe the formation of an intermediate constant state between the left and right states. Of course, since the viscosity is constant and different from zero, when the mesh is refined, the numerical solution converges to what is expected, namely a two-states structure with a smeared chock; in this convergence process, the intermediate state is still present, but becomes closer and closer to the left state.

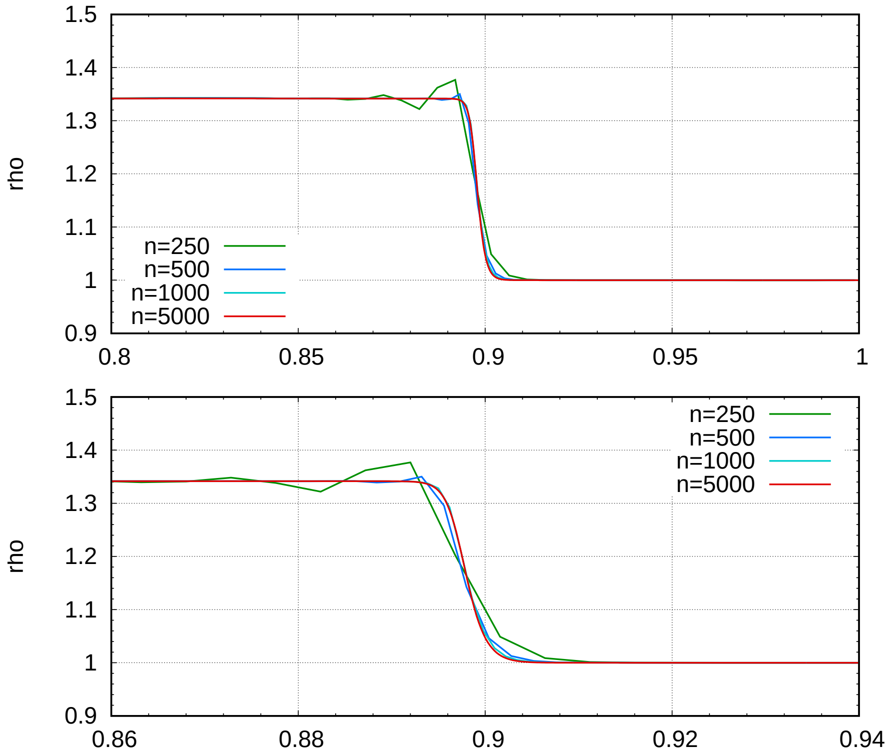

Figure 3.5: Mach 1.2 shock – Density at the final time for various space steps (general view and zoom).

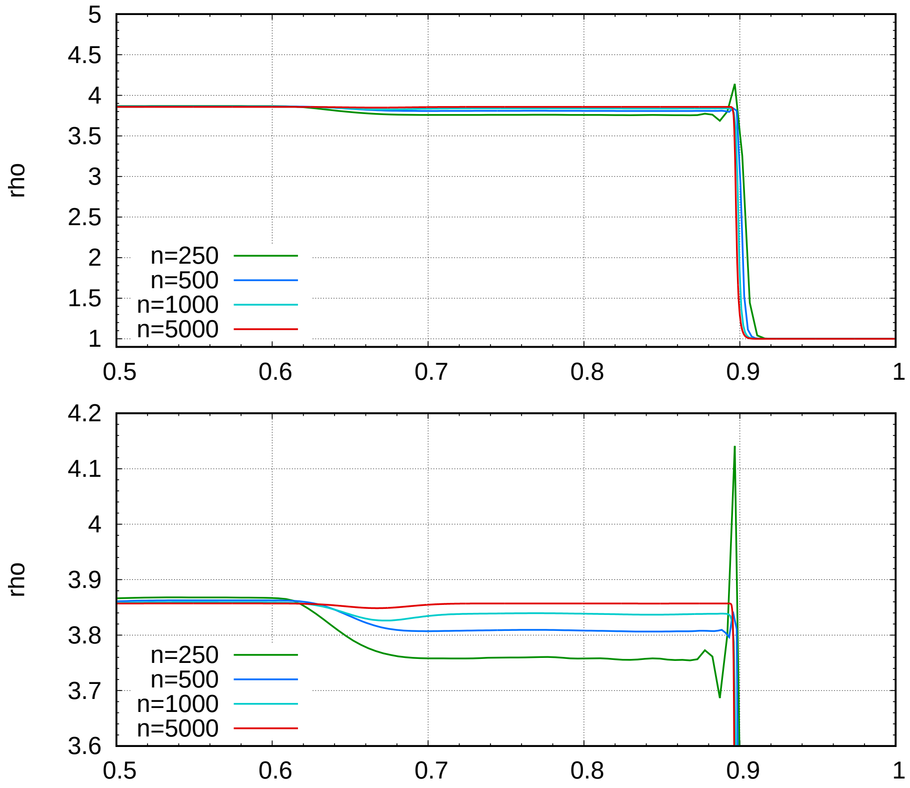

Figure 3.6: Mach 3 shock – Density at the final time for various space steps (general view and zoom).

Remark (A consistent scheme for Euler equations)**.** To obtain a consistent scheme for Euler equations, it is sufficient to compensate the kinetic energy remainder term in the internal energy balance (Grapsas et al., 2021), written under the form (3.66) (*i.e.* after the combination of the three steps of the algorithm). This compensation may be done by splitting the remainder between the steps (the first term of (3.70) is associated to Step 1, the second to Step 2 and the last two ones to Step 3) or adding the whole remainder at Step 3. Since the risk is to loose the positivity of the internal energy and the parts of the remainder associated to Steps 1 and 2 are non-positive, it seems preferable to wait for the last step; in addition, as shown numerically, an almost complete cancelling is obtained, at least for smooth solutions, when taking all the terms into account, so this choice is likely to be unsignificant for the scheme behaviour.
The compensation may be done by adding the quantity R_K^{n+1} given by Equation (3.71) to $\rho_K^{n+1} e_K^{n+1}$ in Step 3, in which case the scheme satisfies a local discrete conservative total energy balance. Note anyway that a different repartition of the face residuals is possible (in fact, for consistency, the difference between the kinetic energy remainder and the internal energy compensation must only tends to zero in the distributional sense (Grapsas et al., 2016)) and the expression of the face densities suggests the following

alternative expression:

$$R_K^{n+1} = \sum_{i=1}^{d} \sum_{\sigma\in\mathcal{E}(K)\cap\mathcal{E}_{\rm int}^{(i)}} \frac{1}{4}\frac{|D_{K,\sigma}|}{\delta t}\Big[\rho_K^n\,\big(v_{\sigma,i}^{n+1}-v_{\sigma,i}^{n}\big)^2 + \rho_K^{(2)}\big(v_{\sigma,i}^{n+1}-v_{\sigma,i}^{(2)}\big)^2 \\ - \rho_K^{(1)}\big(v_{\sigma,i}^{n}-v_{\sigma,i}^{(1)}\big)^2 - \rho_K^{(2)}\big(v_{\sigma,i}^{(1)}-v_{\sigma,i}^{(2)}\big)^2\Big].$$

3.5.4 Decay of isotropic turbulence

The test case presented here is the decay of isotropic turbulence (DIT). An isotropic turbulent velocity field is a field with no mean velocity and no mean gradients. The isotropic field is by default homogeneous: invariant in space. Under the action of viscous forces the turbulent field simply decays.

The numerical simulations are performed in a periodic box $[0, L]$ with $L = 2\pi$ and $N = 32$ nodes per axes. Periodic conditions are enforced at all domain boundaries. The simulations are performed with a time step respecting a CFL number equal to 1/4. The Smagorinsky's subgrid model (3.13) is used in order to compute the SGS turbulent viscosity. The constant C_s is set to $C_s = 0.17$.

The initial velocity field is prescribed using the Random Fourier Method (RFM) that provides a synthetic turbulent velocity field enforcing a given model energy spectrum. This approach has been developed by Kraichnan (1970) and enhanced later by Fung et al. (1992). The Passot-Pouquet model for energy spectrum (Passot and Pouquet, 1987) has been chosen and is written:

$$E(\kappa) = 16\sqrt{\frac{2}{\pi}}\frac{v_{rms}^2}{\kappa_0}\left(\frac{\kappa}{\kappa_0}\right)^4 \exp\left[-2\left(\frac{\kappa}{\kappa_0}\right)^2\right] \tag{3.72}$$

with κ_0 the wave number of the most energetic scales at initialization set to $\kappa_0 = 4\ m^{-1}$, and v_{rms} the root mean square (RMS) of the velocity fluctuations. The number of Fourier modes set to 2000. The initial fields for temperature, pressure and density are set uniform at $T = 300\,\mathrm{K}$, $p = 101325\,\mathrm{Pa}$ and $\rho = 1.18\,\mathrm{kg.m^{-3}}$.

Reference case

Let first introduce some characteristic parameters which will be useful in the following. The turbulent Mach number M_t defined by:

$$\mathrm{M}_t = \frac{q}{c}, \tag{3.73}$$

with $q = \sqrt{3}\,v_{rms}$ the RMS magnitude of the fluctuation velocity, and $c = \sqrt{\gamma(p/\rho)}$ the mean speed of sound, with $\gamma = 1.4$. The microscale Reynolds number is given by:

$$\mathrm{Re}_\lambda = \frac{v_{rms}\,\lambda}{\nu}, \tag{3.74}$$

where $\nu = \mu/\rho$ and λ stand respectively for the kinematic viscosity and the Taylor microscale (*i.e.* the largest of the dissipative scales). The Taylor-eddy-turnover time τ is defined by the ratio of the Taylor length scale λ and the root mean square of the velocity fluctuations v_{rms} :

$$\tau = \frac{\lambda}{v_{rms}}. \tag{3.75}$$

Different DNS or LES numerical results for the decay of isotropic turbulence exist in the literature (Spyropoulos and Blaisdell, 1996; Nagarajan and Lele, 2003; Chai and Mahesh, 2012). Most of them use high initial values for M_t and Re_λ in order to check the numerical scheme robustness. For the reference case studied here, the initial turbulent Mach number is set to $\mathrm{M}_t = 0.4$ and the initial Taylor Reynolds number to $\mathrm{Re}_\lambda = 100$.

Fig. 3.7 shows a comparison between the energy spectrum obtained by CALIF^{3}S and the DNS data of Spyropoulos and Blaisdell (1996) (case 2). Energy spectra are plotted at two specific moments, at $t/\tau = 2.217$ and $t/\tau = 4.37$, with $\tau = 0.18\,\mathrm{s}$. The abscissa denotes the wavenumber and the ordinate represents the energy contained. LES results agree with DNS data.

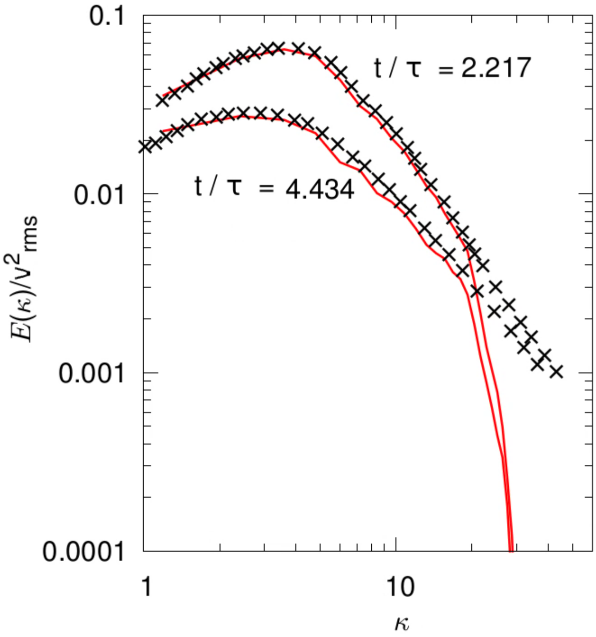

Figure 3.7: Energy spectra at $\mathrm{M}_t = 0.4$ and $\mathrm{Re}_\lambda = 100$. (—): CALIF^{3}S numerical results; (×): DNS by Spyropoulos and Blaisdell (1996).

The production zone is spotted from the first wavenumber to approximately 3 to 4 m^{-1} where the energy spectrum amplitude is at the maximum value. The pic corresponds to the largest turbulent scale L_t. The inertial zone is from the end of the production zone ($\kappa \sim L_t^{-1}$) to the cut-off wavenumber. The eddies size decreases until they become smaller than the mesh size and are not directly resolved anymore.

On the left part of Fig. 3.8, the decay of the turbulent kinetic energy is represented. As the turbulence is considered isotropic, k_t is defined by:

$$k_t = \frac{3}{2} v_{rms}^2. \tag{3.76}$$

In Fig. 3.8, as well as in all the figures representing the decay of the turbulent kinetic energy in this Section, k_t is normalized by its maximum value, in our case, it is reached at the initialization, thus $k_t^{max} = k_t(0)$.

The numerical results obtained with CALIF^{3}S are compared to the LES ones computed by Nagarajan and Lele (2003). After initialization, turbulence is decreasing over time due to the viscous dissipation and the lack of source term. The results are close to those obtained by Nagarajan's *et al.*.

The right part of Fig. 3.8 shows a comparison between the root mean square of the resolved density field through time obtained with CALIF^{3}S and the DNS data of Spyropoulos and Blaisdell (1996). As turbulence increases compressiblity, it also increases density fluctuations. As turbulence decreases, density fluctuations follows the same scheme and decreases too as shown in Fig. 3.8. The RMS density is underestimated by CALIF^{3}S . This is probably due to the fact that the contribution of unresolved scales is not taken into account in the computation of ρ_{rms}.

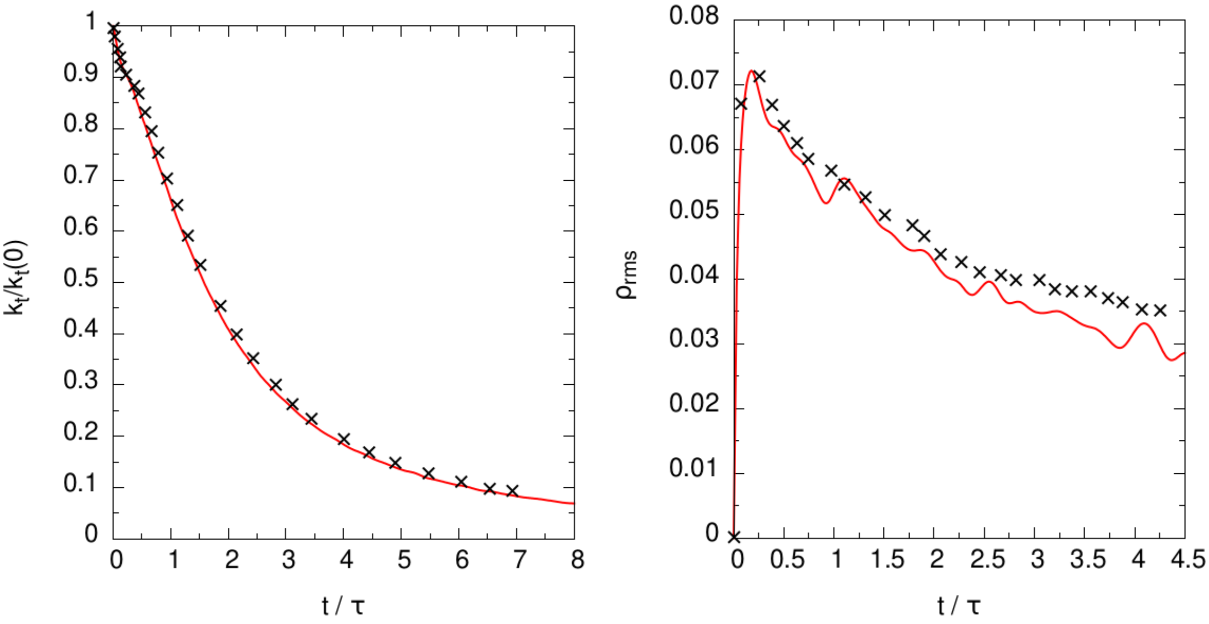

Figure 3.8: Decay of the turbulent kinetic energy (left side) and evolution of RMS density (right side) at $\mathrm{M}_t = 0.4$ and $\mathrm{Re}_\lambda = 100$. (—): CALIF^{3}S numerical results; (×): LES numerical results by Nagarajan and Lele (2003) (left side), DNS data by Spyropoulos and Blaisdell (1996) (right side).

Impact of different numerical parameters

The same test case (*i.e.* with $\mathrm{M}_t = 0.4$ and $\mathrm{Re}_\lambda = 100$) presented above has been performed by varying different numerical parameters such as the momentum convection term discretization and the constant of the Smagorinsky's model. The aim is to comfort some numerical choices made here.

The numerical results computed with the centered scheme for the momentum convection term discretization (equations (3.17c) and (3.18)) are compared to those obtained with the upwind scheme in Fig. 3.9 and Fig. 3.10. The results are compared to the DNS data of

Spyropoulos and Blaisdell (1996) and to the LES data of Nagarajan and Lele (2003) (right part of Fig. 3.10) already shown below.

Fig. 3.9 shows the energy spectra with both convection discretizations. The upwind scheme is more dissipative than the centered one as shown by the drop of the spectral energy.

Smagorinsky's constant effect is observed on the energy spectra by comparing two values for the Smagorinsky's constant C_s, $C_s = 0.17$ and $C_s = 0.25$ (Fig. 3.11). Being directly correlated to the SGS viscosity, rising this constant increases the turbulent viscosity and thus increases the dissipation of turbulent energy. Therefore, it lowers the energy of resolved scales near the cut-off wavenumber.

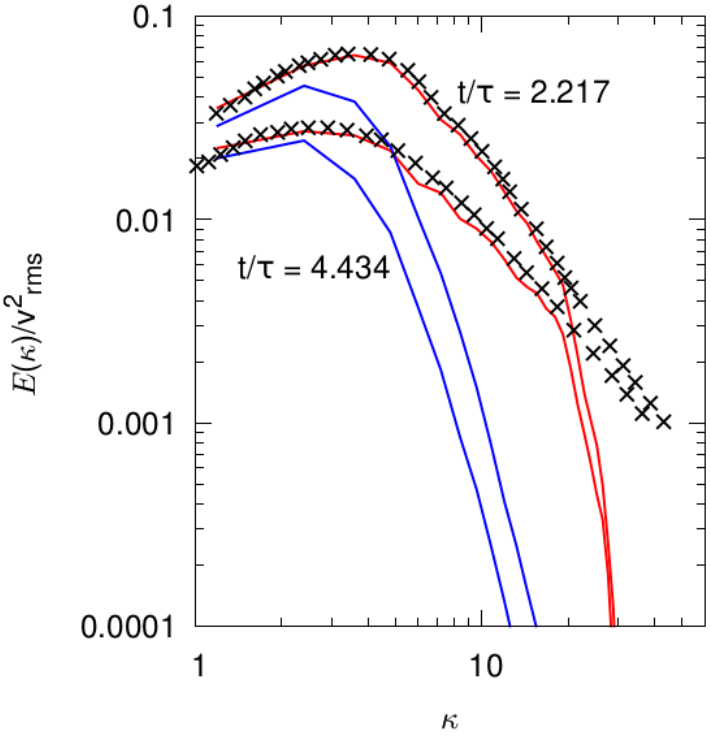

Figure 3.9: Energy spectra with centered and upwind momentum convection schemes (test case: $M_t = 0.4$ and $Re_\lambda = 100$). (━): CALIF^{3}S numerical results with centered scheme; (━): CALIF^{3}S numerical with upwind scheme; (×): DNS by Spyropoulos and Blaisdell (1996).

The decays of the kinetic energy (left side) and of RMS density fluctuations (right side) are plotted on Fig. 3.10. With the upwind scheme, as shown in Fig. 3.9, turbulence is underestimated. A lower turbulence rate induces a less compressible flow and so, the RMS density fluctuations and the kinetic energy are also underestimated.

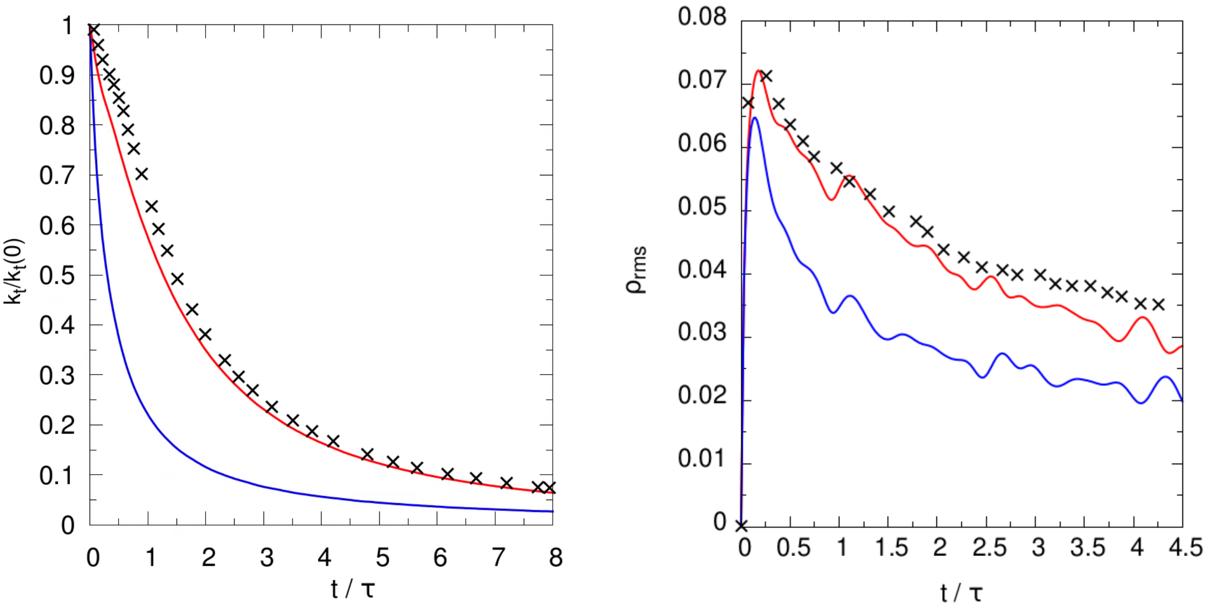

Figure 3.10: Decay of the turbulent kinetic energy (left side) and evolution of RMS density (right side) with centered and upwind momentum convection schemes (test case: $\mathrm{M}_t = 0.4$ and $\mathrm{Re}_\lambda = 100$). (—): CALIF^{3}S numerical results with centered scheme; (—): CALIF^{3}S numerical results with upwind scheme; ($\times$): LES numerical results by Nagarajan and Lele (2003) (left side), DNS data by Spyropoulos and Blaisdell (1996) (right side).

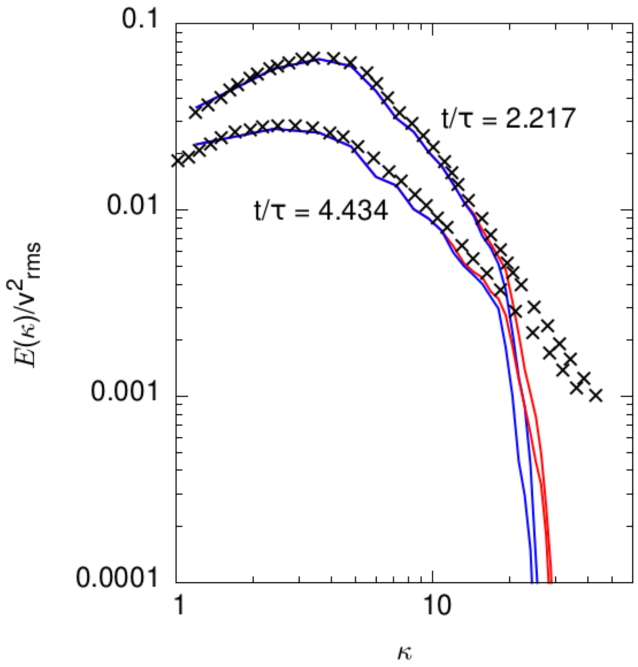

Figure 3.11: Energy spectra for two values of the Smagorinsky's constant C_s (test case: $\mathrm{M}_t = 0.4$ and $\mathrm{Re}_\lambda = 100$). (—): CALIF^{3}S numerical results with $C_s = 0.17$; (—): CALIF^{3}S numerical results with $C_s = 0.25$; ($\times$): DNS by Spyropoulos and Blaisdell (1996).

The RMS density and the turbulent kinetic energy decay are plotted for $Cs = 0.17$ and $Cs = 0.25$ in Fig. 3.12. RMS density and turbulent kinetic energy are both underestimated for a higher value of the Smagorinsky model ($C_s = 0.25$).

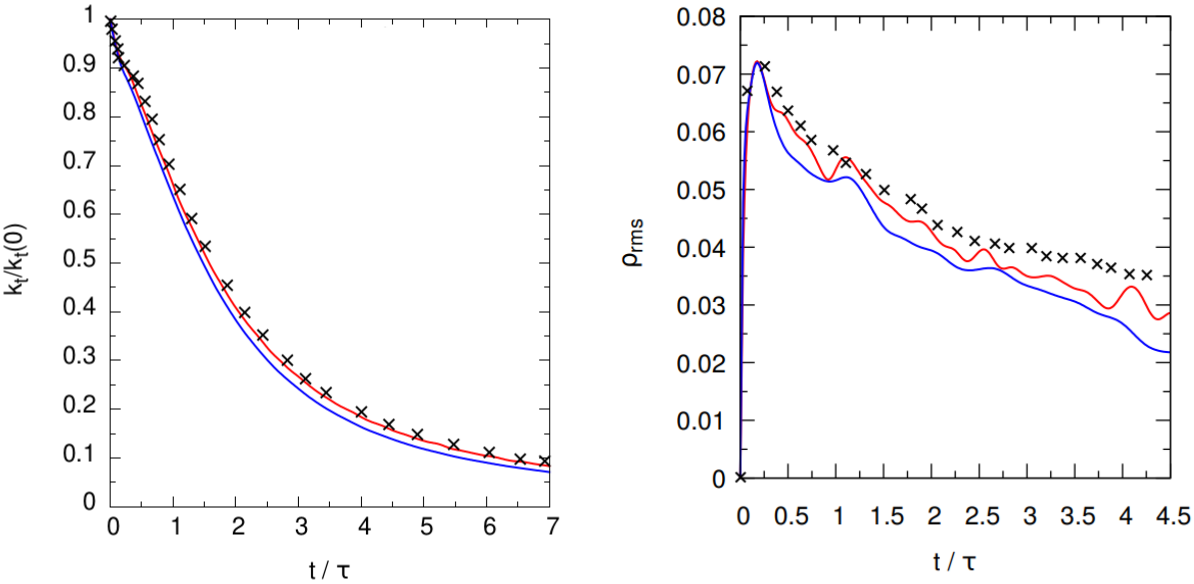

Figure 3.12: Decay of the turbulent kinetic energy (left side) and evolution of RMS density (right side) for two values of the Smagorinsky's constant C_s (test case: $\mathrm{M}_t = 0.4$ and $\mathrm{Re}_\lambda = 100$). (—): CALIF^{3}S numerical results with $C_s = 0.17$; (—): CALIF^{3}S numerical results with $C_s = 0.25$; ($\times$): LES numerical results by Nagarajan and Lele (2003) (left side), DNS data by Spyropoulos and Blaisdell (1996) (right side).

Impact of the turbulent Mach number

The level of compressibility of the initial fields is controlled by varying the initial turbulent Mach number M_t. Tests have been made with three different turbulent Mach numbers: $\mathrm{M}_t = 0.3$, $\mathrm{M}_t = 0.4$ and $\mathrm{M}_t = 0.5$. The initial microscale Reynolds number is set to $\mathrm{Re}_\lambda = 100$.

In Fig. 3.13 are plotted the energy spectra normalized by the square of RMS velocity for the three different initial turbulent Mach numbers. The spectra evolution over time is highly dependent of the initial RMS velocity (and thus of the initial M_t). Indeed, by initializing with a higher turbulent Mach number, turbulence is increased and thus its energy is also raised. In Fig. 3.13 the spectra overlap due to the normalization by the square of RMS velocity. As previously, the results are plotted at different moments: $t/\tau = 2.217$ and $t/\tau = 4.37$, the Taylor-eddy-turnover time τ being obviously different for each initial M_t (see relation (3.75)): $\tau = 0.108\,\mathrm{s}$, $\tau = 0.135\,\mathrm{s}$, and $\tau = 0.18\,\mathrm{s}$ for $\mathrm{M}_t = 0.3$, $\mathrm{M}_t = 0.4$ and $\mathrm{M}_t = 0.5$ respectively. Numerical results are compared to DNS data of Spyropoulos and Blaisdell (1996) (cases 1, 2 and 3). The data are also normalized, thus DNS values overlap for all three M_t cases. Then, in order to lighten Fig. 3.13 only DNS results for $\mathrm{M}_t = 0.4$ are represented. The numerical results obtained with CALIF^{3}S are close to DNS data and overlap, as expected, for the different initial M_t cases.

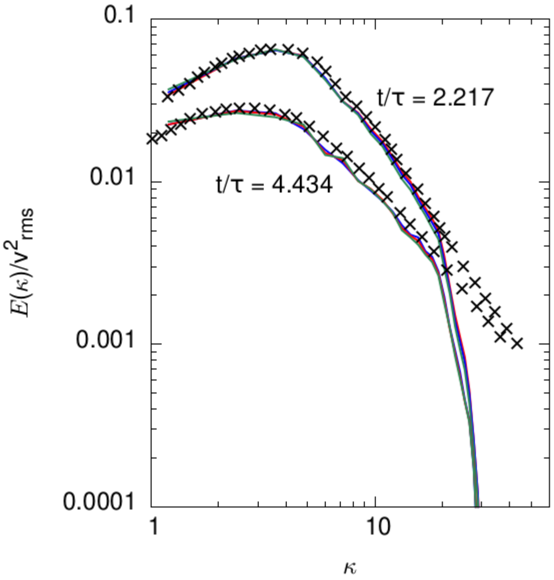

Figure 3.13: Energy spectra for various M_t and $\mathrm{Re}_\lambda = 100$. (—): CALIF^{3}S numerical results with $\mathrm{M}_t = 0.3$; (—): CALIF^{3}S numerical results with $\mathrm{M}_t = 0.4$; (—): CALIF^{3}S numerical results with $\mathrm{M}_t = 0.5$; $(\times)$: DNS by Spyropoulos and Blaisdell (1996) ($\mathrm{M}_t = 0.4$).

The decays of turbulent kinetic energy computed with CALIF^{3}S are plotted on the left part of Fig. 3.14, for $\mathrm{M}_t = 0.3$, $\mathrm{M}_t = 0.4$ and $\mathrm{M}_t = 0.5$. The three curves overlap because the kinetic energy is normalized by its initial value, thus the results become independent from the initial turbulent Mach number. The results are compared to the DNS data computed by Chai and Mahesh (2012) also normalized by the initial value of the kinetic energy. For the same reasons as above, in order to lighten the figure, only DNS results for $\mathrm{M}_t = 0.4$ are plotted. The LES results obtained with CALIF^{3}S are in good agreement with DNS data.

The time evolutions of RMS density obtained with CALIF^{3}S are plotted on the right part of Fig. 3.14, for $\mathrm{M}_t = 0.3$, $\mathrm{M}_t = 0.4$ and $\mathrm{M}_t = 0.5$. The results show the close relation between compressibility and turbulence: by increasing the turbulent Mach number, density fluctuations grow. The comparison with the DNS data of Spyropoulos and Blaisdell (1996) shows that the numerical results are in good agreement with DNS data.

Impact of the microscale Reynolds number

The effect of the initial microscale Reynolds number Re_λ is also examined. Tests have been made with $\mathrm{Re}_\lambda = 100$ and $\mathrm{Re}_\lambda = 1000$ while the initial turbulent Mach number is set to $\mathrm{M}_t = 0.4$.

The energy spectra are plotted in Fig. 3.15 at two different moments $t/\tau = 2.217$ and $t/\tau = 4.37$. According to (3.75), τ depends on the initial microscale Reynolds number. Here, for the two initial $\mathrm{Re}_\lambda = 100$ and $\mathrm{Re}_\lambda = 1000$, the associated Taylor-eddy-turnover are $\tau = 0.135\,\mathrm{s}$ and $\tau = 1.35\,\mathrm{s}$ respectively. Even if the energy is slightly different in the inertial zone, the energy spectra are close for higher wavenumber, independently of the initial microscale Reynolds number. The results are only compared with the DNS data of the reference case (Spyropoulos and Blaisdell, 1996) ($\mathrm{M}_t = 0.4$, $\mathrm{Re}_\lambda = 100$), because no data are available, to our knowledge, for $\mathrm{M}_t = 0.4$, $\mathrm{Re}_\lambda = 1000$.

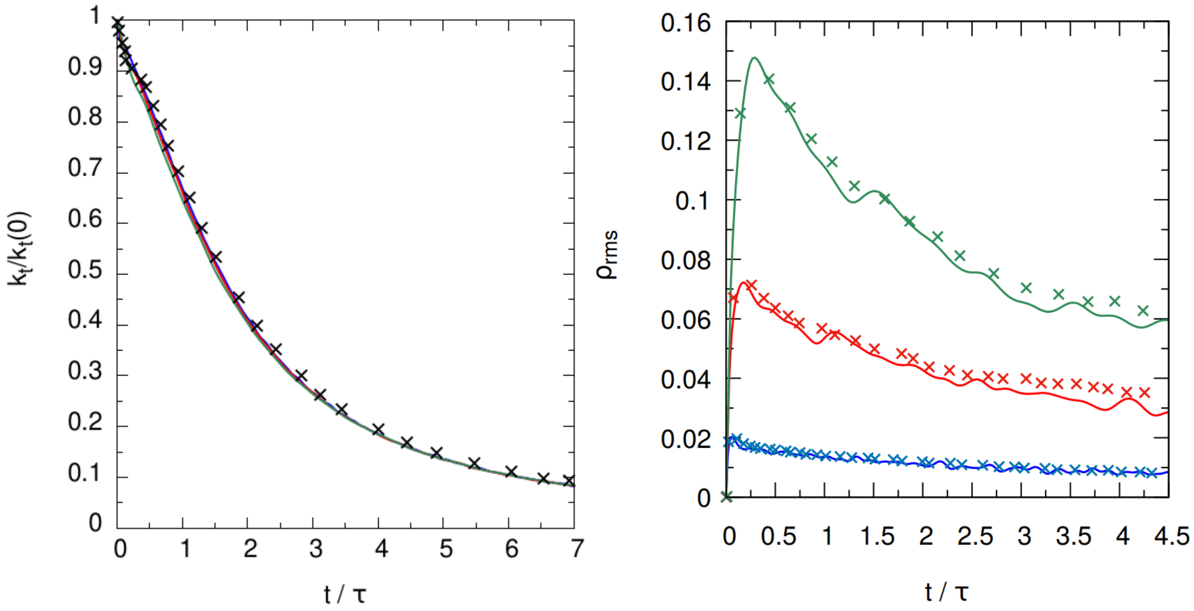

Figure 3.14: Decay of the turbulent kinetic energy (left side) and evolution of RMS density (right side) for various M_t and $\mathrm{Re}_\lambda = 100$. (—): CALIF^{3}S numerical results with $\mathrm{M}_t = 0.3$; (—): CALIF^{3}S numerical results with $\mathrm{M}_t = 0.4$; (—): CALIF^{3}S numerical results with $\mathrm{M}_t = 0.5$; ($\times$): DNS data by Chai and Mahesh (2012) (left side), DNS data by Spyropoulos and Blaisdell (1996) (right side).

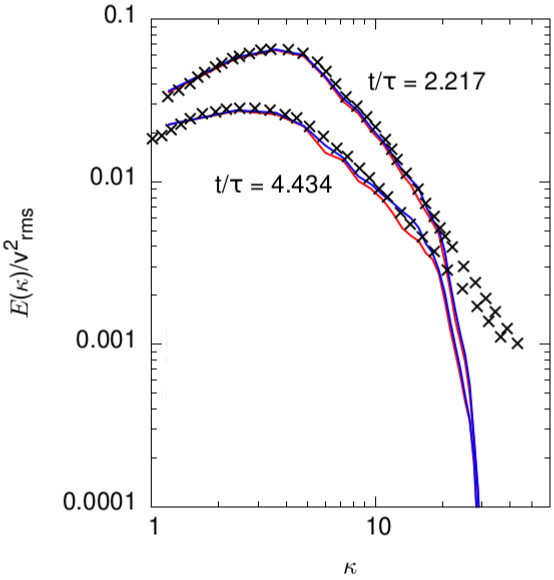

Figure 3.15: Energy spectrum for various Taylor Reynolds numbers at $\mathrm{M}_t = 0.3$. (—): CALIF^{3}S numerical results with $\mathrm{Re}_\lambda = 1000$; (—): CALIF^{3}S numerical results with $\mathrm{Re}_\lambda = 100$; ($\times$): DNS by Spyropoulos and Blaisdell (1996).

The decay of turbulent kinetic energy and the time evolution of RMS density obtained with CALIF^{3}S are plotted in Fig. 3.16 for both initial microscale Reynolds numbers. The results are compared to those computed by Nagarajan and Lele (2003). They are in good agreement with these latest. Fig. 3.16 shows (as already seen on Fig. 3.15) that the initial Taylor Reynolds number has a small impact on the numerical results. Indeed, at large Reynolds numbers, viscous terms become negligible and subgrid terms become responsible for energy dissipation. Thus, increasing Re_λ must have less and less impact on numerical results because the subgrid model does not depend on Re_λ (Nagarajan and Lele, 2003). This trend is captured by the numerical scheme as shown in Fig. 3.16.

Moreover, it should be noted that at high microscale Reynolds numbers, if the numerical scheme is not robust enough, some numerical instabilities can occur at high wavenumbers (Nagarajan and Lele, 2003). Here, the numerical scheme remains stable.

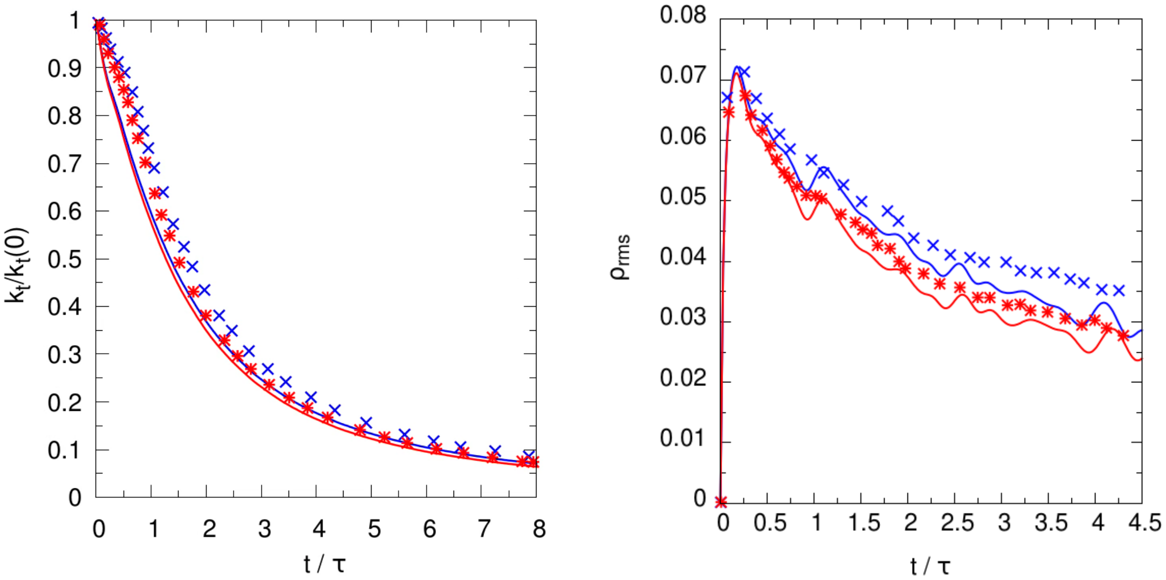

Figure 3.16: Decay of the turbulent kinetic energy (left side) and evolution of the RMS density (right side) for different Taylor Reynolds numbers at $\mathrm{M}_t = 0.3$. (—): CALIF^{3}S numerical results with $\mathrm{Re}_\lambda = 1000$; (—): CALIF^{3}S numerical results with $\mathrm{Re}_\lambda = 100$; (×): LES numerical results with $\mathrm{Re}_\lambda = 1000$ by Nagarajan and Lele (2003); (✳): LES numerical results with $\mathrm{Re}_\lambda = 100$ by Nagarajan and Lele (2003).

3.6 Conclusion

In this chapter, a formally second order explicit scheme dedicated to the numerical simulation of the filtered Navier-Stokes equations for compressible non-reactive flows is proposed. The space discretization is staggered, using the Marker-And-Cell (MAC) scheme for structured grids (Harlow and Amsden, 1971; Harlow and Welch, 1965). Time-stepping is performed with a second order Runge-Kutta scheme, called the Heun scheme.

The equation solved is the so-called sensible energy balance instead of the total energy conservation equation. This choice avoids building an approximation of the total energy which, for staggered discretizations, is a “composite” variable combining quantities discretized on the cells and at the faces. This difficulty may be overstepped by adding, as in Herbin et al. (2014), a corrective term in the discrete sensible energy balance equation.

The scheme enjoys some stability properties: the density is shown to be non-negative at the discrete level under CFL condition. This is obtained thanks to a high-order (MUSCL-type) positivity-preserving convection operator for the mass balance equation. The same MUSCL technique is also used for the discretization of the convection operator of the sensible energy balance equation. In order to obtain the positivity of the internal energy at the discrete level (under CFL condition), a careful design of the viscous dissipation term is needed. To this purpose, we use an idea proposed in Grapsas et al. (2016), which consists in recasting the MAC scheme under a weak form, so that we may closely mimick the continuous expression of the dissipation: *in fine*, the cell dissipation is computed as the integral over the considered cell of the inner product of the stress and strain tensors, linked *a.e.* by the usual (continuous) relation (hence the non-negativity).

In the context of LES of turbulent flows, the control of kinetic energy is an essential requirement for a numerical scheme in order to guarantee not only the stability but also the physical reliability of the results. A local kinetic energy balance for the algorithm with remainder terms is derived, which we show to be of second order in time. Finally, we establish a total energy balance for the scheme, which may be made conservative by adding corrective terms to the sensible energy balance, for instance if one wants to compute shock solutions. Since we address here essentially viscous flows, we do not follow this line; however, we numerically check that the scheme correctly captures the viscous perturbation of mild shocks (similar for instance to the strongest ones which may be generated by deflagrations) even with coarse meshes. On the opposite, for strong shocks (typical of detonations), correcting the discrete sensible energy balance seems to be preferable.

Appendix

3.A Diffusion and dissipation terms

The construction of momentum diffusion and viscous dissipation terms relies on the following formalism (see Grapsas (2017)):

(i) piecewise-constant tensor valued fields, let us say $\boldsymbol{\nabla}_{\mathcal{M}}\boldsymbol{v}$ and $\check{\boldsymbol{\tau}}_{\mathcal{M}}(\boldsymbol{v})$, representing the discrete velocity gradient and stress tensor respectively, are defined,

(ii) then a discrete test function associated to each face is introduced; this allows to derive an expression of $\operatorname{div}(\check{\boldsymbol{\tau}}(\boldsymbol{v}))_{\sigma,i}$ through a weak formulation of this term, which is shown to coincide with the usual finite volume formulation, provided that a specific (and reasonable) space interpolation of the viscosity is chosen in the latter;

(iii) finally, we give to $(\check{\boldsymbol{\tau}}(\boldsymbol{v}) : \boldsymbol{\nabla}\boldsymbol{v})_K$ the following definition:

$$|K|(\check{\boldsymbol{\tau}}(\boldsymbol{v}) : \boldsymbol{\nabla}\boldsymbol{v})_K = \int_K \check{\boldsymbol{\tau}}_{\mathcal{M}}(\boldsymbol{v}) : \boldsymbol{\nabla}_{\mathcal{M}}\boldsymbol{v}\,\mathrm{d}\boldsymbol{x}. \tag{3.77}$$

We first recall here this derivation, for the sake of completeness. Then, we focus on the objective of this section, namely to derive the viscous fluxes (*i.e.* the discrete equivalent of $\operatorname{div}(\check{\boldsymbol{\tau}}(\boldsymbol{v})\boldsymbol{v})$ and the dissipation (*i.e.* the discrete equivalent of $\check{\boldsymbol{\tau}}(\boldsymbol{v}) : \boldsymbol{v}$) which appears in the discrete kinetic energy balances, first posed on the dual mesh and then averaged to obtain an analogue relation on the primal mesh. Since this section only adresses space discretization issues, we omit for short the time index; in the scheme proposed in this chapter, all the quantities are explicit, in the sense that they have to evaluated at the beginning of the step in the Heun algorithm.

As explained above, the first step in the construction of the viscous term is to define piecewise constant partial derivatives of the velocity components, based on specific partitions of the computational domain. For $1 \leq i, j \leq d$, the partial derivative of the i-th component of the velocity v_i with respect to the j-th coordinate, which we denote by $\eth_j v_i$, is defined as a piecewise-constant over each volume D_ϵ of the set $\{D_\epsilon, \epsilon \in \tilde{\mathcal{E}}^{(i,j)}\}$, with $\tilde{\mathcal{E}}^{(i,j)} = \{\epsilon \in \tilde{\mathcal{E}}^{(i)},\ \epsilon \perp \boldsymbol{e}^{(j)}\}$, and

$$D_\epsilon = \left| \begin{array}{ll} \epsilon \times [\boldsymbol{x}_\sigma, \boldsymbol{x}_{\sigma'}], & \text{for } \ \epsilon = \sigma|\sigma' \in \tilde{\mathcal{E}}^{(i)}_{\text{int}}, \\ \epsilon \times [\boldsymbol{x}_\sigma, \boldsymbol{x}_{\sigma,\epsilon}], & \text{for } \ \epsilon \in \tilde{\mathcal{E}}(D_\sigma) \cap \tilde{\mathcal{E}}^{(i)}_{\text{ext}}, \end{array} \right. \tag{3.78}$$

where $\boldsymbol{x}_{\sigma,\epsilon}$ refers to the orthogonal projection of $\boldsymbol{x}_\sigma$ on ϵ. Each set $\{D_\epsilon, \epsilon \in \tilde{\mathcal{E}}^{(i,j)}\}$ is a partition of Ω; a volume D_ϵ of this set is called in the following a (i,j)-gradient cell. For the two-dimensional case, these volumes are sketched on Fig. 3.A.1. When $i = j$, a (i,j)-gradient cell coincides with a primal cell. In addition, we observe that, for $i \neq j$, the set of the (i,j)-gradient cells and the set of the (j,i)-gradient cells are the same; in two space dimensions, such a (i,j)-gradient cell may be associated to a grid vertex, while, in three space dimensions, for $\epsilon = \sigma|\sigma'$, it is associated to the edge equal to $\overline{\sigma} \cap \epsilon = \overline{\sigma}' \cap \epsilon$ (see Grapsas et al. (2016)).

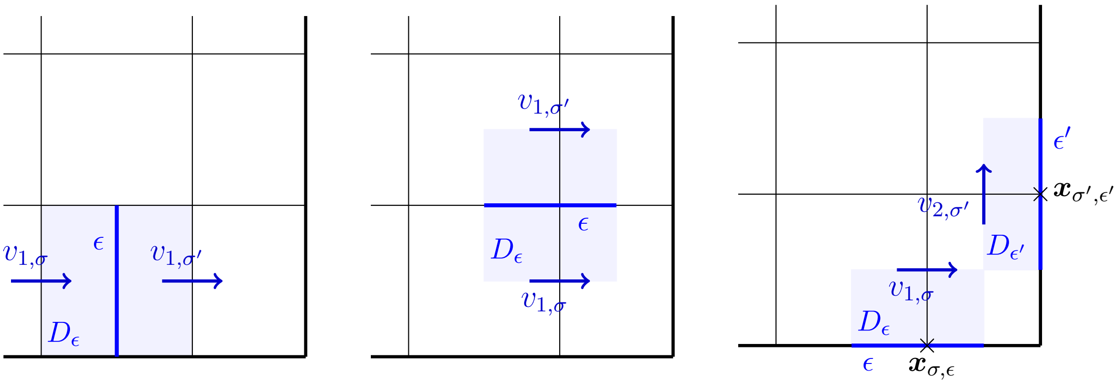

Figure 3.A.1: (i,j)- gradient cells in the two-dimensional case. Left: $\epsilon = \sigma|\sigma' \in \tilde{\mathcal{E}}^{(1)}_{int}$ and $\epsilon \perp \boldsymbol{e}^{(1)}$. Middle: $\epsilon = \sigma|\sigma' \in \tilde{\mathcal{E}}^{(1)}_{int}$ and $\epsilon \perp \boldsymbol{e}^{(2)}$. Right: $\epsilon = \tilde{\mathcal{E}}^{(1)}_{ext} \cap \tilde{\mathcal{E}}(D_\sigma)$ and $\epsilon' = \tilde{\mathcal{E}}^{(2)}_{ext} \cap \tilde{\mathcal{E}}(D'_\sigma)$.

Supposing for short that the velocity obeys homogeneous Dirichlet boundary conditions, for $1 \leq i, j \leq d$, we define $\eth_j v_i$ a.e. in Ω by

$$\eth_j v_i(\boldsymbol{x}) = \left| \begin{array}{ll} \dfrac{v_{\sigma',i} - v_{\sigma,i}}{\boldsymbol{x}_{\sigma',j} - \boldsymbol{x}_{\sigma,j}} & \text{for } \boldsymbol{x} \in D_\epsilon,\ \epsilon \in \tilde{\mathcal{E}}^{(i,j)} \cap \tilde{\mathcal{E}}^{(i)}_{\text{int}},\ \epsilon = \sigma|\sigma', \\ \dfrac{-v_{\sigma,i}}{\boldsymbol{x}_{\sigma,\epsilon} - \boldsymbol{x}_{\sigma,j}} & \text{for } \boldsymbol{x} \in D_\epsilon,\ \epsilon \in \tilde{\mathcal{E}}^{(i,j)} \cap \tilde{\mathcal{E}}^{(i)}_{\text{ext}},\ \epsilon \in \tilde{\mathcal{E}}(D_\sigma). \end{array} \right. \tag{3.79}$$

For $\sigma \in \mathcal{E}^{(i)}_{\text{int}}$, let the discrete velocity field $\boldsymbol{\varphi}^{(i),\sigma}$ be the discrete velocity function defined $(\boldsymbol{\varphi}^{(i),\sigma})_\sigma = 1$ and $(\boldsymbol{\varphi}^{(i),\sigma})_{\sigma'} = 0$ for $\sigma' \in \mathcal{E}$, $\sigma' \neq \sigma$ (so the j-th component(s) of $\boldsymbol{\varphi}^{(i),\sigma}$ are zero for $j \neq i$ and the i-th component has only one degree of freedom set to 1, namely the degree of freedom corresponding to σ). To each gradient cell (which, for $i \neq j$, is both a (i,j)-gradient cell and a (j,i)-gradient cell), we associate a viscosity μ_{D_σ}, and we introduce $d \times d$ viscosity fields defined a.e. in Ω by

$$\mu^{(i,j)}(\boldsymbol{x}) = \mu_{D_\sigma}, \quad \text{for } \boldsymbol{x} \in D_\epsilon, \text{ with } \epsilon \in \tilde{\mathcal{E}}^{(i,j)}.$$

For a discrete velocity field $\boldsymbol{v}$, we are now in position to define a discrete gradient $\boldsymbol{\nabla}_{\mathcal{E}} \boldsymbol{v}$ and a tensor associated to the multiplication of the strain rate by the viscosity, denoted by $(\mu\, \mathbf{S})_{\mathcal{E}}(\boldsymbol{v})$, for a.e. $\boldsymbol{x} \in \Omega$:

$$(\boldsymbol{\nabla}_{\mathcal{E}} \boldsymbol{v})_{i,j}(\boldsymbol{x}) = \eth_j v_i(\boldsymbol{x}), \quad ((\mu \mathbf{S})_{\mathcal{E}}(\boldsymbol{v}))_{i,j} = \mu^{(i,j)}(\boldsymbol{x})\, \frac{\eth_j v_i(\boldsymbol{x}) + \eth_i v_j(\boldsymbol{x})}{2}. \tag{3.80}$$

Finally, we define the stress tensor by

$$\breve{\boldsymbol{\tau}}_{\mathcal{E}}(\boldsymbol{x}) = 2\ (\mu \mathbf{S})_{\mathcal{E}}(\boldsymbol{v})(\boldsymbol{x}) + \frac{2}{3} \mathrm{Tr}\big((\mu \mathbf{S})_{\mathcal{E}}(\boldsymbol{v})(\boldsymbol{x})\big) \boldsymbol{I} \quad \text{for a.e. } \boldsymbol{x} \in \Omega$$

and the diffusion term by:

$$-\,|D_\sigma|\ \operatorname{div}(\breve{\boldsymbol{\tau}}(\boldsymbol{v}))_\sigma = \int_\Omega \breve{\boldsymbol{\tau}}_{\mathcal{E}}(\boldsymbol{x}) : \boldsymbol{\nabla}_{\mathcal{E}}(\boldsymbol{\varphi}^{(i),\sigma})(\boldsymbol{x})\,\mathrm{d}\boldsymbol{x}, \tag{3.81}$$

for $\sigma \in \mathcal{E}^{(i)}_{\rm int}$. The quantity $\mu^n_{D_\epsilon}$ may be approximated by any reasonable average over the neighbouring cells, for instance:

$$\mu^n_{D_\epsilon} = \mu^n_K \text{ if } D_\epsilon = K, \text{ and } |D_\epsilon|\ \mu^n_{D_\epsilon} = \sum_{\substack{K\in\mathcal{M},\\ K\cap D_\epsilon\neq\emptyset}} \frac{|K|}{4}\ \mu^n_K \text{ otherwise.}$$

Kinetic energy balance – In the kinetic energy balance (posed on the dual mesh), the term associated to this diffusion reads, for $\sigma \in \mathcal{E}^{(i)}_{\rm int}$, $1 \le i \le d$:

$$T_{\sigma,i} = -|D_\sigma|\ \operatorname{div}(\breve{\boldsymbol{\tau}}(\boldsymbol{v}))_\sigma\ v_{\sigma,i} = \int_\Omega \breve{\boldsymbol{\tau}}_{\mathcal{E}}(\boldsymbol{x}) : \boldsymbol{\nabla}_{\mathcal{E}}(\boldsymbol{\varphi}^{(i),\sigma})(\boldsymbol{x})\,\mathrm{d}\boldsymbol{x}\ v_{\sigma,i}.$$

Decomposing the integral and using the fact the support of $\boldsymbol{\nabla}_{\mathcal{E}}(\boldsymbol{\varphi}^{(i),\sigma})$ is restricted to the (i,j)-gradient cells D_ϵ where ϵ is a dual face of D_σ, we get:

$$T_{\sigma,i} = \sum_{j=1}^d \sum_{\substack{\epsilon\in\mathcal{E}(D_\sigma),\\ \epsilon\in\tilde{\mathcal{E}}^{(i,j)}}} \int_{D_\epsilon} (\breve{\boldsymbol{\tau}}_{\mathcal{E}}(\boldsymbol{x}))_{i,j} : \eth_j \boldsymbol{\varphi}^{(i),\sigma}(\boldsymbol{x})\,\mathrm{d}\boldsymbol{x}\ v_{\sigma,i}.$$

Let us write $T_{\sigma,i} = T^{\rm diss}_{\sigma,i} + T^{\rm cons}_{\sigma,i}$ with

$$T^{\rm diss}_{\sigma,i} = \frac{1}{2}\sum_{j=1}^d \sum_{\substack{\epsilon\in\mathcal{E}(D_\sigma),\\ \epsilon\in\tilde{\mathcal{E}}^{(i,j)},\ \epsilon=D_\sigma|D_{\sigma'}}} \int_{D_\epsilon} (\breve{\boldsymbol{\tau}}_{\mathcal{E}}(\boldsymbol{x}))_{i,j} : \eth_j \boldsymbol{\varphi}^{(i),\sigma}(\boldsymbol{x})\,\mathrm{d}\boldsymbol{x}\ (v_{\sigma,i} - v_{\sigma',i}),$$

$$T^{\rm cons}_{\sigma,i} = \frac{1}{2}\sum_{j=1}^d \sum_{\substack{\epsilon\in\mathcal{E}(D_\sigma),\\ \epsilon\in\tilde{\mathcal{E}}^{(i,j)},\ \epsilon=D_\sigma|D_{\sigma'}}} \int_{D_\epsilon} (\breve{\boldsymbol{\tau}}_{\mathcal{E}}(\boldsymbol{x}))_{i,j} : \eth_j \boldsymbol{\varphi}^{(i),\sigma}(\boldsymbol{x})\,\mathrm{d}\boldsymbol{x}\ (v_{\sigma,i} + v_{\sigma',i}).$$

For $\epsilon \in \tilde{\mathcal{E}}^{(i,j)}$, with $\epsilon = D_\sigma|D_{\sigma'}$, we have $\eth_j \boldsymbol{\varphi}^{(i),\sigma'}(\boldsymbol{x}) = -\eth_j \boldsymbol{\varphi}^{(i),\sigma}(\boldsymbol{x})$. Considering the support of these two partial derivatives, we get

$$T^{\rm diss}_{\sigma,i} = \frac{1}{2}\sum_{j=1}^d \sum_{\substack{\epsilon\in\mathcal{E}(D_\sigma),\\ \epsilon\in\tilde{\mathcal{E}}^{(i,j)}}} \int_{D_\epsilon} (\breve{\boldsymbol{\tau}}_{\mathcal{E}}(\boldsymbol{x}))_{i,j} : \eth_j (v_i)(\boldsymbol{x})\,\mathrm{d}\boldsymbol{x},$$

which is a natural expression for the dissipation term, considering that the integral at the right-hand side of this relation may be shared, in the part of the kinetic energy balance assocated to the i-th component of the velocity, between the discrete equations associated to σ and to σ'. Still because $\eth_j \boldsymbol{\varphi}^{(i),\sigma'}(\boldsymbol{x}) = -\eth_j \boldsymbol{\varphi}^{(i),\sigma}(\boldsymbol{x})$, the term $T^{\rm cons}_{\sigma,i}$ is conservative. We may thus write

$$T^{\rm cons}_{\sigma,i} = \sum_{\epsilon\in\tilde{\mathcal{E}}(D_\sigma)} G_{\sigma,\epsilon}.$$

Using the definition of the discrete test functions,

$$G_{\sigma,\epsilon} = |\epsilon|\ (\breve{\boldsymbol{\tau}}_{\mathcal{E}})_{i,j,D_\epsilon}\ \frac{v_{\sigma,i} + v_{\sigma',i}}{2}\ \mathbf{n}_{\sigma,\epsilon} \cdot \boldsymbol{e}^{(j)}, \quad \text{for } \epsilon \in \tilde{\mathcal{E}}^{(i,j)}, \tag{3.82}$$

where $(\breve{\boldsymbol{\tau}}_{\mathcal{E}})_{i,j,D_\epsilon}$ stands for the constant value of $(\breve{\boldsymbol{\tau}}_{\mathcal{E}})_{i,j}$ over D_ϵ. This expression is a natural finite volumes discretization of $\mathrm{div}(\breve{\boldsymbol{\tau}} \cdot \boldsymbol{v})_i$.

Kinetic energy balance on the primal cells – The flux given by Equation (3.82) must just be added to the convection flux in Equation (3.62), and the process to obtain the kinetic energy balance over the primal cells is left unchanged. For the dissipation term, we get, by the same process:

$$T_K^{\mathrm{diss}} = \frac{1}{4} \sum_{i,j=1}^{d}\ \sum_{\substack{\sigma \in \mathcal{E}(K),\\ \sigma \in \mathcal{E}_{\mathrm{int}}^{(i)}}}\ \sum_{\substack{\epsilon \in \mathcal{E}(D_\sigma),\\ \epsilon \in \tilde{\mathcal{E}}^{(i,j)}}} \int_{D_\epsilon} \breve{\boldsymbol{\tau}}_{\mathcal{E}}(\boldsymbol{x})_{i,j} : \eth_j(v_i)(\boldsymbol{x})\,\mathrm{d}\boldsymbol{x}, \tag{3.83}$$

This is to be compared with the expression used in the internal energy balance, which reads:

$$\tilde{T}_K^{\mathrm{diss}} = \frac{1}{4} \sum_{i,j=1}^{d} \int_K \breve{\boldsymbol{\tau}}_{\mathcal{E}}(\boldsymbol{x})_{i,j} : \eth_j(v_i)(\boldsymbol{x})\,\mathrm{d}\boldsymbol{x}.$$

We see that the expression (3.83) amounts to perform the integration over a domain roughly speaking 4 times greater than K and dividing by 4 (see Fig. 3.A.2 for the exact comparison of the integration domains). If we suppose that the dissipation is controlled in L^1, the difference between T_K^{diss} and $\tilde{T}_K^{\mathrm{diss}}$ thus tends to zero in a distributional sense; for regular solutions on non-uniform meshes, it may be expected to be vary as the space step in the L^∞-norm. Note that switching from $\tilde{T}_K^{\mathrm{diss}}$ to T_K^{diss} is also possible, up to a slight additional complexity from an algorithmic point of view.

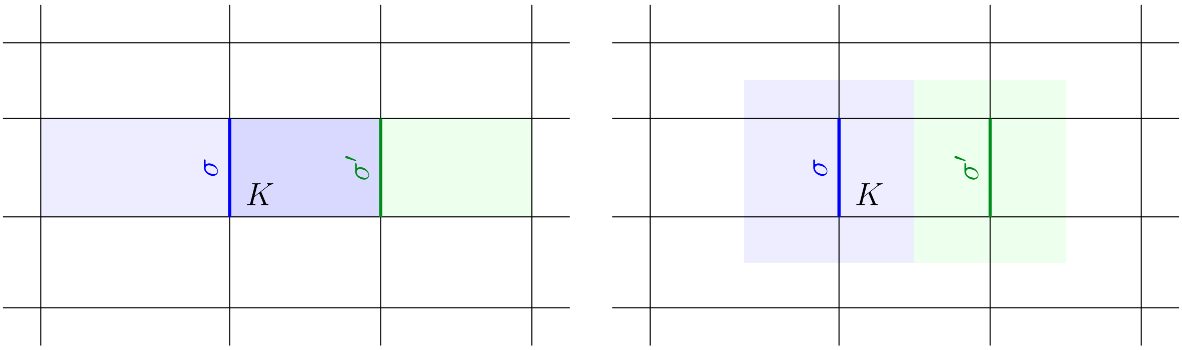

Figure 3.A.2: Integration domains for the dissipation term in the dissipation term. Two-dimensional case, $i = 1$, $j = 1$ (left) and j=2 (right). Light blue: $(1, j)$-gradient cell associated to σ; light green: $(1, j)$-gradient cell associated to σ'; blue: $(1, 1)$-gradient cell associated to both σ and σ'.

3.B The MUSCL scheme

The MUSCL discretization of the convection operators of the mass balance and of the internal energy balance is recalled here for the sake of completeness. It closely follows the technique proposed in Piar et al. (2013) for the transport equation. Formally second-order in space fluxes are computed and then a limiting procedure is applied in order to obtain positivity under a CFL-like condition, since we use an explicit time discretization. This limiting step is purely algebraic: it does not require any geometric argument and thus works on quite general meshes. It is carefully designed to keep the pressure constant in the zones where it actually should be, and in particular across contact discontinuities when the scheme boils to the hyperbolic case.

For any $\sigma \in \mathcal{E}$, the procedure consists in four steps:

- calculate a tentative value for ρ_σ as linear interpolate of nearby values,
- calculate an interval for ρ_σ which guarantee some stability properties for the scheme,
- project the tentative value ρ_σ on this stability interval,
- calculate e_σ as function of projected tentative value ρ_σ.

For the tentative value of $\tilde{\rho}_\sigma$, let us choose some real coefficients $(\varsigma^\rho_{K,\sigma})_{K\in\mathcal{M}}$ such that

$$\boldsymbol{x}_\sigma = \sum_{K\in\mathcal{M}} \varsigma^\rho_{K,\sigma} \boldsymbol{x}_K, \qquad \sum_{K\in\mathcal{M}} \varsigma^\rho_{K,\sigma} = 1.$$

where $\boldsymbol{x}_\sigma$ and $\boldsymbol{x}_K$ stand for the mass centers of σ and K respectively, $\forall \sigma \in \mathcal{E}_{\text{int}}$ and $K \in \mathcal{M}$. The coefficients used in this interpolation are chosen in such a way that as few as possible cells, to be picked up in the closest cells to σ, take part. For example, for $\sigma = K|L$ and if $\boldsymbol{x}_K$, $\boldsymbol{x}_\sigma$, $\boldsymbol{x}_L$ are aligned, only two non-zero coefficients exist in the family $(\varsigma^\rho_{K,\sigma})_{K\in\mathcal{M}}$, namely $\varsigma^\rho_{K,\sigma}$ and $\varsigma^\rho_{L,\sigma}$. Then, these coefficients are used to calculate the tentative value of $\tilde{\rho}_\sigma$ by

$$\tilde{\rho}_\sigma = \sum_{K\in\mathcal{M}} \varsigma^\rho_{K,\sigma} \rho_K.$$

The construction of the stability interval for the density must be such that the following property holds:

$$\begin{aligned} &\forall K \in \mathcal{M},\ \forall \sigma \in \mathcal{E}(K) \cap \mathcal{E}_{\text{int}},\ \exists \beta^\rho_{K,\sigma} \in [0,1] \text{ and } M^\rho_{K,\sigma} \in \mathcal{M} \text{ such that} \\ &\rho_\sigma - \rho_K = \left| \begin{array}{l} \beta^\rho_{K,\sigma}\, (\rho_K - \rho_{M^\rho_{K,\sigma}}),\ \text{if } \boldsymbol{v}_{K,\sigma} \geq 0, \\ \beta^\rho_{K,\sigma}\, (\rho_{M^\rho_{K,\sigma}} - \rho_K),\ \text{otherwise.} \end{array} \right. \end{aligned} \tag{3.84}$$

Similarly, the following property holds for the internal energy:

$$\begin{aligned} &\forall K \in \mathcal{M},\ \forall \sigma \in \mathcal{E}(K) \cap \mathcal{E}_{\text{int}},\ \exists \beta^e_{K,\sigma} \in [0,1] \text{ and } M^e_{K,\sigma} \in \mathcal{M} \text{ such that} \\ &e_\sigma - e_K = \left| \begin{array}{l} \beta^e_{K,\sigma}\, (e_K - e_{M^e_{K,\sigma}}),\ \text{if } F_{K,\sigma} \geq 0, \\ \beta^e_{K,\sigma}\, (e_{M^e_{K,\sigma}} - e_K),\ \text{otherwise.} \end{array} \right. \end{aligned} \tag{3.85}$$

Under these latter hypothesis and a CFL condition, the scheme preserves the positivity of e and ρ.

Remark. Note that, in Assumptions (3.84) and (3.85), only internal faces are considered, since the fluxes through external faces are supposed to vanish due to impermeability boundary conditions. However, the present discussion may easily be generalized to cope with convection fluxes entering the domain.

We have shown in Piar et al. (2013) that Assumption (3.84) (respectively (3.85)) defines an admissible interval for ρ_σ (respectively e_σ), and that a limiting procedure may be obtained by just projecting the tentative value for the density $\tilde{\rho}_\sigma$ (resp. internal energy $\tilde{e}_\sigma$) at the face on this interval. Here, the situation is more complicated, since we also need to keep the pressure constant at contact discontinuities when the scheme boils to the hyperbolic case. Thus, the product $\rho_\sigma\, e_\sigma$ must be equal to $\rho_K\, e_K$ and $\rho_L\, e_L$ when these quantities are the same (recall that we use here the fact that the equation of state is such that the pressure only depends on the product $\rho\, e$). In fact, we require here the more restrictive assumption that $\rho_\sigma\, e_\sigma$ is a convex combination of $\rho_K\, e_K$ and $\rho_L\, e_L$, *i.e.* that there exists $\kappa_\sigma \in [0,1]$ such that:

$$\rho_\sigma\, e_\sigma = \kappa_\sigma\, \rho_K\, e_K + (1-\kappa_\sigma)\, \rho_L\, e_L \tag{3.86}$$

Our aim is thus to find an admissible interval for ρ_σ and for e_σ such that (3.84), (3.85) and (3.86) hold. First, let us suppose that $\sigma \in \mathcal{E}_{\rm int}$, $\sigma = K|L$ and that the flow goes from K to L, that is $F_{K,\sigma} \geq 0$. For the sake of simplicity, we suppose also that the cells $M^\rho_{K,\sigma}$ and $M^e_{K,\sigma}$ are the same and we denote this cell $M_{K,\sigma}$. Assumption (3.84) could be rewritten in the following way:

$$\begin{aligned} &\exists \beta^\rho_\sigma \in [0,1], \alpha^\rho_\sigma \in [0,1] \text{ and } M_\sigma \in \mathcal{M} \text{ such that} \\ &\left|\begin{array}{l} \rho_\sigma - \rho_K = \beta^\rho_\sigma\, (\rho_K - \rho_{M_\sigma}), \\ \rho_\sigma - \rho_L = \alpha^\rho_\sigma\, (\rho_K - \rho_L) \end{array}\right. \end{aligned} \tag{3.87}$$

Analagously, assumption (3.85) could be rewritten in the following way:

$$\begin{aligned} &\exists \beta^e_\sigma \in [0,1], \alpha^e_\sigma \in [0,1] \text{ and } M_\sigma \in \mathcal{M} \text{ such that} \\ &\left|\begin{array}{l} e_\sigma - \rho_K = \beta^e_\sigma\, (e_K - e_{M_\sigma}), \\ e_\sigma - \rho_L = \alpha^e_\sigma\, (e_K - e_L) \end{array}\right. \end{aligned} \tag{3.88}$$

Combining both relations (3.87), we get:

$$\alpha^\rho_\sigma = 1 - \frac{\beta^\rho_\sigma}{r^\rho_\sigma}, \qquad \text{with } r^\rho_\sigma = \frac{\rho_L - \rho_K}{\rho_K - \rho_{M_\sigma}} \tag{3.89}$$

From this relation, it appears that (3.87) is satisfied (and equivalently (3.84)) provided that β^ρ_σ satisfies:

$$0 \leq \beta^\rho_\sigma \leq (\min(1, r^\rho_\sigma))^+$$

where, for $a \in \mathbb{R}$, a^+ is defined by $a^+ = \max(a, 0)$. This observation suggests the following strategy: thanks to the link between the value of and ρ_σ and e_σ induced by (3.86) , try to express the coefficients α^e_σ and β^e_σ as a function of β^ρ_σ, and then express the limiting procedures produced by (3.88) as limiting procedures for β^ρ_σ. Arbitrarly assuming that $\kappa_\sigma = \alpha^\rho_\sigma$ in (3.86) and after some agebraic manipulations (see Gastaldo et al. (2018) for more details), we get:

$$\alpha^e_\sigma = \frac{\rho_K}{\rho_\sigma}\, \alpha^\rho_\sigma, \qquad = \frac{\rho_L}{\rho_\sigma}\, \frac{r^e_\sigma}{r^\rho_\sigma}\, \beta^\rho_\sigma \quad \text{with } r^e_\sigma = \frac{e_L - e_K}{e_K - e_{M_\sigma}} \tag{3.90}$$

Thus, there exists $\alpha_\sigma \in [0,1]$ and $\beta^e_\sigma \in [0,1]$ such that (3.84), (3.85) and (3.86) hold if β^ρ_σ is such that:

$$0 \leq \beta^\rho_\sigma \leq \left(\min(1, r^\rho_\sigma, \frac{\rho_\sigma}{\rho_L}\frac{r^\rho_\sigma}{r^e_\sigma})\right)^+.$$

This relation still does not provide an interval for β^ρ_σ, since it involves ρ_σ which expression itself involves β^ρ_σ. But now, we just need to replace ρ_σ by an explicit lower bound. As $\beta^\rho_\sigma = 0$ is always an admissible value, ρ_K is also an admissible value for ρ_σ. Thus ρ_σ will be obtained by a projection of the tentative value $\tilde{\rho}_\sigma$ on an interval containing ρ_K, which ensures that $\rho_\sigma \geq \min(\rho_K, \tilde{\rho}_\sigma)$. Consequently, we finally choose for admissible interval for β^ρ_σ the interval I_β given by:

$$I_\beta = \left[0, \left(\min(1, r^\rho_\sigma, \frac{\min(\rho_K, \tilde{\rho}_\sigma)}{\rho_L}\frac{r^\rho_\sigma}{r^e_\sigma})\right)^+\right]$$

The admissible range for the density is thus I_ρ with:

$$I_\rho = \{\rho_K + \beta\,(\rho_K - \rho_{M_\sigma}),\ \beta \in I_\beta\}$$

Given $\tilde{\rho}_\sigma$, the limiting algorithm consists in computing ρ_σ by projection on I_ρ, which yields β^ρ_σ. The coefficient β^e_σ is then given by (3.90) and e_σ is computed from the first relation of (3.88) .

3.C The pressure correction scheme

The algorithm described here was first introduced in Grapsas et al. (2016); Herbin et al. (2014) and is recalled here for the sake of completeness.

It solves the same system of equations introduced in Section 3.2, (3.3). Here again, only impermeability conditions are considered, and initial conditions for $\overline{\rho}$, $\widetilde{e}$ and $\widetilde{\boldsymbol{v}}$ are such that:

$$\overline{\rho}(x,0) = \overline{\rho}_0(x),\ \widetilde{e}(x,0) = \widetilde{e}_0(x),\ \widetilde{\boldsymbol{v}}(x,0) = \widetilde{\boldsymbol{v}}_0(x),\ \text{with } \overline{\rho}_0 > 0, \widetilde{e}_0 > 0.$$

From now on, the filter notations are omitted for the sake of clarity and the symbols $\widetilde{\cdot}$ or $\overline{\cdot}$ will denote predicted unknowns instead of filtered ones.

The spatial discretization is staggered and based on the so-called Marker-And Cell (MAC) scheme Harlow and Amsden (1971); Harlow and Welch (1965). But the discretization can be easily extended to non-conforming low-order finite element approximations Grapsas et al. (2016); Grapsas (2017), namely the Rannacher and Turek (RT) element Rannacher and Turek (1992) for quadrilateral or hexahedral meshes, or the lowest degree Crouzeix-Raviart (CR) elementCrouzeix and Raviart (1973) for simplicial meshes.

A fractional step strategy is used; it involves a prediction step for a tentative velocity followed by an elliptic pressure correction step. These steps are both implicit-in-time, to avoid any restriction of the time step other than the one imposed for accuracy reasons.

Let us consider a uniform partition $0 = t_0 < t_1 < \ldots < t_N = T$ of the time interval $(0, T)$, and let $\delta t = t_{n+1} - t_n$ for $n = 0, 1, \ldots, N-1$ be the constant time step. The numerical scheme reads in its fully discrete form, for $0 \leq n \leq N-1$:

Pressure gradient scaling step:

$$\forall \sigma \in \mathcal{E}_{\rm int}, \quad (\overline{\boldsymbol{\nabla} p})_\sigma^{n+1} = \Big(\frac{\rho^n_{D_\sigma}}{\rho^{n-1}_{D_\sigma}}\Big)^{1/2} (\boldsymbol{\nabla} p^n)_\sigma. \tag{3.91a}$$

Prediction step – Solve for $\tilde{\boldsymbol{v}}^{n+1}$:

For $1 \le i \le d, \ \forall \sigma \in \mathcal{E}^{(i)}_{\rm int}$,

$$\frac{1}{\delta t}\ \big(\rho^n_{D_\sigma}\tilde v^{n+1}_{\sigma,i} - \rho^{n-1}_{D_\sigma} v^n_{\sigma,i}\big) + {\rm div}_\sigma(\rho^n \tilde v_i^{n+1}\boldsymbol{v}^n - {\rm div}(\boldsymbol{\tau}(\tilde{\boldsymbol{v}}^{n+1}))_{\sigma,i} + (\overline{\boldsymbol{\nabla} p})^{n+1}_{\sigma,i} = 0 \tag{3.91b}$$

Correction step – Solve for p^{n+1}, e^{n+1}, ρ^{n+1} and $\boldsymbol{v}^{n+1}$:

For $1 \le i \le d, \ \forall \sigma \in \mathcal{E}^{(i)}_{\rm int}$,

$$\frac{1}{\delta t}\ \rho^n_{D_\sigma}\ (v^{n+1}_{\sigma,i} - \tilde v^{n+1}_{\sigma,i}) + (\boldsymbol{\nabla} p^{n+1})_{\sigma,i} - (\overline{\boldsymbol{\nabla} p})^{n+1}_{\sigma,i} = 0, \tag{3.91c}$$

$$\forall K \in \mathcal{M}, \quad \frac{1}{\delta t}(\rho^{n+1}_K - \rho^n_K) + {\rm div}_K(\rho^{n+1}\boldsymbol{v}^{n+1}) = 0 \tag{3.91d}$$

$$\begin{aligned} &\forall K \in \mathcal{M}, \\ &\quad \frac{1}{\delta t}(\rho^{n+1}_K e^{n+1}_K - \rho^n_K e^n_K) + {\rm div}_K(\rho^{n+1} e^{n+1}\boldsymbol{v}^{n+1}) + p^{n+1}_K({\rm div}(\boldsymbol{v}^{n+1}))_K \\ &\qquad\qquad = \big(\boldsymbol{\tau}(\tilde{\boldsymbol{v}}^{n+1}) : \boldsymbol{\nabla}\tilde{\boldsymbol{v}}^{n+1}\big)_K + {\rm div}(q^{n+1})_K + S^{n+1}_K, \end{aligned} \tag{3.91e}$$

$$\forall K \in \mathcal{M}, \quad \rho^{n+1}_K = \varrho(e^{n+1}_K, p^{n+1}_K) = \frac{1}{\gamma - 1}\,\frac{p^{n+1}_K}{e^{n+1}_K}. \tag{3.91f}$$

The first step is a pressure gradient scaling step which is introduced in order to recover a discrete kinetic energy inequality. The second step is a classical semi-implicit solution of the momentum balance equation to obtain a tentative velocity field. The third step is a nonlinear pressure correction step, which couples the mass balance equation with the internal energy balance equation. This coupling is necessary to guarantee the unconditionally stability property of the scheme, *i.e.*, stability respectively of the time and space steps. In addition, in the Euler case, it also allows the scheme to keep the velocity and pressure constant across (1D) contact discontinuities Grapsas (2017). The last equation of this step is the equation of state. Contrary to the explicit numerical scheme (Section 3.4.1) it is recast here as $\rho = \varrho(e, p)$ because, at the algebraic level, the density is first eliminated from the system, this latter is solved for e^{n+1} and p^{n+1}, and ρ^{n+1} is finally given by (3.91f) Grapsas (2017).

The notations appearing on the scheme (3.91) have already been introduced in Section 3.4.1. However, let notice that for the convection terms of the discrete mass balance equation (3.91d) and of the discrete internal energy balance equation (3.91e), the upwind choice is made instead of the MUSCL one. Thus, in (3.91d):

$${\rm div}_K(\rho\,\boldsymbol{v}) = \frac{1}{|K|}\sum_{\sigma\in\mathcal{E}(K)} F_{K,\sigma} = \frac{1}{|K|}\sum_{\sigma\in\mathcal{E}(K)} |\sigma|\ \rho_\sigma\ v_{K,\sigma} \tag{3.92}$$

with for $\sigma = K|L \in \mathcal{E}_{\text{int}}$, $\rho_\sigma = \rho_K$ if $v_{K,\sigma} \geq 0$ and $\rho_\sigma = \rho_L$ otherwise. Analogously, for the discrete internal energy balance equation (3.91e):

$$\operatorname{div}(\rho e \boldsymbol{v})_K = \frac{1}{|K|} \sum_{\sigma \in \mathcal{E}(K)} F_{K,\sigma} e_\sigma, \tag{3.93}$$

with, for $\sigma = K|L \in \mathcal{E}_{\text{int}}$, $e_\sigma = e_K$ if $F_{K,\sigma} \geq 0$ and $e_\sigma = e_L$ otherwise.

In the rescaling step, the pressure gradient (3.91a) the term $(\boldsymbol{\nabla} p)_{\sigma,i}$ stands for the i^{th} component of the discrete pressure gradient at the face σ, which is built as the transpose operator to the natural divergence (see Section 3.4.1, relation (3.33)). The same discretization is used in the correction equation (3.91c) for the discrete pressure gradient.

Finally, the term S_K at the right-hand side of (3.91e) is necessary to obtain a consistent scheme in the Euler case Herbin et al. (2014); its purpose is to compensate some numerical dissipation terms appearing in the discrete kinetic energy balance equation, which may not tend to 0 as the mesh and time step tend to 0 Grapsas (2017).

Les us list the essential features of the scheme described here (for more details we refer to Grapsas et al. (2016); Grapsas (2017)):

- The algorithm presented here is an extension of a solver natively designed for incompressible flows, or for the asymptotic model of low Mach number flows Nerinckx et al. (2005). It boils down to the original incompressible scheme when the Mach number tends to zero (see Herbin et al. (2017) for a rigorous proof in the barotropic case).
- The risk when using a non-iterative pressure correction algorithm is to lose stability. Here, the numerical scheme is proved to be unconditional stable (*i.e.* independent of the time and space step).
- Moreover the same stability properties proven for the explicit scheme hold for the pressure correction scheme: the approximate density and internal energy are non-negative and a discrete kinetic energy balance equation can be established from the discrete momentum balance. We are also able to prove the existence of a solution of the scheme.
- Finally the weak (Lax-Wendroff type) consistency has been proved in Herbin et al. (2018) in one space dimension for the Euler equation.

Chapter 4

A second order explicit scheme for the large-eddy simulation of premixed turbulent flames

We address in this chapter a turbulent deflagration model with a flow governed by the compositional Navier-Stokes equations and the flame propagation represented by a virtually thickened flame formalism combined with a dynamical determination of the subgrid scale flame wrinkling factor to handle unresolved contributions. The numerical scheme works on staggered structured meshes with a time-marching algorithm solving first the chemical species mass balances and then the mass, momentum and energy balances. The approximate solutions respect the physical bounds and satisfy a conservative weakly-consistent discrete total energy balance equation in the inviscid case.

4.1 Introduction

We study in this chapter a numerical scheme for the computation of turbulent deflagrations occurring in a premixed atmosphere. In usual situations, such a physical phenomena is driven by the progress in the atmosphere of a shell-shaped thin zone, where the chemical reaction occurs and which thus separates the burnt area from fresh gases; this zone is called the flame brush. The onset of the chemical reaction is due to the temperature elevation, so the displacement of the flame brush is driven by the heat transfer inside and in the vicinity of this zone. Modelling of deflagrations still remains a challenge, since the flame brush has a very complex structure, due to thermo-convective instabilities or turbulence (Peters, 2000; Poinsot and Veynante, 2012). Whatever the modelling strategy, the problem thus needs a multiscale approach, since the local flame brush structure is out of reach of the computations aimed at simulating the flow dynamics at the observation scale, *i.e.* the whole reactive atmosphere scale. Here, the choice made is to artificially thicken the flame front in order to be resolved on the numerical mesh (Butler and O'Rourke, 1977). A subgrid scale flame wrinkling model is then introduced to handle unresolved contributions (Veynante and Moureau, 2015). This latest is computed dynamically allowing a better description of the flame front propagation, even at the beginning of the transient when the laminar flame gradually becomes turbulent. The model is also adjusted to deal with flame front interactions and flame-wall interactions which can lead to an overestimation of the subgrid model parameters and therefore a wrong description of the flame front propagation, or even give rise to stability problems (Mouriaux et al., 2016).

The numerical scheme, build in this chapter for the large eddy simulation of compressible reactive flows, is an extension to the reactive case of the numerical scheme described and tested in Chapter 3. The space discretization is staggered, and works on structured grids using the so-called Marker-And-Cell (MAC) scheme (Harlow and Amsden, 1971; Harlow and Welch, 1965): the scalar variables are approximated at the cell centers and the normal velocity at the face centers. Time-stepping is segregated, in the sense that balance equations are solved successively, and each step is explicit. The chemical species mass balances are first solved with the Strang algorithm decoupling convection and reaction. The associated reaction energy is introduced into the Navier-Stokes energy balance equation, solved in a second time with a time integration performed by the second order Heun scheme.

The positivity of the density is ensured by construction of the discrete mass balance equation, *i.e.* by the use of a second order MUSCL scheme. In addition, the physical bounds of the mass fractions are preserved thanks to the following (rather standard) arguments: first, building a discrete convection operator which vanishes when the convected unknown is constant thanks to the discrete mass balance equation ensures a positivity-preservation property (Larrouturou, 1991), under a CFL condition (as shown for a simpler problem in Appendix 4.A); second, the discretization of the chemical reaction rate ensures either that it vanishes when the unknown of the equation vanishes (for fuel and oxidizer mass fractions), or that it is non-negative (for products mass fractions). Moreover, with a suitable choice of the coefficients involved in the MUSCL discretization of the chemical species convection terms, the scheme preserves the fact that their sum is equal to 1. Thus, they are also bounded by 1. An algorithm for the computation of the "suitable" choice for these coefficients is given in Appendix 4.B in the 1D case.

The positivity of the sensible energy stems from the same essential argument used in the non-reactive case: the consistency of the discrete convection operator and the mass balance. This holds provided that the equation is exothermic ($\dot{\omega}_T \geq 0$). Moreover, we show in Section 4.5 that the solutions of the scheme satisfy a discrete total energy balance up to reminder terms. This balance may be made conservative by adding corrective terms to the sensible energy balance, for instance if one wants to compute shock solutions.

The chapter is structured as follows. We first recall the physical model in Section 4.2. The fully discrete setting is given in two steps, first describing the space discretization (Section 4.3) and then the scheme itself (Section 4.4). The conservativity of the scheme is shown in Section 4.5.

4.2 Physical model

First, the filtered equations for turbulent compressible reactive flows are described (Section 4.2.1), then the closure laws for the efficiency function (Section 4.2.2).

4.2.1 Governing equations

The computational domain is denoted by $\Omega \subset \mathbb{R}^d$, $1 \leq d \leq 3$. The problem is supposed to be posed over the time interval $[0, T]$.

Hydrodynamics - The hydrodynamics of the flow is governed by the filtered compressible Navier-Stokes equations, which read:

$$\partial_t(\overline{\rho}) + \operatorname{div}(\overline{\rho}\,\widetilde{\boldsymbol{v}}) = 0, \tag{4.1a}$$

$$\partial_t(\overline{\rho}\widetilde{\boldsymbol{v}}) + \operatorname{div}(\overline{\rho}\,\widetilde{\boldsymbol{v}} \otimes \widetilde{\boldsymbol{v}}) + \boldsymbol{\nabla}\overline{p} = \operatorname{div}(\check{\boldsymbol{\tau}}(\widetilde{\boldsymbol{v}})) + \overline{\rho}\,\overline{\boldsymbol{f}}, \tag{4.1b}$$

where $\boldsymbol{v}$, p, ρ and $\boldsymbol{f}$ stand for the velocity, the pressure, the density and a forcing term, respectively. The spatial filtering operation is indicated with the operator $\overline{\cdot}$, while $\widetilde{\cdot}$ denotes the mass-weighted (Favre) spatial filtering (see Chapters 1 or 3 for more details). The viscous stress tensor is composed by a computable and a subgrid scale (SGS) part $\check{\boldsymbol{\tau}} = \overline{\boldsymbol{\tau}} - \boldsymbol{\tau}^{SGS}$. The computable part $\overline{\boldsymbol{\tau}}$ is defined, for a Newtonian fluid, as:

$$\overline{\boldsymbol{\tau}}(\widetilde{\boldsymbol{v}}) = 2\overline{\mu}\left(\widetilde{\mathbf{S}} - \frac{1}{3}\operatorname{Tr}(\widetilde{\mathbf{S}})\,\boldsymbol{I}\right), \tag{4.2}$$

where $\overline{\mu}$ is the "computable" turbulent viscosity, $\boldsymbol{I}$ stands for the $\mathbb{R}^{d\times d}$ identity matrix and $\widetilde{\mathbf{S}}$ is the rate-of-strain tensor of the resolved structures defined as $\widetilde{\mathbf{S}} = 1/2\left(\nabla\widetilde{\boldsymbol{v}} + \nabla^t\widetilde{\boldsymbol{v}}\right)$. We assume that $\overline{\mu} \in L^\infty(\Omega)$ and that it exists $\mu' > 0$ such as $\mu \geq \mu'$ *a.e.*. Thus, the computable shear stress tensor satisfies:

$$\overline{\boldsymbol{\tau}}(\widetilde{\boldsymbol{v}}) : \boldsymbol{\nabla}\widetilde{\boldsymbol{v}} \geq 0, \quad \forall\widetilde{\boldsymbol{v}} \in \mathbb{R}^d. \tag{4.3}$$

The SGS turbulent shear stress $\boldsymbol{\tau}^{SGS}$ is modelled with the Boussinesq's approximation (Boussinesq, 1877):

$$\boldsymbol{\tau}^{SGS}(\widetilde{\boldsymbol{v}}) = \overline{\rho}\,(\widetilde{\boldsymbol{v}\otimes\boldsymbol{v}} - \widetilde{\boldsymbol{v}}\otimes\widetilde{\boldsymbol{v}}) \approx -2\mu_{SGS}\left(\widetilde{\mathbf{S}} - \frac{1}{3}\operatorname{Tr}(\widetilde{\mathbf{S}})\boldsymbol{I}\right). \tag{4.4}$$

where μ_{SGS} is the SGS turbulent viscosity. This latest is computed with the Smagorinsky subgrid scale viscosity model (Smagorinsky, 1963).

Species balance equations - The combustion modelling is based on the thickened flame model for large eddy simulation (TFLES) (see Section 2.4.5 for more details). The flame is artificially thickened by multiplying the diffusion coefficient and dividing the reaction rates by a thickening factor $\mathcal{F}$ (Butler and O'Rourke, 1977). The modified flame front of thickness $\mathcal{F}\,\delta_L^0$ propagates at the same laminar flame speed s_L as the original flame of thickness δ_L^0 . However, the Damköhler number is modified and the flame becomes less sensitive to turbulence (Colin et al., 2000). A wrinkling factor Ξ_Δ, Δ being the combustion filter size, is then introduced to counterbalance the reduction of flame surface induced by the thickening operation (Colin et al., 2000; Charlette et al., 2002a,b; Wang et al., 2011, 2012; Schmitt et al., 2015; Veynante and Moureau, 2015) (see Section 2.4.6 for some examples of wrinkling factor models).

For the sake of simplicity, only four chemical species are supposed to be present in the flow, namely the fuel (denoted by F), the oxydant (O), the product (P) of the reaction, and a neutral gas (N). A one-step irreversible total chemical reaction is considered, which is written:

$$\nu_F F + \nu_O O + \nu_N N \rightarrow \nu_P P + \nu_N N,$$

where ν_F, ν_O, ν_N and ν_P are the molar stoichiometric coefficients of the reaction. We denote by $\mathcal{I}$ the set of the subscripts used to refer to the chemical species in the flow, so $\mathcal{I} = \{F, O, N, P\}$ and the set of mass fractions of the chemical species in the flow reads $\{Y_k,\ k \in \mathcal{I}\}$

(*i.e.* $\{Y_F,\ Y_O,\ Y_N,\ Y_P\}$). The system of the mass balance equations for the chemical species reads:

$$\partial_t(\overline{\rho}\widetilde{Y_k}) + \operatorname{div}(\overline{\rho}\widetilde{Y_k}\widetilde{\boldsymbol{v}}) + \operatorname{div}(\breve{\boldsymbol{j}}_k) = \overline{\dot{\omega}_k}, \qquad \text{for } k \in \mathcal{I}. \tag{4.5}$$

The effective mass flux of the chemical species k, denoted by $\breve{\boldsymbol{j}}_k$, may be written as the sum of a "computable" part (first term at right hand side of (4.6)) and a subgrid scale part (second term at right hand side of (4.6)):

$$\breve{\boldsymbol{j}}_k = \mathcal{F}\,\overline{\boldsymbol{j}_k} + \boldsymbol{j}_k^{SGS}, \quad k \in \mathcal{I}. \tag{4.6}$$

with $\boldsymbol{j}_k^{SGS}$ modelled by:

$$\boldsymbol{j}_k^{SGS} = \overline{\rho}\,(\widetilde{\boldsymbol{v}\,Y_k} - \widetilde{\boldsymbol{v}}\,\widetilde{Y_k}) \approx (\Xi_\Delta - 1)\,\mathcal{F}\,\overline{\boldsymbol{j}_k}, \qquad \text{for } k \in \mathcal{I}. \tag{4.7}$$

Thanks to the Fick's law and assuming that the diffusion coefficients D_k of all chemical species k are equal to a same coefficient, denoted by D, the diffusive flux $\overline{\boldsymbol{j}_k}$ reads:

$$\text{for } k \in \mathcal{I}, \quad \overline{\boldsymbol{j}_k} = -\overline{\rho D \boldsymbol{\nabla} Y_k} \approx -\overline{\rho}\overline{D}\boldsymbol{\nabla}\widetilde{Y_k}. \tag{4.8}$$

Moreover, assuming that the Lewis number is constant and equal to one, then we have:

$$\text{for } k \in \mathcal{I}, \quad \overline{\boldsymbol{j}_k} = -\frac{\overline{\mu}}{\mathrm{Pr}}\,\boldsymbol{\nabla}\widetilde{Y_k}, \tag{4.9}$$

with Pr the laminar Prandtl number (see Section 1.1). The subgrid wrinkling factor Ξ_Δ is modelled using the Veynante and Moureau (2015) expression, described in Section 4.2.2.

The reaction rate of each chemical species may be written as:

$$\overline{\dot{\omega}_k} = \zeta_k \nu_k W_k\, \Xi_\Delta\, \frac{\overline{\dot{\omega}}}{\mathcal{F}}, \qquad \text{for } k \in \mathcal{I},$$

with $\zeta_F = \zeta_O = -1$, $\zeta_P = 1$, $\zeta_N = 0$, ν_k and W_k the stoichiometric coefficient and the molar mass of the species k respectively. The reaction progress rate $\overline{\dot{\omega}}$ is calculated with the Arrhenius law:

$$\overline{\dot{\omega}} = A\,\exp\left[-\frac{E_a}{R\widetilde{T}}\right]\Big(\frac{\overline{\rho}\,\widetilde{Y_F}}{W_F}\Big)\Big(\frac{\overline{\rho}\,\widetilde{Y_O}}{W_O}\Big)^{1/2} \tag{4.10}$$

where E_a stands for the activation energy, A for the pre-exponential factor, T stands for the temperature and $R = 8.31451\,\mathrm{JK}^{-1}\mathrm{mol}^{-1}$ for the perfect gases constant. Note that, since $\sum_{k\in\mathcal{I}} \nu_k\, W_k = 0$, we have $\sum_{k\in\mathcal{I}} \dot{\omega}_k = 0$. In addition, the sum of the unresolved transport fluxes of the chemical species is supposed to vanish everywhere in $\Omega \times (0, T)$: $\sum_{k\in\mathcal{I}} \breve{\boldsymbol{j}}_k = 0$. Thus, summing on $k \in \mathcal{I}$ the species mass balance allows to recover the equivalence between the mass balance and the fact that $\sum_{k\in\mathcal{I}} Y_k = 1$.

Energy balance - The considered energy balance equation is the so-called sensible energy balance equation, which reads:

$$\partial_t(\overline{\rho}\,\widetilde{e}) + \operatorname{div}(\overline{\rho}\,\widetilde{e}\,\widetilde{\boldsymbol{v}}) + \overline{p}\operatorname{div}(\widetilde{\boldsymbol{v}}) = \overline{\dot{\omega}_T} + \overline{\boldsymbol{\tau}}(\widetilde{\boldsymbol{v}}) : \boldsymbol{\nabla}\widetilde{\boldsymbol{v}} + \epsilon_v + \operatorname{div}(\breve{\boldsymbol{q}}) + \overline{\dot{Q}}, \tag{4.11}$$

with e the sensible energy defined as the sum of the sensible energies of the chemical species:

$$e = \sum_{k\in\mathcal{I}} e_k\, Y_k, \quad \text{with } e_k = c_{\mathrm{v},k}\, T,\ \text{for } k \in \mathcal{I}, \tag{4.12}$$

where $c_{\mathrm{v},k}$ stands for the heat capacity at constant volume for the species k (the reference temperature T_0 is supposed to be set at $0\,\mathrm{K}$ for the sake of simplicity, in the following). In the balance equation (4.11), $\dot{Q}$ denotes the heat source term (including a possible external production and the effects of radiative heat transfers), neglected for this chapter. The heat production rate due to the chemical reaction, $\overline{\dot{\omega}_T}$, is given by:

$$\overline{\dot{\omega}_T} = -\sum_{k \in \mathcal{I}} \Delta h^0_{f,k}\, \overline{\dot{\omega}_k}, \tag{4.13}$$

where $\Delta h^0_{f,k}$ stands for the formation enthalpy of the k^{th} chemical species.

The effective heat flux $\breve{\boldsymbol{q}}$ is decomposed into a computable (convective) part $\overline{\boldsymbol{q}}$ and a SGS (diffusive) part $\boldsymbol{q}^{SGS}$:

$$\breve{\boldsymbol{q}} = \mathcal{F}\, \overline{\boldsymbol{q}} + \boldsymbol{q}^{SGS}. \tag{4.14}$$

The SGS heat flux is modelled by:

$$\boldsymbol{q}^{SGS} = \overline{\rho}\,(\widetilde{\boldsymbol{v} e} - \widetilde{\boldsymbol{v}}\widetilde{e}) \approx (\Xi_\Delta - 1)\, \mathcal{F}\, \overline{\boldsymbol{q}}, \tag{4.15}$$

and the computable heat flux is given by:

$$\overline{\boldsymbol{q}} = -\overline{\lambda}\, \boldsymbol{\nabla}\widetilde{T} + \sum_{k \in \mathcal{I}} \widetilde{h}_k\, \overline{\boldsymbol{j}}_k.$$

The sensible enthalpy of the species k, h_k, is given by $h_k = c_{\mathrm{p},k}\, T$, $c_{\mathrm{p},k}$ being the heat capacity at constant pressure for the species k. The thermal conductivity may be expressed by $\overline{\lambda} = \overline{\mu} c_{\mathrm{p}}/\mathrm{Pr}$, with $c_{\mathrm{p}} = \sum_{k \in \mathcal{I}} c_{\mathrm{p},k}\, Y_k$ the heat capacity at constant pressure of the mixture. The unitary Lewis number assumption allow to rewrite the heat diffusion flux in the following way (see Section 1.1):

$$\overline{\boldsymbol{q}} = -\frac{\overline{\mu}}{\mathrm{Pr}} \boldsymbol{\nabla}\widetilde{h},$$

with $h = \sum_{k \in \mathcal{I}} h_k\, Y_k$ the sensible enthalpy of the mixture.

The SGS viscous dissipation term ϵ_v is modelled in order to recover a conservative form of the total energy balance. First, let us obtain the filtered kinetic energy balance equation by the inner product of the filtered momentum balance equation with the filtered velocity:

$$\frac{1}{2}\, \partial_t(\overline{\rho}\, |\widetilde{\boldsymbol{v}}|^2) + \frac{1}{2}\, \mathrm{div}\left(\overline{\rho}\, |\widetilde{\boldsymbol{v}}|^2\, \widetilde{\boldsymbol{v}}\right) + \boldsymbol{\nabla}\overline{p} \cdot \widetilde{\boldsymbol{v}} - \mathrm{div}(\overline{\boldsymbol{\tau}}(\widetilde{\boldsymbol{v}})) \cdot \widetilde{\boldsymbol{v}} = -\mathrm{div}(\boldsymbol{\tau}^{SGS}(\widetilde{\boldsymbol{v}})) \cdot \widetilde{\boldsymbol{v}} \tag{4.16}$$

Summing equations (4.11) and (4.16) gives rise to the filtered total energy balance equation:

$$\begin{aligned} \partial_t(\overline{\rho}\, \widetilde{E}) + \mathrm{div}(\overline{\rho}\, \widetilde{\boldsymbol{v}}\, \widetilde{E}) + \mathrm{div}(\overline{p}\, \widetilde{\boldsymbol{v}}) - \mathrm{div}\left(\overline{\boldsymbol{\tau}}(\widetilde{\boldsymbol{v}}) \cdot \widetilde{\boldsymbol{v}}\right) - \overline{\dot{\omega}_T} \\ = -\mathrm{div}(\breve{\boldsymbol{q}}) - \mathrm{div}\left(\boldsymbol{\tau}^{SGS}(\widetilde{\boldsymbol{v}}) \cdot \widetilde{\boldsymbol{v}}\right) + \boldsymbol{\tau}^{SGS}(\widetilde{\boldsymbol{v}}) : \boldsymbol{\nabla}\widetilde{\boldsymbol{v}} + \epsilon_v. \end{aligned} \tag{4.17}$$

In order to obtain a conservative form of the previous equation, the SGS viscous dissipation is modelled by:

$$\epsilon_v = -\boldsymbol{\tau}^{SGS}(\widetilde{\boldsymbol{v}}) : \boldsymbol{\nabla}\widetilde{\boldsymbol{v}}. \tag{4.18}$$

Therefore the filtered internal energy balance equation reads:

$$\partial_t(\overline{\rho}\, \widetilde{e}) + \mathrm{div}(\overline{\rho}\, \widetilde{\boldsymbol{v}}\, \widetilde{e}) + \overline{p}\, \mathrm{div}(\widetilde{\boldsymbol{v}}) = \overline{\dot{\omega}_T} - \mathrm{div}(\breve{\boldsymbol{q}}) + \breve{\boldsymbol{\tau}}(\widetilde{\boldsymbol{v}}) : \boldsymbol{\nabla}\widetilde{\boldsymbol{v}}. \tag{4.19}$$

Equation of state - Finally, the atmosphere is supposed to be a mixture of perfect gases, which yields the following equation of state:

$$\overline{p} = \varrho(\widetilde{e}, \overline{\rho}, \widetilde{Y}_k) = \overline{\rho}\, R\, \frac{\widetilde{T}}{\overline{\overline{W}}}, \qquad \widetilde{T} = \frac{\widetilde{e}}{\overline{\overline{c_{\rm v}}}}. \tag{4.20}$$

with $W = \sum_{k\in\mathcal{I}} Y_k/W_k$ the mixture molar mass and $c_{\rm v} = \sum_{k\in\mathcal{I}} c_{{\rm v},k}\, Y_k$ the heat capacity at constant volume of the mixture.

Initial and boundary conditions - The system composed by equations (4.1a), (4.1b), (4.5), (4.19) and (4.20) must be supplemented by suitable initial conditions. for $\overline{\rho}$, $\widetilde{e}$, $\widetilde{\boldsymbol{v}}$, $\widetilde{Y}_k$, $k \in \mathcal{I}$ such that:

$$\begin{aligned}
&\overline{\rho}(x,0) = \overline{\rho}_0(x),\ \widetilde{e}(x,0) = \widetilde{e}_0(x),\ \widetilde{\boldsymbol{v}}(x,0) = \widetilde{\boldsymbol{v}}_0(x),\ \text{ with } \overline{\rho}_0 > 0, \widetilde{e}_0 > 0,\\
&\text{for } k \in \mathcal{I}, \quad \widetilde{Y}_k(x,0) = \widetilde{Y}_{k,0}(x),\ \text{ with } \widetilde{Y}_{k,0} \in [0,1] \text{ and } \sum_{k\in\mathcal{I}} \widetilde{Y}_{k,0} = 1 \text{ a.e. in } \Omega.
\end{aligned} \tag{4.21}$$

The boundary of the computational domain is split in an inflow part $\partial\Omega_I$ (where the flow enters the domain, *i.e.* $\boldsymbol{v} \cdot \mathbf{n} < 0$ with $\mathbf{n}$ the outward normal vector to the boundary) and an outflow part $\partial\Omega_O$ (where the flow leaves the domain, *i.e.* $\boldsymbol{v} \cdot \mathbf{n} \geq 0$) of positive $(d-1)$ measure, with $\partial\Omega = \partial\Omega_I \cup \partial\Omega_O$.

The velocity is prescribed over $\partial\Omega_I$ and the inflow density, denoted ρ_I is deduced from the inflow temperature and composition of the flow. A Neumann boundary condition holds over $\partial\Omega_O$:

$$(\breve{\boldsymbol{\tau}} - \overline{p}\, \boldsymbol{I}) \cdot \mathbf{n} = \overline{\boldsymbol{g}},$$

where $\boldsymbol{g}$ is a known surface force field. At the inflow boundary, the total flux (*i.e.* the sum of the convection and of the diffusion fluxes) is prescribed and, at the outflow boundary, the diffusion flux is supposed to vanish, for $k \in \mathcal{I}$:

$$\text{on } \partial\Omega_I, \qquad (\overline{\rho}\widetilde{Y_k}\widetilde{\boldsymbol{v}} + \breve{\boldsymbol{j}}_k) \cdot \mathbf{n} = (\widetilde{Y_k})_I\, \widetilde{\boldsymbol{v}} \cdot \mathbf{n}, \tag{4.22}$$

$$\text{on } \partial\Omega_O, \qquad \breve{\boldsymbol{j}}_k \cdot \mathbf{n} = 0. \tag{4.23}$$

Analogous boundary conditions are applied to the sensible energy:

$$\text{on } \partial\Omega_I, \qquad (\overline{\rho}\widetilde{e}\widetilde{\boldsymbol{v}} + \breve{\boldsymbol{q}}) \cdot \mathbf{n} = (\widetilde{e})_I\, \widetilde{\boldsymbol{v}} \cdot \mathbf{n}, \tag{4.24}$$

$$\text{on } \partial\Omega_O, \qquad \breve{\boldsymbol{q}} \cdot \mathbf{n} = 0. \tag{4.25}$$

4.2.2 Closure law for the subgrid wrinkling factor

Various models have been developed for the wrinkling factor (see Section 2.4.6 for a brief literature). In the present work, the wrinkling factor is modeled using the Veynante and Moureau (2015) expression:

$$\Xi_\Delta = \left(\frac{\Delta}{\delta_c}\right)^{\beta} \tag{4.26}$$

where δ_c is the inner cutoff scale (*i.e.* the lowest wrinkling scale) usually proportional to the laminar flame thickness (Volpiani, 2017). The model parameter β is dynamically determined

(Schmitt et al., 2015; Veynante and Moureau, 2015) equating flame surfaces computed at filtered and test-filtered scales (Germano-like identity, Germano et al. (1991)):

$$\langle\ \widehat{\Xi_\Delta |\nabla \tilde{c}|}\ \rangle = \langle\ \Xi_{\gamma\Delta} |\nabla\ \widehat{\tilde{c}}\ |\ \rangle, \tag{4.27}$$

with c the progress variable, increasing from 0 in fresh to 1 in burnt gases and computed here from the fuel mass fraction:

$$c = \frac{Y_F - Y_F^u}{Y_F^b - Y_F^u} \tag{4.28}$$

where u and b denote quantities in the fresh (u) and in the burnt gas (b). The $\widehat{\ }$ symbol denotes the test-filtering operator and $\langle . \rangle$ denotes the averaging operator over the entire domain. The effective filter scale is given by $\hat{\Delta} = \gamma\Delta$ with:

$$\gamma = \sqrt{1 + \left(\widehat{\Delta}\ / \Delta \right)^2}, \tag{4.29}$$

when combining two Gaussian filters of width $\widehat{\Delta}$ and Δ (Moureau et al., 2011). The averaging operation is replaced by another Gaussian filter of width Δ_{avg} because it is easier to implement in case of unstructured grids and parallel solver utilisation. The model parameter β is given by combining equations (4.26) and (4.27) and assuming that β is equal at scales Δ and $\hat{\Delta}$ and constant over the averaging domain. Nonphysical wrinkling factors values may appear when the flame front interacts with walls (*i.e.* at a distance $d < \hat{\Delta}$) or when more than one flame front interact at scale lower than $\hat{\Delta}$ due to a pathological behavior of $|\nabla \tilde{c}|$, thus the subgrid model is slightly modified from its original version (we refer to Chapter 1 Section 2.4.6 and to Mouriaux et al. (2016) for more details). The wrinkling factor exponent β is then given by:

$$\beta = \frac{\log\left(\Sigma_1 / \Sigma_2\right)}{\log\left(\gamma\right)}. \tag{4.30}$$

where:

$$\begin{aligned} \Sigma_1 &= \langle\ \widehat{|\nabla \tilde{c}|}\ \rangle && (4.31) \\ \Sigma_2 &= (1 - \hat{\zeta}) |\ \widehat{\nabla \tilde{c}}\ | + \hat{\zeta}\ \widehat{|\nabla \tilde{c}|\, \boldsymbol{n} \cdot \boldsymbol{N}}\ . && (4.32) \end{aligned}$$

The sensor denoted by ζ allows to detect flame front interactions and is defined as:

$$\zeta = \left| \begin{array}{ll} 1 & \text{if } \boldsymbol{n} \cdot \boldsymbol{N} < 1 - \varepsilon \\ 0 & \text{elsewhere} \end{array} \right. \tag{4.33}$$

where $\boldsymbol{n} = -\nabla \tilde{c} / |\nabla \tilde{c}|$ and $\boldsymbol{N} = -\nabla\ \widehat{\tilde{c}}\ / |\nabla\ \widehat{\tilde{c}}\ |$ and the parameter ε is set in this work to 0.1.

4.3 Meshes and unknowns

For the resolution of the model equations, the reduced variable z, called mixture mass fraction, is introduced:

$$z = \frac{s\, Y_F + (1 - Y_O)}{s + 1}, \tag{4.34}$$

$s = (\nu_O W_O)/(\nu_F W_F)$ being the mass stoichiometric ratio. Note that, combining the fuel and the oxidizer mass balance equations, the variable z satisfies an homogeneous equation; for this reason, we replace the oxidizer mass balance equation by the balance equation for z (since, given the values of z and Y_F , we may deduce Y_O). For perfectly premixed mixtures (such the ones studied during this thesis), the mixture fraction is constant, thus, only the mass balance equation for the fuel is solved as Y_O computation is straight forward.

The space discretization is performed by a finite volume technique, using a staggered arrangement of the unknowns (the scalar variables are approximated at the cell centers and the velocity components at the face centers), using the MAC scheme (Harlow and Amsden, 1971; Harlow and Welch, 1965).

The notations already introduced in Chapter 3, Section 3.3, are used here. Let us simply clarify here that the degrees of freedom for the new (comparing to the previous chapter) unknowns, *i.e.* the mixture, the fuel and the neutral gas mass fractions, are associated to the cells of the mesh $\mathcal{M}$ so the set of the scalar variables unknowns reads:

$$\{p_K, \rho_K, e_K, Y_{F,K}, Y_{N,K}, z_K,\ K \in \mathcal{M}\}\,.$$

The set of faces included in the boundary of Ω, $\mathcal{E}_{ext}$ is split in two disjoint subsets, $\mathcal{E}_{ext} = \mathcal{E}_{ext,I} \cup \mathcal{E}_{ext,O}$, where $\mathcal{E}_{ext,I}$ (respectively $\mathcal{E}_{ext,O}$) stands for the set of boundary faces included in $\partial\Omega_I$ (respectively $\partial\Omega_O$). The rest of the space discretization is the same as the one presented in Chapter 3, Section 3.3.

4.4 The numerical scheme

4.4.1 The overall algorithm

Let us consider a partition $0 = t_0 < t_1 < \cdots < t_N = T$ of the time interval $(0, T)$, which we suppose uniform, and let $\delta t = t_{n+1} - t_n$ for $n = 0, 1, \cdots, N-1$ be the (constant) time step. The time-marching algorithm is of segregated type, and consists in solving the three following steps:

- **Chemistry step -** Solution of the mass balance equations for the chemical species.
- **Hydrodynamics step -** Solution of the mass, momentum and energy balance for the mixture. At the end of of this step, the species mass fractions, the temperature and the pressure are known, and the density is updated using the equation of state.
- **Turbulence step -** Computation of the turbulent viscosity and of the subgrid wrinkling factor and evaluation of the effective diffusion coefficients.

The discretization of the chemistry step is given in Section 4.4.2. The algorithm for the solution of the Navier-Stokes equations has been already introduced in Chapter 3. The differences between the non reactive and reactive set of equations stand in the heat production rate and in the heat diffusion term, appearing in the sensible energy balance equation. The algorithm is recalled in Section 4.4.3 together with the discretization of these latest terms. Finally, the discretization of the subgrid models is described in Section 4.4.4.

4.4.2 The chemistry step

Let first introduce the density at "time step $n-1/2$", $\rho_K^{n-1/2}$, given by a linear combination of the density at time n and $n-1$:

$$\rho_K^{n-1/2} = \frac{1}{2}(\rho_K^n + \rho_K^{n-1}), \quad \forall K \in \mathcal{M}. \tag{4.35}$$

Thanks to the mass balance at time n, $\rho_K^{n-1/2}$ satisfies the two following relations:

$$\begin{aligned} \frac{\rho_K^{n-1/2} - \rho_K^{n-1}}{\delta t/2} + \mathrm{div}_K(\rho^n \boldsymbol{v}^n) &= 0, \quad \forall K \in \mathcal{M}, && (4.36) \\ \frac{\rho_K^n - \rho_K^{n-1/2}}{\delta t/2} + \mathrm{div}_K(\rho^n \boldsymbol{v}^n) &= 0, \quad \forall K \in \mathcal{M}. && (4.37) \end{aligned}$$

The numerical scheme for the solution of the system of chemical species mass balances is based on the Strang operator splitting method consisting in performing one half-step of homogeneous transport of Y_k, then dealing with the reaction terms and finishing by the second half-step of transport of Y_k. Relations (4.36) and (4.37) can be seen respectively as the mass balances for the first and the last step of this algorithm. The positivity of the chemical species is then ensured, under a CFL condition, thanks to the chemical species convection operator discretization and to relations (4.36) and (4.37) (Larrouturou, 1991) (see Appendix 4.A and Lemma 4.5.1 below).

The chemistry step numerical scheme reads, for $0 \leq n \leq N-1$:

1 - **Transport step I**

Mixture mass fraction computation – Solve for $\tilde{z}^{n+1/2}$, $\forall K \in \mathcal{M}$:

$$\frac{\rho_K^{n-1/2}\, \tilde{z}_K^{n+1/2} - \rho_K^{n-1}\, z_K^n}{\delta t/2} + \mathrm{div}_K(\rho^n\, z^n\, \boldsymbol{v}^n) - \mathrm{div}_K\left(\mathcal{F}\, \Xi_\Delta^n\, \frac{\mu}{\mathrm{Pr}}\, \boldsymbol{\nabla} z^n\right) = 0. \tag{4.38a}$$

Neutral gas mass fraction computation – Solve for $\tilde{Y}_N^{n+1/2}$, $\forall K \in \mathcal{M}$:

$$\frac{\rho_K^{n-1/2}\, \tilde{Y}_{N,K}^{n+1/2} - \rho_K^{n-1}\, Y_{N,K}^n}{\delta t/2} + \mathrm{div}_K(\rho^n\, Y_N^n\, \boldsymbol{v}^n) - \mathrm{div}_K\left(\mathcal{F}\, \Xi_\Delta^n\, \frac{\mu}{\mathrm{Pr}}\, \boldsymbol{\nabla} Y_N^n\right) = 0. \tag{4.38b}$$

Fuel mass fraction computation – Solve for $\tilde{Y}_F^{n+1/2}$, $\forall K \in \mathcal{M}$:

$$\frac{\rho_K^{n-1/2}\, \tilde{Y}_{F,K}^{n+1/2} - \rho_K^{n-1}\, Y_{F,K}^n}{\delta t/2} + \mathrm{div}_K(\rho^n\, Y_F^n\, \boldsymbol{v}^n) - \mathrm{div}_K\left(\mathcal{F}\, \Xi_\Delta^n\, \frac{\mu}{\mathrm{Pr}}\, \boldsymbol{\nabla} Y_F^n\right) = 0. \tag{4.38c}$$

Product mass fraction computation – Solve for $\tilde{Y}_P^{n+1/2}$, $\forall K \in \mathcal{M}$:

$$\tilde{Y}_{F,K}^{n+1/2} + \tilde{Y}_{O,K}^{n+1/2} + \tilde{Y}_{N,K}^{n+1/2} + \tilde{Y}_{P,K}^{n+1/2} = 1. \tag{4.38d}$$

2 - **Reactive step**

Mixture mass fraction computation – Solve for $z^{n+1/2}$, $\forall K \in \mathcal{M}$:

$$\frac{\rho_K^{n-1/2}\left[z_K^{n+1/2} - \tilde{z}_K^{n+1/2}\right]}{\delta t} = 0. \tag{4.39a}$$

Neutral gas mass fraction computation – Solve for $Y_N^{n+1/2}$, $\forall K \in \mathcal{M}$:

$$\frac{\rho_K^{n-1/2}\left[Y_{N,K}^{n+1/2} - \tilde{Y}_{N,K}^{n+1/2}\right]}{\delta t} = 0. \tag{4.39b}$$

Fuel mass fraction computation – Solve for $Y_F^{n+1/2}$, $\forall K \in \mathcal{M}$:

$$\frac{\rho_K^{n-1/2}\left[Y_{F,K}^{n+1/2} - \tilde{Y}_{F,K}^{n+1/2}\right]}{\delta t} = (\dot{\omega}_F)_K^{n+1/2}. \tag{4.39c}$$

Product mass fraction computation – Solve for $Y_P^{n+1/2}$, $\forall K \in \mathcal{M}$:

$$Y_{F,K}^{n+1/2} + Y_{O,K}^{n+1/2} + Y_{N,K}^{n+1/2} + Y_{P,K}^{n+1/2} = 1. \tag{4.39d}$$

3 - **Transport step II**

Mixture mass fraction computation – Solve for z^{n+1}, $\forall K \in \mathcal{M}$:

$$\frac{\rho_K^n\, z_K^{n+1} - \rho_K^{n-1/2}\, z_K^{n+1/2}}{\delta t/2} + \mathrm{div}_K(\rho^n\, z^{n+1/2}\, \boldsymbol{v}^n) - \mathrm{div}_K\left(\mathcal{F}\, \Xi_\Delta^n\, \frac{\mu}{\mathrm{Pr}}\, \boldsymbol{\nabla} z^{n+1/2}\right) = 0. \tag{4.40a}$$

Neutral gas mass fraction computation – Solve for Y_N^{n+1}, $\forall K \in \mathcal{M}$:

$$\frac{\rho_K^n Y_{N,K}^{n+1} - \rho_K^{n-1/2} Y_{N,K}^{n+1/2}}{\delta t/2} + \mathrm{div}_K(\rho^n Y_N^{n+1/2}\, \boldsymbol{v}^n) - \mathrm{div}_K\left(\mathcal{F}\Xi_\Delta^n \frac{\mu}{\mathrm{Pr}} \boldsymbol{\nabla} Y_N^{n+1/2}\right) = 0. \tag{4.40b}$$

Fuel mass fraction computation – Solve for Y_F^{n+1}, $\forall K \in \mathcal{M}$:

$$\frac{\rho_K^n Y_{F,K}^{n+1} - \rho_K^{n-1/2} Y_{F,K}^{n+1/2}}{\delta t/2} + \mathrm{div}_K(\rho^n Y_F^{n+1/2} \boldsymbol{v}^n) - \mathrm{div}_K\left(\mathcal{F}\Xi_\Delta^n \frac{\mu}{\mathrm{Pr}} \boldsymbol{\nabla} Y_F^{n+1/2}\right) = 0. \tag{4.40c}$$

Product mass fraction computation – Solve for Y_P^{n+1}, $\forall K \in \mathcal{M}$:

$$Y_{F,K}^{n+1} + Y_{O,K}^{n+1} + Y_{N,K}^{n+1} + Y_{P,K}^{n+1} = 1. \tag{4.40d}$$

The initial value of the chemical variables is the mean value of the initial conditions over the primal cells:

$$\forall K \in \mathcal{M}, \quad z_K^0 = \frac{1}{|K|} \int_K z_0(\boldsymbol{x})\, \mathrm{d}\boldsymbol{x}, \quad Y_{k,K}^0 = \frac{1}{|K|} \int_K Y_{k,0}(\boldsymbol{x})\, \mathrm{d}\boldsymbol{x}, \text{ with } k = N, F,$$

where the reduced variable z is the linear combination of Y_F and Y_O given by Equation (4.34).

Equations (4.38a)-(4.40d) are solved successively. Let consider the first step of the Strang algorithm. It is important to remark that Equations (4.38a)-(4.38d) are equivalent to the following system:

$$\frac{\rho_K^{n-1/2}\, \tilde{Y}_{k,K}^{n+1/2} - \rho_K^{n-1}\, Y_{k,K}^n}{\delta t/2} + \mathrm{div}_K(\rho^n\, Y_k^n\, \boldsymbol{v}^n) - \mathrm{div}_K\left(\mathcal{F}\, \Xi_\Delta^n\, \frac{\mu}{\mathrm{Pr}}\, \boldsymbol{\nabla} Y_k^n\right) = 0, \quad k \in \mathcal{I}. \tag{4.41}$$

Indeed, a suitable combination of (4.38c) and (4.38a) yields the desired mass balance equation for the oxydant chemical species for the first step of the Strang algorithm. Finally, we suppose that the product mass balance holds:

$$\frac{\rho_K^{n-1/2}\,\tilde{Y}_{P,K}^{n+1/2} - \rho_K^{n-1}\,Y_{P,K}^{n}}{\delta t/2} + \mathrm{div}_K(\rho^n\,Y_P^n\,\boldsymbol{v}^n) - \mathrm{div}_K\left(\mathcal{F}\,\Xi_\Delta^n\,\frac{\mu}{\mathrm{Pr}}\,\boldsymbol{\nabla} Y_P^n\right) = 0. \tag{4.42}$$

Summing all the chemical species mass balances, we have for $\Sigma = Y_F + Y_O + Y_N + Y_P$:

$$\frac{\rho_K^{n-1/2}\,\tilde{\Sigma}_K^{n+1/2} - \rho_K^{n-1}\,\Sigma_K^{n}}{\delta t/2} + \mathrm{div}_K(\rho^n\,\Sigma^n\,\boldsymbol{v}^n) - \mathrm{div}_K\left(\mathcal{F}\,\Xi_\Delta^n\,\frac{\mu}{\mathrm{Pr}}\,\boldsymbol{\nabla}\Sigma^n\right) = 0. \tag{4.43}$$

and this equation may equivalently replace the product equation (4.42). Indeed, thanks to the half the mass balance, we see that, provided that Σ^n satisfies $\Sigma^n = 1$ everywhere in Ω, the solution to Equation (4.43) is $\tilde{\Sigma}^{n+1/2} = 1$ everywhere in Ω. Analogously, (4.39a)-(4.39d) are equivalent to:

$$\frac{\rho_K^{n-1/2}\left[Y_{k,K}^{n+1/2} - \tilde{Y}_{k,K}^{n+1/2}\right]}{\delta t} = \zeta_k \nu_k W_k\,\dot{\omega}_K^{n+1/2}, \quad k \in \mathcal{I}, \tag{4.44}$$

where we recall that $\zeta_F = \zeta_O = -1$, $\zeta_P = 1$ and $\zeta_N = 0$. Using the same procedure than for the first step, the second step of the products mass balance (*i.e.* Equation (4.44) with $k = P$) may equivalently be replaced by an homogeneous balance equation for $\Sigma^{n+1/2}$, since the sum of the chemical reaction terms vanishes. Finally, considering the third step of the Strang algorithm, (4.40a)-(4.40d) are equivalent to the following system, $k \in \mathcal{I}$:

$$\frac{\rho_K^{n} Y_{k,K}^{n+1} - \rho_K^{n-1/2} Y_{k,K}^{n+1/2}}{\delta t/2} + \mathrm{div}_K(\rho^n Y_k^{n+1/2}\boldsymbol{v}^n) - \mathrm{div}_K\left(\mathcal{F}\Xi_\Delta^n\,\frac{\mu}{\mathrm{Pr}}\boldsymbol{\nabla} Y_k^{n+1/2}\right) = 0. \tag{4.45}$$

The same procedure shows that the product mass fraction $Y_{P,K}^{n+1}$ can be directly calculated from the expression (4.40d) since, as it will be shown later at discrete level (cf. Lemma 4.5.2), the sum of the mass fractions is equal to 1 everywhere in Ω.

Finally, note that, when the chemical step is performed, the mass balance at step $n+1$ is not yet solved; hence the (unusual) backward time shift for the densities and for the mass fluxes in the equations of the chemistry scheme.

> **Remark** (A more compact formulation of the time-marching scheme)**.** The chemistry step may be written under the following equivalent form:
>
> $$\begin{aligned} \rho_K^{n-1/2}\,Y_{k,K}^{n+1/2} = {} & \rho_K^{n-1}\,Y_{k,K}^{n} - \frac{\delta t}{2}\mathrm{div}_K(\rho^n\,Y_k^n\,\boldsymbol{v}^n) + \frac{\delta t}{2}\mathrm{div}_K\left(\mathcal{F}\,\Xi_\Delta^n\,\frac{\mu}{\mathrm{Pr}}\,\boldsymbol{\nabla} Y_k^n\right) \\ & + \delta t\,\zeta_k \nu_k W_k\,\dot{\omega}_K^{n+1/2}, \quad k \in \mathcal{I}, \end{aligned} \tag{4.46}$$
>
> $$\begin{aligned} \rho_K^{n} Y_{k,K}^{n+1} = {} & \rho_K^{n-1} Y_{k,K}^{n} - \frac{\delta t}{2}\left[\mathrm{div}_K(\rho^n\,Y_k^n\,\boldsymbol{v}^n) + \mathrm{div}_K(\rho^n Y_k^{n+1/2}\boldsymbol{v}^n)\right] \\ & + \frac{\delta t}{2}\left[\mathrm{div}_K\left(\mathcal{F}\,\Xi_\Delta^n\,\frac{\mu}{\mathrm{Pr}}\,\boldsymbol{\nabla} Y_k^n\right) + \mathrm{div}_K\left(\mathcal{F}\Xi_\Delta^n\,\frac{\mu}{\mathrm{Pr}}\boldsymbol{\nabla} Y_k^{n+1/2}\right)\right] \\ & + \delta t\,\zeta_k \nu_k W_k\,\dot{\omega}_K^{n+1/2}, \quad k \in \mathcal{I}. \end{aligned} \tag{4.47}$$

> The first step (4.46) is simply obtained by introducing (4.44) in (4.41). Let notice that the scheme obtained in not of second order in time. In order to reach this accuracy, a second order in time discretization (for example the Heun scheme for explicit steps) must be introduced at each step of the algorithm.

We now define each of the discrete operators featured in System (4.38)-(4.40).

The discretization of the convection terms is performed by a discrete operator of the form:

$$|K| \operatorname{div}_K(\rho\, x\, \boldsymbol{v}) = \sum_{\sigma\in\mathcal{E}(K)} J_{K,\sigma}\, x_\sigma \tag{4.48}$$

where x stands respectively for z or Y_k, $k = N, F$, according to the discretized equation. With $J_{K,\sigma}$, we denote the mass flux across σ outward K updated at the end of the hydrodynamics step at time n, given by (4.56). The evaluation of the value at the face $\sigma = K|L$, x_σ, is performed by a second order MUSCL-like interpolation (Piar et al., 2013). The algebraic condition required for this reconstruction is that $\forall K \in \mathcal{M}$ and $\forall \sigma \in \mathcal{E}(K) \cap \mathcal{E}_{\rm int}$, there exists $\beta^x_{K,\sigma} \in [0,1]$ and $M^x_{K,\sigma} \in \mathcal{M}$ such that:

$$x_\sigma - x_K = \left| \begin{array}{ll} \beta^x_{K,\sigma}(x_K - x_{M^x_{K,\sigma}}) & \text{if } J_{K,\sigma} \geq 0, \\ \beta^x_{K,\sigma}(x_{M^x_{K,\sigma}} - x_K) & \text{otherwise.} \end{array} \right. \tag{4.49}$$

For faces of $\mathcal{E}_{ext,I}$, we suppose that x_σ is given by the boundary conditions, which we denote by $x_\sigma = x_{I,\sigma}$. For faces of $\mathcal{E}_{ext,O}$, the upwind choice is made for x_σ, *i.e.* $x_\sigma = x_K$.

The definition of the convection fluxes respects "by construction" the physical bounds satisfied by the chemical species in the continuous case (under suitable conditions for $\beta^x_{K,\sigma}$, see Section 4.5).

For the discretization of the diffusive terms, the usual two-points approximation for the flux at the face is used (Eymard et al., 2000), so we get, for a generic scalar variable x:

$$\operatorname{div}_K\left(\mathcal{F}\,\Xi_\Delta \frac{\mu}{\rm Pr}\boldsymbol{\nabla} x\right) = -\mathcal{F}\frac{\mu}{\rm Pr} \sum_{\sigma=K|L,\sigma\in\mathcal{E}(K)} \frac{|\sigma|}{d_\sigma}\,(\Xi_\Delta)_\sigma\,(x_K - x_L), \tag{4.50}$$

with, for $\sigma = K|L$, $(\Xi_\Delta)_\sigma$, the harmonic value of the subgrid wrinkling factor approximation on K and L, weighted by the distances $|\boldsymbol{x}_K - \boldsymbol{x}_\sigma|$ and $|\boldsymbol{x}_K - \boldsymbol{x}_\sigma|$ respectively ($\boldsymbol{x}_K$, $\boldsymbol{x}_L$ and $\boldsymbol{x}_\sigma$ being the mass centers of K, L and σ, respectively). Note that the definition is restricted to the internal faces of K since, by assumption, the diffusion fluxes vanish at the boundaries (more precisely speaking, they are supposed to vanish at the outlet boundary and the total flux is written as a convection flux at the inlet boundary, so already taken into account in the definition above).

In the reactive step, Equation (4.39c), the reaction term $(\dot\omega_F)_K$ is approximated as follows:

$$\begin{aligned} (\dot\omega_F)^{n+1/2}_K &= \nu_F\, W_F\, \dot\omega^{n+1/2}_K \\ &= \nu_F\, W_F\, \frac{(\Xi^{n+1}_\Delta)_K}{\mathcal{F}}\, A\, \exp\left(\frac{-E_a}{R\,T^n_K}\right) \left[\frac{\rho^{n-1/2}_K\, Y^{n+1/2}_{F,K}}{W_F}\right] \left[\frac{\rho^{n-1/2}_K\, Y^{n+1/2}_{O,K}}{W_O}\right]^{1/2} \end{aligned} \tag{4.51}$$

The oxidant mass fraction, $Y_{O,K}^{n+1/2}$ may be expressed thanks to (4.34) as a function of $Y_{F,K}^{n+1/2}$ and $z_K^{n+1/2}$; since the mixture fraction $z^{n+1/2}$ is known at this step, Equation (4.39c) indeed may be solved for $Y_F^{n+1/2}$. The reaction term being nonlinear, a Newton algorithm is used in order to perform this reactive step.

4.4.3 The hydrodynamics step

The time integration is performed by the second order Heun scheme (which falls in the class of Runge-Kutta schemes) which is written under the following compact formulation:

$$\boldsymbol{W}^{(1)} = \boldsymbol{W}^n - \delta t\ \mathcal{F}(\boldsymbol{W}^n), \tag{4.52}$$

$$\boldsymbol{W}^{n+1} = \boldsymbol{W}^n - \frac{\delta t}{2}\ \big[\mathcal{F}(\boldsymbol{W}^n) + \mathcal{F}(\boldsymbol{W}^{(1)})\big], \tag{4.53}$$

where $\boldsymbol{W}$ stands for the vector of conservative variables and $\mathcal{F}$ is a function which gathers the divergence of the fluxes complemented, in the sensible energy balance, with the reactive and non-conservative terms. In the time semi-discrete stetting, $\boldsymbol{W} = (\rho, \rho\boldsymbol{v}, \rho e)^t$ and

$$\mathcal{F}(\boldsymbol{W}) = \begin{pmatrix} \mathrm{div}(\rho\boldsymbol{v}) \\ \mathrm{div}(\rho\boldsymbol{v}\otimes\boldsymbol{v}) + \boldsymbol{\nabla} p - \mathrm{div}(\breve{\boldsymbol{\tau}}(\boldsymbol{v})) \\ \mathrm{div}(\rho e\boldsymbol{v}) + p\ \mathrm{div}\boldsymbol{v} - \mathrm{div}(\mathcal{F}\Xi\breve{\boldsymbol{q}}) - \breve{\boldsymbol{\tau}}(\boldsymbol{v}) : \boldsymbol{\nabla}\boldsymbol{v} - \dot{\omega}_T \end{pmatrix}.$$

This system differs from the system treated in Chapter 3 by three points:

- the energy balance equation includes a reaction term $\dot{\omega}_T$ (which vanishes in the non-reactive case),
- the heat diffusive term is written as a function of the sensible enthalpy, instead of the internal energy, and is weighted by the product of the subgrid wrinkling factor and the thickening factor,
- the equation of state depends on the mass fractions in the mixture (which are known at this step).

The discretization used is the same than the one introduced in Chapter 3 Section 3.4.1. Then, we introduce in the following the discrete quantities involved in (4.52) and in (4.53) that differ from the non-reactive discrete system, and refer to Chapter 3 Section 3.4.1 for more details on the other terms.

Discrete mass balance

The mass flux over the primal faces of the cell K, $\mathrm{div}_K(\rho\,\boldsymbol{v})$, is defined by (3.22) where we recall that:

$$F_{K,\sigma} = |\sigma|\ \rho_\sigma\ v_{K,\sigma}, \quad \forall\sigma\in\mathcal{E}(K) \tag{4.54}$$

with $v_{K,\sigma}$ an approximation of the normal velocity to the face σ outward K given by (3.24) and ρ_σ the density at the face σ. If $\sigma\in\mathcal{E}(K)$ is an internal face, ρ_σ is approximated by the second order MUSCL-like interpolation (3.25). If σ is an external face adjacent to K, lying on the inlet part of the boundary (*i.e.* $\sigma\in\mathcal{E}_{ext,I}$), ρ_σ is computed from the equation of state as a function of the data for the species mass fractions and the temperature. For an external face adjacent to K, lying on the outlet part of the boundary (*i.e.* $\sigma\in\mathcal{E}_{ext,O}$), $\rho_\sigma = \rho_K$.

This approximation allows, under CFL condition, to guarantee the positivity of the density (see Chapter 3 Section 3.4.2).

Let introduce the following notation for the convection term of the mass balance in (4.53):

$$\frac{1}{2}\Big[\mathrm{div}_K(\rho^n\,\boldsymbol{v}^n)+\mathrm{div}_K(\rho^{(1)}\,\boldsymbol{v}^{(1)})\Big]=\frac{1}{|K|}\sum_{\sigma\in\mathcal{E}(K)}J^{n+1}_{K,\sigma},\quad\forall K\in\mathcal{M},\tag{4.55}$$

where $J^{n+1}_{K,\sigma}$ is the average value of the mass fluxes across σ outward K at time n and (1):

$$J^{n+1}_{K,\sigma}=\frac{1}{2}(F^n_{K,\sigma}+F^{(1)}_{K,\sigma}),\quad\forall\sigma\in\mathcal{E}(K).\tag{4.56}$$

Discrete sensible energy balance

Let consider the approximation of the sensible energy balance over the primal cell K. The convection operator is defined by (3.26). The discretization of the sensible energy at the primal faces uses the same MUSCL technique as for the density (detailed in Chapter 3 Section 3.B) to ensure the positivity of the convection operator (extension of Lemma 3.4.2 provided the reaction is exothermic). If $\sigma\in\mathcal{E}(K)$ is an internal face, e_σ is approximated by the second order MUSCL-like interpolation (3.27). If σ is an inlet external face (*i.e.* $\sigma\in\mathcal{E}_{ext,I}$), e_σ is computed as a function of the temperature and of the species mass fractions prescribed on the boundary. If σ is an external face lying on the outlet part of the boundary (*i.e.* $\sigma\in\mathcal{E}_{ext,O}$), $e_\sigma=e_K$.

The heat diffusion term $\mathrm{div}(\mathcal{F}\,\Xi^n_\Delta\,\breve{\boldsymbol{q}})_K$ is discretized with the same method than for the species diffusion term, *i.e.* relation (4.50) with $x=h$. The sensible enthalpy is computed in the following way:

$$h_K=e_K+\frac{p_K}{\rho_K},\quad\forall K\in\mathcal{M}.\tag{4.57}$$

Thus the heat diffusion term reads:

$$\mathrm{div}_K\big(\mathcal{F}\,\Xi_\Delta\,\breve{\boldsymbol{q}}\big)\;=\;-\mathcal{F}\,\frac{\mu}{\mathrm{Pr}}\sum_{\sigma=K|L,\sigma\in\mathcal{E}(K)}\frac{|\sigma|}{d_\sigma}\,(\Xi_\Delta)_\sigma\,(h_K-h_L).\tag{4.58}$$

The heat production term $(\dot\omega_T)_K$ is written in the following way:

$$(\dot\omega_T)_K=-\sum_{k\in\mathcal{I}}\Delta h^0_{f,k}\,(\dot\omega_k)_K=\big(\nu_F\,W_F\,\Delta h^0_{f,F}+\nu_O\,W_O\,\Delta h^0_{f,O}-\nu_P\,W_P\,\Delta h^0_{f,P}\big)\,\dot\omega_K.$$

Discrete momentum balance

We now turn to the discrete momentum balance. The term $(\boldsymbol{\nabla}p)_{\sigma,i}$ stands for the i^{th} component of the discrete pressure gradient at the face σ. The gradient operator is built as the transpose of the discrete operator for the divergence of the velocity on the primal mesh (Grapsas et al., 2016). If $\sigma\in\mathcal{E}_{\mathrm{int}}$, $(\boldsymbol{\nabla}p)_{\sigma,i}$ is written in the same way than for the unreactive system (*i.e.* relation (3.33)). If σ is an outlet external face (*i.e.* $\sigma\in\mathcal{E}_{ext,O}$), the pressure gradient reads:

$$(\boldsymbol{\nabla}p)_{\sigma,i}=\frac{|\sigma|}{|D_\sigma|}\,(p_{ext}-p_K)\,\mathbf{n}_{K,\sigma}\cdot\boldsymbol{e}^{(i)},$$

where p_{ext} stands for the external pressure involved in the outlet boundary condition. If $\sigma\in\mathcal{E}_{ext,I}$, $(\boldsymbol{\nabla}p)_{\sigma,i}$ is set to zero.

Equation of state

Finally, the equation of state is obtained from (4.20) and reads, $\forall K \in \mathcal{M}$:

$$p_K = \varrho(e_K, \rho_K, Y_{k,K}) = \rho_K\, R \, \frac{T_K}{\displaystyle\sum_{k\in\mathcal{I}} \frac{Y_{k,K}}{W_k}}, \quad \text{with } T_K = \frac{e_K}{\displaystyle\sum_{k\in\mathcal{I}} Y_{k,K}\, c_{\mathrm{v},k}}.$$

4.4.4 The turbulence step

The subgrid wrinkling factor Ξ_Δ reads, at the discrete level, $\forall K \in \mathcal{M}$:

$$(\Xi_\Delta)^n_K = \left(\frac{\Delta_K}{\delta_c}\right)^{\beta^n_K}. \tag{4.59}$$

The exponent β^{n+1}_K is computed at each time step and reads:

$$\beta^n_K = \frac{1}{\log(\gamma)} \log\left[\frac{(\Sigma_1)^n_K}{(\Sigma_2)^n_K}\right], \quad \forall K \in \mathcal{M}, \tag{4.60}$$

with $(\Sigma_1)^n_K$ and $(\Sigma_2)^n_K$ the approximations on the cell K of Σ_1 and Σ_2 given by (4.31) and (4.32) respectively. In order to be able to compute $(\Sigma_1)^n_K$ and $(\Sigma_2)^n_K$ the following discrete formulations must be given. The progress variable c^n_K is computed from the fuel mass fraction Y_K thanks to expression (4.28):

$$c^n_K = \frac{Y^n_{F,K} - Y^u_F}{Y^b_F - Y^u_F}, \quad \forall K \in \mathcal{M}. \tag{4.61}$$

The gradient of the progress variable $(\nabla c)_{i,K}$ reads:

$$(\nabla c)^n_{i,K} = \frac{1}{|K|} \sum_{\sigma\in\mathcal{E}(K)} |\sigma| c^n_\sigma\, \boldsymbol{e}^{(i)} \cdot \mathbf{n}_{K,\sigma}, \quad \text{for } 1 \le i \le d,\ \forall K \in \mathcal{M}.$$

where the centered choice is made for the approximation of the progress variable on σ. Finally, the Euclidian norm $|\cdot|$ is applied to $(\nabla c)^n_K$:

$$|(\nabla c)^n_K| = \Big[\sum_{i=1}^{d} [(\nabla c)^n_{i,K}]^2\Big]^{1/2}, \quad \forall K \in \mathcal{M}.$$

In order to compute the subgrid wrinkling factor, the fields obtained may be filtered with Gaussian filters of width $\widehat{\Delta}$ (test filter) or Δ_{avg} (replacing the averaging over the domain $\langle\cdot\rangle$). This is perform by solving a diffusion equation as explained in Appendix 4.C (Moureau et al., 2011; Sun and Xiao, 2015).

The subgrid scale viscosity μ^{SGS} is approximated by the same technique used for the non reactive system and is given by (3.35).

4.5 Properties of the scheme

In this section we first prove that at the discrete level, the mass fractions preserve the same physical bounds as at the continuous level. Then we discuss the energy preservation properties of the scheme: following the same procedure used in Chapter 3, we obtain that the scheme conserves the total energy up to remainder terms.

Boundedness of the chemical mass fractions

Let us first introduce some notations. For any given family $(x^n_K)_{K\in\mathcal{M}} \in \mathbb{R}^d$, we denote:

$$\bar{x}^n = \max\{(x^n_K)_{K\in\mathcal{M}}, (x_{I,\sigma})_{\sigma\in\mathcal{E}_{ext,I}}\}, \qquad \underline{x}^n = \min\{(x^n_K)_{K\in\mathcal{M}}, (x_{I,\sigma})_{\sigma\in\mathcal{E}_{ext,I}}\}.$$

In the following, when no ambiguity arises, the notation x^n will be used to refer to the family $(x^n_K)_{K\in\mathcal{M}}$. For example $x^n > 1$, means $\forall K \in \mathcal{M}$, $x^n_K > 1$.

Definition 1. — *The so-called CFL number reads for any* $0 \le n \le N-1$*:*

$$\mathrm{CFL}^n = \max_{K\in\mathcal{M}} \left[\frac{\delta t/2}{|K|} \max\left(\frac{1}{\rho^n_K}, \frac{1}{\rho^{n-1/2}_K}\right) \left[\sum_{\sigma\in\mathcal{E}(K)} \left|J^n_{K,\sigma}\right| + |K|\,\mathcal{F}\,\frac{\mu}{\mathrm{Pr}} \sum_{\sigma\in\mathcal{E}(K)} \frac{|\sigma|}{d_\sigma} (\Xi_\Delta)^n_\sigma \right]\right].$$

Lemma 4.5.1 (Boundedness of the chemical mass fractions). *For* $0 \le n \le N-1$*, suppose that for* $k \in \mathcal{I}$ $Y^n_k \ge 0$, $\rho^n \ge 0$, $\mathrm{CFL}^n \le 1$ *and that the mass balance in* (4.53) *holds.*

(i) For $k \in \mathcal{I}$ *and* $K \in \mathcal{M}$, $Y^{n+1}_{k,K} \ge 0$.

(ii) $Y^{n+1}_{F,K} \le \bar{Y}^n_F$, $Y^{n+1}_{O,K} \le \bar{Y}^n_O$, $Y^{n+1}_{N,K} \in [\underline{Y}^n_N, \bar{Y}^n_N]$ *and* $Y^{n+1}_{P,K} \ge \underline{Y}^n_P$, $\forall K \in \mathcal{M}$.

Proof. Let first consider the neutral mass fraction. If $k = N$, a straightforward extension of Lemma 4.A.1 to cope with diffusive terms and with convection fluxes entering the domain, allow to write Y^{n+1}_N as a combination of $\left\{ Y^n_{N,K}, \left(Y^n_{N,M^{Y_N}_{K,\sigma}}\right)_{M^{Y_N}_{K,\sigma}\in\mathcal{N}_{Y_N}(K)}, ((Y_N)^n_{I,\sigma})_{\sigma\in\mathcal{E}_{ext,I}} \right\}$, with $\mathcal{N}_{Y_N}(K)$ the set of cells $M^{Y_N}_{K,\sigma}$, $\sigma \in \mathcal{E}(K)$ which are such that (4.49) is satisfied. Thanks to the mass balance in (4.53) (or more precisely thanks to mass balances (4.36) and (4.37)), this combination is convex under the hypothesis that $\mathrm{CFL} \le 1$. This concludes the proof for $k = N$.

If $k \in \{F, O, P\}$, the proof follows the same technique used for Lemma 4.A.1. Thanks to the mass balance (4.36), we have:

$$\rho^{n-1}_K = \rho^{n-1/2}_K + \frac{\delta t/2}{|K|} \sum_{\sigma\in\mathcal{E}(K)} J^n_{K,\sigma}.$$

Replacing this expression in the discrete balance equation (4.41), $\tilde{Y}^{n+1/2}_{k,K}$ can be written as a convex combination of $\left\{ Y^n_{k,K}, \left(Y^n_{k,M^{Y_k}_{K,\sigma}}\right)_{M^{Y_k}_{K,\sigma}\in\mathcal{N}_{Y_k}(K)}, ((Y_k)^n_{I,\sigma})_{\sigma\in\mathcal{E}_{ext,I}} \right\}$, under the following

CFL condition:

$$\frac{\delta t/2}{|K|\ \rho_K^{n-1/2}}\ \left[\sum_{\sigma\in\mathcal{E}(K)} |J^n_{K,\sigma}| + |K|\,\mathcal{F}\,\frac{\mu}{\mathrm{Pr}}\ \sum_{\sigma\in\mathcal{E}(K)} \frac{|\sigma|}{d_\sigma}\ (\Xi_\Delta)^n_\sigma\right] \leq 1$$

which is satisfied if $\mathrm{CFL}^n \leq 1$. Thus, the solution of (4.41) satisfies $\underline{Y}^n_k \leq \tilde{Y}^{n+1/2}_k \leq \bar{Y}^n_k$, *i.e.* given the non negativity of Y^n_k, $0 \leq \tilde{Y}^{n+1/2}_k \leq \bar{Y}^n_k$.

Let us turn to the second step of the Strang method. If $k = P$, The second step of the Strang splitting method (4.44) may be written as follows:

$$\left(\frac{\rho_K^{n-1/2}}{\delta t}\ I_K\right)\ Y_P^{n+1/2} = \frac{\rho_K^{n-1/2}}{\delta t}\tilde{Y}_P^{n+1/2} + (\dot{\omega}_P)_K^{n+1/2}, \tag{4.62}$$

where I_K denotes the K-th line of the identity matrix. Given the non-negative sign of $\rho_K^{n-1/2}$, of $\tilde{Y}_P^{n+1/2}$ and of $\dot{\omega}_P$, the right hand side of relation (4.62) is non-negative. Moreover, the operator at the left-hand side of relation (4.62) is associated to a positive inverse matrix, thus $Y_P^{n+1/2} \geq 0$. The second inequality (*i.e.* $Y^{n+1/2}_{P,K} \geq \underline{Y}^n_P$) follows by the same computation, applying the operator at the left-hand side of relation (4.62) to $(Y_P^{n+1/2} - \underline{Y}^n_P)$.

When the reaction term may take negative values, *i.e.* if $k \in \{F, O\}$, let us rewrite the reaction term as:

$$\text{for } k \in \{F,O\} \quad (\widetilde{\omega}_k)_K^{n+1/2} = \left|\begin{array}{ll} 0 \qquad \text{if } \min\left[\dfrac{Y_F^{n+1/2}}{W_F\,\nu_F}, \dfrac{Y_O^{n+1/2}}{W_O\,\nu_O}\right] \leq 0, \\[2ex] Y_k^{n+1/2}\ \dfrac{(\dot{\omega}_k)_K^{n+1/2}}{Y_k^{n+1/2}} \qquad \text{otherwise.}\end{array}\right. \tag{4.63}$$

The second step of the Strang splitting method may be written as follows:

$$\left(\frac{\rho_K^{n-1/2}}{\delta t}\ I_K - (\widetilde{\omega}_k)_K^{n+1/2}\ I_K\right)\ Y_k^{n+1/2} = \frac{\rho_K^{n-1/2}}{\delta t}\tilde{Y}_k^{n+1/2}. \tag{4.64}$$

Given the non-negative sign of $\rho_K^{n-1/2}$ and of $\tilde{Y}_k^{n+1/2}$, the right hand side of relation (4.64) is non-negative. By definition of $\widetilde{\omega}_k$, the operator at the left-hand side of relation (4.64) is associated to a positive inverse matrix, thus $Y_k^{n+1/2} \geq 0$. The second inequality follows by the same computation, applying the operator at the left-hand side of relation (4.64) to $(\bar{Y}^n_k - Y_k^{n+1/2})$.

Finally, let consider the last step of the Strang splitting method. The same technique used for the first step is applied. By assumption thanks to the mass balance (4.37), we get:

$$\rho_K^{n-1/2} = \rho_K^n + \frac{\delta t/2}{|K|} \sum_{\sigma\in\mathcal{E}(K)} J^n_{K,\sigma}.$$

Replacing this expression of $\rho_K^{n-1/2}$ in the discrete balance equation of $Y^{n+1}_{k,K}$, $k \in \{F, O, P\}$ (4.45), this latest can be written, under the following condition, as a convex combination of

$\left\{Y_{k,K}^{n+1/2}, \left(Y_{k,M_{K,\sigma}^{Y_k}}^{n+1/2}\right)_{M_{K,\sigma}^{Y_k}\in\mathcal{N}_{Y_k}(K)}, ((Y_k)_{I,\sigma}^{n+1/2})_{\sigma\in\mathcal{E}_{ext,I}}\right\}$:

$$\frac{\delta t/2}{|K|\,\rho_K^n}\left[\sum_{\sigma\in\mathcal{E}(K)}|J_{K,\sigma}^n| + |K|\,\mathcal{F}\,\frac{\mu}{\mathrm{Pr}}\sum_{\sigma\in\mathcal{E}(K)}\frac{|\sigma|}{d_\sigma}\,(\Xi_\Delta)_\sigma^n\right]\leq 1.$$

This condition is satisfied if $\mathrm{CFL}^n \leq 1$. The fact that $0 \leq Y_{k,K}^{n+1/2} \leq \bar{Y}_k^n$ (respectively that $Y_{P,K}^{n+1/2} \geq \underline{Y}_P^n$) concludes the proof for $k \in \{F, O\}$ (respectively for $k = P$). □

In order to prove that the numerical scheme preserves the fact that the sum of the chemical species is equal to 1 (and thus that $Y_{k,K}^n \leq 1$, for all $K \in \mathcal{M}$, $0 \leq n \leq N$ and $k \in \mathcal{I}$) some additional assumptions must be made on the coefficients $\beta_{K,\sigma}^x$ and the cells $M_{K,\sigma}^x$ involved in the MUSCL discretization of the chemical species convection terms. Without these hypothesis, as shown in Appendix 4.B, the scheme does not preserve the upper physical bound of the chemical species. An algorithm for the computation of the coefficients $\beta_{K,\sigma}^x$ (in such a way that Lemma 4.5.2 holds) is stated in Appendix 4.B in the 1D case. It can be easily extended to higher dimension cases.

LEMMA 4.5.2. *For $0 \leq n \leq N-1$, let us suppose that for all $K \in \mathcal{M}$, $\sum_{k\in\mathcal{I}} Y_{k,K}^n = 1$ and that for all $\sigma \in \mathcal{E}(K)$ relation* (4.49) *holds with the same coefficient $\beta_{K,\sigma}^x$ and the same cell $M_{K,\sigma}^x$ for $x = Y_k^n$, $k \in \mathcal{I}$. Let suppose also that the mass balance in* (4.53) *holds and that* $\mathrm{CFL}^n \leq 1$ *for $0 \leq n \leq N-1$. Then, any solution to the discrete chemical fraction balance equations satisfies for all $K \in \mathcal{M}$, $\sum_{k\in\mathcal{I}} Y_{k,K}^{n+1} = 1$.*

Proof. Let denote $\beta_{K,\sigma}$ and $M_{K,\sigma}$ respectively the coefficient and the cell involved in relation (4.49). Summing over $k \in \mathcal{I}$ the discrete chemical fraction balance equations involved in the first step of the Strang algorithm (4.41) yields, $\forall K \in \mathcal{M}$:

$$\begin{aligned}\frac{\rho_K^{n-1/2}}{\delta t/2}\sum_{k\in\mathcal{I}}\tilde{Y}_{k,K}^{n+1/2} &= \frac{\rho_K^{n-1}}{\delta t/2} - \frac{1}{|K|}\sum_{\sigma\in\mathcal{E}(K)}(J_{K,\sigma}^n)^+\sum_{k\in\mathcal{I}}\Big[(\beta_{K,\sigma}+1)\,Y_{k,K}^n - \beta_{K,\sigma}Y_{k,M_{K,\sigma}}^n\Big]\\ &+ \frac{1}{|K|}\sum_{\sigma\in\mathcal{E}(K)}(J_{K,\sigma}^n)^-\sum_{k\in\mathcal{I}}\Big[(1-\beta_{K,\sigma})\,Y_{k,K}^n + \beta_{K,\sigma}Y_{k,M_{K,\sigma}}^n\Big],\end{aligned}$$

where we use the fact that by construction the sum of the species diffusive fluxes vanishes. Using the assumption that for all $K \in \mathcal{M}$, $\sum_{k\in\mathcal{I}} Y_{k,K}^n = 1$, yields:

$$\forall K \in \mathcal{M},\quad \frac{\rho_K^{n-1/2}}{\delta t/2}\sum_{k\in\mathcal{I}}\tilde{Y}_{k,K}^{n+1/2} = \frac{\rho_K^{n-1}}{\delta t/2} - \frac{1}{|K|}\sum_{\sigma\in\mathcal{E}(K)}J_{K,\sigma}^n.$$

Then, recalling that, thanks to the mass balance (4.36):

$$\rho_K^{n-1/2} = \rho_K^{n-1} - \frac{\delta t/2}{|K|}\sum_{\sigma\in\mathcal{E}(K)}J_{K,\sigma}^n,$$

we have that $\sum_{k\in\mathcal{I}}\tilde{Y}_{k,K}^{n+1/2} = 1$, $\forall K \in \mathcal{M}$.

Let now consider the second step of the Strang algorithm. Summing over $k \in \mathcal{I}$ and recalling that by construction $\forall K \in \mathcal{M}$, $\sum_{k\in\mathcal{I}} (\dot\omega_k)_K^{n+1/2} = 0$, yields that $\sum_{k\in\mathcal{I}} Y_{k,K}^{n+1/2} = 1$, $\forall K \in \mathcal{M}$.

Finally, using the same procedure for the third step of the Strang algorithm yields:

$$\forall K \in \mathcal{M}, \quad \frac{\rho_K^n}{\delta t/2} \sum_{k\in\mathcal{I}} Y_{k,K}^{n+1} = \frac{\rho_K^{n-1/2}}{\delta t/2} - \frac{1}{|K|} \sum_{\sigma\in\mathcal{E}(K)} J_{K,\sigma}^n.$$

Using the mass balance (4.37), the following relation holds:

$$\rho_K^n = \rho_K^{n-1/2} - \frac{\delta t/2}{|K|} \sum_{\sigma\in\mathcal{E}(K)} J_{K,\sigma}^n.$$

This concludes the proof. □

Energy balances

To obtain a conservation equation for the total energy, we need to derive a discrete sensible+chemical energy balance. Then, this relation will be added to the kinetic energy balance posed on the primal mesh, already obtained in Chapter 3, Section 3.4.2, to obtain the desired discrete balance equation. This process fully applies when the viscosity is set to zero, and we restrict here the exposition to this case; the momentum diffusion terms being already treated in the appendix 3.A. Moreover, for the sake of simplicity, we restrict here to impermeability conditions.

First let apply the formulation (4.53) of the scheme to the sensible energy balance, to obtain:

$$\frac{|K|}{\delta t}\left[\rho_K^{n+1} e_K^{n+1} - \rho_K^n e_K^n\right] + \sum_{\sigma\in\mathcal{E}(K)} H_{K,\sigma}^{n+1} + (p\,\mathrm{div}\boldsymbol{v})_K^{n+1} = (\dot\omega_T)_K^{n+1}, \quad \forall K \in \mathcal{M}, \tag{4.65}$$

with, thanks to Equation (3.26) for the sensible energy convection flux and Equation (4.58) for the heat diffusion flux:

$$\begin{aligned}
H_{K,\sigma}^{n+1} &= \frac{1}{2}\Big[F_{K,\sigma}^n\, e_\sigma^n + F_{K,\sigma}^{(1)}\, e_\sigma^{(1)} \\
&\qquad + \mathcal{F}\frac{\mu}{\mathrm{Pr}}(\Xi_\Delta)_\sigma^{n+1}\,\frac{|\sigma|}{d_\sigma}\,(h_K^n - h_L^n) + \mathcal{F}\frac{\mu}{\mathrm{Pr}}(\Xi_\Delta)_\sigma^{n+1}\,\frac{|\sigma|}{d_\sigma}\,(h_K^{(1)} - h_L^{(1)})\Big], \\
(p\,\mathrm{div}\boldsymbol{v})_K^{n+1} &= \frac{1}{2}\Big[p_K^n\,\mathrm{div}_K(\boldsymbol{v}^n) + p_K^{(1)}\,\mathrm{div}_K(\boldsymbol{v}^{(1)})\Big], \\
(\dot\omega_T)_K^{n+1} &= \frac{1}{2}\Big[(\dot\omega_T)_K^n + (\dot\omega_T)_K^{(1)}\Big].
\end{aligned} \tag{4.66}$$

We now derive from this relation a discrete (sensible and chemical) internal energy balance. Multiplying the mass fraction balance equations (4.47) by the corresponding formation enthalpy $(\Delta h_{f,k}^0)_{k\in\mathcal{I}}$ and summing over $k \in \mathcal{I}$ yields:

$$\frac{1}{\delta t}\sum_{k\in\mathcal{I}} \Delta h_{f,k}^0\left[\rho_K^n Y_{k,K}^{n+1} - \rho_K^{n-1} Y_{k,K}^n\right] + \sum_{\sigma\in\mathcal{E}(K)} L_{K,\sigma}^{n+1} = \sum_{k\in\mathcal{I}} \Delta h_{f,k}^0\;(\dot\omega_k)_K^{n+1/2} = -(\dot\omega_T)_K^{n+1}, \tag{4.67}$$

with, using relation (4.48) for the species convection flux and relation (4.50) for the species diffusion flux:

$$
\begin{aligned}
L^{n+1}_{K,\sigma} = \frac{1}{2}\, J^{n}_{K,\sigma} \sum_{k\in\mathcal{I}} \Delta h^{0}_{f,k} \Big[Y^{n}_{k,\sigma} + Y^{n+1/2}_{k,\sigma} \Big] \\
+ \mathcal{F} \frac{\mu}{\mathrm{Pr}} (\Xi_\Delta)^{n+1}_{\sigma}\, \frac{1}{2}\, \frac{|\sigma|}{d_\sigma} \sum_{k\in\mathcal{I}} \Delta h^{0}_{f,k} \Big[(Y^{n}_{k,K} - Y^{n}_{k,L}) + (Y^{n+1/2}_{k,K} - Y^{n+1/2}_{k,L}) \Big].
\end{aligned}
\tag{4.68}
$$

Adding Equation (4.67) to (4.65), we can state that, in the inviscid case, the numerical solutions of the scheme satisfy the following sensible+chemical energy balance.

LEMMA 4.5.3 (Discrete sensible+chemical energy balance). *In the inviscid case, the solutions to the scheme satisfy the following discrete sensible + chemical energy balance equation, for any* $K \in \mathcal{M}$ *and* $0 \le n < N-1$*:*

$$
\frac{1}{\delta t} \big[(\rho e_c)^{n+1}_K - (\rho e_c)^{n}_K \big] + \sum_{\sigma\in\mathcal{E}(K)} N^{n+1}_{K,\sigma} + (p\, \mathrm{div}\boldsymbol{v})^{n+1}_K = 0,
\tag{4.69}
$$

where

$$
\begin{aligned}
&(\rho e_c)^{\ell}_K = \rho^{l}_K e^{\ell}_K + \rho^{\ell-1}_K \sum_{i\in\mathcal{I}} \Delta h^{0}_{f,k} Y^{\ell}_{k,K}, \qquad \text{for } \ell = n \text{ or } \ell = n+1. \\
&N^{n+1}_{K,\sigma} = H^{n+1}_{K,\sigma} + L^{n+1}_{K,\sigma}
\end{aligned}
$$

where $H^{n+1}_{K,\sigma}$ *gathers the discrete sensible energy convection flux and the heat diffusion flux (see Equation* (4.66)*) and* $L^{n+1}_{K,\sigma}$ *gathers the discrete species convection flux and the species diffusion flux multiplied by the formation enthalpy (see Equation* (4.68)*).*

Using the kinetic energy balance on the primal mesh recovered in Chapter 3, Section 3.4.2, the following total energy balance can be stated in the inviscid case.

Theorem 4.5.1 (Discrete total energy balance) In the inviscid case, the solutions to the scheme satisfy the following discrete total energy balance equation:

$$
\frac{|K|}{\delta t} \big[(\rho E)^{n+1}_K - (\rho E)^{n}_K \big] + \sum_{\sigma\in\mathcal{E}(K)} \big(G^{n+1}_{K,\sigma} + N^{n+1}_{K,\sigma} + I^{n+1}_{K,\sigma} \big) = -R^{n+1}_K,
\tag{4.70}
$$

where $G^{n+1}_{K,\sigma}$ is the discrete kinetic energy convection flux given by (3.64), $N^{n+1}_{K,\sigma}$ gathers the discrete sensible+chemical energy convection flux and the sensible+chemical diffusion flux, $I^{n+1}_{K,\sigma}$ is the flux associated to the continuous counterpart $p\,\boldsymbol{v}$ and given by (3.68) and $(\rho E)^{\ell}_K = (\rho e_c)^{\ell}_K + (e^{\ell}_k)_K$, $\ell = n$ and $\ell = n+1$, with the kinetic energy e_k given by (3.64).

4.6 Conclusion

In order to deal with reactive compressible flows such those encountered during an explosion, the filtered Navier-Stokes equations are complemented with chemical species balance equations and the reactive terms needed are added in the sensible energy balance. The virtually thickened flame model has been chosen for combustion modelling. The wrinkling model of Veynante and Moureau (2015) is used for the subgrid model incorporating the Mouriaux et al. (2016) correction for front/front interactions and front/wall interactions.

The numerical scheme developed in the previous chapter for the non-reactive case is extended to the reactive case. A Strang splitting method is used for the resolution of the chemical species. One explicit half-step of homogeneous transport for the chemical species is first performed, then an implicit step deals with the reaction terms. Finally, a second explicit half-step of transport for the chemical species is performed. The associated reaction energy is introduced into the energy balance of Navier-Stokes equations, solved in a second time.

The positivity of the density is ensured by construction of the discrete mass balance equation, *i.e.* by the use of a second order MUSCL scheme. In addition, the positivity of the mass fractions are preserved thanks to the following argument: first, building a discrete convection operator which vanishes when the convected unknown is constant thanks to the discrete mass balance equation ensures a positivity-preservation property (Larrouturou, 1991), under a CFL condition; second, the discretization of the chemical reaction rate ensures either that it vanishes when the unknown of the equation vanishes (for fuel and oxidizer mass fractions), or that it is non-negative (for product mass fractions). Consequently, mass fractions are non-negative. Moreover, with a suitable choice of the coefficients involved in the MUSCL discretization of the chemical species convection terms, the sum of the chemical species is equal to 1. Thus, they are also bounded by 1. An algorithm for the computation of these latter coefficients is given.

Finally, we establish a discrete total energy balance for the scheme, which may be made conservative by adding corrective terms to the sensible energy balance, for instance if one wants to compute shock solutions. Since we address here essentially viscous flows, we do not follow this line.

Appendix

4.A A stability result for the Strang splitting method

Let consider the following system of equations:

$$\begin{aligned} &\partial_t \rho + \operatorname{div}(\rho \boldsymbol{v}) = 0, \\ &\partial_t (\rho \boldsymbol{v}) + \operatorname{div}(\rho \boldsymbol{v} Y) = 0. \end{aligned} \tag{4.71}$$

We suppose for short that this system is complemented by impermeability boundary conditions, *i.e.* that the normal velocity, both at the continuous and the discrete level, vanishes on the boundary of the computational domain.

In this appendix, we build a numerical scheme for the solution of the above system. The convection fluxes are build in such a way that the numerical scheme respects "by construction" the physical bounds satisfied by the variables in the continuous case. To this purpose, let notice that an operator which satisfies a maximum principle must vanish when applied to constant functions (Larrouturou, 1991). Indeed, denoting by $\mathcal{L}$ such an operator, an initially constant solution ξ to the equation $\partial_t \xi + \mathcal{L}(\xi) = 0$ must remain constant, since the upper and lower bounds of the solution have to be preserved (provided, of course, that boundary conditions are consistent with this constant solution). This yields $\partial_t \xi = 0$ and so $\mathcal{L}(\xi) = 0$. Here, the numerical scheme for the solution of the system (4.71) uses the Strang operator splitting method for the chemical species mass fraction computation. This method consists in performing one half-step of homogeneous transport of Y, then dealing with the reaction terms (set to zero in this case) and finishing by the second half-step of transport of Y. Thus, two convection operators must be approximated, for the first and the last step of the Strang algorithm. The fact that these operators vanish when applied to constant functions is closely related to the fact that these equations may be recast under non-conservative form thanks to the mass balance. A density at "time step $n - 1/2$", $\rho_K^{n-1/2}$, is thus introduced and defined by a linear combination of the density at time n and $n - 1$:

$$\rho_K^{n-1/2} = \frac{1}{2}(\rho_K^n + \rho_K^{n-1}), \quad \forall K \in \mathcal{M}. \tag{4.72}$$

This latest satisfies the following discrete mass balance equations (where the same notations introduced in this chapter have been used):

$$\frac{\rho_K^{n-1/2} - \rho_K^{n-1}}{\delta t/2} + \frac{1}{|K|} \sum_{\sigma \in \mathcal{E}(K)} F_{K,\sigma}^n \quad = \quad 0 \tag{4.73}$$

$$\frac{\rho_K^{n} - \rho_K^{n-1/2}}{\delta t/2} + \frac{1}{|K|} \sum_{\sigma \in \mathcal{E}(K)} F_{K,\sigma}^n \quad = \quad 0 \tag{4.74}$$

which can be related respectively to the first and the last step of the Strang algorithm. The MUSCL discretization is used for the convection operators of the chemical species balance which closely follows the technique proposed in Piar et al. (2013). Then, the following property holds:

$$\begin{aligned} &\forall K \in \mathcal{M},\ \forall \sigma \in \mathcal{E}(K) \cap \mathcal{E}_{\text{int}},\ \exists \beta_K^\sigma \in [0,1] \text{ and } M_K^\sigma \in \mathcal{M} \text{ such that} \\ &Y_\sigma - Y_K = \left| \begin{array}{l} \beta_K^\sigma \, (Y_K - Y_{M_K^\sigma}), \text{ if } F_{K,\sigma}^n \geq 0, \\ \beta_K^\sigma \, (Y_{M_K^\sigma} - Y_K), \text{ otherwise.} \end{array} \right. \end{aligned} \tag{4.75}$$

Under this latter hypothesis and a CFL condition, the scheme preserves the initial bounds of Y (see Lemma 4.A.1 below).

> **Remark.** Note that, in Assumption (4.75), only internal faces are considered, since the fluxes through external faces are supposed to vanish. However, the present discussion may easily be generalized to cope with convection fluxes entering the domain.

The numerical scheme for the solution of the system (4.71) reads, for $0 \leq n \leq N-1$:

1 - **Chemical species mass fraction computation** - Strang splitting method:

Transport step I – Solve for $\tilde{Y}^{n+1/2}$:

$$\frac{\rho_K^{n-1/2} \tilde{Y}_K^{n+1/2} - \rho_K^{n-1} Y_K^n}{\delta t/2} + \frac{1}{|K|} \sum_{\sigma \in \mathcal{E}(K)} F_{K,\sigma}^n Y_\sigma^n = 0, \qquad \forall K \in \mathcal{M}. \tag{4.76a}$$

Reactive step – Solve for $Y^{n+1/2}$:

$$\frac{\rho_K^{n-1/2} \left[Y_K^{n+1/2} - \tilde{Y}_K^{n+1/2} \right]}{\delta t} = 0, \qquad \forall K \in \mathcal{M}. \tag{4.76b}$$

Transport step II – Solve for Y^{n+1} :

$$\frac{\rho_K^n Y_K^{n+1} - \rho_K^{n-1/2} Y_K^{n+1/2}}{\delta t/2} + \frac{1}{|K|} \sum_{\sigma \in \mathcal{E}(K)} F_{K,\sigma}^n Y_\sigma^{n+1/2} = 0, \qquad \forall K \in \mathcal{M}. \tag{4.76c}$$

2 - **Mass balance computation** - Solve for ρ^{n+1}:

$$\frac{\rho_K^{n+1} - \rho_K^n}{\delta t} + \frac{1}{|K|} \sum_{\sigma \in \mathcal{E}(K)} F_{K,\sigma}^{n+1} = 0, \qquad \forall K \in \mathcal{M}. \tag{4.77}$$

Definition 2. — *The so-called CFL number reads for any* $0 \leq n \leq N$*:*

$$\text{CFL}^n = \max_{K \in \mathcal{M}} \left\{ \frac{\delta t/2}{|K|} \max\left(\frac{1}{\rho_K^n}, \frac{1}{\rho_K^{n-1/2}} \right) \sum_{\sigma \in \mathcal{E}(K)} \left| F_{K,\sigma}^n \right| \right\}.$$

Lemma 4.A.1. *Let us suppose that* $\mathrm{CFL}^n \leq 1$. *For* $K \in \mathcal{M}$, *let us note by* $\mathcal{V}(K)$ *the union of the set of cells* M_K^σ, $\sigma \in \mathcal{E}(K) \cap \mathcal{E}_{\mathrm{int}}$ *such that* (4.75) *holds. Then* $\forall K \in \mathcal{M}$, *the value of* Y_K^{n+1} *is a convex combination of* $\{Y_K^n, (Y_M^n)_{M \in \mathcal{V}(K)}\}$.

Proof. Let first consider the first step of the Strang splitting method. Thanks to the discrete mass balance equation (4.73), we have:

$$\rho_K^{n-1} = \rho_K^{n-1/2} + \frac{\delta t/2}{|K|} \sum_{\sigma \in \mathcal{E}(K)} F_{K,\sigma}^n.$$

Replacing this expression of ρ_K^{n-1} in the discrete balance equation of $\tilde{Y}_K^{n+1/2}$ (4.76a) and using the relations provided by (4.75), we obtain:

$$\begin{aligned}
\rho_K^{n-1/2} \tilde{Y}_K^{n+1/2} &= \rho_K^{n-1} Y_K^n - \frac{\delta t/2}{|K|} \sum_{\sigma \in \mathcal{E}(K)} F_{K,\sigma}^n Y_\sigma^n \\
&= \rho_K^{n-1/2} Y_K^n - \frac{\delta t/2}{|K|} \sum_{\sigma \in \mathcal{E}(K)} F_{K,\sigma}^n (Y_\sigma^n - Y_K^n) \\
&= \rho_K^{n-1/2} Y_K^n - \frac{\delta t/2}{|K|} \sum_{\sigma \in \mathcal{E}(K)} \big(F_{K,\sigma}^n\big)^+ (Y_\sigma^n - Y_K^n) + \frac{\delta t/2}{|K|} \sum_{\sigma \in \mathcal{E}(K)} \big(F_{K,\sigma}^n\big)^- (Y_\sigma^n - Y_K^n) \\
&= \rho_K^{n-1/2} Y_K^n - \frac{\delta t/2}{|K|} \sum_{\sigma \in \mathcal{E}(K)} \big(F_{K,\sigma}^n\big)^+ \beta_K^\sigma (Y_K^n - Y_{M_K^\sigma}^n) \\
&\qquad + \frac{\delta t/2}{|K|} \sum_{\sigma \in \mathcal{E}(K)} \big(F_{K,\sigma}^n\big)^- \beta_K^\sigma (Y_{M_K^\sigma}^n - Y_K^n).
\end{aligned}$$

This relation yields:

$$\tilde{Y}_K^{n+1/2} = Y_K^n \Big(1 - \frac{\delta t/2}{\rho_K^{n-1/2}\, |K|} \sum_{\sigma \in \mathcal{E}(K)} \beta_K^\sigma \, \big|F_{K,\sigma}^n\big| \Big) + \frac{\delta t/2}{\rho_K^{n-1/2}\, |K|} \sum_{\sigma \in \mathcal{E}(K)} Y_{M_K^\sigma}^n \beta_K^\sigma \, \big|F_{K,\sigma}^n\big|,$$

which is a convex combination of $\{Y_K^n, (Y_{M_K^\sigma}^n)_{M_K^\sigma \in \mathcal{V}(K)}\}$ under the hypothesis that $\mathrm{CFL} \leq 1$.

The second step of the Strang splitting method (4.76b) simply yields:

$$Y_K^{n+1/2} = \tilde{Y}_K^{n+1/2}.$$

Finally, let consider the third step (4.76c) of the Strang algorithm. The mass balance equation (4.74) yields:

$$\rho_K^{n-1/2} = \rho_K^n + \frac{\delta t/2}{|K|} \sum_{\sigma \in \mathcal{E}(K)} F_{K,\sigma}^n.$$

Replacing this expression of $\rho_K^{n-1/2}$ in the discrete balance equation of Y_K^{n+1} (4.76c) and using the same procedure than for the first step, we obtain:

$$\begin{aligned}
\rho_K^n Y_K^{n+1} &= \rho_K^{n-1/2} Y_K^{n+1/2} - \frac{\delta t/2}{|K|} \sum_{\sigma\in\mathcal{E}(K)} F_{K,\sigma}^n Y_\sigma^{n+1/2} \\
&= \rho_K^n Y_K^{n+1/2} - \frac{\delta t/2}{|K|} \sum_{\sigma\in\mathcal{E}(K)} F_{K,\sigma}^n (Y_\sigma^{n+1/2} - Y_K^{n+1/2}) \\
&= \rho_K^n Y_K^{n+1/2} - \frac{\delta t/2}{|K|} \sum_{\sigma\in\mathcal{E}(K)} \big(F_{K,\sigma}^n\big)^+ \beta_K^\sigma (Y_K^{n+1/2} - Y_{M_K^\sigma}^{n+1/2}) \\
&\qquad + \frac{\delta t/2}{|K|} \sum_{\sigma\in\mathcal{E}(K)} \big(F_{K,\sigma}^n\big)^- \beta_K^\sigma (Y_{M_K^\sigma}^{n+1/2} - Y_K^{n+1/2}).
\end{aligned}$$

This relation yields:

$$Y_K^{n+1} = Y_K^{n+1/2}\Big(1 - \frac{\delta t/2}{\rho_K^n\,|K|} \sum_{\sigma\in\mathcal{E}(K)} \beta_K^\sigma \,|F_{K,\sigma}^n|\Big) + \frac{\delta t/2}{\rho_K^n\,|K|} \sum_{\sigma\in\mathcal{E}(K)} Y_{M_K^\sigma}^{n+1/2} \beta_K^\sigma \,|F_{K,\sigma}^n|,$$

which concludes the proof under the hypothesis that CFL ≤ 1. □

4.B A MUSCL discretization which preserves the upper bound of chemical species

In the continuous case, the bound $Y_k \leq 1$, $k \in \mathcal{I}$ is obtained indirectly: summing the chemical mass balance equations, we obtain that their sum is always equal to one; since they are non-negative, each of them is also bounded by 1. Unfortunately, applying (in a decoupled way) a nonlinear scheme for each of the mass balance equation does not allow to recover this property at the discrete level (Tran, 2008): this is shown hereafter by a counter-example. This phenomenon may be circumvented by a an adaptation of the algorithm, which, schematically speaking, consists in applying the same limitation at all the species; this limitation is built as to imply individual limitations, and thus may be more stringent (*i.e.* yields a more diffusive scheme). The aim of this section is to describe this algorithm and to show that on one side, it preserves the positivity of the mass fractions and, on the other side, it yields a maximum preserving discrete transport equation for their sum (in fact, for any affine combination of the Y_k). We restrict the exposition to the 1D case, but the method readily extends to structured multidimensional situations.

Let first recall the procedure for the computation of $Y_{k,\sigma}$, for $k \in \mathcal{I}$ and $\sigma \in \mathcal{E}_{\rm int}$ (we refer to Piar et al. (2013) for more details). The first step consists in calculating a tentative value for $Y_{k,\sigma}$ as a linear interpolate of nearby values. Let us choose some real coefficients $(\varsigma_{K,\sigma}^k)_{K\in\mathcal{M}}$ such that

$$\boldsymbol{x}_\sigma = \sum_{K\in\mathcal{M}} \varsigma_{K,\sigma}^k \boldsymbol{x}_K, \qquad \sum_{K\in\mathcal{M}} \varsigma_{K,\sigma}^k = 1.$$

where $\boldsymbol{x}_\sigma$ and $\boldsymbol{x}_K$ stand for the mass centers of σ and K respectively, $\forall \sigma \in \mathcal{E}_{\rm int}$ and $K \in \mathcal{M}$. These coefficients are then used to calculate the tentative value of $\tilde{Y}_{k,\sigma}$ by

$$\tilde{Y}_{k,\sigma} = \sum_{K\in\mathcal{M}} \varsigma_{K,\sigma}^k Y_{k,K}. \tag{4.78}$$

The second step is to define an admissible interval such that the following property holds, for $k \in \mathcal{I}$:

$$\forall K \in \mathcal{M},\ \forall \sigma \in \mathcal{E}(K) \cap \mathcal{E}_{\text{int}},\ \exists \beta^k_{K,\sigma} \in [0,1] \text{ and } M^k_{K,\sigma} \in \mathcal{M} \text{ such that}$$
$$Y_{k,\sigma} - Y_{k,K} = \left| \begin{array}{l} \beta^k_{K,\sigma}\,(Y_{k,K} - Y_{k,M^k_{K,\sigma}}),\ \text{if } F_{K,\sigma} \geq 0, \\ \beta^k_{K,\sigma}\,(Y_{k,M^k_{K,\sigma}} - Y_{k,K}),\ \text{otherwise.} \end{array} \right. \tag{4.79}$$

Let $\sigma \in \mathcal{E}_{\text{int}}$, let us denote by V^- and V^+ the upstream and downstream cell separated by σ, and by $\mathcal{N}_\sigma(V^-)$ and $\mathcal{N}_\sigma(V^+)$ two sets of neighbouring cells of V^- and V^+ respectively. According to Piar et al. (2013), the following two assumptions are sufficient conditions for (4.79) to hold:

(H1) – there exists $M \in \mathcal{N}_\sigma(V^+)$ such that $Y_{k,\sigma} \in [\![Y_{k,M}, Y_{k,M} + \dfrac{\zeta^+}{2}(Y_{k,V^+} - Y_{k,M})]\!]$,

(H2) – there exists $M \in \mathcal{N}_\sigma(V^-)$ such that $Y_{k,\sigma} \in [\![Y_{k,V^-}, Y_{k,V^-} + \dfrac{\zeta^-}{2}(Y_{k,V^-} - Y_{k,M})]\!]$,

where, for $a,\ b \in \mathbb{R}$, we denote by $[\![a,b]\!]$ the interval $\{\alpha\, a + (1-\alpha)\, b,\ \alpha \in [0,1]\}$, and ζ^+ and ζ^- are two numerical parameters lying in the interval $[0,2]$.

Thus, for each face σ of the mesh, after determining V^- and V^+ according to the sign of the mass flux through σ, the assumptions (H1) and (H2) are exploited to obtain an admissible interval $I_{k,\sigma}$ for the value of the unknown at the face. This interval is not empty: indeed for $\sigma \in \mathcal{E}_{\text{int}}$, since $V^- \in \mathcal{N}_\sigma(V^+)$, the upstream choice $Y_{k,\sigma} = Y_{k,V^-}$ always satisfies the conditions (H1) and (H2), and is the only one to satisfy them if we choose $\zeta^- = \zeta^+ = 0$ (Piar et al., 2013).

Finally, the last step of the procedure consists in computing $Y_{k,\sigma}$ as the nearest point to $\tilde{Y}_{k,\sigma}$ in $I_{k,\sigma}$.

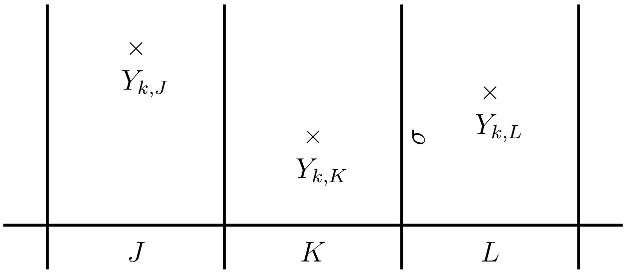

Figure 4.B.1: 1D case: notations.

Let us take the example of an interface σ separating K and L in a 1D case (see Figure 4.B.1 for the notations). First, let compute a tentative value $\tilde{Y}_{k,\sigma}$ for the unknown at the face σ, by Relation (4.78), which yields an affine interpolation at the mass centre of the face. The coefficients used in this interpolation are chosen in such a way that as few as possible cells, to be picked up in the closest cells to σ, take part. For example, in this case, only two non-zero coefficients exist in the family $(\varsigma^k_{K,\sigma})_{K\in\mathcal{M}}$, namely $\varsigma^k_{K,\sigma}$ and $\varsigma^k_{L,\sigma}$. Thus, the tentative value of $\tilde{Y}_{k,\sigma}$ is given by:

$$\tilde{Y}_{k,\sigma} = \varsigma^k_{K,\sigma} Y_{k,K} + (1 - \varsigma^k_{K,\sigma})\, Y_{k,L}. \tag{4.80}$$

Let us restrict ourselves to a positive advection velocity, so that $V^- = K$ and $V^+ = L$. In 1D, a natural choice is $\mathcal{N}_\sigma(K) = \{J\}$ and $\mathcal{N}_\sigma(L) = \{K\}$.
If $\zeta^- = \zeta^+ = 2$, rewritten assumptions (H1) (H2) yields:
(H1) – $Y_{k,\sigma} \in [\![Y_{k,K}, Y_{k,L}]\!]$,
(H2) – $Y_{k,\sigma} \in [\![Y_{k,K}, 2\,Y_{k,K} - Y_{k,J}]\!]$.
Thus the admissible interval $I_{k,\sigma}$ reads:

$$I_{k,\sigma} = [\![Y_{k,K}, Y_{k,L}]\!] \cap [\![Y_{k,K}, 2\,Y_{k,K} - Y_{k,J}]\!]. \tag{4.81}$$

Let notice that $\tilde{Y}_{k,\sigma}$ satisfies (H1) by construction.

4.B.1 The procedure for the computation of $Y_{k,\sigma}$ does not preserve $\sum_{k\in\mathcal{I}} Y_k = 1$: an example

Let suppose that only three chemical species are involved in the mixture and that the subscripts $\mathcal{I}$ reads $\mathcal{I} = \{1, 2, 3\}$ so that the set of mass fractions of the chemical species in the flow reads $\{Y_1, Y_2, Y_3\}$. Let $\varepsilon \leq 1/4$ be a constant real number and let $Y^n_{k,K}$, for $k \in \mathcal{I}$, take the following values in the cells in the vicinity of σ at time n:

$$\left|\begin{array}{l} Y^n_{1,J} = 1-\varepsilon \\ Y^n_{1,K} = 1-\varepsilon \\ Y^n_{1,L} = 1/2 \end{array}\right. \qquad \left|\begin{array}{l} Y^n_{2,J} = 0 \\ Y^n_{2,K} = \varepsilon/2 \\ Y^n_{2,L} = 2\varepsilon \end{array}\right. \qquad \left|\begin{array}{l} Y^n_{3,J} = \varepsilon \\ Y^n_{3,K} = \varepsilon/2 \\ Y^n_{3,L} = 1/2 - 2\varepsilon \end{array}\right. \tag{4.82}$$

Let notice that $\sum_{k\in\mathcal{I}} Y^n_{k,K} = \sum_{k\in\mathcal{I}} Y^n_{k,J} = \sum_{k\in\mathcal{I}} Y^n_{k,L} = 1$ and that for ε small enough the mass fractions are non-negative. The tentative values $\tilde{Y}^n_{k,\sigma}$ lie in the following intervals:

$$\tilde{Y}^n_{1,\sigma} \in [\![1/2, 1-\varepsilon]\!], \quad \tilde{Y}^n_{2,\sigma} \in [\![\varepsilon/2, 2\,\varepsilon]\!], \quad \tilde{Y}^n_{3,\sigma} \in [\![\varepsilon/2, 1/2 - 2\,\varepsilon]\!].$$

According to expression (4.81), the admissible intervals $I_{k,\sigma}$ are the intersection of the previous intervals with the following (corresponding to condition (H2)):

$$\tilde{I}_{1,\sigma} = [\![1-\varepsilon, 3/2 - 2\,\varepsilon]\!], \quad \tilde{I}_{2,\sigma} = [\![\varepsilon/2, \varepsilon]\!], \quad \tilde{I}_{3,\sigma} = [\![0, \varepsilon/2]\!].$$

The projection of $\tilde{Y}^n_{k,\sigma}$ in $I_{k,\sigma}$, for $k \in \mathcal{I}$, leads to the following values for $Y^n_{k,\sigma}$:

$$Y^n_{1,\sigma} = 1-\varepsilon, \quad Y^n_{2,\sigma} = \varepsilon, \quad Y^n_{3,\sigma} = \varepsilon/2.$$

Thus $\sum_{k\in\mathcal{I}} Y^n_{k,\sigma} = 1 + \varepsilon/2 > 1$.

Let consider the following discrete chemical fraction balance equation written, for each $k \in \mathcal{I}$, as:

$$\frac{\rho^{n+1}_K\, Y^{n+1}_{k,K} - \rho^n_K\, Y^n_{k,K}}{\delta t} + \frac{1}{|K|} \sum_{\sigma\in\mathcal{E}(K)} F^n_{K,\sigma}\, Y^n_{k,\sigma} = 0 \tag{4.83}$$

where the diffusive and reactive terms have been omitted (by construction the sum over $k \in \mathcal{I}$ of the species diffusive fluxes and of the reactive terms vanishes). Summing over $k \in \mathcal{I}$ the previous equations yields, $\forall K \in \mathcal{M}$:

$$\begin{aligned}\frac{\rho_K^{n+1}}{\delta t}\sum_{k\in\mathcal{I}} Y_{k,K}^{n+1} &= \frac{\rho_K^n}{\delta t} - \frac{1}{|K|}\sum_{\sigma\in\mathcal{E}(K)} F_{K,\sigma}^n \sum_{k\in\mathcal{I}} Y_{k,\sigma}^n \\ &= \frac{\rho_K^n}{\delta t} - \frac{1}{|K|}\sum_{\sigma\in\mathcal{E}(K)} F_{K,\sigma}^n \big(1+\frac{\varepsilon}{2}\big)\end{aligned}$$

Then, assuming that the following mass balance holds, we have:

$$\rho_K^{n+1} = \rho_K^n - \frac{\delta t}{|K|}\sum_{\sigma\in\mathcal{E}(K)} F_{K,\sigma}^n, \tag{4.84}$$

Using this latest relation, the sum of $Y_{k,K}^{n+1}$ reads:

$$\sum_{k\in\mathcal{I}} Y_{k,K}^{n+1} = 1 - \frac{\delta t}{\rho_K^n}\frac{1}{|K|}\sum_{\sigma\in\mathcal{E}(K)} F_{K,\sigma}^n\frac{\varepsilon}{2},$$

thus $\sum\limits_{k\in\mathcal{I}} Y_{k,K}^{n+1} \neq 1$.

4.B.2 A corrected algorithm for the computation of $Y_{k,\sigma}$

Let now give the algorithm for the discretization of the convection term which allows to preserve not only the lower but also the upper physical bound of chemical species:

1. For each $k \in \mathcal{I}$, compute a tentative value $\hat{Y}_{k,\sigma}$ as usual:
   (a) compute a tentative value of $\tilde{Y}_{k,\sigma}$ for the unknown at the face σ, by relation (4.80), which yields an affine interpolation at the mass centre of the face,
   (b) determine V^- and V^+ according to the sign of the mass flux through σ, and exploit (H1) and (H2) to obtain an admissible interval $I_{k,\sigma}$ for the value of the unknown at the face,
   (c) compute $\hat{Y}_{k,\sigma}$ as the projection of $\tilde{Y}_{k,\sigma}$ in $I_{k,\sigma}$.
2. Define $\varsigma_{K,\sigma} = \min\limits_{k\in\mathcal{I}} \varsigma_{K,\sigma}^k$, with $\varsigma_{K,\sigma}^k$ obtained in step 1.(a). By construction, $\varsigma_{K,\sigma} \in [0,1]$.
3. For each $k \in \mathcal{I}$, compute $Y_{k,\sigma}$ given by:

$$Y_{k,\sigma} = \varsigma_{K,\sigma} Y_{k,K} + (1-\varsigma_{K,\sigma})\, Y_{k,L}.$$

By construction, for each $k \in \mathcal{I}$, $Y_{k,\sigma} \in I_{k,\sigma}$. Indeed, we recover (4.79) (which is equivalent to conditions (H1) and (H2)), that is for $\sigma \in \mathcal{E}(K)\cap\mathcal{E}_{\rm int}$ and for each $k \in \mathcal{I}$, $Y_{k,\sigma}$ can be rewritten as:

$$Y_{k,\sigma} - Y_{k,K} = \beta_{K,\sigma}\,(Y_{k,K} - Y_{k,M_{K,\sigma}}), \text{ if } F_{K,\sigma} \geq 0$$

with $M_{K,\sigma} = L$ and $\beta_{K,\sigma} = \varsigma_{K,\sigma} - 1$ which not depend anymore on k. Analogously, $Y_{k,\sigma}$ can be rewritten as:

$$Y_{k,\sigma} - Y_{k,K} = \beta_{K,\sigma}\,(Y_{k,M_{K,\sigma}} - Y_{k,K}), \text{ if } F_{K,\sigma} < 0$$

with $M_{K,\sigma} = L$ and $\beta_{K,\sigma} = 1 - \varsigma_{K,\sigma}$.

With this procedure, the coefficients $\beta^k_{K,\sigma}$ and the cells $M^k_{K,\sigma}$ involved in the MUSCL discretization of the chemical species convection terms do not depend on the k. Summing over $k \in \mathcal{I}$ the discrete chemical fraction balance equations (4.83) yields, $\forall K \in \mathcal{M}$:

$$\begin{aligned} \frac{\rho_K^{n+1}}{\delta t} \sum_{k\in\mathcal{I}} Y_{k,K}^{n+1} &= \frac{\rho_K^n}{\delta t} - \frac{1}{|K|} \sum_{\sigma\in\mathcal{E}(K)} (F^n_{K,\sigma})^+ \sum_{k\in\mathcal{I}} \Big[(\beta_{K,\sigma}+1)\, Y^n_{k,K} - \beta_{K,\sigma} Y^n_{k,M_{K,\sigma}} \Big] \\ &+ \frac{1}{|K|} \sum_{\sigma\in\mathcal{E}(K)} (F^n_{K,\sigma})^- \sum_{k\in\mathcal{I}} \Big[(1-\beta_{K,\sigma})\, Y^n_{k,K} + \beta_{K,\sigma} Y^n_{k,M_{K,\sigma}} \Big], \end{aligned}$$

Then, if for all $K \in \mathcal{M}$, $\sum_{k\in\mathcal{I}} Y^n_{k,K} = 1$, we have:

$$\forall K \in \mathcal{M}, \quad \frac{\rho_K^{n+1}}{\delta t} \sum_{k\in\mathcal{I}} Y_{k,K}^{n+1} = \frac{\rho_K^n}{\delta t} - \frac{1}{|K|} \sum_{\sigma\in\mathcal{E}(K)} F^n_{K,\sigma}.$$

Finally, the mass balance (4.84) leads to $\sum_{k\in\mathcal{I}} Y^{n+1}_{k,K} = 1$, $\forall K \in \mathcal{M}$.

4.C Filtering method

In order to compute the subgrid scale wrinkling factor Ξ_Δ, fields may be filtered at a filter width $\widetilde{\Delta}$ (which can be $\widehat{\Delta}$ or Δ_{avg}). A filtering operator is thus needed.

Consider the diffusion equation for $\phi(\boldsymbol{x},\tau) \in \Omega \times [0,\mathcal{T}]$, Ω being the computational domain:

$$\left| \begin{array}{l} \partial_\tau \phi = \alpha \boldsymbol{\nabla}^2 \phi \\ \phi(\boldsymbol{x},0) = \phi_0 \end{array} \right. \tag{4.85}$$

where τ is a pseudo-time, which should be distinguished from the physical time t used in the numerical scheme proposed here, and α a constant diffusion coefficient. The solution of the previous equation has the following form at a fixed pseudo-time $\tau = \mathcal{T}$. This latest is the convolution of ϕ with a function of the same form of a Gaussian filter (Sun and Xiao, 2015):

$$G(\boldsymbol{x}) = \frac{1}{(4\pi\alpha\,\mathcal{T})^{3/2}} \exp\left[-\frac{1}{4\,\alpha\,\mathcal{T}} \sum_{i=1}^{d} x_i^2 \right].$$

Indeed, we recover (1.50) by setting $\alpha\,\mathcal{T} = \tilde{\Delta}/24$.

The system (4.85) may be solved implicitly or explicitly. Let us consider a partition $0 = \tau_0 < \tau_1 < \cdots < \tau_N = \mathcal{T}$ of the time interval $(0,\mathcal{T})$, which we suppose uniform, and let $\delta\tau = \tau_{n+1} - \tau_n$ for $n = 0, 1, \cdots, N-1$ be the (constant) time step (set here to 1). The discrete formulation reads, for $0 \le n \le N-1$:

$$\frac{|K|}{\delta\tau} \Big(\phi_K^{n+1} - \phi_K^n \Big) = \sum_{\sigma\in\mathcal{E}(K),\sigma=K|L} \frac{\sigma}{d_\sigma} \alpha\, (\phi_L^\star - \phi_K^\star), \quad \forall K \in \mathcal{M} \tag{4.86}$$

where $\star$ stands to $n+1$ if the system is solved implicitly or n if the system is solved explicitly. The same notations introduced in Section 4.3 are used here.

If the resolution is explicit, we have:

$$\phi_K^{n+1} = \phi_K^n \Big(1 - \frac{\delta\tau}{|K|} \sum_{\sigma\in\mathcal{E}(K),\sigma=K|L} \frac{\sigma}{d_\sigma}\alpha\Big) + \frac{\delta\tau}{|K|} \sum_{\sigma\in\mathcal{E}(K),\sigma=K|L} \frac{\sigma}{d_\sigma}\alpha\, \phi_L^n$$

thus, the following stability criterion must be satisfied:

$$\alpha\,\delta\tau \sum_{\sigma\in\mathcal{E}(K),\sigma=K|L} \frac{\sigma}{d_\sigma} \leq |K|. \tag{4.87}$$

This filtering technique has been implemented in the CALIF^{3}S - P^{2}REMICS software and validated on simple cases, where analytical solutions exist, as shown in Fig. 4.C.1. In this figure, a one-dimensional step function is filtered at different filter widths $\widetilde{\Delta} = 8,\ 16$ and $32\ \Delta_x$ (with Δ_x the mesh size). The numerical results are compared to the analytical solutions given by: $\widehat{\phi}\,(x) = \left(1 + \mathrm{erf}\left(x\sqrt{6}/\widetilde{\Delta}\right)\right)/2$ (Moureau et al., 2011). Fig. 4.C.1 shows that the step function has been correctly filtered at the expected filters widths.

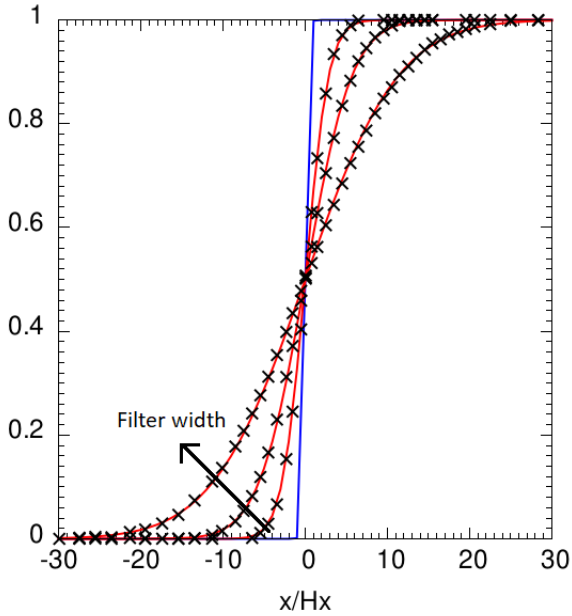

Figure 4.C.1: Filtering of a step function. The filter width Δ takes the values 4, 8, 16 and 32 times the mesh size Δ_x. (—): filtered profiles; (—): initial value of the step function; (×): analytical solutions.

Part III

Thickened flame model for large eddy simulation: calibration and application on an accelerated deflagration

Chapter 5

Simulation of a one-dimensional laminar steady premixed flame

In this chapter, a one-dimensional laminar steady premixed flame is simulated with the CALIF^{3}S-P^{2}REMICS open-source software. The aim is to assess the laminar behavior of the combustion model and its capacity to reproduce the early stages of a deflagration. This test case may be considered as a prerequisite before applications to turbulent reactive problems in two or three dimensions.

5.1 Introduction

At early stages of a deflagration taking place in a fluid at rest, the flame kernel growths and may not be wrinkled by turbulence. In order to reproduce these first moments, the combustion model used should be able to reproduce the laminar flame front propagation. In this work, the combustion is modelled with a virtually thickened flame formalism (TFLES) combined with a dynamical determination of the sub-grid scale flame wrinkling factor (Butler and O'Rourke, 1977; Colin et al., 2000) (see Chapter 2 Section 2.4.5 for more details). In order to be able to reproduce the beginning of the transient, the dynamic model must predict wrinkling values close to unity when the flame kernel is quasi laminar.

In this chapter, the behavior of the dynamic model is verified for a one-dimensional laminar steady premixed flame. The simulations have been performed with the CALIF^{3}S-P^{2}REMICS open-source software (CALIF^{3}S-P^{2}REMICS, 2020). The quasi non-dissipative second-order explicit scheme presented in Chapter 4 is used to solve the Navier-Stokes equations complemented with the species balance equations.

The chapter is structured as follows. First, the one-dimensional governing equations are presented in Section 5.2. The mean features of the planar laminar flame (laminar flame speed, characteristics of the burned mixture) are calculated and used as reference values in order to validate the implemented model. After the presentation of the numerical setup (Section 5.3), the numerical results obtained are presented (Section 5.4). Several computations have been performed by varying the thickening flame factor and the number of points used for the flame front description.

5.2 Governing equations

Let consider a one-dimensional laminar (no subgrid wrinkling factor model is thus needed) premixed flame. The mixture is composed by N_s species reacting through a one-step irreversible chemical reaction:

$$\sum_{k=1}^{N_s} \nu'_k \mathcal{M}_k \to \sum_{k=1}^{N_s} \nu''_k \mathcal{M}_k \tag{5.1}$$

where $\mathcal{M}_k$ is the chemical species symbol, ν'_k and ν''_k are respectively the molar stoichiometric coefficient of the reacting and product species. We assume that all the species have the same diffusion coefficient D, so that all Lewis numbers are equal ($\mathrm{Le}_k = \mathrm{Le}$, for $1 \leq k \leq N_s$). We suppose also that species and heat diffuse in the same way so that $\mathrm{Le} = 1$. With these assumptions and considering that viscous heating can be neglected, the flow is governed by the following system of equations:

$$\begin{aligned}
&\partial_t \rho + \partial_x(\rho\, v) = 0, \\
&\partial_t(\rho\, Y_k) + \partial_x(\rho\, Y_k\, v) = \partial_x(\rho\, D \partial_x Y_k) + \dot{\omega}_k, \quad \text{for } 1 \leq k \leq N_s, \\
&\partial_t(\rho\, v) + \partial_x(\rho\, v^2) + \partial_x p = \partial_x(\mu\, \partial_x v), \\
&\partial_t(\rho\, e) + \partial_x(\rho\, e\, v) + p\, \partial_x v = \dot{\omega}_T + \partial_x \left(\frac{\lambda}{c_p}\, \partial_x h \right),
\end{aligned}$$

with the same notations used throughout this Chapter. This system of equations is complemented by the following state law:

$$p = \rho\, \frac{R\, T}{W}. \tag{5.3}$$

When the flame is steady, writing the previous governing equations in the reference frame of the flame (moving at speed s_L) leads to:

$$\partial_x(\rho\, v) = 0, \tag{5.4a}$$

$$\partial_x(\rho\, Y_k\, v_x) = \partial_x(\rho\, D \partial_x Y_k) + \dot{\omega}_k, \quad \text{for } 1 \leq k \leq N_s, \tag{5.4b}$$

$$\partial_x(\rho\, v_x^2) + \partial_x p = \partial_x(\mu\, \partial_x v), \tag{5.4c}$$

$$\partial_x(\rho\, e\, v) + p\, \partial_x \boldsymbol{v} = \dot{\omega}_T + \partial_x \left(\frac{\lambda}{c_p}\, \partial_x h \right). \tag{5.4d}$$

The first relation (5.4a) can be rewritten as:

$$\rho_u\, v_u = \rho_b\, v_b = \rho_u\, s_L, \tag{5.5}$$

where the subscripts u and b denote respectively the fresh and the burnt mixtures.

The integration of the species mass balance (5.4b) between $x = -\infty$ and $x = +\infty$ (*i.e.* between fresh mixture and burnt mixture) leads to the following relation for the consumption speed s_L:

$$s_L = -\frac{1}{\rho_u\, (Y_k^u - Y_k^b)} \int_{-\infty}^{+\infty} \dot{\omega}_k\, dx, \quad 1 \leq k \leq N_s, \tag{5.6}$$

with Y_k^u and Y_k^b the fresh and the burnt mass fraction of species k, respectively. Let notice that if the species k is the fuel (*i.e.* if $k = F$) and if the mixture is lean or stoichiometric, by assuming that the combustion is complete and that the total mass of fuel has reacted, the previous relation is simplified:

$$s_L = -\frac{1}{\rho_u Y_F^u} \int_{-\infty}^{+\infty} \dot{\omega}_F \, dx. \tag{5.7}$$

The pressure drop between the burnt gases and the fresh gases is calculated following the same approach on the momentum balance equation (5.4c):

$$p_b - p_u = \rho_u s_L^2 \left(1 - \frac{\rho_u}{\rho_b}\right). \tag{5.8}$$

This pressure drop is usually of the order of 1 Pa, thus pressure is usually considered as constant in a one-dimensional premixed flame. Let notice that with this assumption, thanks to the state law (5.3), the density ratio reads:

$$\frac{\rho_u}{\rho_b} = \frac{W_u T_b}{W_b T_u}.$$

Assuming that burnt and fresh mixtures have the same molecular weight, the relation (5.8) can be rewritten as:

$$p_b - p_u = \rho_u s_L^2 \left(1 - \frac{T_b}{T_u}\right). \tag{5.9}$$

Finally, integrating the energy balance equation (5.4d) and assuming that the pressure drop can be neglected yields:

$$\rho_u \, s_L \, (e_b - e_u) + (p_b \, v_b - p_u \, v_u) = \int_{-\infty}^{+\infty} \dot{\omega}_T,$$

with e_u and e_b respectively the fresh and the burnt sensible energies. Using the state law (5.3) and recalling the definition of the sensible energy:

$$e = h - \frac{p}{\rho}, \tag{5.10}$$

where h stands for the sensible energy, leads to:

$$\rho_u \, s_L \, (h_b - h_u) = \int_{-\infty}^{+\infty} \dot{\omega}_T, \tag{5.11}$$

with h_u and h_b respectively the fresh and the burnt sensible enthalpies. Let recall that the heat production rate is given by:

$$\dot{\omega}_T = -\sum_{k=1}^{N_s} \Delta h_{f,k}^0 \, \dot{\omega}_k,$$

with $\Delta h_{f,k}^0$ for the formation enthalpy of the species k. Assuming that chemistry proceeds only through one irreversible reaction, $\dot{\omega}_T$ can be rewritten as a function of the fuel reaction rate $\dot{\omega}_F$ as:

$$\dot{\omega}_T = -Q\dot{\omega}_F, \tag{5.12}$$

where Q is the mass heat of the reaction given by:

$$Q = \sum_{k=1}^{N_s} \Delta h^0_{f,k} \, \frac{W_k \nu_k}{W_F \nu_F}, \tag{5.13}$$

with ν_k and ν_F the stoichiometric coefficients of the species k and of the fuel. Then, we obtain the following form for (5.11):

$$\rho_u s_L \, (h_b - h_u) = -Q \int_{-\infty}^{+\infty} \dot{\omega}_F \, dx. \tag{5.14}$$

Introducing the left side of equation (5.6) in the previous relation, yields:

$$h_b = h_u + Q \, (Y_F^u - Y_F^b). \tag{5.15}$$

The burnt temperature, which corresponds here to the adiabatic flame temperature can then be recovered using the sensible enthalpy definition, recalled here:

$$h = \sum_{k=1}^{N_s} \int_{T_0}^{T} c_{\mathrm{p},k} \, Y_k \, dT \tag{5.16}$$

where T_0 stands for the reference temperature and $c_{\mathrm{p},k}$ for the heat capacity at constant pressure for the species k. To have the adiabatic flame temperature order of magnitude, a constant heat capacity between fresh and burnt gases assumption may be made.

5.3 Numerical setup

In order to verify the good behavior of the combustion model in the laminar case, the equations are filtered. The combustion is modelled with the artificially thickened flame approach (detailed in Section 4.2.1) combined with a dynamical determination of the sub-grid scale flame wrinkling factor (Butler and O'Rourke, 1977; Colin et al., 2000). The aim is to verify that the dynamical wrinkling factor Ξ_Δ tends to one in this case (for laminar one-dimensional flames, the wrinkling factor exponent is expected to be zero).

The fresh mixture is composed of methane and air at stoichiometric conditions ($\phi = 1$ with ϕ given by (2.1)). A one step global reaction is considered:

$$CH_4 + 2 \, (O_2 + 3.76 N_2) \longrightarrow CO_2 + 2 H_2O + 7.52 N_2 \tag{5.17}$$

The molar fractions in the fresh mixture are then computed in the following way:

$$X_k^u = \frac{\nu_k'}{\sum\limits_k \nu_k'}, \tag{5.18}$$

where ν_k' is the molar stoichiometric coefficient of the reactant k. In the burnt gases, only the products remain and the molar fractions are given by:

$$X_k^b = \frac{\nu_k''}{\sum\limits_k \nu_k''}, \tag{5.19}$$

where ν_k'' is the molar stoichiometric coefficient of the product k. The corresponding mass fractions are thus computed such as:

$$Y_k^u = \frac{X_k^u\, W_k^u}{\sum\limits_k X_k^u\, W_k^u}, \qquad Y_k^b = \frac{X_k^b\, W_k^b}{\sum\limits_k X_k^b\, W_k^b}, \tag{5.20}$$

with W_k^u and W_k^b the molar mass of the species k respectively in the fresh and in the burnt mixtures. In order to have an initial state as close as possible from the solution, the fuel mass fraction is initialized with the following function:

$$Y_F^0 = 0.5 \left[1 - \operatorname{erf}\left(\frac{4}{\delta_r}\left(x - X_{ign}\right)\right)\right] Y_F^u,$$

with Y_F^u computed with (5.20), X_{ign} the flame front position and δ_r the numerical flame thickness such as $\delta_r = \delta_L^0\, \mathcal{F}$. This choice allows to initialize the flame kernel directly with a thickened flame front. In order to compute the other chemical species, the neutral gas mass fraction and the mixture fraction must be defined. The first one is obtained with (5.20), the second one with (4.34) taking into account that the mixture fraction is the same in the fresh and in the burnt mixtures for a perfectly premixed flame.

The initial temperature is initialized with the following function:

$$T_0 = 0.5 \left[1 + \operatorname{erf}\left(\frac{4}{\delta_r}\left(x - X_{ign}\right)\right)\right] \left(T_b - T_u\right) + T_u$$

where the fresh temperature is set to $T_u = 300\,\mathrm{K}$, whereas the burnt gases temperature is computed using expression (5.15). The adiabatic flame temperature obtained in such way is close to 2300 K (with a constant heat capacity assumption). The initial velocity field is computed using relation (5.5):

$$v_0 = \frac{v_u \rho_u}{\rho_0}$$

where the fresh gases velocity is set at the laminar flame speed: $v_u = s_L$ and the initial density ρ_0 is obtained thanks to the equation of state (5.3). The pressure is considered as uniform at the initialization $p_0 = 101325\,\mathrm{Pa}$.

The reaction rate is computed with the Arrhenius law as described in equation (4.10). The pre-exponential coefficient is $A = 6\ 10^5$ uSI and the activation energy is $E_a = 8.3\ 10^4\ \mathrm{J.mol^{-1}}$.

The combustion filter size is set to $\Delta = 1.4\, \mathcal{F}\, \delta_L^0$. For a stochiometric methane/air flame at atmospheric conditions, like those studied here, $\delta_L^0 \approx 0.42\,\mathrm{mm}$ (Quillatre, 2014). The test filter width is set to $\widehat{\Delta} = 1.5\,\Delta$, whereas the size of the Gaussian filter which replace the averaged operator $\langle\cdot\rangle$ is set to $\Delta_{avg} = 3\,\Delta$. The inner cut-off length scale is set at $\delta_c = 2\delta_L^0$.

The simulations are performed on a one-dimensional computational domain $[0, L]$ with $L = 40\,\mathrm{mm}$. The mesh size Δ_x is set in function of the thickening factor $\mathcal{F}$, the laminar flame thickness δ_L^0, and the number of grid points in the front n, such as: $\Delta_x = \delta_L^0\, \mathcal{F}/n$. The flame front position is located in the middle of the domain: $X_{ign} = L/2 = 20$ mm.

On the burnt gas side, inlet boundary conditions are imposed, with an inlet velocity equal to the laminar flame speed $s_L = 0.42\,\mathrm{m.s^{-1}}$ (Yu et al., 1986; Poinsot and Veynante, 2012), in order to maintain the flame at the same position. On the fresh gas side, the boundary condition corresponds to a free outlet condition ensuring a constant thermodynamic pressure over time.

The time step is computed to have an acoustic Courant-Friedrichs-Lewy condition CFL = 0.33 for all the simulations. In order to reach a steady state, 0.04 s are simulated.

5.4 Numerical results

Several simulations are performed by varying the thickening factor value and the number of points used in order to describe the flame front. A numerical simulation with a forced efficiency factor is also made in order to show the impact of Ξ_Δ on the numerical results. The test cases studied here are summarized in Table 5.1.

Name	$\mathcal{F}$	n	Δ_x	dt	Ξ_Δ
case 1 (reference)	1	10	$42\,\mu$m	$0.038\,\mu$s	dynamic
case 2	5	10	$210\,\mu$m	$0.19\,\mu$s	dynamic
case 3	10	5	$840\,\mu$m	$0.76\,\mu$s	dynamic
case 4	10	10	$420\,\mu$m	$0.38\,\mu$s	dynamic
case 5	10	3	$1400\,\mu$m	$1.27\,\mu$s	dynamic
case 6	10	10	$420\,\mu$m	$0.38\,\mu$s	2

Table 5.1: List of the one-dimensional simulations.

Reference case (case 1)

The first steady laminar flame simulated has a thickening factor $\mathcal{F} = 1$ and $n = 10$ grid points in the front. Therefore, the mesh grid is very fine allowing a precise description of the reactive flow. This case will be used as a reference for all the simulations presented here.

The mesh grid size is set at $\Delta_x = \mathcal{F}\delta_L^0/n = 42\,\mu$m. Thus, the total number of cells in the domain is 952. The time step is set at $0.038\,\mu$s.

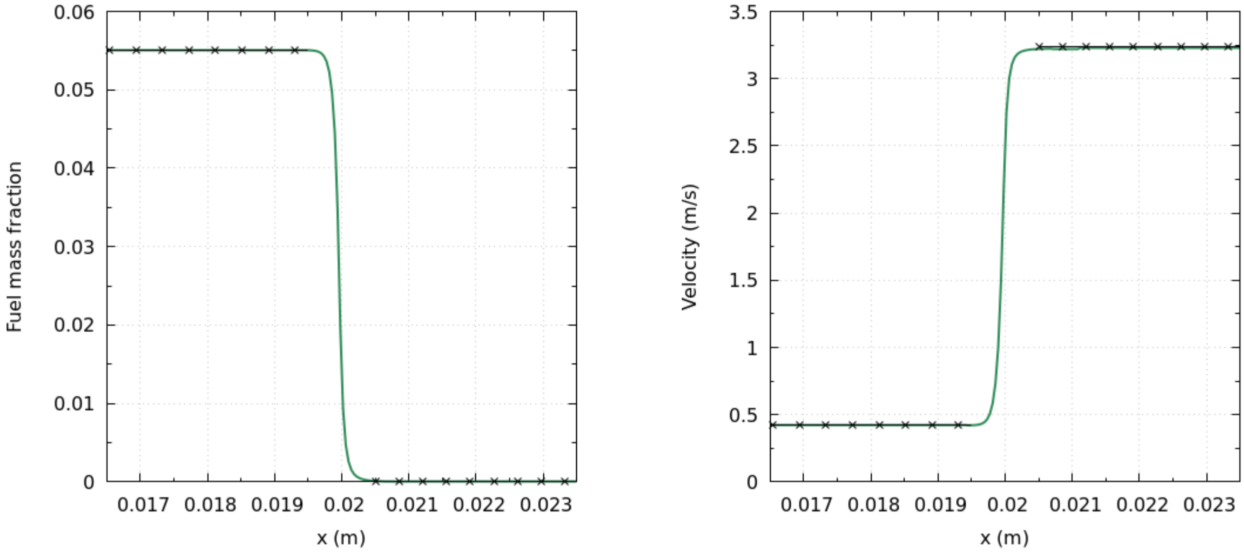

Figure 5.1: Fuel mass fraction (left side) and flow velocity (right side) for a one dimensional laminar flame. (—): case 1; (—×—): reference values.

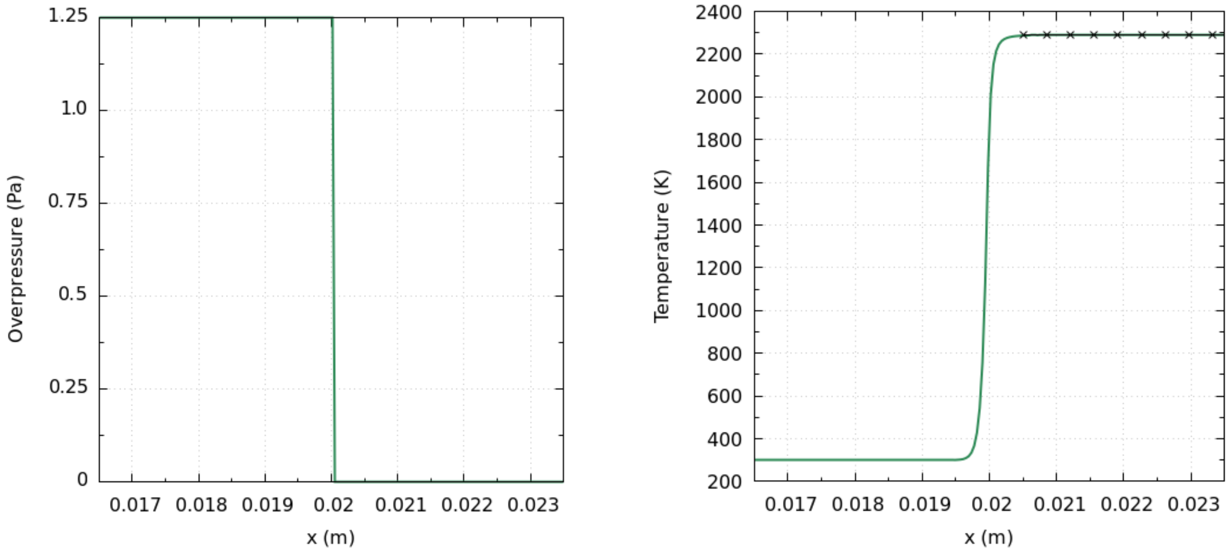

Figure 5.2: Overpressure (left side) and temperature (right side) for a one dimensional laminar flame. (—): case 1; (—×—): reference values.

In Fig. 5.1 are plotted respectively the fuel mass fraction and the velocity obtained at the end of the computation. The left side of the domain corresponds to the fresh gases zone and the right side to the burnt gases zone. For a stoichiometric mixture, as all the reactant are transformed in products, the fuel mass fraction is completely consumed in the burnt gases zone. On the right part of Fig. 5.1, the numerical velocity is compared to the reference values obtained with the mass conservation equation. The reference burnt gases speed is computed as $v_b = v_u\, \rho_u/\rho_b$, ρ_u and ρ_b being obtained thanks to the equation of state (5.3) by setting $p_u = p_b = 101325\,\mathrm{Pa}$. The simulation results are in good agreement with the reference values for both the fuel mass fraction and the velocity fields.

Fig. 5.2 shows the pressure (left side) and the temperature (right side). The reference temperature in the burnt gases is estimated to be equal to the adiabatic flame temperature calculated using expression (5.15) and represented on this figure. The simulation results matches the reference values. As expected the pressure drop is low: it is of the order of magnitude of 1.25 Pa. It can be estimated using expression (5.8).

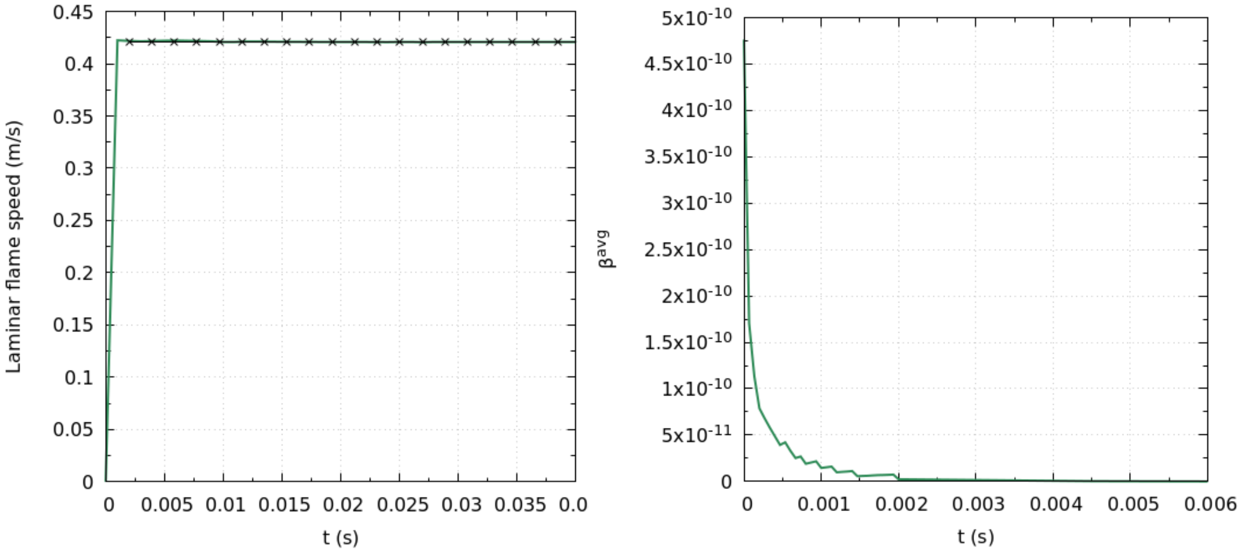

Figure 5.3: Laminar flame speed (left side) and mean dynamic wrinkling factor exponent parameter (right side) for a one dimensional laminar flame. (—): case 1; (×): experimental value.

The left side of Fig. 5.3 shows the laminar flame speed. This latest is calculated from numerical results using equation (5.6) matching the experimental value 0.42 $\mathrm{m.s^{-1}}$ (Yu et al., 1986; Poinsot and Veynante, 2012). The simulation converges and reaches the right value for the laminar flame speed in a short time and stays stable showing that the initial profiles are close to the solution.

The statistical quantity β^{avg} defined by:

$$\beta^{avg} = \frac{\int_{\mathcal{V}_f} \beta \, d\mathcal{V}}{\int_{\mathcal{V}_f} d\mathcal{V}}, \tag{5.21}$$

is the spatially averaged β parameter over the flame volume $\mathcal{V}_f$ defined such as: $0.05 < \tilde{c} < 0.95$. The time evolution of β^{avg} is plotted on the right side of Fig. 5.3. When the flow is laminar, the wrinkling factor has to be equal to one, and thus β must be equal to zero, as there is no subgrid scale turbulence. As shown in Fig. 5.3, the mean winkling factor exponent is almost null, as expected. Let notice that here, only the beginning of the computation is plotted for the sake of clarity. The dynamic formulation for the combustion model behaves correctly in case of laminar regime.

Impact of the thickening factor (cases 1, 2 and 4)

The simulations presented here have different thickening factors while keeping constant the number of grid points in the front. The aim is to validate the implemented numerical scheme by verifying that the results overlap after doing a variable change such as $x' = x/\mathcal{F}$ (see Chapter 2 Section 2.4.5). The two simulations presented here (cases 2 and 4) have a thickening factor of $\mathcal{F} = 5$ and $\mathcal{F} = 10$ respectively with the same number of grid points: $n = 10$. The simulation of case 1, presented above, is kept here in order to be used as a reference.

The mesh grid size is $\Delta_x = 0.21\,\text{mm}$ (190 cells) for case 2 and $\Delta_x = 0.42\,\text{mm}$ (95 cells) for case 4. The time step is set at $0.19\,\mu\text{s}$ and $0.38\,\mu\text{s}$ for cases 2 and 4 respectively.

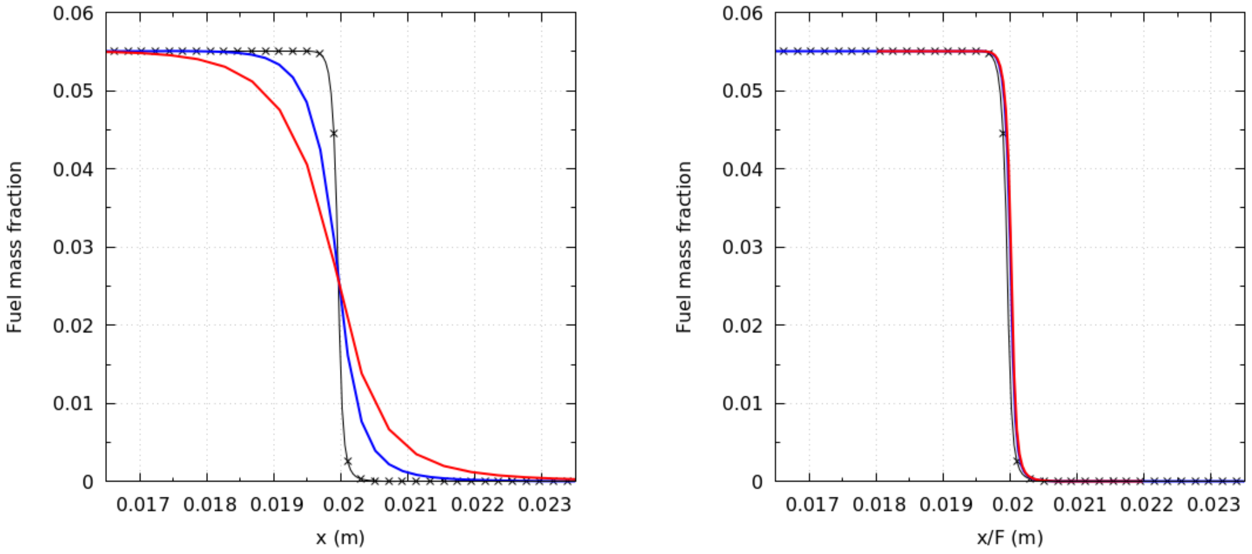

Figure 5.4: Fuel mass fraction without (left side) and with (right side) a normalized by $\mathcal{F}$ x-axis for a one dimensional laminar flame. (—×—): case 1; (—): case 2 and (—): case 4.

Fig. 5.4 represents the fuel mass fraction with (right side) and without (left side) normalizing the space coordinate by the $\mathcal{F}$ factor. The left side of Fig. 5.4 shows that the flame front thickness is $\mathcal{F}\,\delta_L^0$ for both simulations, as expected. The normalization of the x-axis leads to a superposition of the fields as shown on the right side of Fig. 5.4. Cases 2 and 4 matches well the reference case showing that the fuel has been fully consumed in the front flame leaving only products in the burnt gases (and inert gases).

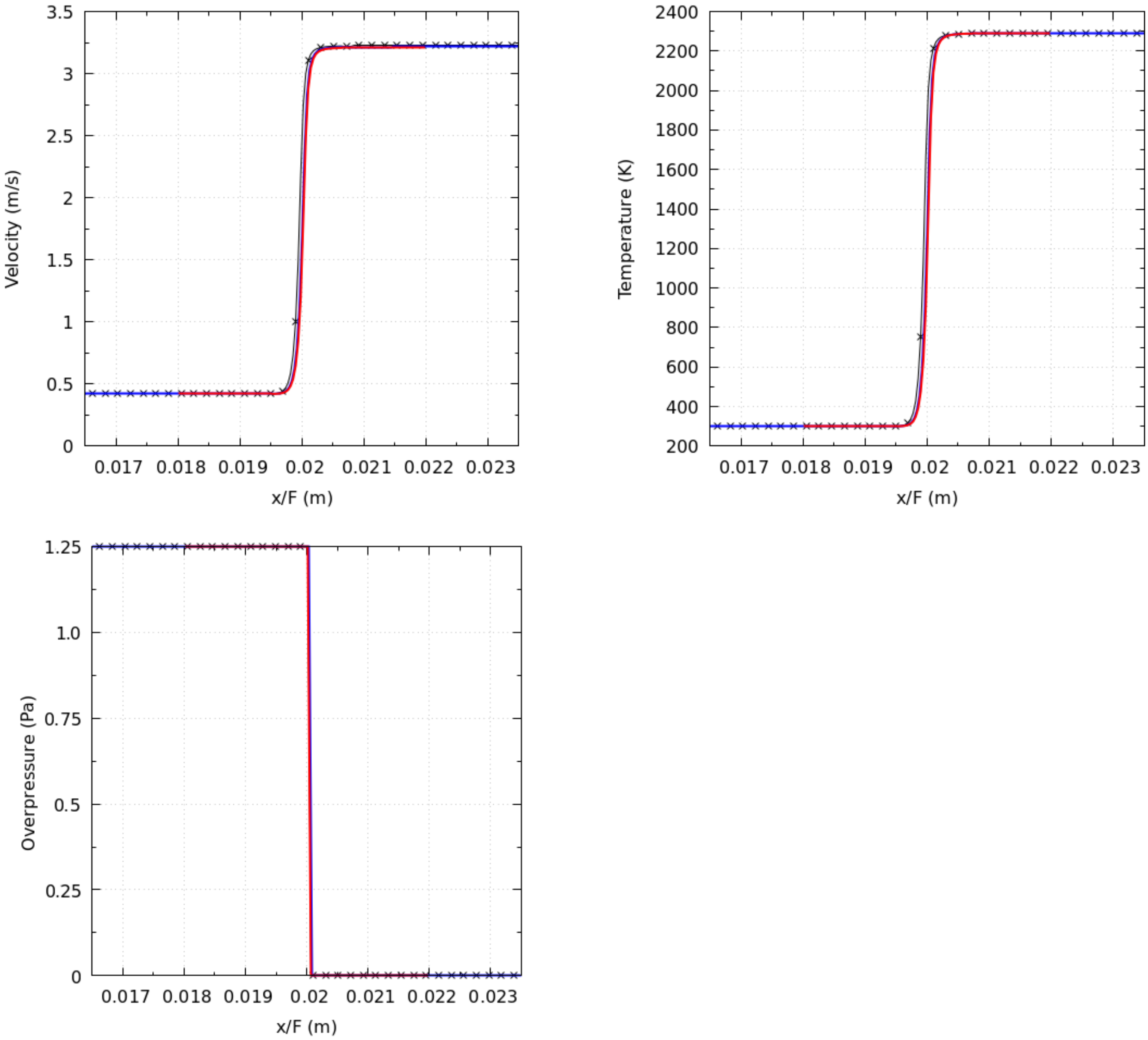

Figure 5.5: Velocity (top left side), temperature (top right side) and pressure (bottom) for a one dimensional laminar flame. (—×—): case 1; (🟦): case 2 and (🟥): case 4.

The velocity, the temperature and the pressure profiles for cases 2 and 4 are shown in Fig. 5.5 and compared to the reference case results. The normalization of the x-axis by $\mathcal{F}$ leads to a superposition of the profiles whatever the value of $\mathcal{F}$ is.

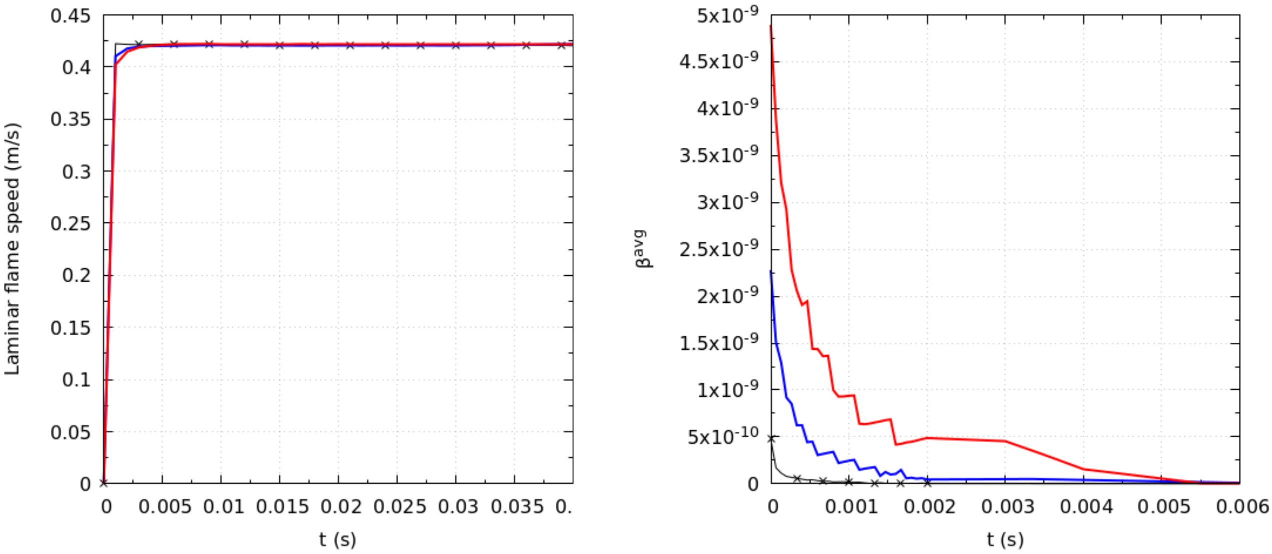

Figure 5.6: Laminar flame speed (left side) and mean dynamic wrinkling factor exponent (right side) for a one dimensional laminar flame. (—×—): case 1; (—): case 2 and (—): case 4.

In the left part of Fig. 5.6, the laminar flame speed computed for cases 2 and 4 are compared to the reference case. The numerical results progressively converges to the same value of s_L, independently of the $\mathcal{F}$ factor value.

In the right part of Fig. 5.6, the mean wrinkling factor parameter β^{avg} is plotted for cases 2 and 4. The β^{avg} parameter values are small enough to be considered as null. Therefore the wrinkling factor is unitary whatever the $\mathcal{F}$ factor is.

Impact of the number of grid points in the flame front (cases 3, 4 and 5)

Now let us observe cases 3 and 5. The purpose here is to analyse the influence of the mesh resolution on the numerical results. The thickening factor is set to $\mathcal{F} = 10$. Case 3 and case 5 have respectively $n = 5$ and $n = 3$ points in the front. The mesh grid size is $\Delta_x = 0.84\,\text{mm}$ for case 3 (48 cells) and $\Delta_x = 1.4\,\text{mm}$ for case 5 (29 cells). The time step is set to $0.19\,\mu\text{s}$ for case 3 and to $1.27\,\mu\text{s}$ for case 5. The case 4 shown previously, is kept here for comparison.

The laminar flame speeds computed for cases 3 and 5 are plotted in Fig. 5.7 and compared to the ones computed for case 1 and case 4. Fig. 5.7 shows close results between case 3 and 4. The other unknowns computed for case 3 are also quite similar to those obtained for case 4 and are not shown here. The convergence is not reached for case 5 because of too few grid points in the flame front ($n < n_{min}$), leading to a incorrect resolution of the laminar flame.

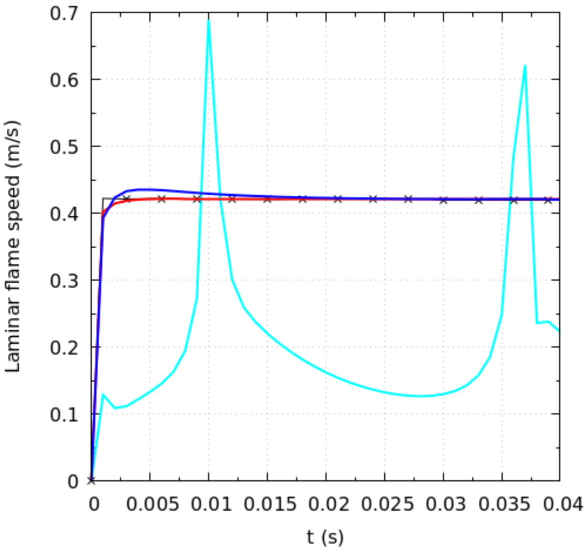

Figure 5.7: Laminar flame speed of a one dimensional laminar flame cases 1, 3, 4 and 5: (−×−): case 1; (—): case 3; (—): case 4; (—): case 5.

Constant efficiency function (case 6)

The thickening factor is set to $\mathcal{F} = 10$ and the number of cells in the flame front to $n = 10$. The mesh grid size is thus $\Delta_x = 0.42\,\text{mm}$. The total number of cells is 95. The time step is set to $0.38\,\mu\text{s}$. The value of the efficiency function Ξ_Δ is constant and is forced at 2. The aim here is to validate the proper functioning of the implemented subgrid wrinkling model by verifying the proportionality between laminar flame speed and imposed wrinkling factor.

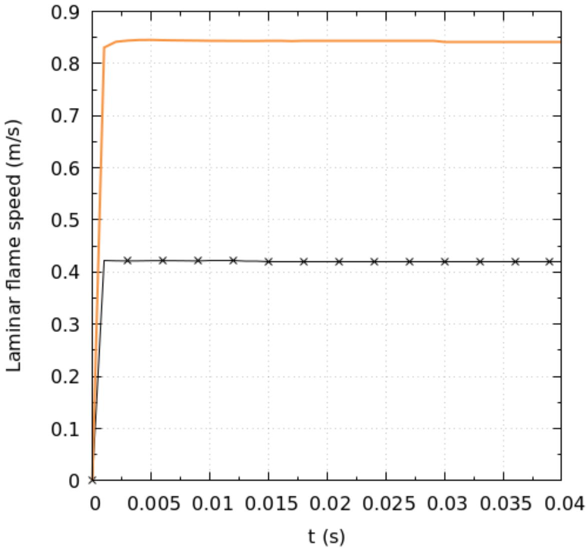

Figure 5.8: Laminar flame speed of cases 1, 4 and 6. (−×−): case 1; (—): case 6.

Fig. 5.8 shows the laminar flame speed computed for case 6 and compared to the reference case. The laminar flame speed is expected to be twice of the laminar flame speed computed when the wrinkling factor is forced at $\Xi_\Delta = 2$. This conclusion is confirmed by the results plotted on Fig. 5.8.

5.5 Conclusion

Large eddy simulations of a steady laminar planar methane/air flame were run in order to validate the implemented artificially thickened flame model. The numerical results recover the exact values of temperature, flow velocity and pressure ahead and behind the flame front. The laminar flame speed is computed and match the experimental data for a stoichiometric methane/air flame. The laminar behavior of the dynamic subgrid model is assessed: the dynamic model predicts winkling values close to unity. The number of grid points needed for a good description of the flame front is at least 5. These one-dimensional simulations allow us to conclude that the implemented combustion model is able to reproduce laminar premixed flame propagation.

This test case may be considered as a prerequisite before applications to turbulent reactive problems in two or three dimensions. However, the conclusions reached here (for example the minimum number of points in the front) may differ for more complicated cases such as turbulent reactive flows in two or three dimensional simulations.

Chapter 6

Simulations of an accelerated deflagration in a semi confined chamber

An accelerated deflagration in an obstructed rectangular semi-confined chamber has been simulated with three different obstacle position configurations. The simulations are first performed with the LES approach presented in the previous Chapters. The combustion is modelled using a virtually thickened flame formalism combined with a dynamical determination of the subgrid scale flame wrinkling factor. Two-dimensional and three-dimensional simulations are performed. The influence of the location of obstacles and the impact of the thickened flame approach parameters are investigated. The results are compared with experimental data. The LES approach is then compared to the RANS approach already implemented in the CALIF^{3}S -P^{2}REMICS *software using a turbulent flame speed closure combustion model. The influence of the location of obstacles on the flame propagation is well captured by LES. Moreover, LES results highlight the importance of the wrinkling factor dynamical formulation to capture the transition from laminar to turbulent regimes. Regarding the RANS approach, the results computed with different turbulent flame speed closure are compared. Most of them are not able to describe properly the flame front propagation and underestimate the overpressure peak.*

6.1 Introduction

Accelerated turbulent deflagrations, potentially transiting to detonation, are a major hazard in industrial plants, and more specifically in nuclear power plants. The pressure increase is governed by a complex unsteady interaction between flame propagation, turbulence and geometry. This overpressure is often considered as the key parameter, since it controls the severity of the explosion and corresponding damages. This complex phenomenon is very challenging for computational fluid dynamics problems since it involves a large spectrum of spatial and time scales and a large range of flow and combustion regimes.

In this chapter accelerated turbulent deflagration in a semi-confined chamber are studied. In semi-confined situations such as the ones discussed later, two main mechanisms explain the pressure variations:

- the combustion rises the gas volume leading to a pressure increase in the chamber as long as the combustion lasts,
- the flame reaching the chamber exit leads to the decrease of pressure.

Most of the time, a combination of these two mechanisms is responsible for the overpressure generated. When a flame propagates through a flammable mixture, two parameters may affect the overpressure amplitude:

- the flame front speed: the faster is the flame, the higher is the burning rate, which tends to increase the pressure,
- the obstruction of the flow: the more the flow meets obstacles, the more the fresh gases propagation is blocked, leading to an increase of the pressure.

Obstacles influence the overpressure amplitude as they play a role in the two previous features. Indeed, obstacles generate turbulent motions which accelerates the flame. The obstacles shape, size and position are important features in the generated overpressure. However, other parameters influence the overpressure behavior such as: domain geometry, type of fuel, proportion of fuel in the oxidant, ignition conditions, state of the flow before ignition... (Bradley and Mitcheson, 1978; Ibrahim and Masri, 2001; Gubba et al., 2009; Bauwens et al., 2010; Chao et al., 2010)

Some experiences have been carried out in semi-confined configurations obstructed by obstacles to study the interactions between flame and turbulence as well as the impact of geometry and fuel type on the overpressure and front propagation (Fairweather et al., 1999; Masri et al., 2000; Patel et al., 2002a; Kent et al., 2005a; Hall et al., 2009; Masri et al., 2012; Wen et al., 2013). The front may also transit to detonation after an significant acceleration of the front (Oran and Gamezo, 2007; Dorofeev, 2011). In our framework, only deflagrations (subsonic explosions) are simulated.

In order to simulate explosions, CFD is today the best method to approach the phenomena. Few decades ago, CFD was not considered for real industrial purposes, now, it is more and more spread in the community. LES approach has been popularized thanks to the evolving computational resources and massively parallel machines (Janicka and Sadiki, 2004; Pitsch, 2006; Poinsot and Veynante, 2012; Gicquel et al., 2012). LES of explosions in semi-confined chamber have already been carried out in literature (Patel et al., 2002b; Kirkpatrick et al., 2003; Di Sarli et al., 2009a,b, 2010; Gubba et al., 2009; Ibrahim et al., 2009; Wen et al., 2012; Quillatre, 2014; Xu et al., 2015; Mouriaux et al., 2016; Volpiani, 2017; Li et al., 2018; Elshimy et al., 2021).

In this chapter the experimental set-up of Wen et al. (2013) is simulated. The experimental set-up is an obstructed rectangular semi-confined chamber. The influence of the obstacles locations on the flame propagation is studied. Three different configurations for the obstacles location are available. One of those configurations has some similarities with Patel et al. (2002a) experience. The simulations are performed with the CALIF^{3}S-P^{2}REMICS open-source software (CALIF^{3}S-P^{2}REMICS, 2020). The combustion is modelled using a virtually thickened flame formalism (TFLES) (Butler and O'Rourke, 1977; Colin et al., 2000) (see Chapter 2 Section 2.4.5 for more details). The subgrid scale flame wrinkling is computed dynamically and modelled with the Veynante and Moureau (2015) expression improved in order to take into account flame front interactions and flame-wall interactions (Mouriaux et al., 2016) (see Chapter 2 Section 2.4.6 for more details). The quasi non-dissipative second-order explicit scheme presented in Chapter 4 is used to solve the filtered Navier-Stokes equations complemented with the species balance equations.

Another approach is available for the turbulent deflagration modelling in the CALIF^{3}S -P^{2}REMICS software. It is based on a RANS description of turbulence and on a *turbulent flame-speed closure* combustion model (Lipatnikov and Chomiak, 2002; Peters, 2000). The flame brush location is determined, solving the so-called level set G-equation. To handle partially premixed situations, the species mass balances are solved, but reaction rates are expressed from the level-set function. The model is closed by a turbulent flame speed correlation (Peters, 2000; Bradley et al., 1992b; Bray, 1990; Zimont, 2000; Goulier, 2015). A comparison between this two different approaches is made in this chapter.

The chapter is structured as follows. First, the experimental set-up of Wen et al. (2013) is described in Section 6.2. Then, two-dimensional simulations are presented using the LES approach in Section 6.3. The purpose of these simulations is twofold: first, the model parameters are adjusted for the three-dimensional computations more expensive in terms of CPU time, second they allow at a moderate cost to investigate several parameters such as the impact of the obstacle location, the thickening factor, the dynamic computation of the wrinkling factor, the Mouriaux et al. (2016) correction... Afterward, three-dimensional simulations have been carried out on the most turbulent configuration. The numerical results are described in Section 6.4. Finally, after a description of the combustion model used for the RANS approach, a comparison between RANS and LES numerical results on the most turbulent obstacle configuration is presented in Section 6.6.

6.2 Experimental set-up

The experimental configurations investigated by Wen et al. (2013) are chosen for the numerical simulations. The combustion chamber has a 150 mm square cross section and a height of 500 mm. The bottom of the chamber is closed whereas the top is an open-end, which is sealed at first with a thin polyvinyl chloride membrane to contain the premixed flammable mixture before ignition. The facility is plotted in Fig. 6.1.

When deflagration occurs, the membrane is ruptured allowing unburnt and burnt mixtures to escape. The chamber is equipped with three obstacles of 75 mm length, 150 mm width and 10 mm height, designated by S1, S2 and S3 in Fig. 6.1. The first one is located at 100 mm from the bottom of the facility. The vertical distance between each obstacle is 100 mm. Three configurations with different transverse obstacle locations are studied here (see Fig. 6.1). For the first one, the obstacles are placed at the center of the chamber. In the second one, they are all on one side of the chamber and in the third configuration, obstacles are staggered on both sides of the chamber.

The explosive atmosphere is a stoichiometric methane-air mixture at initial ambient pressure and temperature. Initially, the fluid is assumed to be at rest in the device. The ignition point is located at the bottom of the facility (see Fig. 6.1).

Overpressure is detected with a pressure transmitter at the bottom of the chamber next to the ignition location. This sensor has a saving frequency of 5 kHz with a range of $0-1$ bar and a total error of 0.25 %. The experimental overpressure curves are obtained by repeating the same experience several times and then, the profiles are time shifted in order to coincide the overpressure peak moments. Afterwards, the profiles are averaged to alleviate any impact of external uncertainties.

A high-speed digital camera allowing to have high resolution images (2000 images per second) is used to visualize the flame front and its turbulent structures. In addition, the experimental flame front position is obtained thanks to these images of the flame front. Experimental data on flame front velocity are available, but the experimental speed computation method has not been detailed by the authors. Thus, the experimental flame front velocity data are not used for the comparison with numerical results.

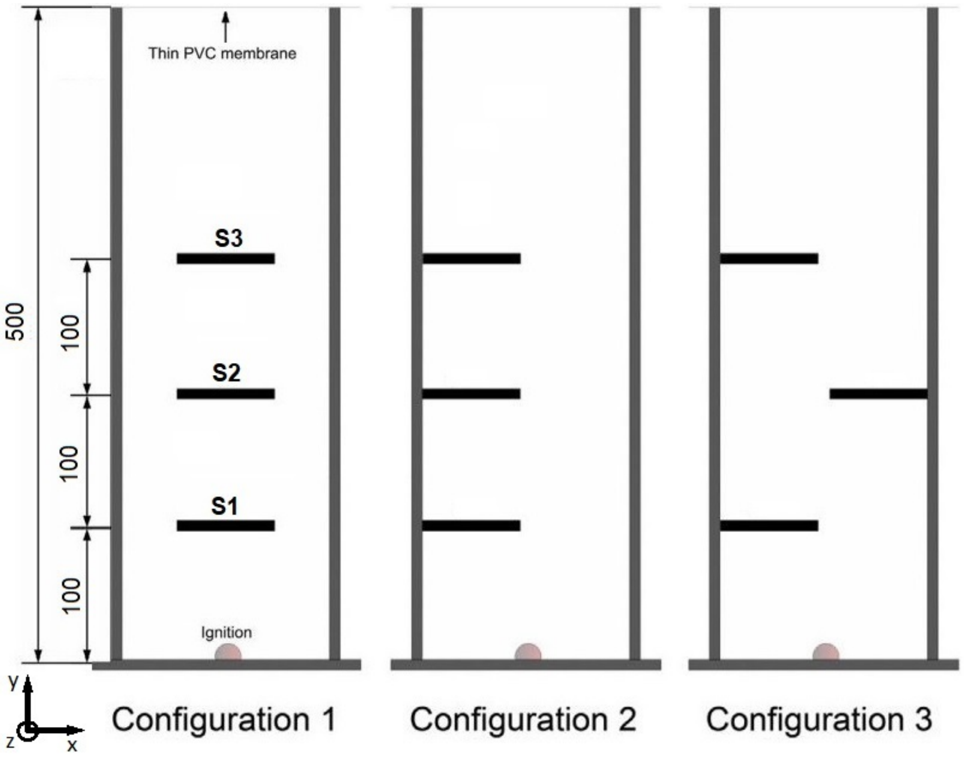

Figure 6.1: Experimental set-up.

6.3 LES numerical results: two-dimensional simulations

The numerical set-up and the simulation results obtained with the CALIF^{3}S - P^{2}REMICS software with the LES approach in the two-dimensional domain are presented in this section.

6.3.1 Numerical set-up for a two-dimensional domain

The longitudinal plan (x, y) is simulated in order to perform at first, two-dimensional simulations. The computational domain is shown in Fig. 6.2 for the three configurations of obstacles. The computational domain is extended outside the combustion chamber (the atmospheric zone is framed by a red rectangle at the top right of Fig. 6.2) in order to push further away the outlet boundary condition at the chamber end, reducing pressure waves reflection on the boundary generated by the deflagration, and to allow a more realistic reproduction of the gas expansion exiting from the combustion chamber into the atmosphere. The mesh is composed by a non-uniform structured grid with rectangular cells. Inside the chamber, the mesh size Δ_x is kept constant (as seen on the zoom in around the obstacle at the bottom left of Fig. 6.2). In the atmospheric zone, two separate regions are distinguished, right after the chamber exit ($y = 500\,\mathrm{mm}$), the green rectangular surface shown in Fig. 6.2 has the same mesh size like inside the chamber ($y < 500\,\mathrm{mm}$). The second zone, which is the rest of the atmospheric zone, the mesh size increases linearly along the y and x axis in the atmospheric zone ($y > 500\,\mathrm{mm}$) until having a mesh size 20 times larger than Δ_x allowing to reduce significantly the number of cells.

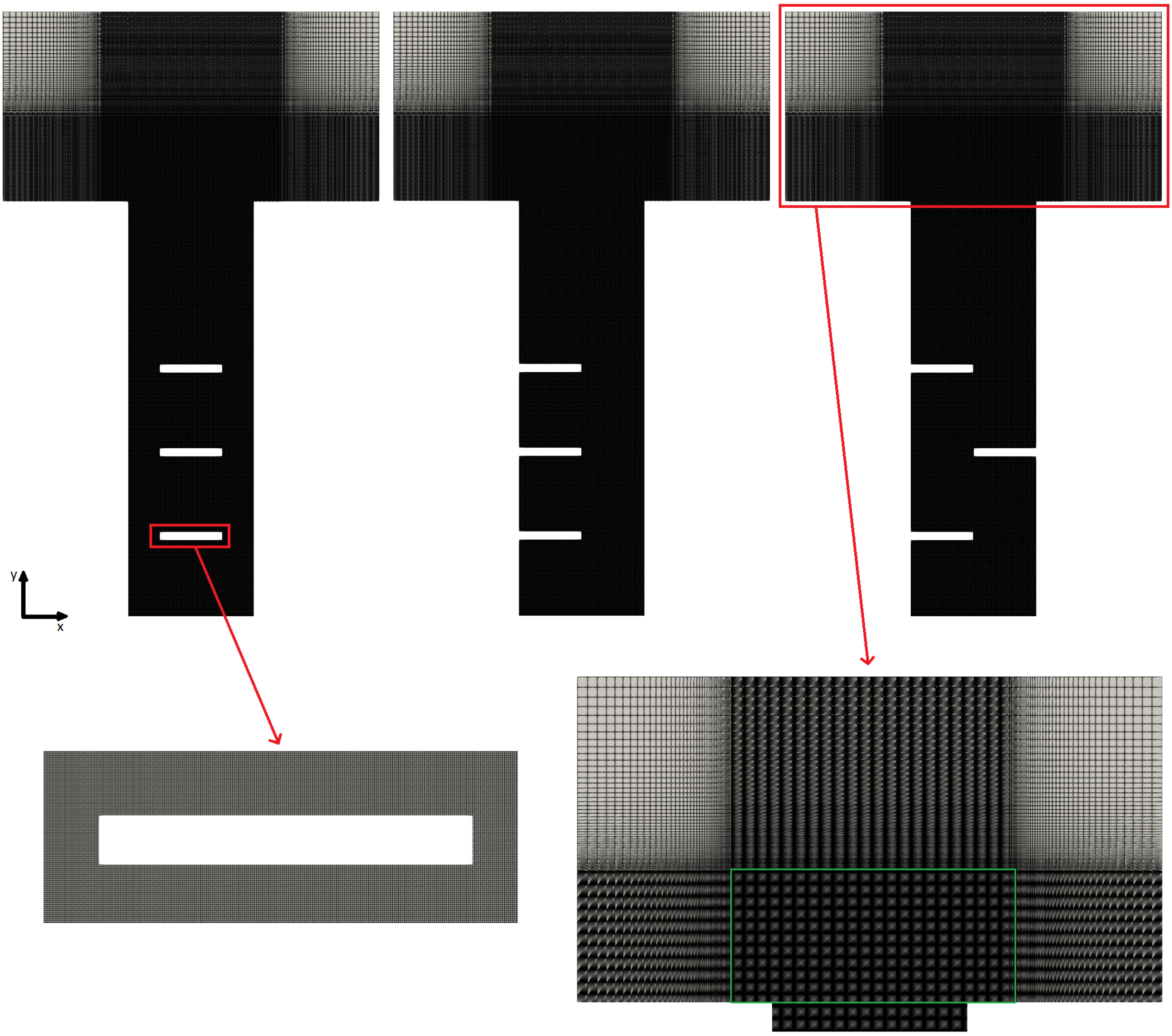

Figure 6.2: Two-dimensional mesh grid of the three configurations of Wen et al. (2013) (top) and zoom on the grid around an obstacle (bottom). (🟥): zoom in; (🟩): fine meshes in the atmospheric zone.

Adiabatic and no-slip wall boundary conditions were applied at the solid interfaces (chamber and obstacle walls). A free outlet condition is enforced at the atmospheric zone boundaries where the pressure is maintained at $p_{ext} = 101325\,\mathrm{Pa}$.

The chemistry is simply described with a one step global reaction which reads for a methane/air mixture at stochiometric conditions:

$$CH_4 + 2\,(O_2 + 3.76N_2) \longrightarrow CO_2 + 2H_2O + 7.52N_2. \tag{6.1}$$

The reaction rate is computed with the Arrhenius law described in expression (4.10). The pre-exponential coefficient is $A = 6\ 10^5$ uSI and the activation energy is $E_a = 8.3\ 10^4$ J.mol^{-1}.

The ignition is made with an initial flame kernel radius $r = r_c$, r being the distance between the flame front and the ignition point. The fuel mass fraction and the temperature are initialized with the following expression:

$$\phi_0 = \frac{1}{2}\left[1 + \mathrm{erf}\left(\frac{4}{\mathcal{F}\delta_L^0}(r - r_c)\right)\right](\phi_b - \phi_u) \tag{6.2}$$

where ϕ stands for the fuel mass fraction or the temperature and the subscripts b and u denotes respectively the burnt and the fresh mixture. Such initialization has the advantage of avoiding any complex ignition scheme and directly set the flame front to a thickness $\mathcal{F}\,\delta_L^0$, with $\mathcal{F}$ the thickening factor and δ_L^0 the laminar flame thickness. The initial kernel radius r_c value has been investigated, a too small radius does not allow the explosion ignition, in the other hand, a too large radius would influence the flow dynamics (Volpiani, 2017). The initial kernel radius value is set at the minimum kernel radius allowing ignition of the explosion: $r_c = 8\,\mathrm{mm}$. The fluid is assumed to be at rest in the facility.

The thickening factor $\mathcal{F}$ is calculated as a function of the laminar flame thickness δ_L^0 and the space step Δ_x such as $\mathcal{F} = n\Delta_x/\delta_L^0$, with n the number of cells needed to resolve the flame front. For a stochiometric methane/air flame at atmospheric conditions, like those studied here, $\delta_L^0 \approx 0.42\,\mathrm{mm}$ (Quillatre, 2014). The wrinkling factor is modeled using Veynante and Moureau (2015) expression with Mouriaux et al. (2016) correction, briefly reminded here:

$$\Xi_\Delta = \left(\frac{\Delta}{\delta_c}\right)^{\beta}, \tag{6.3}$$

with Δ the combustion filter size, δ_c the inner cut-off length size. The wrinkling factor exponent β then is expressed by:

$$\beta = \frac{\log\left(\Sigma_1/\Sigma_2\right)}{\log(\gamma)}. \tag{6.4}$$

with $\gamma = \sqrt{1 + \left(\widehat{\Delta}/\Delta\right)^2}$, $\widehat{\Delta}$ being the test-filter size corresponding to a Gaussian filter (details on the implementation are given in Chapter 4 Appendix 4.C), and

$$\begin{aligned} \Sigma_1 &= \langle\ \widehat{|\nabla\tilde{c}|}\ \rangle & (6.5)\\ \Sigma_2 &= \langle\ (1-\hat{\zeta})|\,\widehat{\nabla\tilde{c}}\,| + \hat{\zeta}\,\widehat{|\nabla\tilde{c}|\,\boldsymbol{n}\cdot\boldsymbol{N}}\ \rangle. & (6.6)\end{aligned}$$

where c is the progress variable given by (4.28) and ζ the sensor which allows to detect flame front interactions and given by (4.33). To compute the wrinkling factor exponent, needs to set some parameters. The combustion filter size is set to $\Delta = 1.4\,\mathcal{F}\,\delta_L^0$. The test filter width is set to $\widehat{\Delta} = 1.5\,\Delta$, whereas the size of the Gaussian filter which replace the averaged operator $\langle\cdot\rangle$ is set to $\Delta_{avg} = 3\,\Delta$. The inner cut-off length scale is set at $\delta_c = 2\,\delta_L^0$ for all the simulations. The resolved flame surface fractal behavior is inspected in Appendix 6.A in order to validate the test-filter size.

The wrinkling factor Ξ_Δ is computed dynamically at a fixed frequency in order to save computational costs linked to the filtering operations. Indeed, the numerical time step is based on the acoustic Courant-Friedrichs-Lewy (CFL) condition while the model parameter is expected to evolve with convective times. Therefore, the dynamic procedure is not applied at every time step. A simple analysis that computes the flame convective times shows that updating the model parameter every 150 time steps is enough for capturing the subgrid scale motions. More frequent updates do not change the results significantly. The computation duration is considerably reduced. For example, LES 3 (see Table 6.1 below) computing duration was about 13 hours and 12 minutes over 180 cores with a total of 1 hour and 3 minutes only for the wrinkling factor computation and the filtering operations (approximately 7.95% of the computing time).

The time step is selected to have an acoustic Courant-Friedrichs-Lewy condition CFL = 0.1 for all the simulations.

Several simulations are performed by varying the thickening factor value and the number of points used to describe the flame front. A numerical simulation with a constant wrinkling factor exponent β (LES 4) and another (LES 5) without the Mouriaux et al. (2016) correction of β for front/wall interactions and flame fronts interactions (expression (2.61)) are also made. Table 6.1 summarizes up all two-dimensional simulations.

Name	Configuration	$\mathcal{F}$	n	Δ_x in the chamber	Number of cells	β	β correction
LES 1	1	6	6	0.4 mm	643 819	dynamic	yes
LES 2	2	6	6	0.4 mm	643 819	dynamic	yes
LES 3	3	6	6	0.4 mm	643 819	dynamic	yes
LES 4	3	6	6	0.4 mm	643 819	0.33	yes
LES 5	3	6	6	0.4 mm	643 819	dynamic	no
LES 6	3	6	5	0.48 mm	447 374	dynamic	yes
LES 7	3	6	10	0.24 mm	1 791 554	dynamic	yes
LES 8	3	9	10	0.36 mm	796 066	dynamic	yes
LES 9	3	12	10	0.48 mm	447 374	dynamic	yes

Table 6.1: List of two-dimensional simulations.

A backward time shift for each simulation is applied to numerical results to match the experimental overpressure peak. This calibration is also common in experimental set-ups as the ignition duration may vary between each run due to external parameters (ambient temperature, pressure, variation in spark energy, ...).

6.3.2 Impact of obstacles location

First, the impact of the obstacles location on the flame front propagation is studied. The simulations performed are reminded in Table 6.2.

Name	Configuration	$\mathcal{F}$	n	Δ_x in the chamber	Number of cells	β	β correction
LES 1	1	6	6	0.4 mm	643 819	dynamic	yes
LES 2	2	6	6	0.4 mm	643 819	dynamic	yes
LES 3	3	6	6	0.4 mm	643 819	dynamic	yes

Table 6.2: Numerical parameters of LES 1, 2 and 3.

Flame front structure

The numerical flame shapes for the three configurations are compared to the experimental high-speed images (Wen et al., 2013) and plotted in Fig. 6.3, 6.4 and 6.5 for configurations 1, 2 and 3 respectively. The (a) sub-figures of each figure show the temperature field with the velocity vectors, the (b) sub-figures represent the flow vorticity layered by the heat release, to superpose the heat release with the flow vorticity, only the results above a threshold value are colored in red. The velocity vectors in the (a) sub-figures allow to show the flow accelerating frame after frame. The large eddies are also seen thanks to the velocity vectors. The vorticity is shown in blue in the (b) sub-figures visualising resolved turbulent motions.

The time shift applied at each simulation is equal to 12.4 ms, 7 ms, and 12.2 ms for LES 1, 2 and 3 respectively. The snapshots have been taken at the same (shifted) moments as the experimental images.

Initially, the flame structure is similar for the three configurations. The flame is unwrinkled at the beginning and propagates slowly with a spherical shape (two first frames of Fig. 6.3, Fig. 6.4 and Fig. 6.5). Turbulence is generated downstream the obstacles by the thermal expansion of burnt gases. Moreover, in all configurations, small turbulent motions appear right above the obstacles even before the flame front reaches the first obstacle (for instance, see the third frame of 6.3b). These downstream eddies contribute in the flame front acceleration when the flame front reaches them. For configurations 2 and 3, the time needed for the flame to reach the first obstacle is about 27 ms, which is less than for configuration 1 ($\approx$ 30 ms). Before the flame arrives to the first obstacle, the flame front structure differs from one configuration to the other. The front flattens off slightly for the first configuration (Fig. 6.3). Then, two fronts are observed for configuration 1 (on both sides of the obstacles) whereas only one front is observed for the other two set-ups. In configurations 2 (Fig. 6.4) and 3 (Fig. 6.5), the flame fronts gradually distort and tend to move towards the chamber open-end (second frame of the upper sub-figures).

The flame accelerates due to turbulence generated by the obstructions, the flame is faster in configurations 1 and 3 compared to configuration 2. This is due to a higher level of turbulence intensity as a result of the interactions of the flow with the obstacles as said by Wen et al. (2013). The second configuration disposes of a large path on the right side without obstacles where the flame front goes through. Due to this path, flame front interaction with turbulence is reduced, thus, the flame front accelerates less in this configuration. As shown in Fig. 6.3, Fig. 6.4 and Fig. 6.5 the flame front structure becomes distorted and turbulent and the flame surface increases.

Experimentally, the flame exits the chamber faster in configuration 1 (40.5 ms), even though the flame propagates slowly in the initial stages (Wen et al., 2013). This result is probably due to the fact that after passing the first obstacle a pair of symmetrical flames develops (Fig. 6.3). In addition, a narrower section is available (between the side walls and the obstacles) for the flame propagation, increasing the interaction between turbulence and flame front. The flame surface is thus higher than those in the other two configurations and may lead to a more significant increase in burning rate and thus flame speed. The slower flame is obtained with the second configuration. The experimental flame exits the chamber after 43.5 ms.

In all simulations, from the first frame to the third, the flame evolves without being wrinkled by turbulence and stays smooth before transiting in a more turbulent regime. At this stage, the numerical flame shapes are close to the experimental ones. Yet, the simulated flames is delayed compared to the experimental flames at this stage. The simulated flame fronts reach the first obstacle later than in the experiments for all configurations (as shown in Fig. 6.3, Fig. 6.4 and Fig. 6.5). This inaccuracy in the flame velocity in the early stages of the experiment is not surprising. Indeed, no ignition model is used for all simulated cases. Igniting with an initial volume of burnt gases and a flow at rest is not physical leading to this kind of delays. In addition, a mass of burnt gases is initially present in order to allow the deflagration ignition whereas the flow is at rest. In the experiment, the ignition point is very small. When the experimental flame kernel reaches the size of the simulated initial flame kernel, the flow in the whole chamber is already in movement. This explains the mismatch between the experiment and the simulation. However, the simulated flames seem to catch up the experimental ones by accelerating more than the experiment between the first and second obstacle. After the second obstacle until the end, the simulated flames matches well the experimental images.

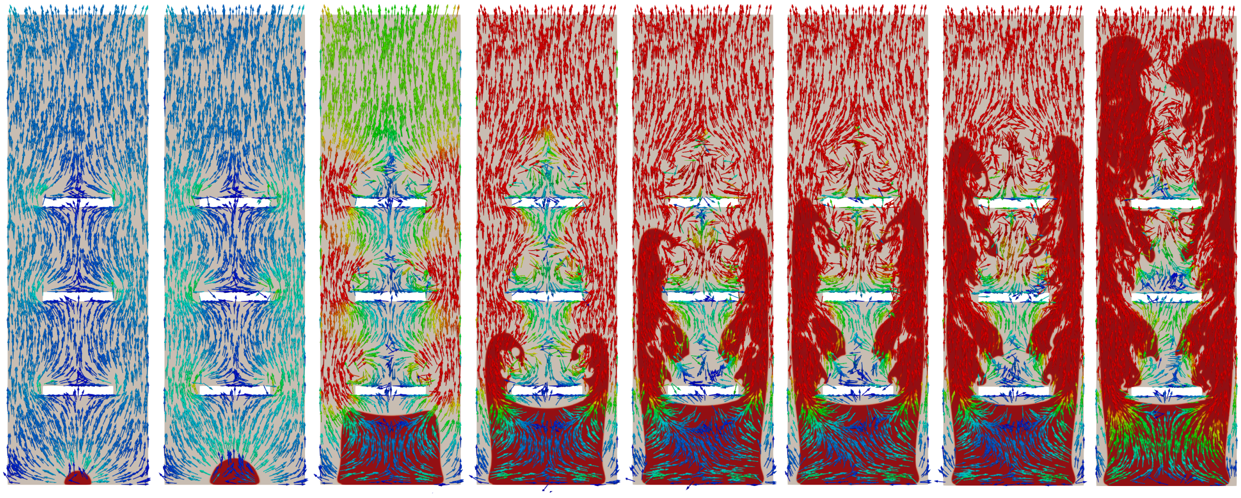

(a) Snapshots of the temperature field and velocity vectors of LES 1

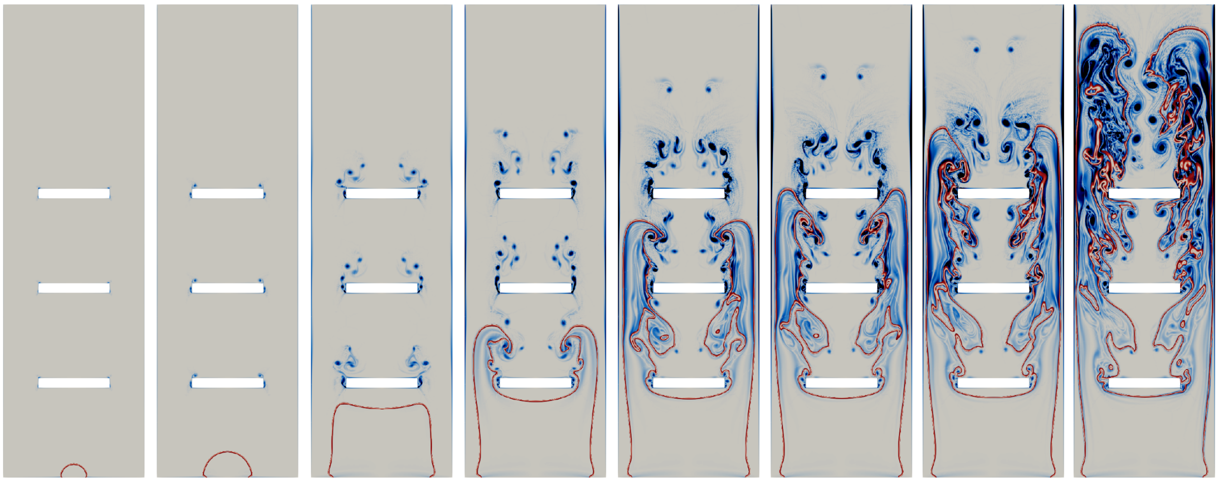

(b) Snapshots of the heat release and the flow vorticity of LES 1

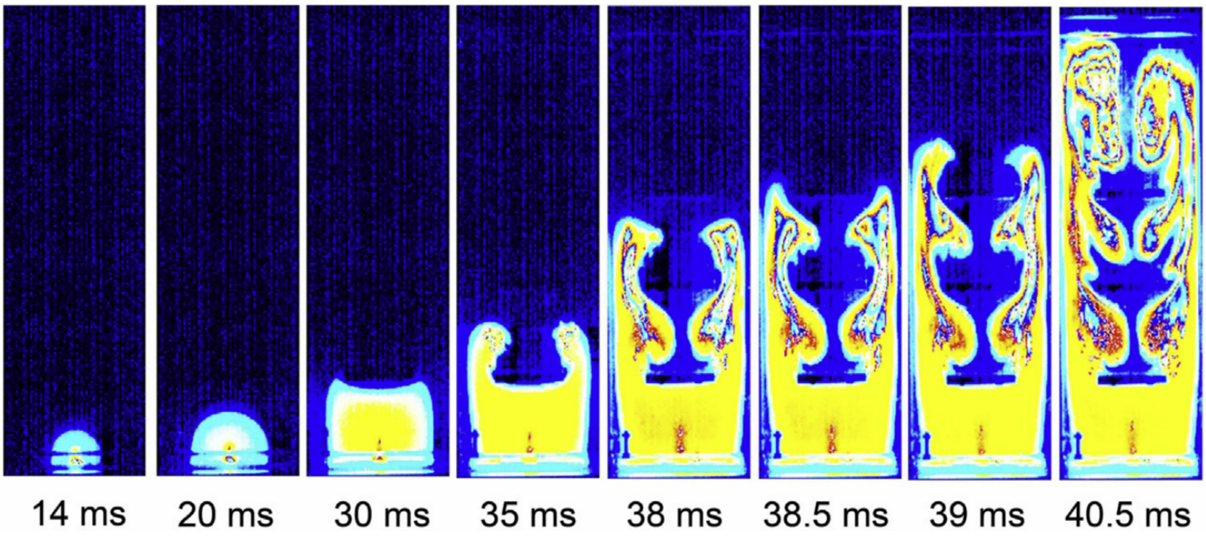

(c) Sequential images

Figure 6.3: Snapshots of (a): temperature with velocity fields; (b): heat release and vorticity fields and experimental images (c) showing deflagration flame propagation in configuration 1 from Wen et al. (2013).

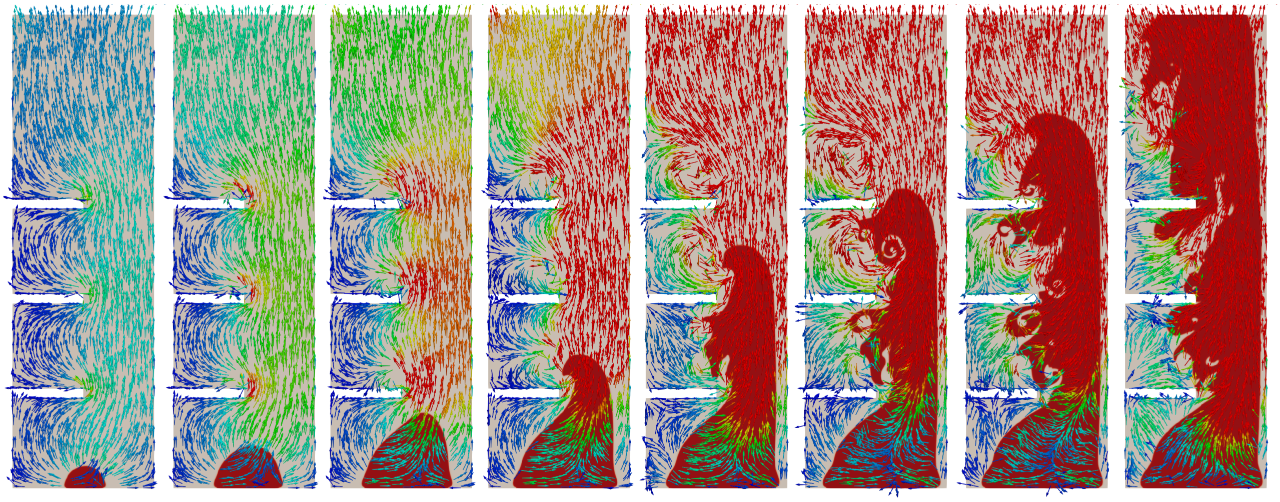

(a) Snapshots of the temperature field and velocity vectors of LES 2

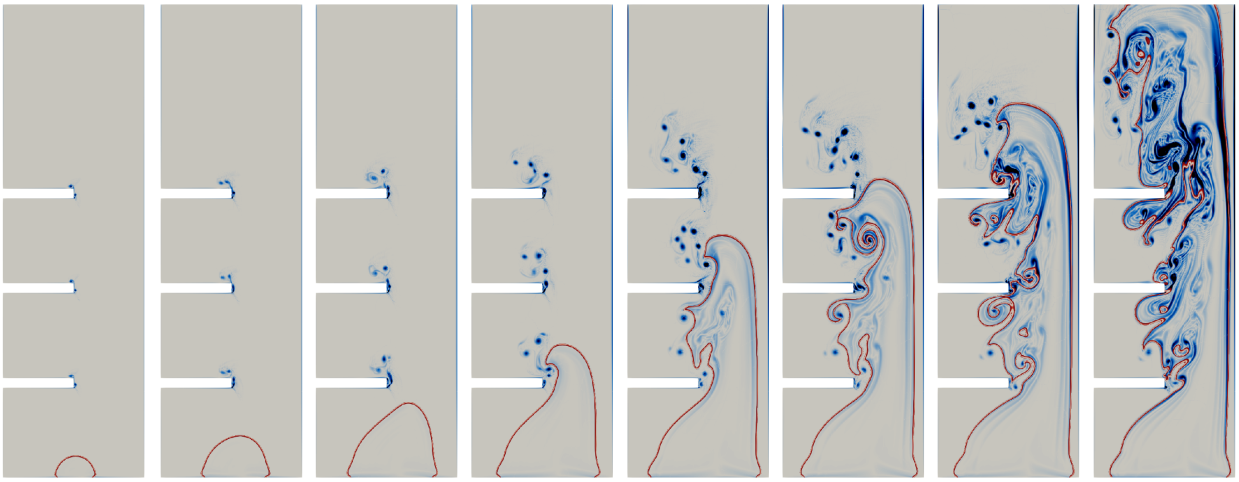

(b) Snapshots of the heat release and the flow vorticity of LES 2

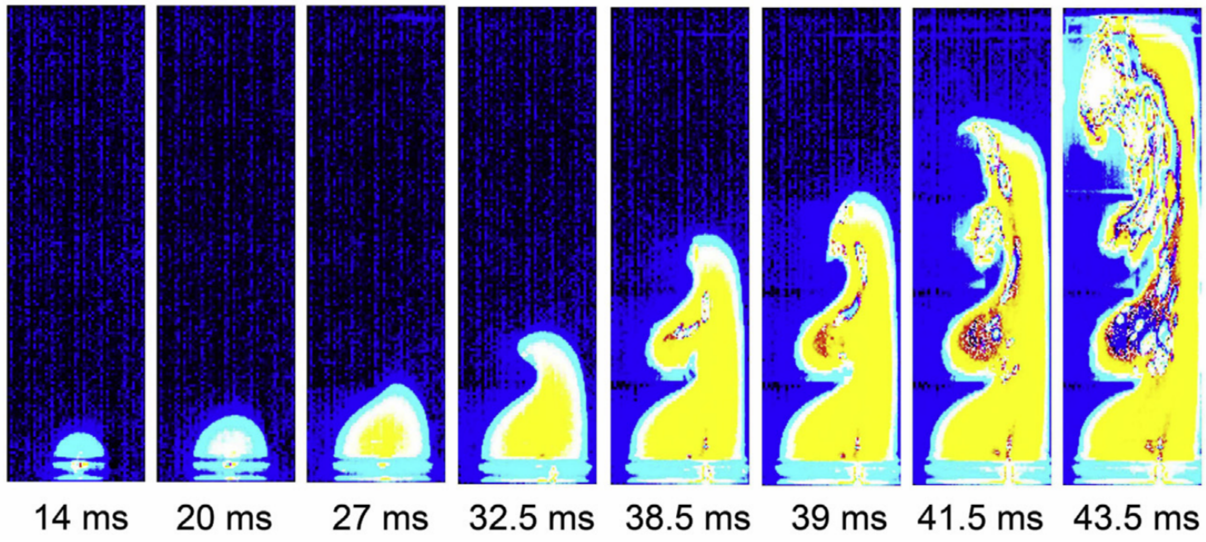

(c) Sequential images

Figure 6.4: Snapshots of (a): temperature with velocity fields; (b): heat release and vorticity fields and experimental images (c) showing deflagration flame propagation in configuration 2 from Wen et al. (2013).

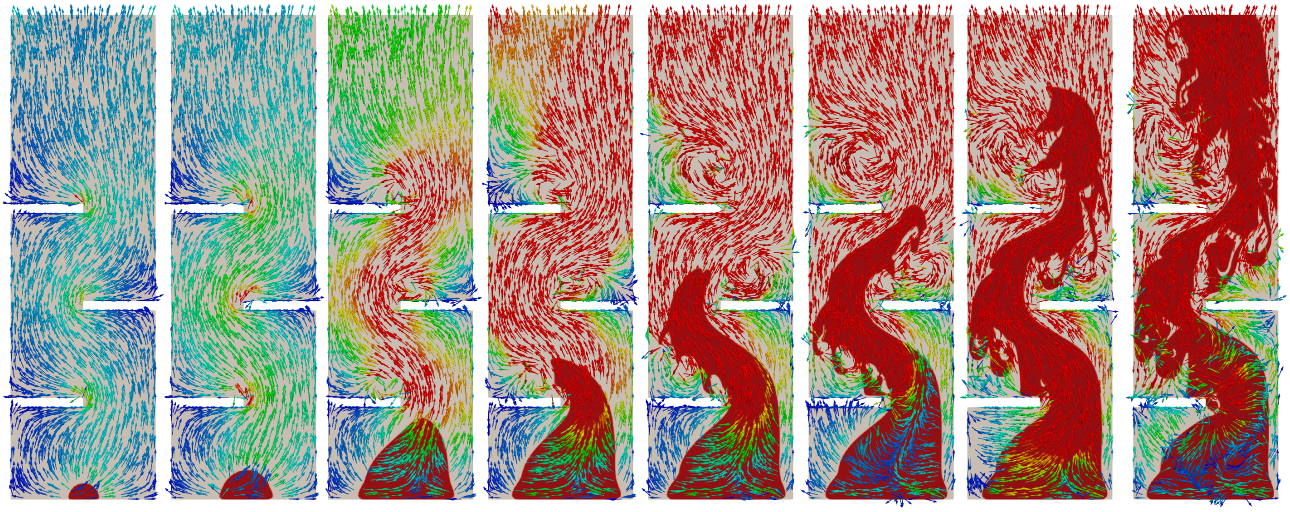

(a) Snapshots of the temperature field and velocity vectors of LES 3

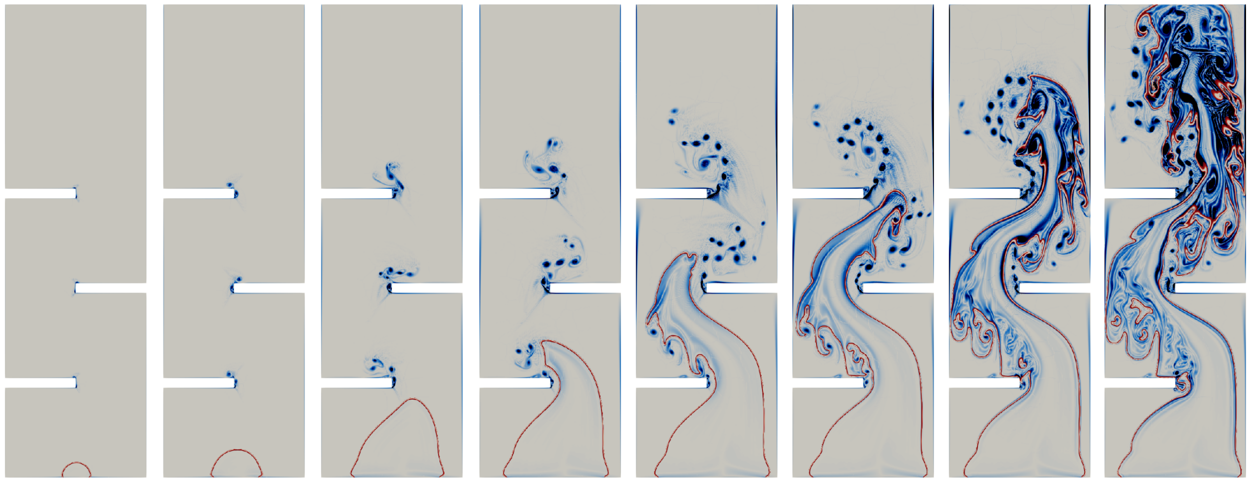

(b) Snapshots of the heat release and the flow vorticity of LES 3

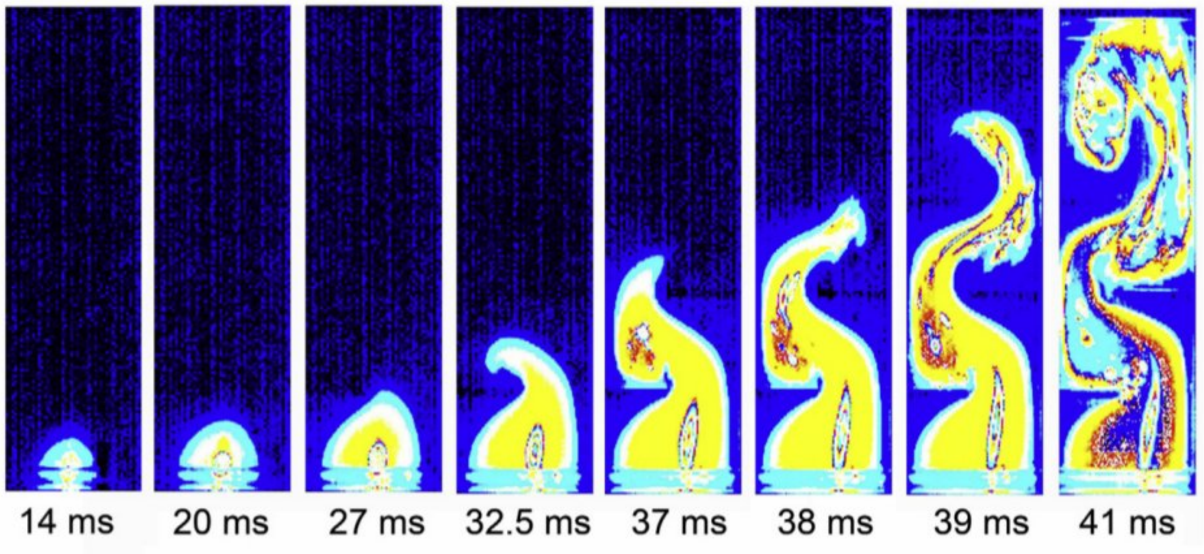

(c) Sequential images

Figure 6.5: Snapshots of (a): temperature with velocity fields; (b): heat release and vorticity fields and experimental images (c) showing deflagration flame propagation in configuration 3 from Wen et al. (2013).

Flame front position and speed

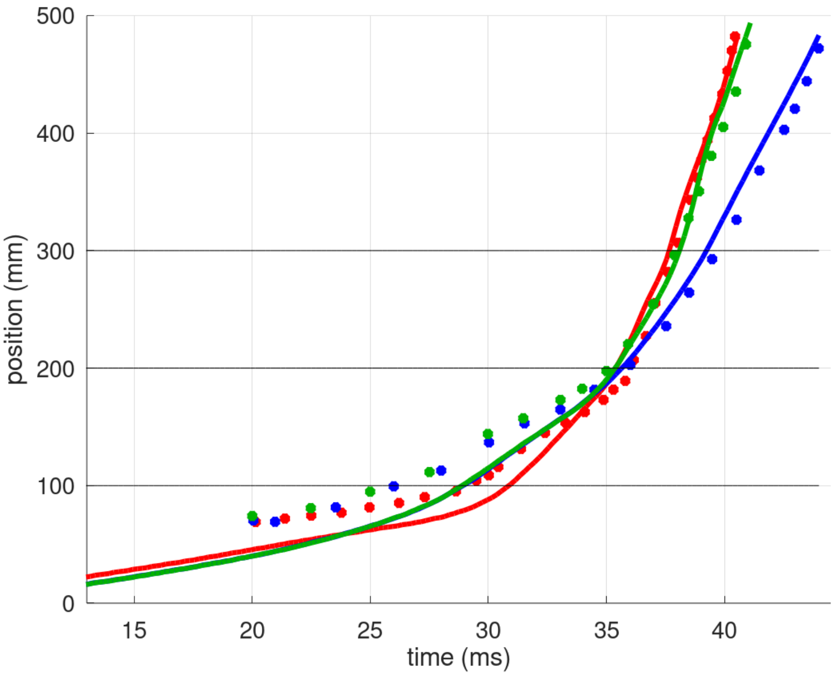

Figure 6.6: Flame front position for all configurations. (—): LES 1; (—): LES 2; (—): LES 3; (●): experimental data of configuration 1; (●): experimental data of configuration 2; (●): experimental data of configuration 3; (—): obstacles locations.

The flame front positions obtained with LES 1, 2 and 3 (thus for configurations 1, 2 and 3) are compared to the experimental data for all configurations in Fig. 6.6 (Wen et al., 2013) (the available experimental data of the flame front position starts only from 20 ms). The location is measured as the maximum downstream distance of the flame front. Fig. 6.7 represents the flame front velocity (derivation of the simulated flame front position). The experimental velocity is not represented along the simulation results as the experimental speed computation method has not been detailed by the authors Wen et al. (2013).

Before the first obstacle, flame positions increase linearly through time. The numerical slopes are close to the experimental ones, showing that the TFLES model is able to reproduce the laminar to turbulent transition. After the first obstacle, the slopes of the curves become steeper, thus the flames continue to accelerate throughout the chamber. For all configurations, the numerical slopes are steeper in the region located between the first and the second obstacles than experimental ones. The flame is thus slightly faster in this region than in the experiment.

As shown in Fig. 6.7, the three simulations predict a similar flame front speed before the first obstacle (even if the flame speed of LES 1 is slightly slower than those computed by LES 2 and LES 3). After then the flame speeds increase. LES 2 and 3 have similar flame speeds until $y \approx 180$ mm (the same observation is made in Fig. 6.6 where LES 2 and 3 flame front position profiles overlap). Between the first and the second obstacles, the flame speed predicted by LES 1 in Fig. 6.7 (as well as the numerical slope reported on Fig. 6.6) is higher (respectively steeper) than those computed by LES 2 and LES 3. Afterwards, LES 3 flame front speed accelerates more than LES 1 flame front, allowing the flame front position of LES 3 to catch up with LES 1 flame front position (as shown in Fig. 6.6).

The flame front propagation in the second configuration is slower than the others, which can be explained by a weaker turbulence intensity as explained by Wen et al. (2013). Moreover, as explained earlier, the second configuration disposes of a large path on the right side without obstacles where the flame front goes through. Due to this path, flame front interaction with turbulence is reduced, thus, the flame front accelerates less in this configuration.

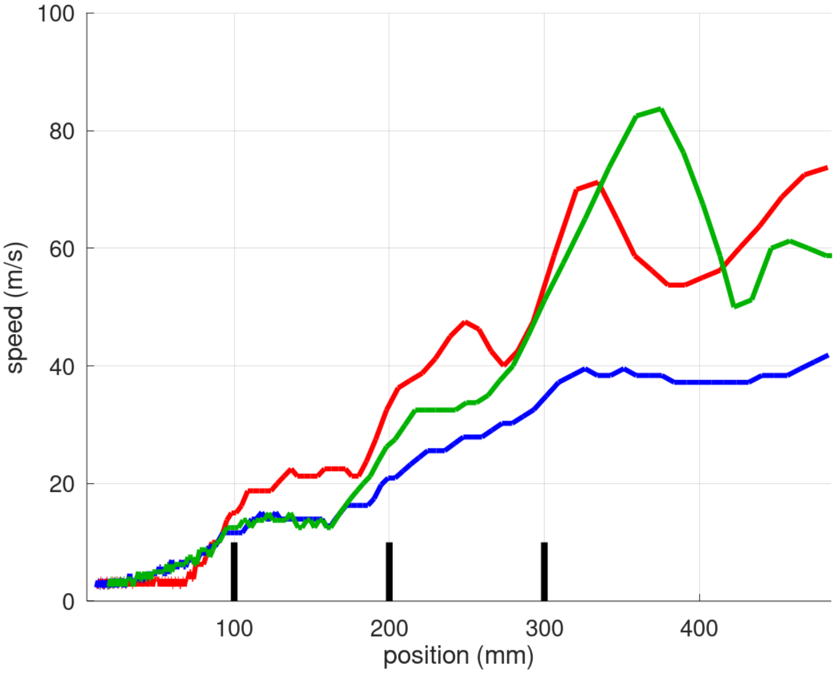

Figure 6.7: Flame front speed for all configurations. (—): LES 1; (—): LES 2; (—): LES 3 and (▬): obstacles locations.

Overpressure dynamics

A particular interest is given to the overpressure prediction as the overpressure peak is representative of the damages resulting from an explosion. In Fig. 6.8, the simulated overpressure time evolutions are compared to the experimental data for configurations 1, 2 and 3 (Wen et al., 2013).

The experimental overpressure profiles show a first peak in all configurations at 28 ms corresponding to the sealing film disintegration at the end of the chamber and it is not recovered in the simulations. The major peak occurs at 39.7 ms, 41.5 ms and 41.1 ms for configurations 1, 2 and 3 respectively. The overpressure peak amplitudes are around 124 mbar, 69 mbar, and 183 mbar for configurations 1, 2 and 3 respectively.

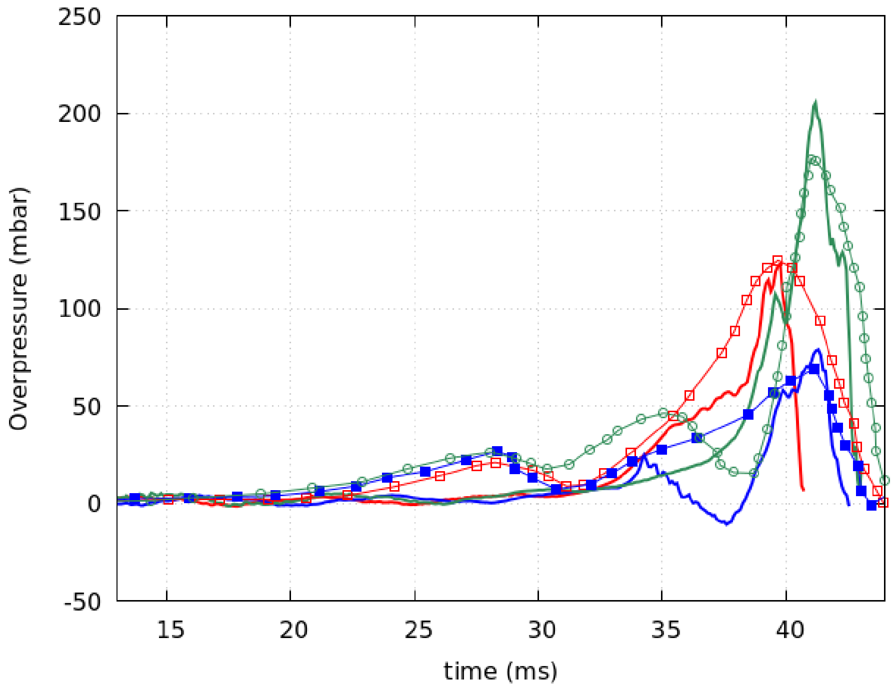

Figure 6.8: Overpressure evolution for all configurations. (━): LES 1; (━): LES 2; (━): LES 3. (□) experimental data of configuration 1. (■) experimental data of configuration 2. (⊖) experimental data of configuration 3.

For configuration 1, the major overpressure peak corresponds experimentally to the time when the flame front reconnects after crossing the last obstacle (Wen et al., 2013). For configuration 2, it occurs experimentally when the flame front is located between the last obstacle and the chamber exit. The experimental overpressure of configuration 3 occurs when the flame exits the chamber due to a more significant turbulent flow condition induced by the staggered obstacles as explained by Wen et al. (2013). The overpressure peak reached is indeed higher than those of configurations 1 and 2.

The inability of simulating the sealing film holding back the inflammable gases generates difficulties to compare the simulated and experimental overpressure profiles when the sealing breaks (before the major peak).

The major experimental and simulated peaks happen at the same time since the simulated peaks are time shifted to match the experiments.

LES results show that the major peak, for configurations 1 and 2, occurs when the flame front tips are located between the last obstacle and the chamber exit (in accordance with experiments). The overpressure peaks amplitude are 123.6 mbar and 78.3 mbar for the first and the second configurations respectively.

The simulated overpressure evolution for configuration 3 is similar to those reported for configurations 1 and 2 but the peak happens right after the flame front tip exits the chamber (the flame exits the chamber approximately at 40.8 ms, whereas the peak occurs at 41.1 ms). Also, LES 3 has a higher peak amplitude of 204.8 mbar. This may be due to the more significantly turbulent flow condition induced by the staggered obstacles.

Numerically, the overpressure peaks match quite well for both first and second configurations. The overpressure peak for LES 3 is less accurate (11% higher than the experimental peak), but it stays quite close to the experimental data.

Small fluctuations are observed in LES. These fluctuations are due to the pressure waves reflections on the walls and on the obstructions. As explained in the experimental set-up section, the experimental overpressure curves are obtained by repeating the same experience several times and then averaging the profiles. The fluctuations observed in the simulations are not present in the experimental results probably due to this averaging process and also because the fluctuations may be smaller than the sensor uncertainties. One should keep in mind that these fluctuations may also be present in the simulation and not in the experiment because the simulation has a two-dimensional domain.

In LES 1, a smaller first peak is observed at 39.5 ms, before the major peak at 39.7 ms. When comparing the overpressure profile to the snapshots in Fig. 6.3a, the flame front splits at the left and right of the obstacles, the flame is not perfectly symmetrical which may lead to this type of small peak delays.

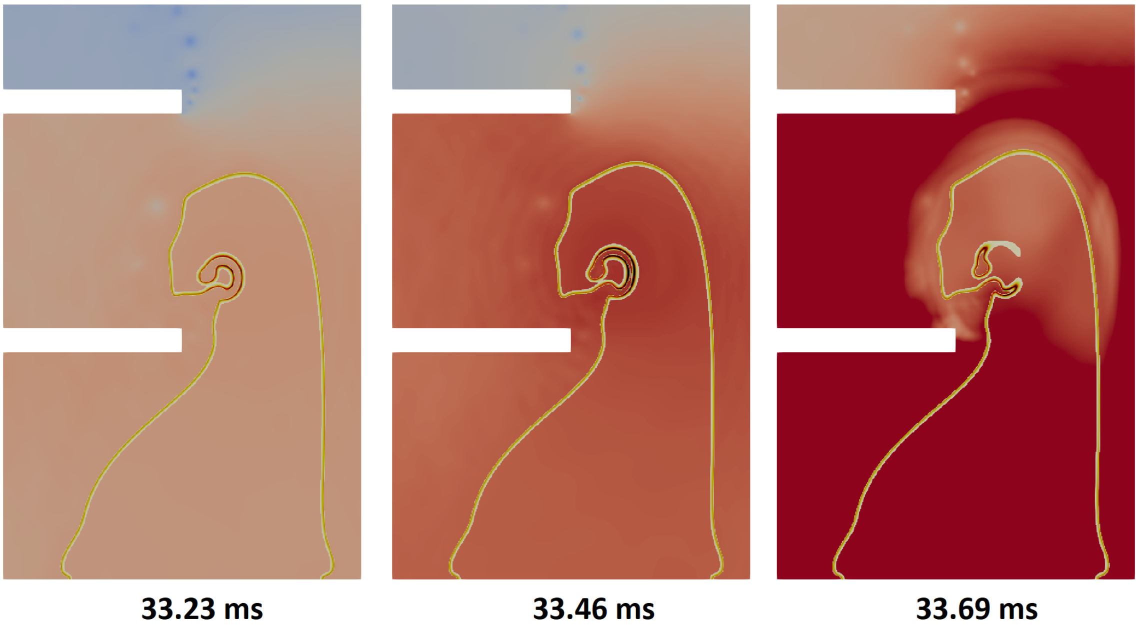

Figure 6.9: Instantaneous pressure fields layered by the heat release at three consecutive moments for LES 2.

Another observed phenomena in the simulation of configuration 2 is the small peak of pressure at $t = 33.7$ ms. This peak occurs when the flame front is located just before the second obstacle. It may be due to the beginning of the flame acceleration (change of slope between the first and the second obstacle in Fig. 6.6) or to numerical issues. The pressure field layered with the heat release is observed in Fig. 6.9 for three consecutive moments. These three snapshots are taken at the moment when the perturbation in the overpressure field occurs. The snapshots shows that a pocket of fresh gases got trapped in the burnt gases. The fresh gases have been consumed, thus pressure waves have been generated at this location and propagate until the sensor leading to the small pressure peak.

The pressure decrease after the first peak may be due to numerical reasons. Further investigations on the outlet boundary conditions which reflects the pressure waves should be done.

The numerical overpressure profile of LES 3 shows a first small peak at 39.6 ms while the flame front tip is located between the last obstacle and the chamber exit. Right after this small peak, the pressure in the chamber increases quickly until the major peak at 41.1 ms. One reason of this latest peak may be the fact that while the flame expends, the flame seems to obstruct the flow next to the obstacles creating the effect of a plug at $y = 100\,\mathrm{mm}$. After then, the flame exits and a consequent amount of burnt gases is evacuated, the pressure drops in the whole chamber leading to the decrease of the overpressure profile.

The flame front tip position through time gives an information on the global dynamics downstream of the reactive flow. Indeed, small perturbations in the flame such as the one observed in configuration 2 do not impact the overall flow dynamics. In order to have a global overview, the heat release has been integrated over the chamber and discussed hereafter.

Heat release

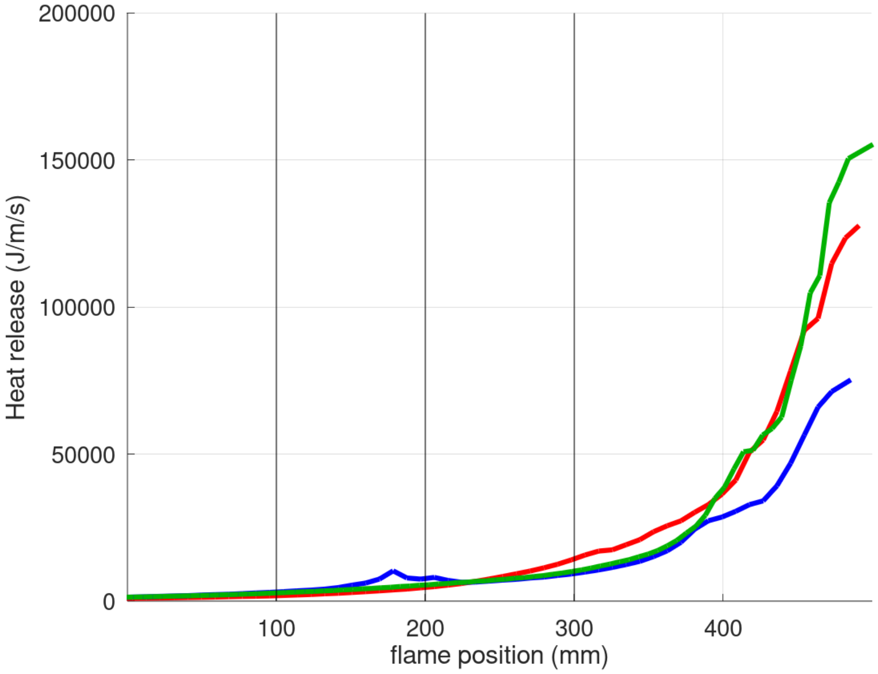

Figure 6.10: Heat release for all configurations. (🟥): LES 1; (🟦): LES 2; (🟩): LES 3; (—): obstacles positions.

The heat release $\dot{\omega}_T$ (expression (4.13)) is integrated over the chamber volume and plotted in function of the flame front tip position for the three configurations in Fig. 6.10. As the flame propagates, the flame front surface increases (shown later in Fig. 6.13) leading to an increasing reaction rate and thus an increasing heat release in the chamber. LES 1 has a more important heat release after the second obstacle. This may be explained by the double front on each side of the obstacles allowing the flame to cover more surface and thus, leading to higher values of the integrated over the chamber heat release. However, LES 3 heat release catches up with LES 1 while approaching the chamber exit. This is also seen on the total flame surface discussed later in this section.

Here, the numerical perturbation observed on the pressure for the second configuration is also seen in the heat release right before the second obstacle. A small peak is noticeable which corresponds to the reaction rate increase while the pocket of fresh gases is consumed as represented in Fig. 6.9. A further study with a thinner mesh or a computation on a three dimensional domain should be done.

Wrinkling factor exponent

The statistical quantity β^{avg} defined as:

$$\beta^{avg} = \frac{\int_{\mathcal{V}_f} \beta \, d\mathcal{V}}{\int_{\mathcal{V}_f} d\mathcal{V}}, \tag{6.7}$$

is the spatially averaged β parameter over the flame volume $\mathcal{V}_f$ defined such as: $0.05 < \tilde{c} < 0.95$. Such statistical tool provides an overall idea of the evolution of the wrinkling factor exponent through time.

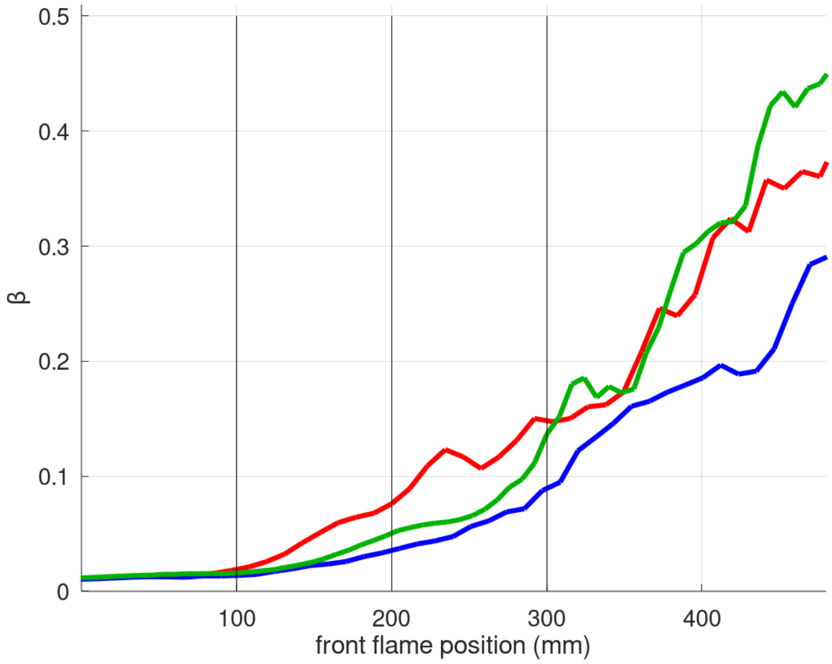

Figure 6.11: Plot of β^{avg} as a function of the front position for the three configurations. (—): LES 1; (—): LES 2; (—): LES 3; (—): obstacles positions.

Fig. 6.11 shows the statistical quantity β^{avg} as a function of the flame front tip positions, for the three configurations.

Wang et al. (2012) have shown that the wrinkling factor exponent is not null for a spherical laminar kernel even though the flame is not wrinkled at early stages. The wrinkling factor exponent is in the range of 10^{-2} (negligible impact on the fluid dynamics) which explains the small offset at the early stages in Fig. 6.11.

As shown in Fig. 6.7, the flame front in the first configuration has a more important acceleration between the first and the third obstacles than the two other configurations. This may be explained by a more important turbulent intensity which would explain higher values of β^{avg} in this zone as shown in Fig. 6.11.

After the third obstacle, the turbulent intensity increases significantly for LES 3 leading to higher values of β^{avg}. The flame front tip in LES 2 is the slowest among the three configurations with the lowest turbulent intensity, thus, β^{avg} amplitude is the least important.

Figure 6.12: Zoom in of a screenshot of LES 3 representing the local wrinkling factor exponent and the flame contour at 35.8 ms. (Blue color map): wrinkling factor exponent and (—): flame contour such as $\tilde{c} = 0.5$.

One should keep in mind that in our situation, at a given time, the wrinkling factor exponent is a space variable and is not uniform in the whole domain. More precisely, in Fig. 6.12 where the instantaneous local wrinkling factor exponent field and the flame contour at 35.8 ms is represented, the flame is almost not wrinkled from the bottom of the chamber to the first obstacle. Even after the first obstacle, the right side of the flame front is not wrinkled and the β parameter is null. However, there are local values of the β parameter reaching 0.45. Therefore averaging the β parameter over the whole flame would lower its value as β is close to zero in the non wrinkled parts of the flame. This observation is also pointed out on the three-dimensional simulation presented later in this chapter.

Flame surfaces

For LES, a way to observe the subgrid scale model effects is to plot the resolved flame surface $S_r(t)$ and the total flame surface $S_t(t)$ (Veynante and Vervisch, 2002) which are defined as follows:

$$S_r(t) = \int_{\mathcal{V}} |\nabla \tilde{c}| \, d\mathcal{V}, \quad S_t(t) = \int_{\mathcal{V}} \Xi_\Delta \, |\nabla \tilde{c}| \, d\mathcal{V} \tag{6.8}$$

with $\mathcal{V}$ the computational volume.

The resolved and total flame surfaces for the three configurations as a function of the flame front tip positions are reported in Fig. 6.13. Before the flame front reaches the first obstacle, the flame is not wrinkled yet by turbulence, thus $\Xi_\Delta \approx 1$, total and resolved flame surface profiles match. Afterwards, turbulence wrinkles the flame front and the wrinkling factor increases to take into account the non-resolved flame surface, leading to a higher value of the total flame surface.

The resolved flame surface of LES 1 is higher than the two other simulated flame surfaces. This is due to the fact that the obstacles in configuration 1 creates two different fronts. Therefore, the flame surface in configuration 1 is more important than the two others as represented in Fig. 6.13. The fact that the total flame surface of LES 1 is mostly superior to the two other flame surfaces explains why LES 1 reaches the chamber exit faster than the two other simulations as shown in Fig. 6.6.

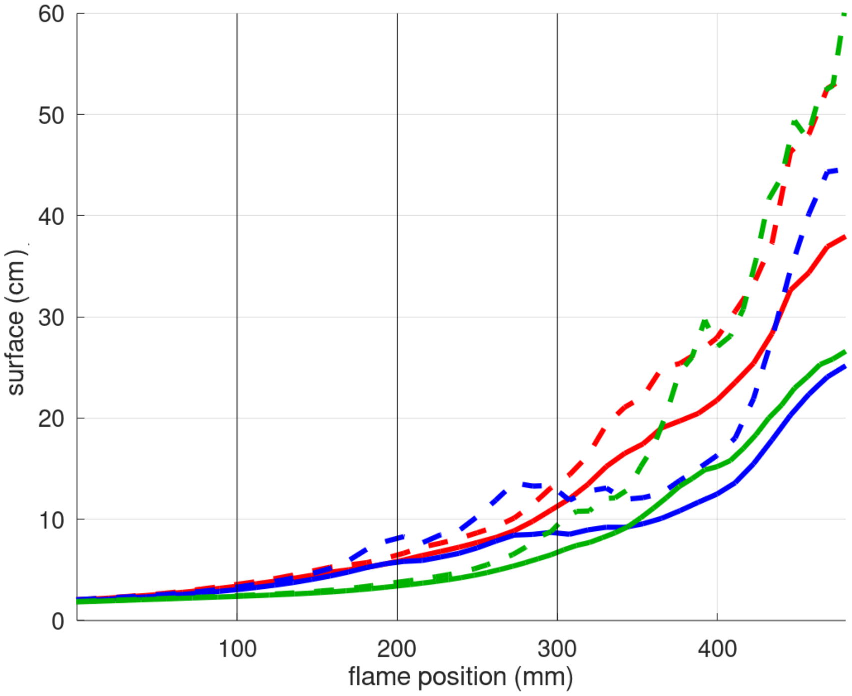

Figure 6.13: Resolved flame surface and total flame surface of LES 1, 2 and 3. (—): resolved flame surface of LES 1; (—): resolved flame surface of LES 2; (—): resolved flame surface of LES 3; (- - -): total flame surface of LES 1; (- - -): total flame surface of LES 2;(- - -): total flame surface of LES 3; (—): obstacles locations.

The resolved and the total surfaces for configuration 2 are close until the flame reaches 400 mm (between the third obstacle and the chamber exit). At this stage of the transient, β increases more quickly (see Fig. 6.11) and the total flame surface rises. LES 2 has globally an inferior total flame surface compared to the two others (except between the second and third obstacles) and it is the slowest case. This may be explained by a lower turbulent intensity leading to a less important flame front acceleration and thus, a slower flame front of LES 2 as shown in Fig. 6.6.

Regarding configuration 3, the difference between total and resolved flame surfaces quickly increases after the third obstacle. This is due to a more important turbulent intensity impacting directly the wrinkling factor and thus, increasing the total flame surface. The same behavior can be observed for the wrinkling factor exponent in Fig. 6.11. Despite the fact that the total flame surface of configurations 1 and 3 are similar at the end, the resolved flame surface of configuration 1 is almost twice superior than configuration 3 due to the double front on each side of the chamber in configuration 1. Therefore the wrinkling is more important in configuration 3 than configuration 1 (as shown in Fig. 6.11).

6.3.3 Impact of the number of grid points in the flame front

The purpose in this section is to analyse the influence of the mesh resolution on the numerical results. The most turbulent configuration of obstacles is chosen. Three simulations of the third configuration are compared (listed up in Table 6.3) with different number of grid points in the flame fronts and thus different mesh sizes. We recall that the number of points in the flame front is a function of the mesh size Δ_x, the thickening factor $\mathcal{F}$ and the laminar flame thickness δ_L^0 such as $n = \mathcal{F}\delta_L^0/\Delta_x$. The value of $\mathcal{F}$ is fixed at $\mathcal{F} = 6$ (*i.e.* the resolved flame thickness is the same in the three simulations), the number of grid points in the front has been changed in three different simulations leading to compare LES 3, 6 and 7 where $n = 5$, 6 and 10 respectively.

Name	Configuration	$\mathcal{F}$	n	Δ_x in the chamber	Number of cells	β	β correction
LES 3	3	6	6	0.4 mm	643 819	dynamic	yes
LES 6	3	6	5	0.48 mm	447 374	dynamic	yes
LES 7	3	6	10	0.24 mm	1 791 554	dynamic	yes

Table 6.3: Numerical parameters of LES 3, 6 and 7.

Fig. 6.14 shows the resolved and total flame surface of LES 3, 6 and 7. The three simulations have approximately the same resolved and total flame surface even if LES 7 is slightly above the two others. The difference between resolved and total flame surface represents the wrinkling factor contribution. Therefore, the wrinkling factors behave approximately the same for the three cases. The test-filter size and the inner cut-off length scale are the same for each simulation as the $\mathcal{F}$ factor is kept constant. Therefore, expressions (6.3) and (6.4) are the same for each case, meaning that the model exponent β behaves almost similarly in each simulation (as shown also in Fig. 6.15) and is only dependent of the fluid flow behavior.

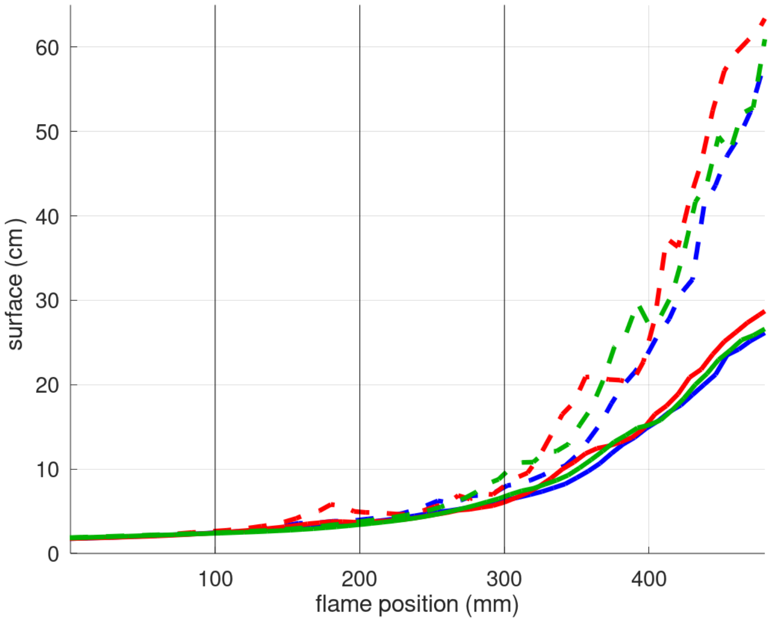

Figure 6.14: Resolved flame surface and total flame surface for LES 3, 6 and 7. (—): resolved flame surface of LES 3; (- - -): total flame surface of LES 3; (—): resolved flame surface of LES 6; (- - -): total flame surface of LES 6; (—): resolved flame surface of LES 7; (- - -): total flame surface of LES 7 and (—): obstacles locations.

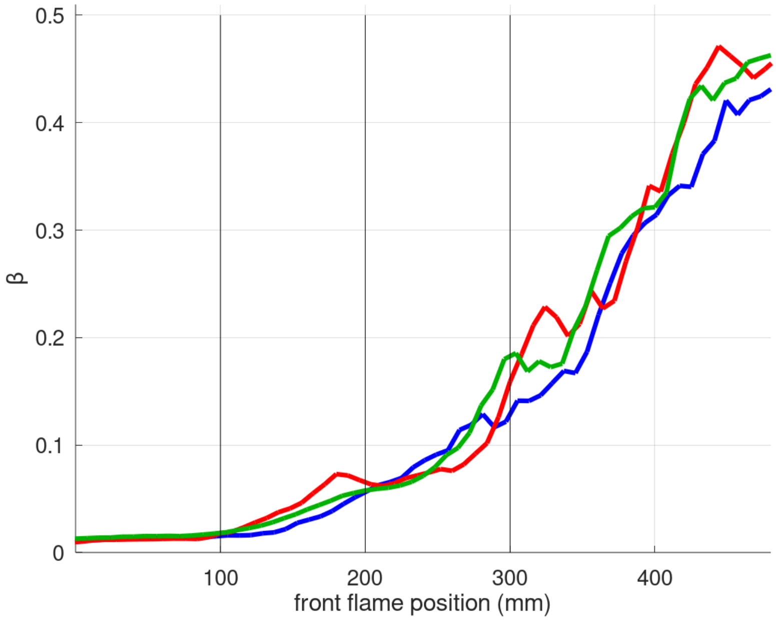

Figure 6.15: Plot of β^{avg} as a function of the front position for LES 3, 6 and 7. (—): LES 3; (—): LES 6; (—): LES 7 and (—): obstacles locations.

The overpressure evolution is shown in Fig. 6.16 where the same time shift is applied to the three simulations. The overpressure peak occurs approximately at the same moment for all these simulations. The peak amplitudes are fairly close even if the case with $n = 10$ is slightly closer to the experimental data. In addition, it has the ability to capture smaller fluctuations as the mesh grid is finer. Leading to the bump seen at $t = 37\,\mathrm{ms}$ which corresponds to the moment when the flame front tip reaches the last obstacle. Globally, the results are quite close even if the number of mesh grid in the chamber is more important in LES 7 compared to LES 6. However, LES 3 with $n = 6$ is kept as the reference case for the rest of the two-dimensional simulations as the overpressure and wrinkling evolutions match well LES 7. In addition, the computing time stays acceptable for LES 3. Indeed, the computing time on one processor is estimated at approximately 99 days for LES 3, 191 days for LES 6 and 537 days for LES 7.

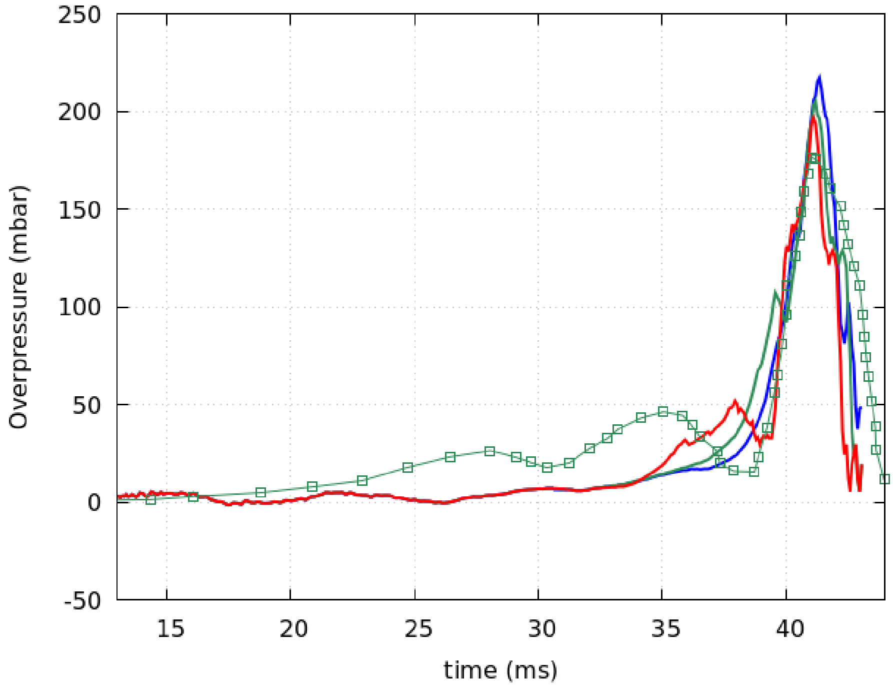

Figure 6.16: Overpressure evolution of LES 3, 6 and 7. (—): LES 3; (—): LES 6; (—): LES 7 and (□): experimental data of configuration 3.

6.3.4 Impact of the thickening factor $\mathcal{F}$

The simulations presented here have different thickening factors keeping the same number of grid points in the front. The aim is to analyse the impact of the $\mathcal{F}$ factor on the numerical results. The simulations presented here (LES 8 and LES 9) have a thickening factor of $\mathcal{F} = 9$ and $\mathcal{F} = 12$ respectively with the same number of grid points: $n = 10$ (summarized up in Table 6.4). The results are compared to the case LES 7 presented above.

Name	Configuration	$\mathcal{F}$	n	Δ_x in the chamber	Number of cells	β	β correction
LES 7	3	6	10	0.24 mm	1 791 554	dynamic	yes
LES 8	3	9	10	0.36 mm	796 066	dynamic	yes
LES 9	3	12	10	0.48 mm	447 374	dynamic	yes

Table 6.4: Numerical parameters of LES 7, 8 and 9.

The resolved flame surfaces change with the variation of the thickening factor as shown in Fig. 6.17. Increasing the flame thickness ultimately reduces the resolved flame surface becoming less sensitive to turbulent motions. Therefore the wrinkling factor exponent decreases (as shown in Fig. 6.18 which represents the spatially averaged wrinkling factor exponent β^{avg}).

However, the total flame surface is well conserved (*i.e.* the total flame surface of LES 7, 8 and 9 are quite similar as shown in Fig. 6.17). Because the combustion filter size Δ entering in Ξ_Δ (expression (6.3)) increases linearly with $\mathcal{F}$. Therefore the loss of resolved flame surface when increasing $\mathcal{F}$ is compensated by the subgrid scale model evidencing its robustness.

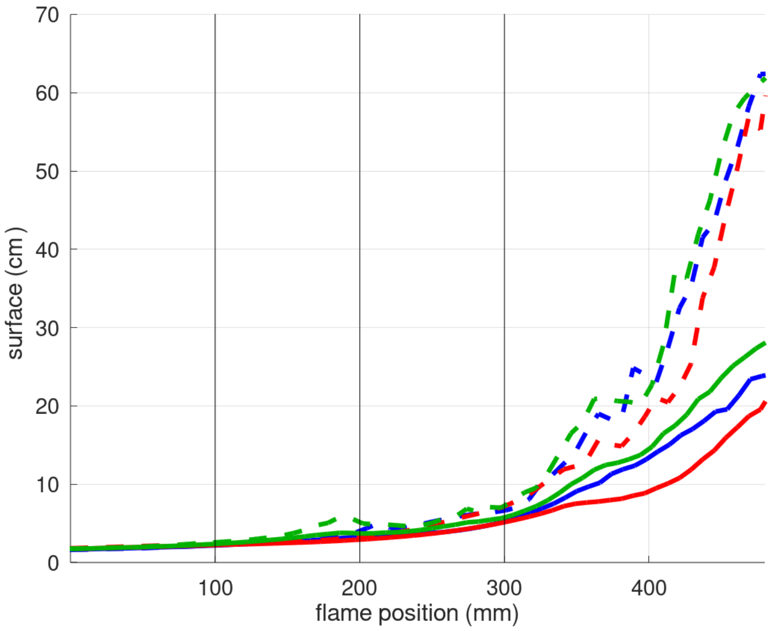

Figure 6.17: Resolved flame surface and total flame surface for LES 7, 8 and 9. (—): resolved flame surface of LES 7; (- - -): total flame surface of LES 7; (—): resolved flame surface of LES 8; (- - -): total flame surface of LES 8; (—): resolved flame surface of LES 9; (- - -): total flame surface of LES 9 and (—): obstacles locations.

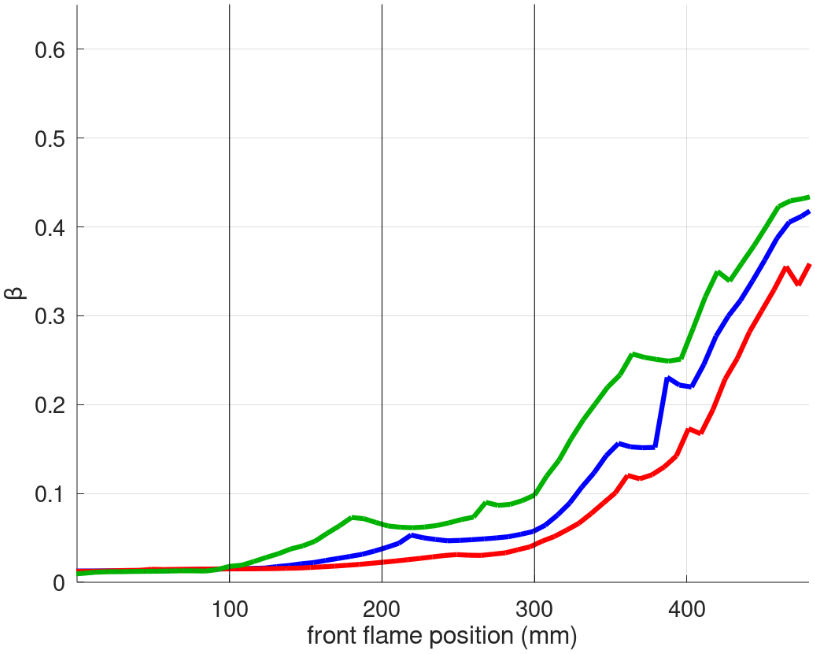

Figure 6.18: Plot of β^{avg} as a function of the front position for LES 7, 8 and 9. (—): LES 7; (—): LES 8; (—): LES 9 and (—): obstacles locations.

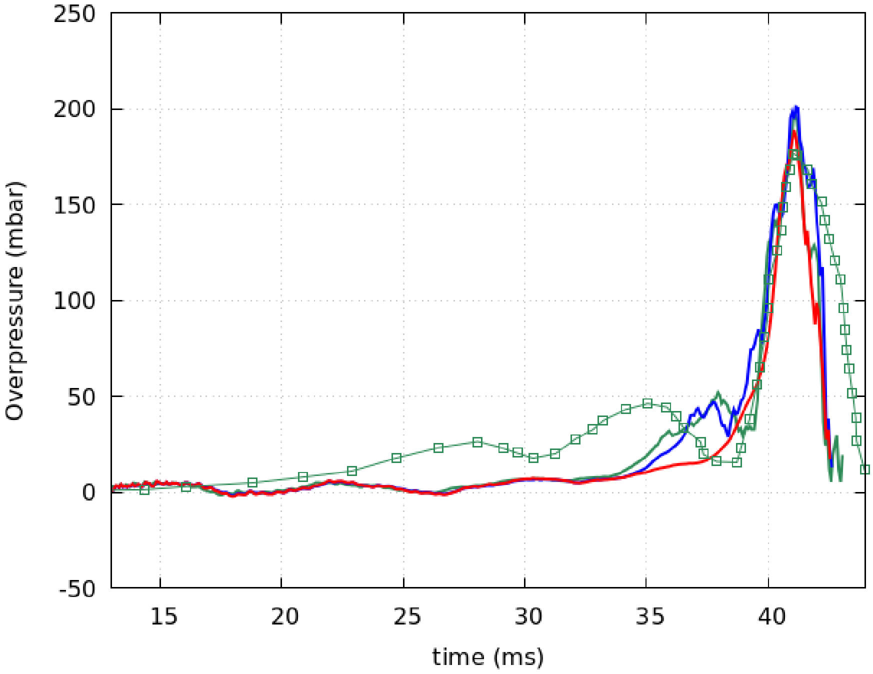

Figure 6.19: Overpressure evolution of LES 7 and LES 8 and 9. (—): LES 7; (—): LES 8; (—): LES 9 and (□): Experimental data of configuration 3.

The overpressure evolution is represented in Fig. 6.19. The profiles are quite similar for the three simulations, reaching almost the same amplitude peak.

Even if LES 9 gives good results, to avoid too thick flame fronts and allow a more precise description of turbulence, LES 3 is kept as reference for further studies.

6.3.5 Constant vs dynamic wrinkling factor exponent β

Here, the need of a dynamical model for the wrinkling factor exponent is highlighted by confronting LES 3 and LES 4 (detailed in Table 6.5) in which the β exponent is set at 0.33 for the whole domain and through time corresponding to a turbulent flow value. The thickening factor is set at $\mathcal{F} = 6$ and the number of cells in the flame front at $n = 6$.

Name	Configuration	$\mathcal{F}$	n	Δ_x in the chamber	Number of cells	β	β correction
LES 3	3	6	6	0.4 mm	643 819	dynamic	yes
LES 4	3	6	6	0.4 mm	643 819	0.33	yes

Table 6.5: Numerical parameters of LES 3 and 4.

The resolved and total flame surface for LES 3 and 4 are plotted in Fig. 6.20. For LES 4, the total flame surface is globally superior than the resolved flame surface even before reaching the first obstacle (during the laminar phase where unitary wrinkling factor is expected). This results in a wrong estimation of the flame front tip position as shown in Fig. 6.21 where both plots have the same time shift (12.2 ms) to highlight the flame front velocity of LES 4. The flame front speed (shown in Fig. 6.22) is overestimated for LES 4 from the beginning leading to a completely wrong result for the flame front position. Indeed, the flame surface being too important from the start, the flame front propagation is too fast.

Setting a lower value for the β parameter in order to connect with the laminar phase would only underestimate the flame surface, speed and position in the fully turbulent zones (after the third obstacle).

The overpressure evolution for the two simulations is plotted in Fig. 6.23 where once again, the same time shift is used for both simulations. The overpressure peak is largely overestimated for LES 4 due to the flame speed overestimation.

A dynamical model for the wrinkling factor is necessary for reproducing transiting phenomena such as explosions.

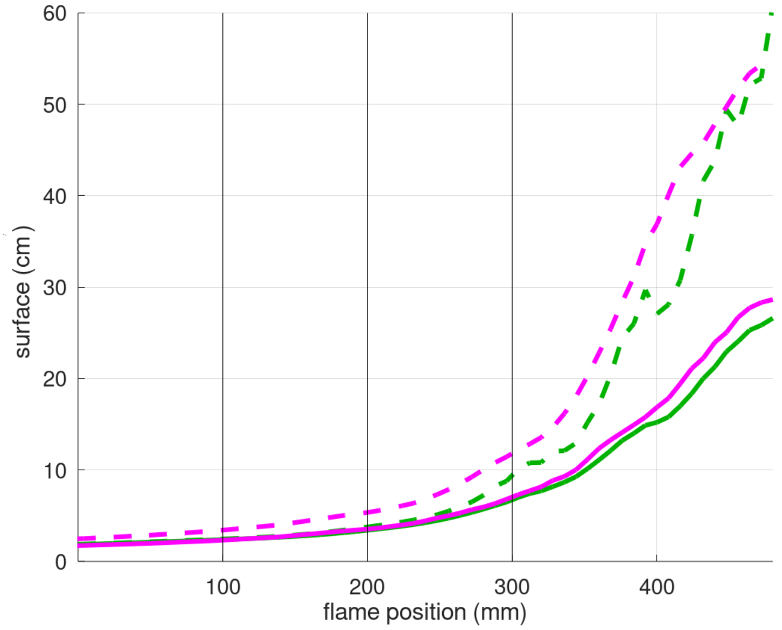

Figure 6.20: Resolved flame surface and total flame surface for LES 3 and 4. (- - -): total flame surface of LES 3; (—): resolved flame surface of LES 3; (- - -): total flame surface of LES 4; (—): resolved flame surface of LES 4; (—): obstacles locations.

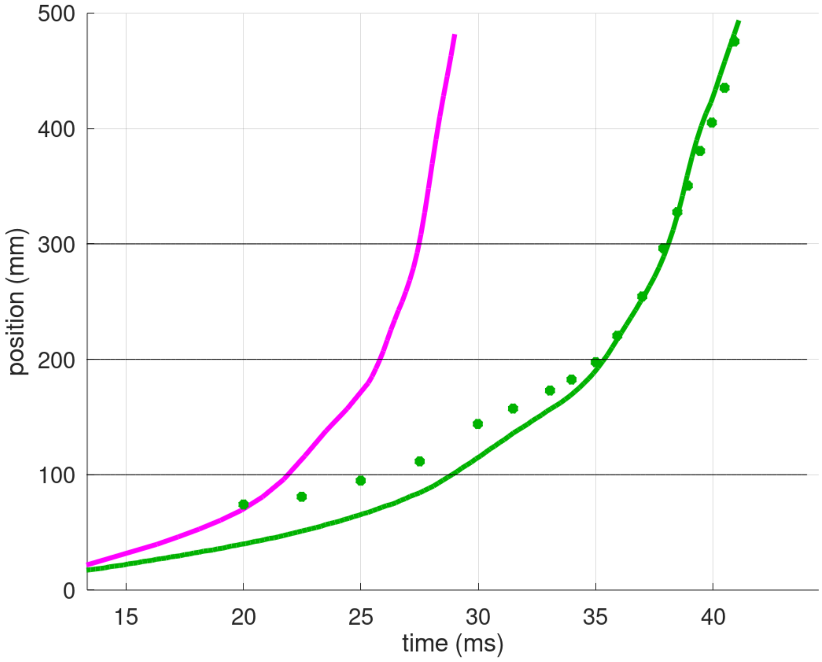

Figure 6.21: Flame front position for LES 3 and 4. (—): LES 3; (—): LES 4; (●): experimental data of configuration 3 and (—): obstacles positions.

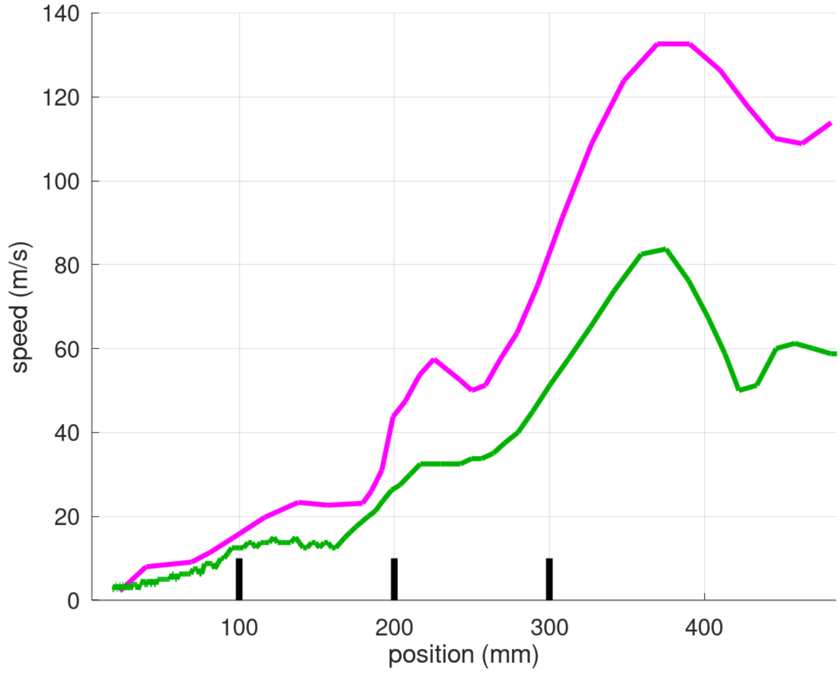

Figure 6.22: Flame front spreed for LES 3 and 4. (—): LES 3; (—): LES 4 and (▬): obstacles locations.

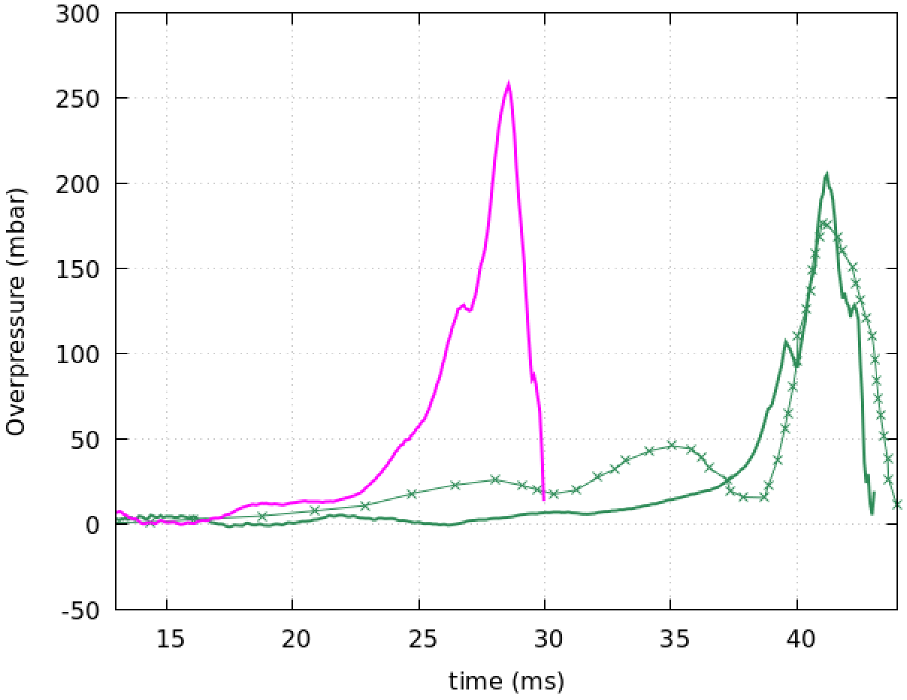

Figure 6.23: Overpressure evolution of LES 3 and LES 4. (—): LES 3; (—): LES 4 and (✳): experimental data of configuration 3.

6.3.6 Wrinkling factor exponent correction (Mouriaux et al., 2016)

Flame fronts interactions generate nonphysical values of the wrinkling factor exponent. Mouriaux et al. (2016) have developed a correction to the β exponent as presented in Chapter 2 Section 2.4.6. Here, the effects of this correction are investigated by confronting LES 3 and LES 5 simulations (described in Table 6.6).

Name	Configuration	$\mathcal{F}$	n	Δ_x in the chamber	Number of cells	β	β correction
LES 3	3	6	6	0.4 mm	643 819	dynamic	yes
LES 5	3	6	6	0.4 mm	643 819	dynamic	no

Table 6.6: Numerical parameters of LES 3 and 5.

The instantaneous field of the β parameter superposed with the flame contour ($\tilde{c} = 0.5$) of LES 3 is represented in the right part of Fig. 6.24 at $t = 37.8$ ms. Starting from the numerical results obtained with LES 3 simulation at $t = 37.8$ ms, the simulation was rerun for one iteration but without the Mouriaux et al. (2016) wrinkling factor exponent correction. The instantaneous field of the β parameter superposed with the flame contour ($\tilde{c} = 0.5$) obtained with this procedure is plotted on the left part of Fig. 6.24. The purpose is to show the impact of the Mouriaux et al. (2016) winkling factor exponent correction on the β parameter in case of flame fronts interaction.

First, we can notice that the more the flame is wrinkled (*i.e.* the more the turbulence is high), the more the β parameter takes high values. Above the first obstacle, the wrinkled flame curls until the flame front (marked by the green number "1") reconnects to itself (marked by the green number "2"). Moreover, the distance between the two fronts is smaller than the effective filter size, leading to front interactions. The maximum value reached by β without Mouriaux et al. (2016) correction is approximately 1.6 (left side of Fig. 6.24) whereas it is approximately 0.65 (right side of Fig. 6.24) with Mouriaux et al. (2016) correction. Even with the front interactions correction, fronts still reconnect, however, the sudden increase of the β parameter does not happen allowing to suppress the nonphysical results.

Fig. 6.25 compares LES 3 and 5 overpressure profiles. The overestimation of the wrinkling factor exponent leads to an overestimation of the total flame surface and may conduct to an over acceleration of the flame front. In our cases, these sudden nonphysical β parameter increase are local and last a brief moment but explains the pressure rise compared to LES 3.

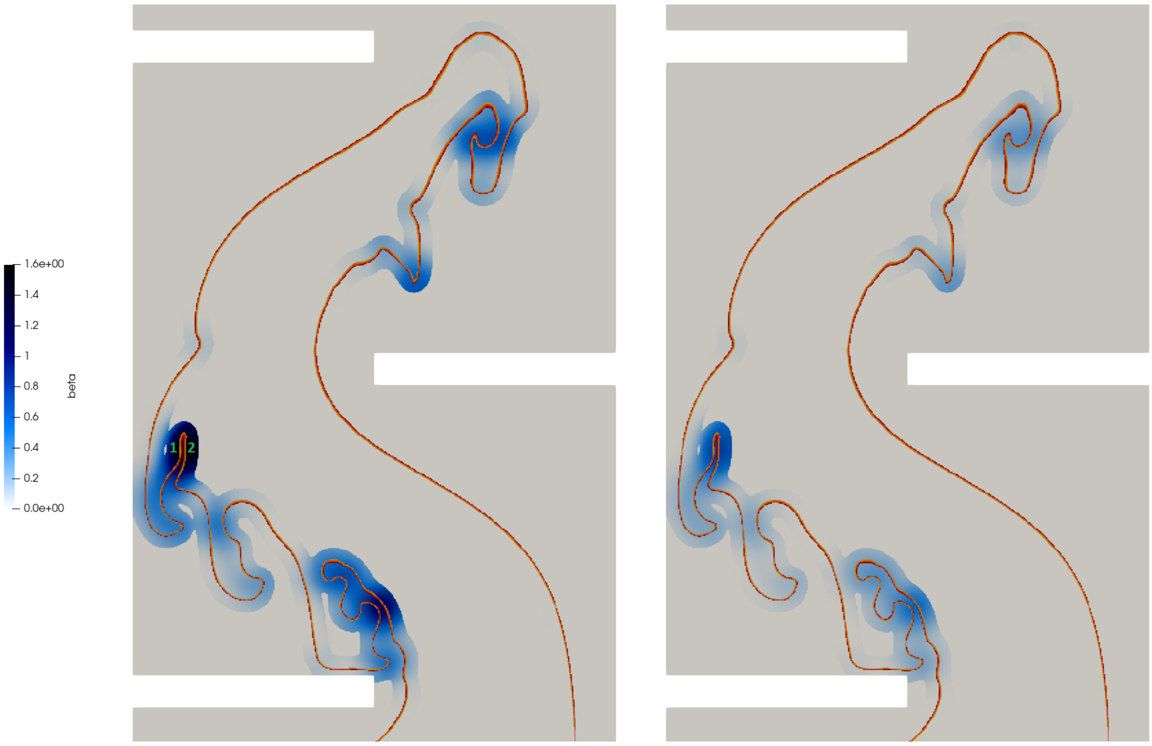

Figure 6.24: Zoom in of a screenshot representing the wrinkling factor exponent with (right side) and without (left side) Mouriaux et al. (2016) winkling factor exponent correction and the flame contour at 37.8 ms. (Blue color map): wrinkling factor exponent and (━): flame contour such as $\tilde{c} = 0.5$.

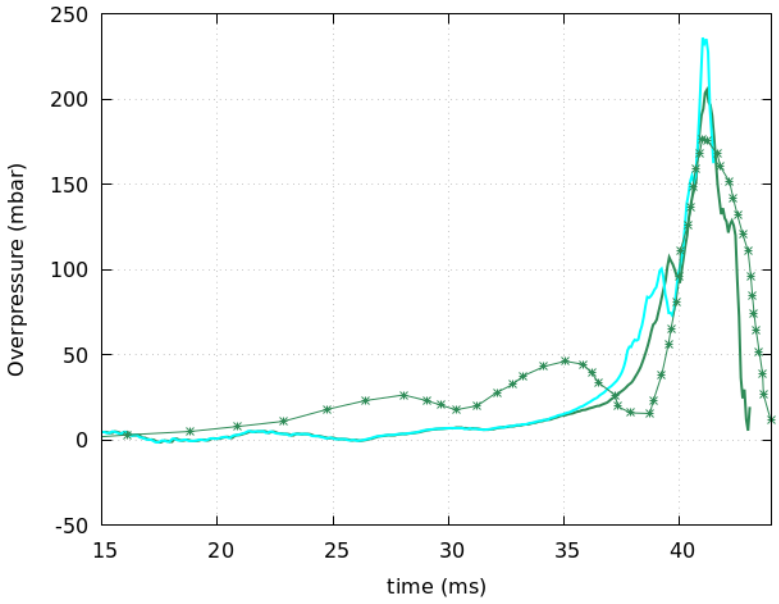

Figure 6.25: Overpressure evolution for configuration 3 without the Mouriaux correction. (━): LES 3; (✳): experimental data of configuration 3; (━): LES 5.

6.4 LES numerical results: three-dimensional simulations

Based on the two-dimensional simulations made previously, configuration 3 of Wen et al. (2013) has been simulated with a three-dimensional simulation presented hereafter.

6.4.1 Numerical set-up of the three-dimensional domain

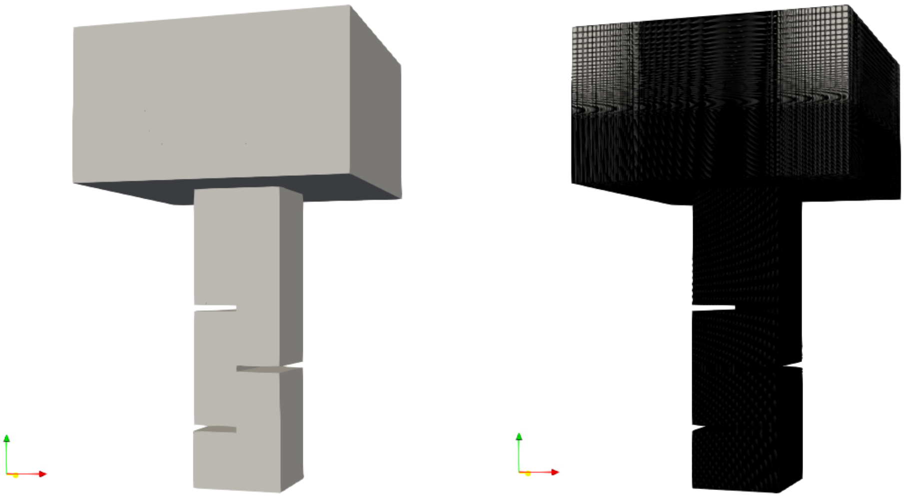

Figure 6.26: 3D representation of configuration 3 with the added atmospheric zone (left side) and its mesh grid (right side).

Figure 6.27: Front view of configuration 3 mesh grid.

Likewise the two-dimensional simulations, the computational domain is extended outside the combustion chamber (or atmospheric zone) in order to push further away the outlet boundary condition at the chamber exit allowing a more realistic reproduction of the gas expansion exiting from the combustion chamber into the atmosphere and reducing pressure waves reflection generated by the deflagration on the boundary.

The mesh size is kept constant in the chamber before getting gradually expanded outside the chamber as shown in Fig. 6.27, where the top corners of the atmospheric zone have less cells. The atmospheric zone mesh grid is twenty time coarser on its boundaries (equivalent to the mesh partition explained in Fig. 6.2).

Adiabatic and no-slip wall boundary conditions were applied at the solid interfaces (bottom face, vertical faces of the chamber and obstacle faces). An outlet condition is enforced at the boundaries of the atmospheric zone where the pressure is maintained at $p_{ext} = 101325\,\mathrm{Pa}$ Pa.

The chemistry is simply described with a one step global reaction which reads for a methane/air mixture at stochiometric conditions:

$$CH_4 + 2\,(O_2 + 3.76N_2) \longrightarrow CO_2 + 2H_2O + 7.52N_2. \tag{6.9}$$

Likewise the two-dimensional flame simulated earlier in this chapter, the reaction rate is computed with the Arrhenius law described in expression (4.10). The pre-exponential coefficient is $A = 6\ 10^5\,\mathrm{uSI}$ and the activation energy is $E_a = 8.3\ 10^4\,\mathrm{J.mol^{-1}}$.

The ignition approach is identical to the one used for the two-dimensional simulations. The simulation starts with a volume of burnt gases using expression (6.2) with $r_c = 8\,\mathrm{mm}$.

The dynamical TFLES approach with the Mouriaux et al. (2016) correction for front interactions is used for simulations (see Section 6.3.1). The thickening factor $\mathcal{F}$ is calculated as a function of the laminar flame thickness δ_L^0 ($\delta_L^0 \approx 0.42\,\mathrm{mm}$ Quillatre 2014) and the space step Δ_x such as $\mathcal{F} = n\Delta_x/\delta_L^0$, with n the number of cells needed to resolve the flame front. The $\mathcal{F}$ factor is set at 6 and 5 grid points are used for the flame front description leading to a mesh size in the chamber of 0.48 mm and a total number of cells of 161 million. The combustion filter size is set to $\Delta = 1.4\,\mathcal{F}\,\delta_L^0$. The test-filter size is set for all simulations at $\widehat{\Delta} = 1.5\,\Delta$. The averaging filter operator needed in the expression of β is set at $\Delta_{avg} = 3\,\Delta$. The inner cut-off length scale is set at $\delta_c = 2\delta_L^0$. The wrinkling factor Ξ_Δ is computed dynamically at a fixed frequency (each 150 time steps).

The time step is computed in order to have an acoustic Courant-Friedrichs-Lewy condition CFL = 0.1.

The three-dimensional simulation of configuration 3 has been performed on the supercomputer Topaze CCRT (2021) at the Research and Technology Computing Center (CCRT). The CCRT is a high performance computing infrastructure at the CEA (French Commission for Atomic Energy and Alternative Energies), hosting supercomputers. The CPU time is approximately 21 days on 2500 cores (about 260000 iterations for 31 ms simulated time).

A backward time shift is applied to numerical results in order to circumvent the lack of description at the beginning of the simulation. This time shift is applied by superposing the experimental and numerical overpressure peaks. This calibration is also common in experimental set-ups as the ignition duration may vary between each repetition due to external parameters (ambient temperature, pressure, ...). The time shift is here 11.4 ms.

6.4.2 Numerical results

Flame front structure

The numerical flame shape for the third configuration is compared to the experimental high-speed images (Wen et al., 2013) and plotted in Fig. 6.28. The instantaneous progress variable contours ($\tilde{c} = 0.5$) are represented in Fig. 6.28a. The snapshots have been taken at the same (shifted) moments as the experiment.

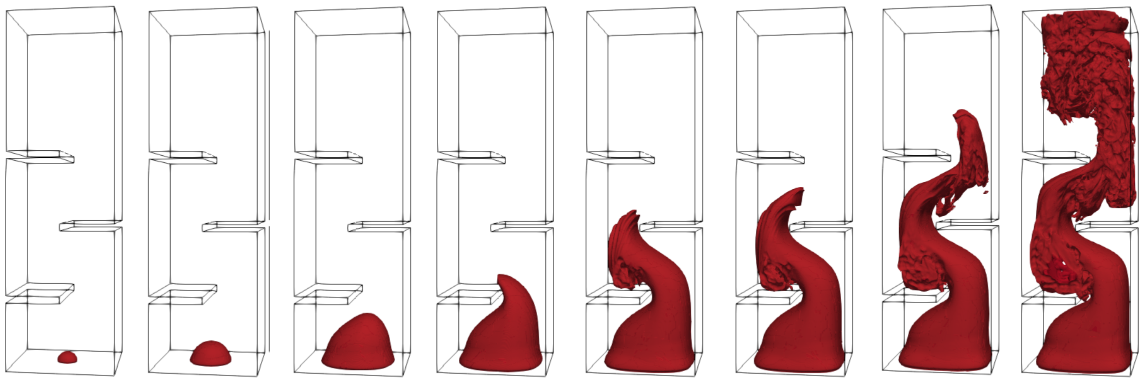

(a) Snapshots of the resolved progress variable contour ($\tilde{c} = 0.5$)

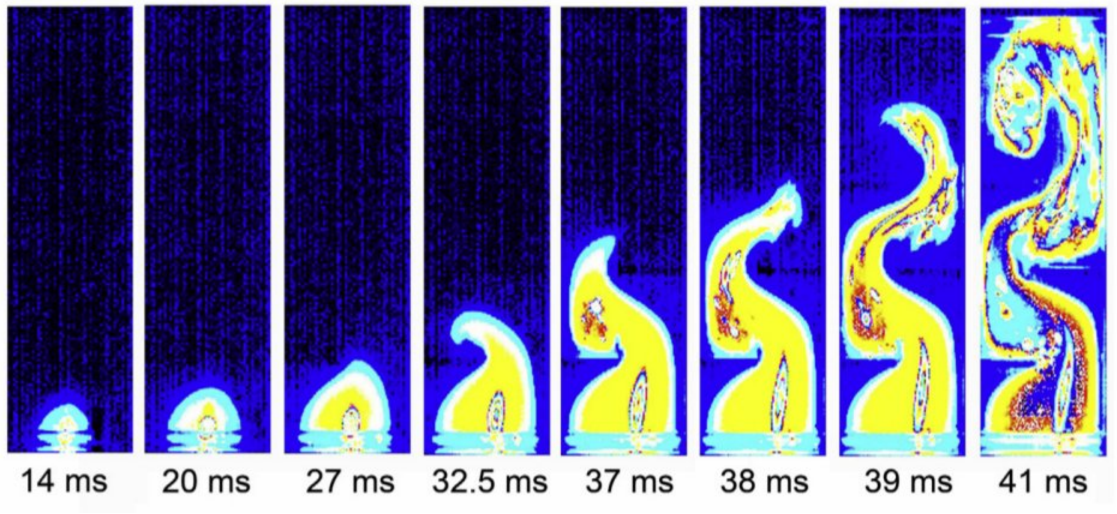

(b) Sequential images

Figure 6.28: Snapshots of the resolved progress variable contour ($\tilde{c} = 0.5$) (a) and experimental images (b) showing deflagration flame propagation in configuration 3 from Wen et al. (2013).

From the first frame to the fourth, the flame evolves without being wrinkled by turbulence and stays smooth before transiting in a more turbulent regime. The simulated flame seems to be delayed beside the experimental one at this stage. In the simulation, no ignition model is used. In addition, a mass of burnt gases is initially present in order to allow the deflagration ignition whereas the flow is at rest. In the experiment, the ignition point is very small. When the experimental flame kernel reaches the size of the simulated initial flame kernel, the flow in the whole chamber is already in movement. This explains the discrepancies between the experiment and the simulation.

In the fifth frame, we can see that the flame front is getting wrinkled by flow vortices located at the corner above the first obstacle. The tip of the front moves toward the next obstacle in a less turbulent streamline leading to a smoother flame before getting wrinkled again in the corner above the second obstacle as shown in the sixth frame. In the last frame, the major part of the flame surface is wrinkled by turbulence.

The last frame in Fig. 6.28a seems to have no delay compared to the experimental flame, probably due to the time shift. More details on the simulated flame front delay over the experimental flame are given in the next subsection.

Flame front position and speed

Fig. 6.29 shows the flame front tip position as a function of time (time shifted according to the overpressure peak). The flame front position is found by taking the position of the furthest front from the chamber bottom. The flame front velocity is computed as the derivative through time of the flame position and is plotted in Fig. 6.30.

Before the first obstacle, the flame position increases linearly through time matching a quasi constant flame speed (as shown also in Fig. 6.30). Then, flow vortices appear behind each obstacle, the flame becomes turbulent and the flame surface area increases.

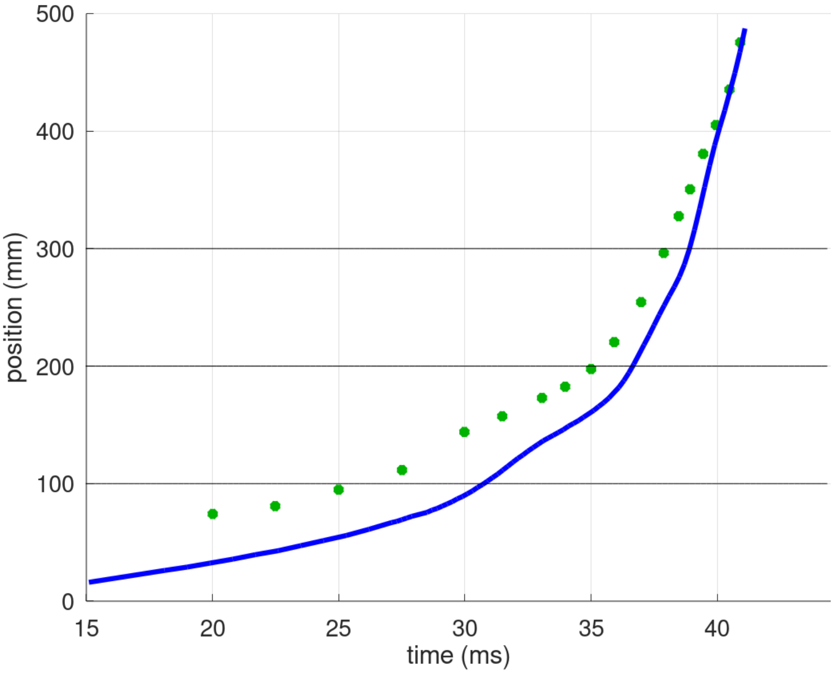

Figure 6.29: Flame front position for LES 3D. (▬): LES 3D; (—): obstacles locations and (●): experimental data of Wen et al. (2013).

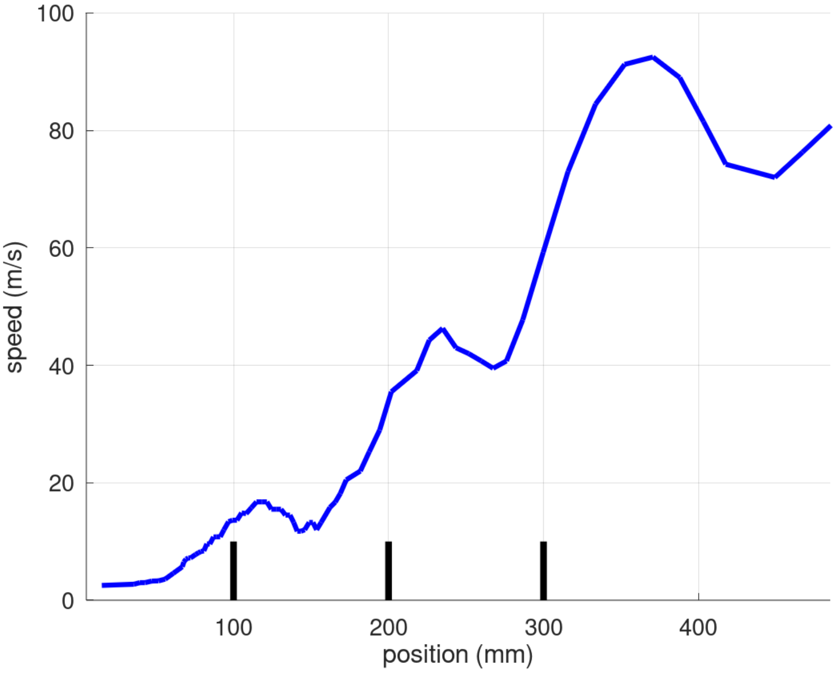

Figure 6.30: Flame front speed for LES 3D. (━): LES 3D and (━): obstacles locations.

The flame continues to accelerate throughout the chamber (as shown also in Fig. 6.30). The numerical slope seems steeper in the region between the first obstacle and the chamber exit with respect to experimental data. The flame seems thus faster in this region. Unfortunately, the flame velocity can not be compared to experimental data given that experimental speed computation method has not been detailed by the authors Wen et al. (2013). This phenomenon is more denoted after the third obstacle, the numerical flame accelerates more than the experimental flame at the end catching up with the experimental flame front position as shown in Fig. 6.29. In this region the flame front velocity reaches its maximum value, which is almost $93\,m.s^{-1}$.

Numerical results are in good accordance with the experimental position. Due to the ignition issues discussed previously, the simulation results slightly differ at the beginning and then get closer to the experimental position progressively through time.

Overpressure dynamics

Fig. 6.31 represents the overpressure profiles through time. The experimental and numerical overpressure profiles are extracted at the same location in the chamber (bottom). A backward time shift is applied to numerical results in order to match the experimental overpressure peak. That is why the experimental and simulated peaks happen at the same moment in Fig. 6.31. The first pressure peak measured during experiments is due to the thin membrane rupture located at the chamber exit containing the gases in the chamber before ignition. As this membrane is not present in the simulations, this peak is not observed in the simulation results.

The experimental major peak reaches 183 mbar. The peak happens after the flame fronts exit the chamber. One reason of this overpressure peak is that the flame obstructs partially the way next to the first obstacle making the effect of a plug while the flame continues to expand. Therefore a particularly high overpressure located at the bottom of the chamber is observed. The simulated overpressure peak is underestimated by about 23% with a peak amplitude of 140 mbar. The gap between the numerical and experimental peak amplitudes may be due to the lack of ignition model. Another explanation may be that the number of points used for the flame front description is rather low. Another computations with a finer description of the flame front will be useful.

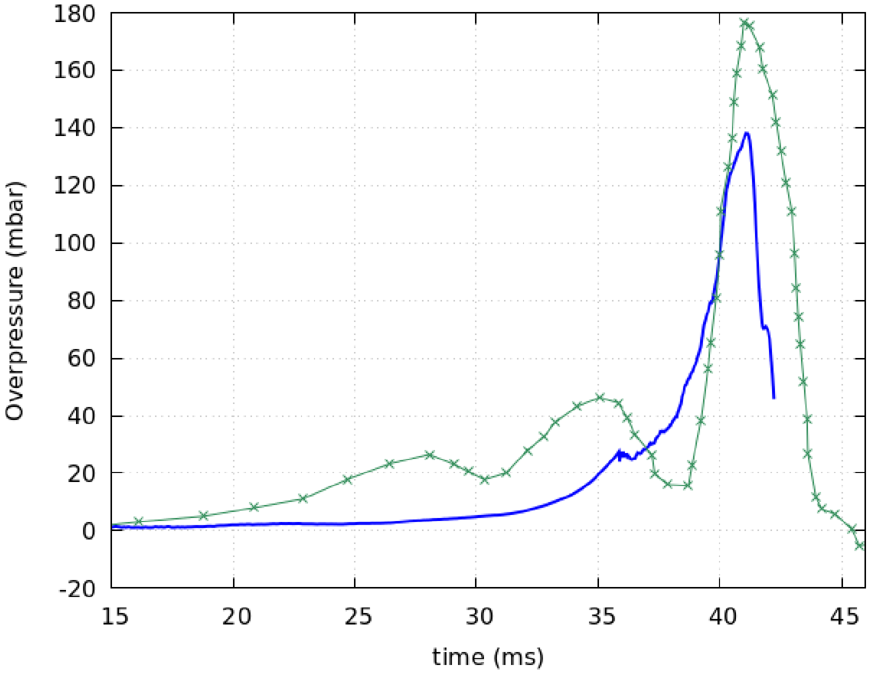

Figure 6.31: Overpressure evolution for LES 3D. (—): LES 3D and (●): experimental data of Wen et al. (2013).

Wrinkling factor exponent

Fig. 6.32 shows two snapshots at $t = 40.1$ ms. The flame front is represented in red with $\tilde{c} = 0.5$ for both snapshots. The snapshot on the right side is layered with the model parameter β. In order to visualize the instantaneous field, the blue colormap representing the β parameter, has a threshold value of 0.05, under which the wrinkling factor exponent is not represented. By comparing the left side and the right side of Fig. 6.32, we can see that the wrinkling factor exponent parameter is almost null in the smooth parts of the flame and locally reaches values close to 0.5 in the fully turbulent zones. The beta parameter varies where the flame is wrinkled as expected by the subgrid model. The same observation as in two-dimensional simulations (in Fig. 6.12) is made, the β parameter is almost null where the flame is smooth.

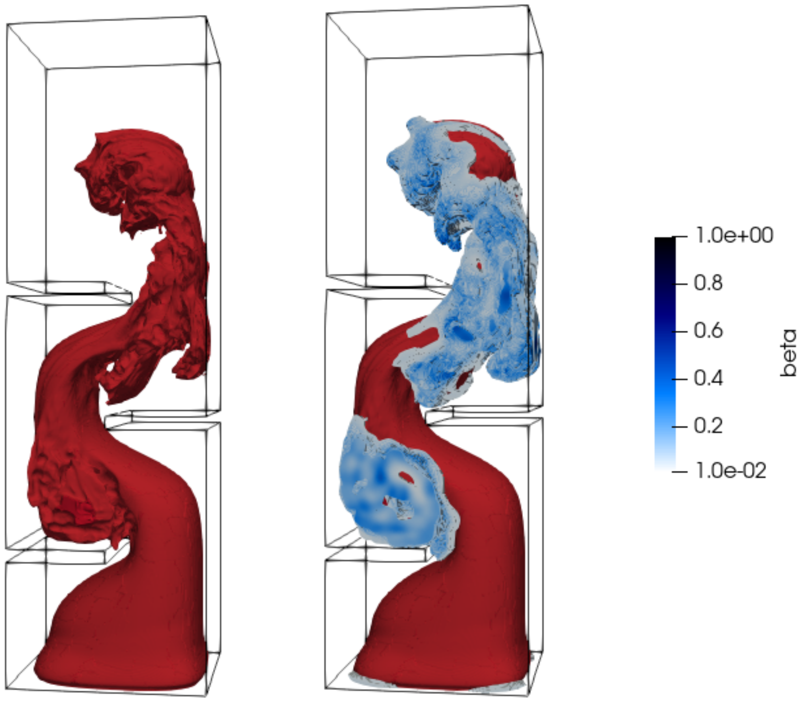

Figure 6.32: Snapshots of the instantaneous flame front such as $\tilde{c} = 0.5$ on the left side and the instantaneous flame front layered with the model parameter β.

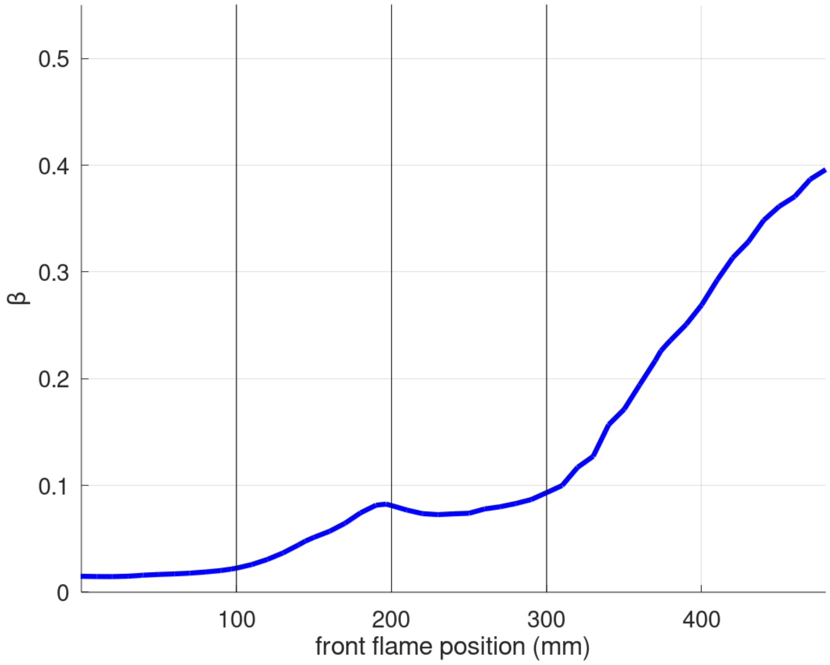

Figure 6.33: Spatial averaged dynamic β-parameter as a function of the flame front position. (▬): LES 3D and (—): obstacles locations.

In order to observe the behavior of the model parameter β through time, the spatial averaged parameter β^{avg} defined by expression (6.7) is plotted in Fig. 6.33 as a function of the flame front tip position. At the early stages of the transient (before the first obstacle), the wrinkling factor exponent is almost null as the flame is smooth, in our case, it is in the range of 10^{-2}. The profile of β^{avg} increases quickly after the flame front reaches the first obstacle. Then, as explained earlier, the flame front alternating between wrinkled and smooth zones (*i.e.* zones locally less turbulent and thus, with a β parameter less important) leading to a slight decrease of the integrated wrinkling factor exponent before the third obstacle. After the third obstacle, the flame front is more and more wrinkled leading to high values of β^{avg}.

Flame surfaces

Fig. 6.34 shows the resolved flame surface $S_r(t)$ and the total flame surface $S_t(t)$ as a function of the flame front position. These surfaces are defined by expression (6.8).

Before the first obstacle the flame is not wrinkled, leading to an identical total and resolved flame surfaces. Then, from the first obstacle to the third, the transition from laminar to turbulent starts to rise leading to small values of the wrinkling factor as the turbulent intensity is still low. Thus, the total flame surface starts to increase slightly. Until the third obstacle, the resolved and total flame surface are still close to each other. Afterwards, when the flow becomes fully turbulent the resolved flame surface slope becomes steeper. The total flame surface is significantly larger than the resolved flame surface (twice more important when the flame reaches the chamber exit) meaning that the subgrid wrinkling contribution becomes significant.

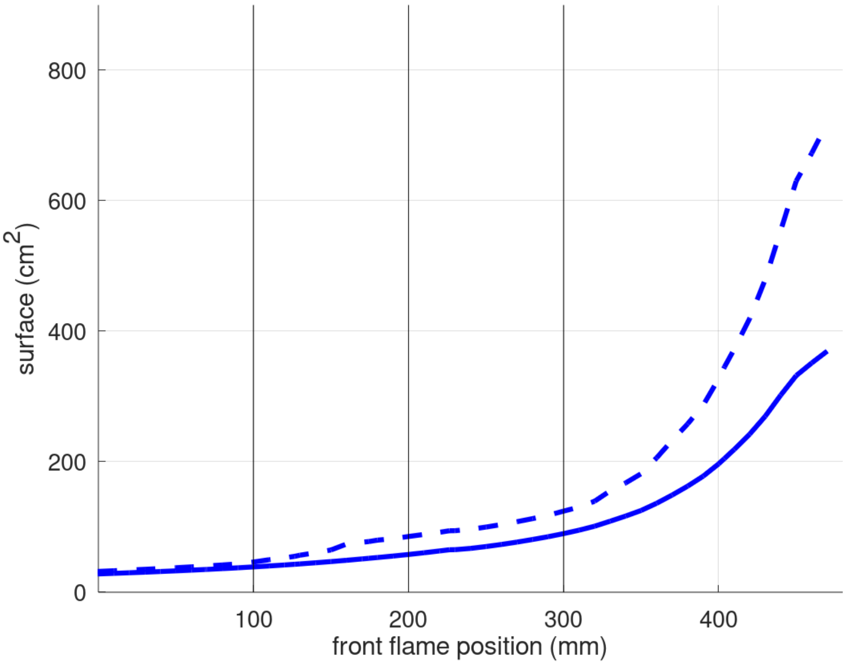

Figure 6.34: Resolved and total flame surface for LES 3D. (—): Resolved flame surface; (- - -): total flame surface and (—): obstacles locations.

Heat release

The heat release $\dot{\omega}_T$ (expression (4.13)) is integrated over the chamber volume and plotted in Fig. 6.35. Here, the heat release increases with the reaction rate which increases in accordance with the flame surface shown in Fig. 6.34.

In order to investigate the proportionality between the reaction rate (or the heat release) and total flame surface, we introduce the integrated reaction rate of the fuel, ω_t, given by:

$$\omega_t = - \int_{\mathcal{V}} \dot{\omega}_F \, d\mathcal{V} \tag{6.10}$$

with $\mathcal{V}$ the computational volume. The aim is to investigate the reaction rate behavior in accordance with the total flame surface. The same computation can obviously be performed using the heat release $\dot{\omega}_T$. Here $\dot{\omega}_F$ has been chosen for the sake of simplicity.

Fig. 6.36 shows the time evolution of the ratio between the integrated reaction rate ω_t and the total flame surface $S_t(t)$ (given by expression (6.8)). The ratio remains relatively constant through the simulation showing that the reaction rate increases mostly thanks to the flame surface rise. The lack of ignition model associated to a coarse mesh grid lead to a short delay observed in Fig. 6.36 before reaching a plateau of approximately 0.025 kg/m^3/s. Despite the small fluctuations of the ratio due to the flame stretch, the ratio stays relatively constant from the laminar zone (before the first obstacle) to the fully turbulent zone (after the last obstacle). In addition, the same plateau value has been found for the one-dimensional laminar flame and represented in Fig. 6.36.

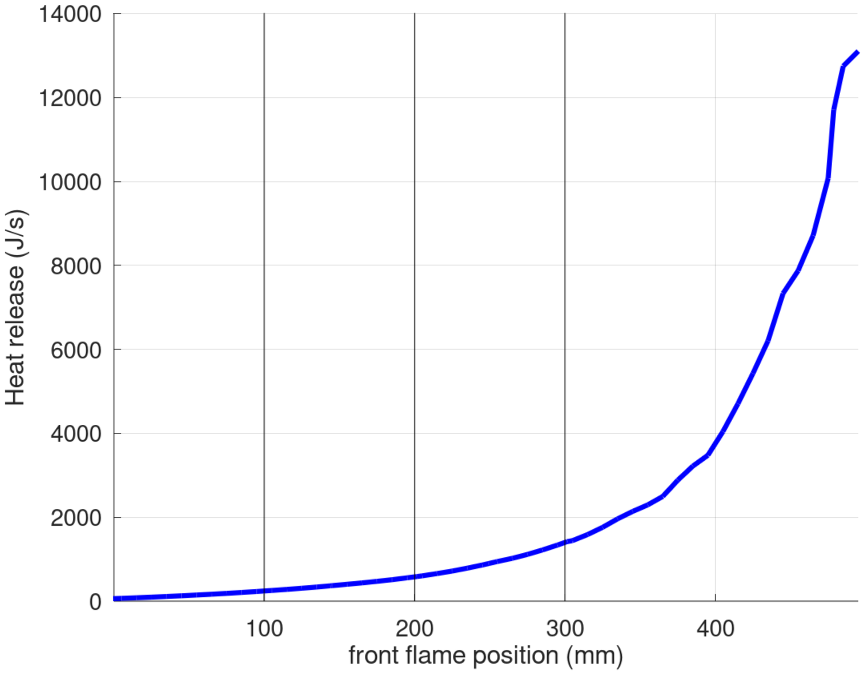

Figure 6.35: Heat release of LES 3D. (━): LES 3D and (—): obstacles locations.

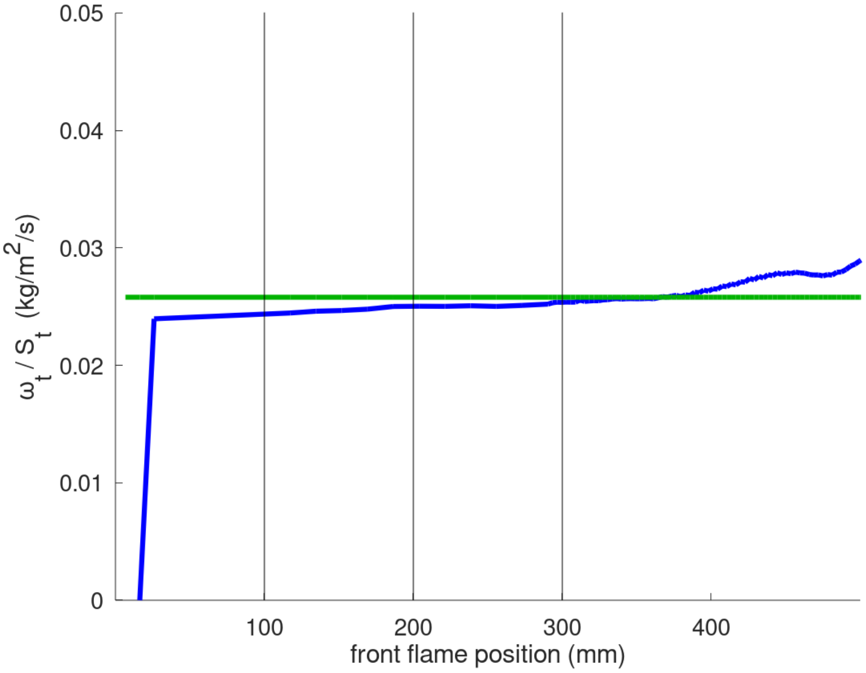

Figure 6.36: Ratio between the integrated reaction rate and the total flame surface. (—): LES 3D, (—): one-dimensional LES plateau and (—): obstacles locations.

6.5 LES numerical results: comparison between two and three-dimensional simulations

The two-dimensional simulation with $\mathcal{F} = 6$ and $n = 6$ (LES 3 detailed in table 6.1 and used as a reference case) is compared to the previous three-dimensional simulation. This study allow to check if the three-dimensional simulation can be predicted from the two-dimensional simulation. To lighten the notation, the two-dimensional simulation is denoted by LES 2D and the three-dimensional simulation is denoted by LES 3D.

Flame front structure

Fig. 6.37 aims to compare the flame front structure between the two-dimensional and three-dimensional flames. In this figure, a time shift of 12.2 ms is applied to LES 2D and of 11.4 ms to LES 3D.

When the flame is smooth, from the first frame until the fourth, both simulations looks alike. However, when turbulence wrinkles the flame front, LES 3D seems to be more wrinkled. This effect is due to the fact that turbulent structures are not only in one plan, the flame front is wrinkled as well in the longitudinal plan but also in depth. However, the global shape of the flame is conserved in both cases.

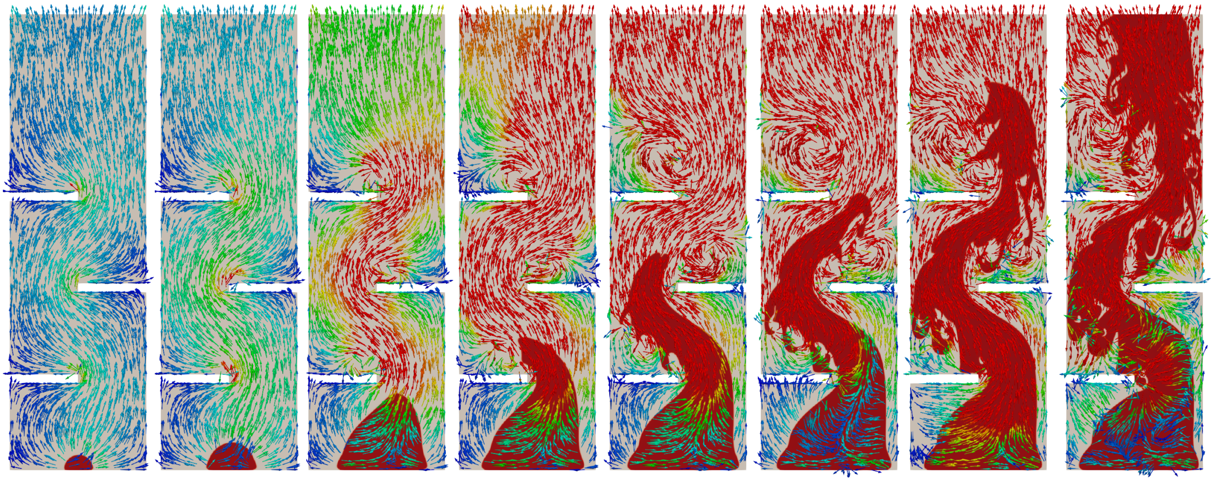

(a) Snapshots of the temperature field and velocity vectors of LES 2D

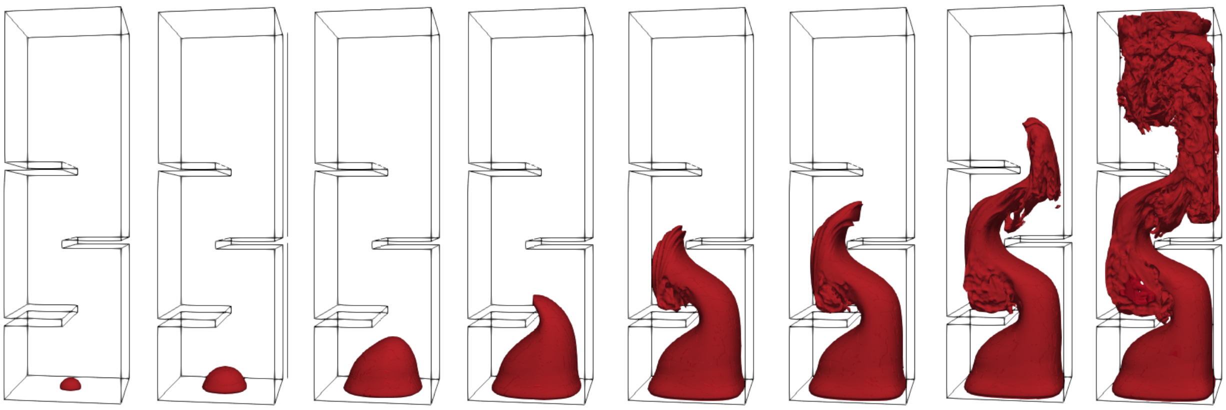

(b) Snapshots of the resolved progress variable contour ($\tilde{c} = 0.5$) of LES 3D

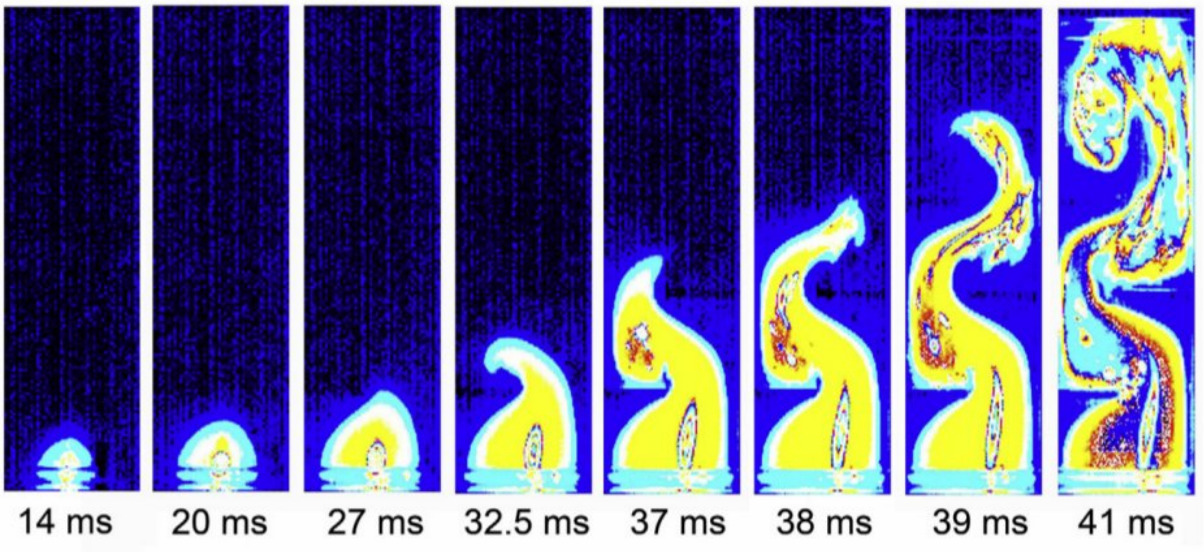

(c) Sequential images

Figure 6.37: (a) Snapshots of the temperature field and velocity vectors of LES 2D; (b) Snapshots of the resolved progress variable contour ($\tilde{c} = 0.5$) of LES 3D and (c) experimental images showing deflagration flame propagation in configuration 3 from Wen et al. (2013).

Flame front position and speed

The flame front tip position is plotted for 2D and 3D simulations in Fig. 6.38. The same time shift is applied at both simulations which is the LES 3D time shift: 11.4 ms.

Fig. 6.39 represents the flame front velocity (derivation of the simulated flame front position). The experimental velocity is not represented along the simulation results as the experimental speed computation method has not been detailed by the authors Wen et al. (2013).

LES 2D is faster than the three-dimensional simulation at the first moments of the simulation. The difference is caused by the initialization method. Indeed, for the two-dimensional flame, the surface covered by the initial cylindrical flame kernel is slightly superior than the surface of LES 3D initial spherical flame kernel leading to a higher reaction rate at the ignition. Then, between the first and last obstacles, the flame front tip positions behave similarly. Both velocity profiles are quite close.

The flame speed computed with LES 3D is slightly higher than the one computed with the two-dimensional simulation from the first and until the second obstacle. At the end, after $y = 400$ mm, LES 3D flame seems to catch up by accelerating more than LES 2D, as shown in Fig. 6.39.

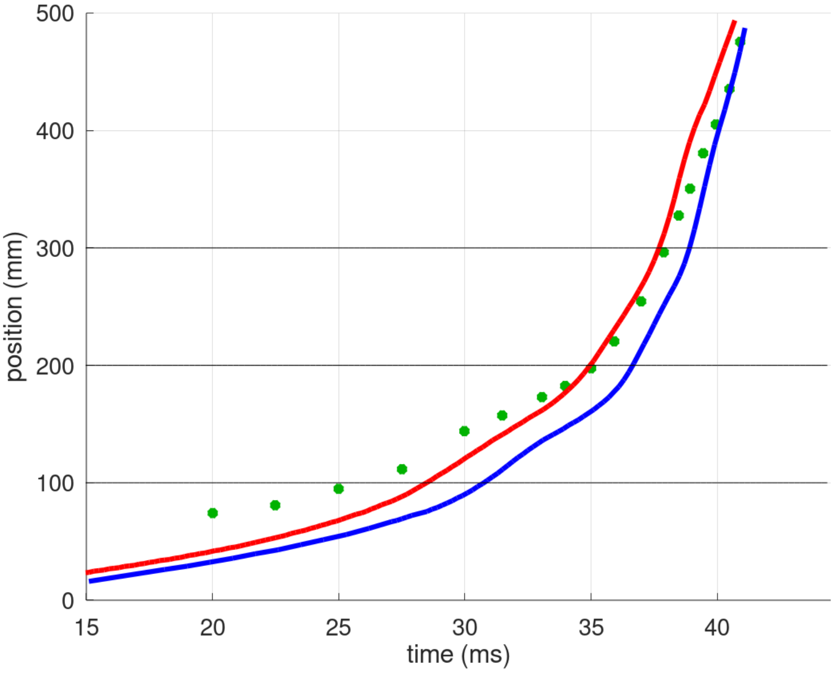

Figure 6.38: Flame front position for LES 2D and LES 3D. (—): LES 3D; (—): LES 2D; (—): obstacles locations and (●): experimental data of Wen et al. (2013).

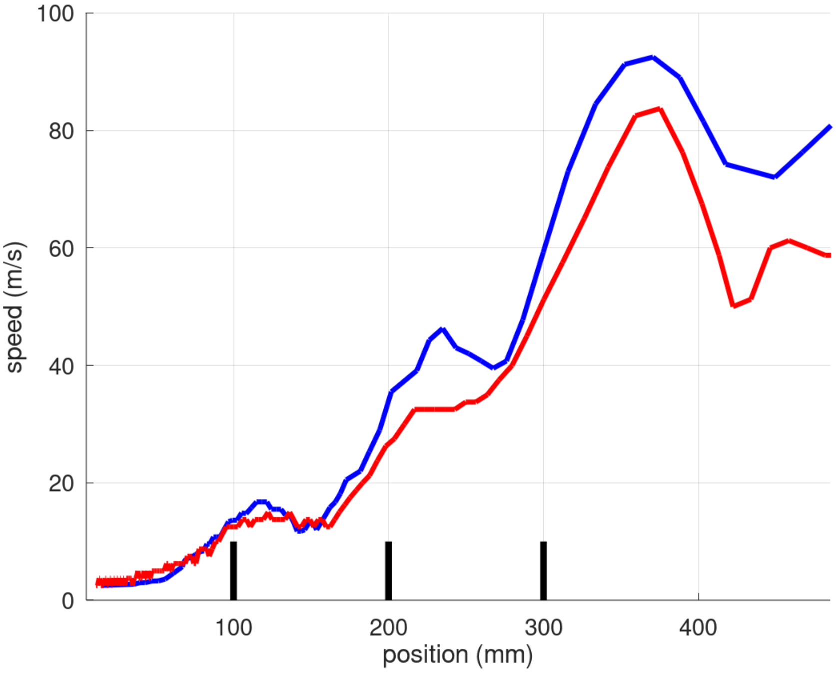

Figure 6.39: Flame front speed for LES 2D and LES 3D. (—): LES 3D; (—): LES 2D and (—): obstacles locations.

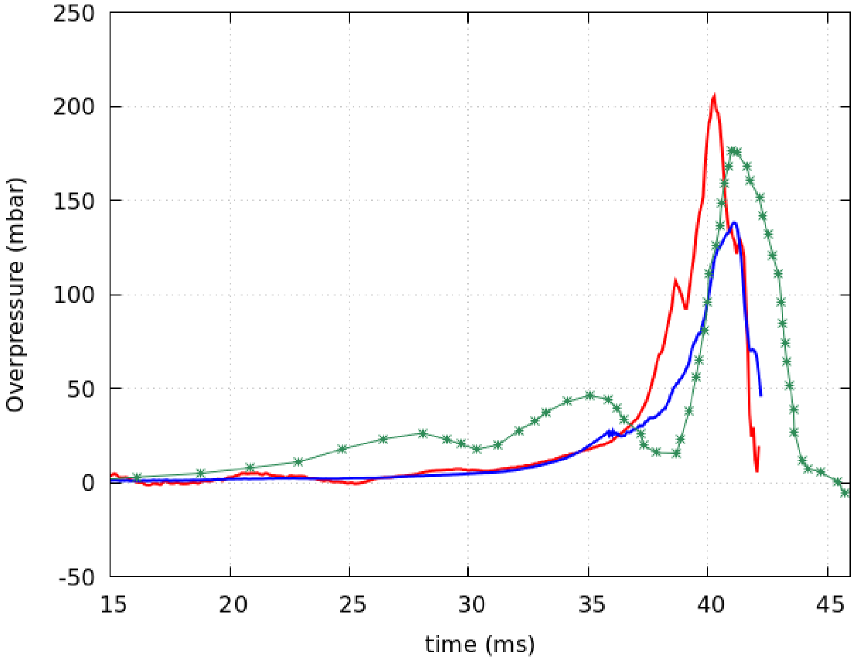

Figure 6.40: Overpressure evolution for LES 2D and LES 3D. (—): LES 3D; (—): LES 2D and (●): experimental data of Wen et al. (2013).

Overpressure dynamics

The overpressure evolutions obtained with 2D and 3D simulations are represented in Fig. 6.40. The time shift applied is the same as previously, identical for both cases.

The LES 2D peak has a higher amplitude and occurs before LES 3D. The two-dimensional overpressure peak is almost 25% above the experimental value whereas the three-dimensional is 23% below.

Flame surfaces

In order to compare the flame surfaces between the 2D and 3D simulations, the total and resolved flame surfaces of LES 2D have been multiplied by the channel depth length (15 cm). Therefore the flame is considered as a planar surface in the depth, this assumption leads to two main consequences: first, the flame is not wrinkled in the depth. Second, the flame loses its spherical shape and becomes more rectangular. The resolved and total flame surfaces for both LES 2D and LES 3D simulations are plotted in Fig. 6.41.

Right after ignition, the flame kernel is circular in LES 2D and spherical in LES 3D. However, converting the two-dimensional surface by multiplying its value by the depth leads to a cylindrical kernel. Thus, the resolved and total flame surfaces are larger in the converted LES 2D than the LES 3D surfaces.

Moreover, in both cases, the total and resolved flame surfaces are identical at the beginning. Then, when the flame gets wrinkled, the total flame surface becomes superior than the resolved flame surface. In LES 2D, the total flame surface is noticeably superior after the second obstacle while this separation happens after the first obstacle for LES 3D. Therefore, the subgrid wrinkling model reacts earlier in LES 3D than in LES 2D.

Fig. 6.41 shows that the difference between LES 2D and 3D is lower for the resolved than the total flame surfaces. However, the subgrid wrinkling model acts differently in 2D and 3D computations. The earlier activation of the wrinkling factor in LES 3D may explain its flame front speed superiority despite a higher flame front surface for LES 2D.

Heat release

The integrated heat release over the chamber volume obtained with LES 3D is compared to the integrated heat release obtained with LES 2D (after multiplying the profile by the chamber depth) and plotted in Fig. 6.42. Right after ignition, the flame kernel is cylindrical in LES 2D (due to the two-dimensional surface conversion) and spherical in LES 3D. Thus, the flame surface is larger in the converted LES 2D than the LES 3D surface (as shown in Fig. 6.41) leading to a more important integrated reaction rate (*i.e.* integrated heat release) as shown in Fig. 6.42. Globally, the converted LES 2D heat release is superior than the LES 3D heat release. This result was expected as the converted total flame surface is more important.

The two-dimensional simulation does not retrieve the exact deflagration physical features but it is in the same order of magnitude as LES 3D. Two-dimensional simulation is useful for adjusting the numerical parameters (such as $\mathcal{F}$, n, test-filter size...) for the three-dimensional simulation.

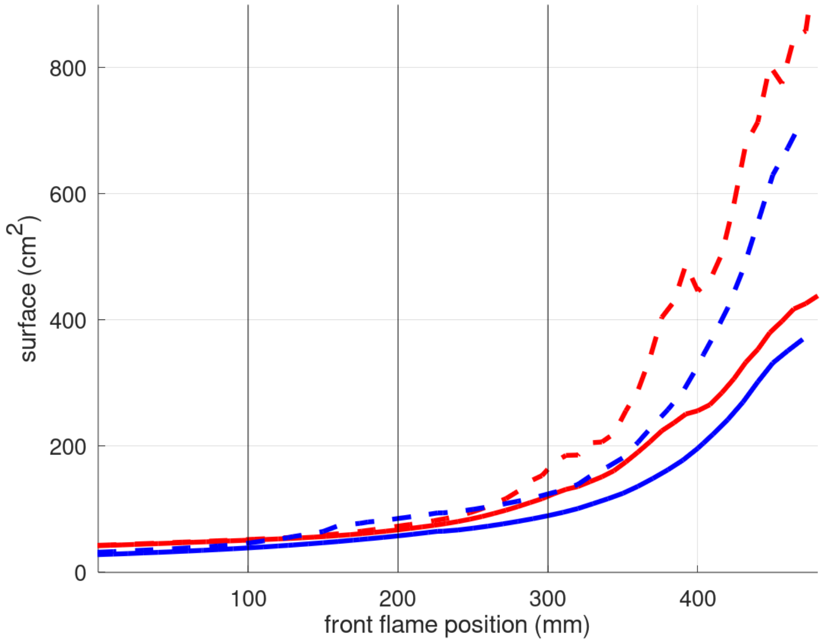

Figure 6.41: Resolved and total flame surface for LES 2D and LES 3D. (—): Resolved flame surface of LES 3D; (—): resolved flame surface of LES 2D; (- - -): total flame surface of LES 3D; (- - -): total flame surface of LES 3D and (—): obstacles locations.

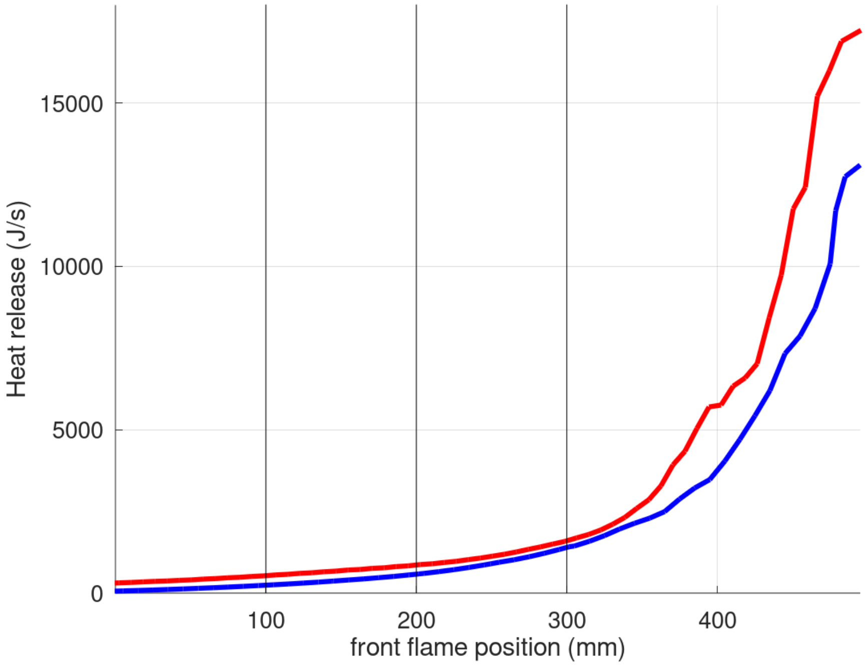

Figure 6.42: Heat release of LES 2D and LES 3D. (—): LES 3D; (—): LES 2D and (—): obstacles locations.

6.6 RANS simulations: two-dimensional simulations

Now, let us confront the results of the LES approach and the RANS approach for the same experimental configuration (third configuration of Wen et al. 2013).

One should keep in mind that the RANS model is designed for situations where the turbulence is fully developed, which is not the case at the beginning of the simulation. However, the turbulent flame speed correlation of Goulier (2015) takes into account the transition effects for unsteady flows (Gostintsev et al., 1988).

6.6.1 RANS approach

An alternative approach is available in CALIF^{3}S -P^{2}REMICS for the simulation of turbulent deflagrations. A statistical description of turbulence is used: a wide range of RANS models are available (”high-Reynolds” variants, with the usual wall laws, and low-Reynolds models). In the present studies, turbulence is described with the so-called $k-\omega$ SST model (Wilcox, 1988; Menter, 1994; Menter et al., 2003).

The combustion modelling is based on a *turbulent flame-speed closure* approach. The flame brush location is determined by a phase-field-like technique, solving a transport equation for a characteristic function (more precisely speaking, a *Hamilton-Jacobi* equation), leading to a formulation which is reminiscent of the so-called G-equation based models (Kerstein et al., 1988; Lipatnikov and Chomiak, 2002). The unknown of this transport equation is thus denoted here by G and referred to hereafter as the "G-field". It obeys the following relation:

$$\partial_t(\overline{\rho}\widetilde{G}) + \mathrm{div}(\overline{\rho}\widetilde{G}\widetilde{\boldsymbol{v}}) + \rho_u v_f |\boldsymbol{\nabla}\widetilde{G}| = 0, \tag{6.11}$$

where the quantity ρ_u is a constant density, which stands for a characteristic value for the unburnt gases density, and v_f is the turbulent flame velocity relatively to fresh gases. Flame ignition is obtained by setting $G = 0$ in a small neighbourhood of the ignition point and $G = 1$ elsewhere.

Usually, G-equation based models apply to perfectly premixed flows (*i.e.* flows with constant initial composition), and the chemical state of the flow is governed by the value of G only, here we consider: for $G \geq 0.5$, the mixture is supposed to be in its fresh (initial) state and $G < 0.5$ is supposed to correspond to the burnt state; in both cases, the composition of the fuel is known (to the initial value in the fresh zones, and to the state resulting from a complete chemical reaction in the burnt one). The flame front is located at $G = 0.5$. However, for partially premixed turbulent flows (*i.e.* flows with non-constant initial composition), the situation is more complex, since the composition of the mixture can no more be deduced from the value of G. The line followed here to circumvent this difficulty consists in keeping the classical reactive formulation of the chemical species mass balance equations (1.9), but evaluating the reaction term as a function of G. The reaction rate of each chemical species may be written as:

$$\overline{\dot{\omega}_i} = \nu_i W_i \overline{\dot{\omega}}, \qquad \text{for } 1 \leq i \leq N_s,$$

where ν_i is the stoichiometric coefficient of the species i. The rate of progress of the reaction $\overline{\dot{\omega}}$ is supposed to vanish when either the fuel mass fraction Y_F or the oxidant mass fraction Y_O vanishes and, as announced, is governed by the value of G (CALIF^{3}S-P^{2}REMICS, 2020;

Gastaldo et al., 2017):

$$\bar{\dot{\omega}} = \frac{v_f}{\delta}\,\eta(\widetilde{Y_F},\widetilde{Y_O})\,(\widetilde{G}-0.5)^-, \quad \eta(\widetilde{Y_F},\widetilde{Y_O}) = \min\Big(\frac{\widetilde{Y_F}}{\nu_F W_F},\frac{\widetilde{Y_O}}{\nu_O W_O}\Big)$$

where for $a \in \mathbb{R}$, $a^- = -\min(a,0)$, ν_F and ν_O are the fuel and oxidant molar stoichiometric coefficients, W_F and W_O stand for the molar masses of the fuel and oxidant respectively. δ is a quantity homogeneous to a length scale, which governs the thickness of the reaction zone.

The model is closed by a correlation for the turbulent flame speed. The correlations which are the most frequently encountered in the literature are implemented in the CALIF^{3}S - P^{2}REMICS software (Bradley et al., 1992b; Bray, 1990; Zimont, 2000; Lipatnikov and Chomiak, 2002; Peters, 2000). Among them, the following closure relations have been retained for the simulations presented in this chapter:

- The Goulier (2015) correlation:

  $$v_f = \max\left[s_L, s_L\,1.613\left(\frac{r}{L_t}\right)^{0.333}\left(\frac{v'}{s_L}\right)^{0.526}\mathrm{Le}^{-0.14}\right], \tag{6.12}$$

  where v' is the root mean square of the velocity fluctuations and L_t is the integral length scale of turbulent structures computed such as:

  $$v' = \sqrt{\frac{3}{2}k} \quad \text{and} \quad L_t = k^{3/2}/\varepsilon \tag{6.13}$$

  with k the turbulent kinetic energy, s_L the laminar flame speed, r the distance between the flame front and the ignition point and Le the Lewis number of the unburnt mixture. The dissipation rate ε is estimated as: $\varepsilon = C_\mu\,\omega\,k$ with ω the specific dissipation and $C_\mu = 0.09$ a model constant.

- The Bray (1990) correlation :

  $$v_f = \max\left[s_L, 0.875\,\mathrm{Ka}^{-0.392}\,v'\right], \tag{6.14}$$

  with Ka the dimensionless Karlovitz stretch factor given by (Abdel-Gayed et al., 1987):

  $$\mathrm{Ka} = 0.157\left(\frac{v'}{s_L}\right)^2 \mathrm{Re}_T^{-0.5},$$

  with Re_T the turbulent Reynolds number defined such as:

  $$\mathrm{Re}_T = \frac{v' L_t}{\nu}. \tag{6.15}$$

- The closure relation developed by Zimont (2000) (Lipatnikov and Chomiak, 2002):

  $$v_f = \max\left[s_L, A\,v'\,\mathrm{Da}^{1/4}\right], \tag{6.16}$$

  where A is a constant ($A = 0.53$ for methane/air explosive atmospheres), Da is the Damköhler number.

This system is solved by a fractional-step pressure correction algorithm (an extension to reactive case of the numerical scheme presented in Chapter 3 Section 3.C), which ensures all natural stability properties, as keeping the species mass fractions or thermodynamic variables (pressure, internal energy) within their physical bounds (Gastaldo et al., 2017; Grapsas et al., 2021).

6.6.2 Numerical set-up

The RANS simulations are performed on a 2D computational domain. Outside the combustion chamber, the computational domain is extended in order to allow a more realistic reproduction of the exit of the expanding gas from the combustion chamber into the atmosphere and to push further away the reflection on the boundary of the pressure waves generated by the deflagration (see Section 6.3.1). The computational domain for RANS simulations is the same as that used for LES simulations (see Section 6.3.1). The mesh is composed by a non-uniform structured grid with rectangular cells. The mesh size is kept constant in the chamber ($\Delta_x = 0.5\,\mathrm{mm}$) before getting gradually expanded outside the chamber (like for LES computations). The atmospheric zone mesh grid is twenty time coarser on its boundaries (equivalent to the mesh partition explained in Fig. 6.2).

Adiabatic and no-slip wall boundary conditions were applied at the solid interfaces (bottom and vertical faces of the chamber, faces of the obstacles). A free outlet condition is enforced at the atmospheric zone boundaries where the pressure is maintained at $p_{ext} = 101325\,\mathrm{Pa}$.

The chemistry is simply described with a one step global reaction (as for LES simulations). The ignition is made with an initial flame kernel radius $r = 8\,\mathrm{mm}$, r being the distance between the flame front and the ignition point, by setting $G = 0$ in this zone. Initially the fluid is assumed to be at rest in the facility. The initial turbulent kinetic energy is set to $k_0 = 10^{-5}\,\mathrm{m}^2.\mathrm{s}^{-2}$. The initial specific dissipation ω_0 is set to $\omega_0 = \rho_0\, k_0/(r_\nu\, \mu_l)$, $r_\nu = 10$ being the turbulent viscosity ratio (defined as the ratio of turbulent and laminar viscosities).

The time step is computed in order to have an acoustic Courant-Friedrichs-Lewy condition CFL = 0.5. Even if the mesh size used in RANS computation is fairly close to the LES computation, the time step is bigger as the time scheme is implicit (see Section 3.C and Grapsas et al. (2021) for more details). The CPU time (computing time multiplied by the number of processors used) associated to the two-dimensional LES (LES 3) is approximately 99 days on one processor (13 hours on 180 processors) whereas the CPU time for the RANS approach is estimated at almost 30 days on one processor (15 hours on 48 processors). The CPU time is approximately 21 days on 2500 cores for the three dimensional simulation performed with the LES approach.

The third configuration of the Wen et al. (2013) experiments is simulated. The numerical results obtained with the RANS approach are first compared to the LES 3 numerical results. Then, the results are compared with the numerical results obtained in the three dimensional domain with the LES approach. Finally, three simulations with different turbulent flame speed correlations are compared. Simulations are listed in Table 6.7 with their numerical parameter details.

Name	Configuration	$\mathcal{F}$	n	Δ_x in the chamber	Number of cells	δ_c	Unresolved flame speed
LES 3	3	6	6	0.4 mm	643 819	TFLES	$\Xi_\Delta s_L$
LES 3D	3	6	5	0.48 mm	161M	TFLES	$\Xi_\Delta s_L$
RANS 1	3	$\varnothing$	$\varnothing$	0.5 mm	409 066	G-equation	Goulier (2015)
RANS 2	3	$\varnothing$	$\varnothing$	0.5 mm	409 066	G-equation	Bray (1990)
RANS 3	3	$\varnothing$	$\varnothing$	0.5 mm	409 066	G-equation	Zimont (2000)

Table 6.7: Numerical parameters of RANS 1, 2, 3, LES 3 and LES 3D.

A backward time shift for each simulation is applied to numerical results in order to circumvent the lack of description at the beginning of the simulation. To match the overpressure peaks, a time shift for RANS 1 is set at 10 ms, RANS 2 at 6.1 ms and RANS 3 at 5 ms. We recall that the time shift is set at 12.2 ms for LES 3 and 11.4 ms for LES 3D.

6.6.3 Comparison between two-dimensional LES and RANS simulations

The two-dimensional RANS approach denoted by RANS 1 in Table 6.7 is compared here against the two-dimensional LES approach denoted by LES 3 in Table 6.1.

Flame front structure

Snapshots of the temperature field and velocity vectors for RANS 1 and LES 3 simulations alongside the experimental images are shown in Fig. 6.43. The temperature field allows to visualize the flame front and the velocity vectors show the flow acceleration frame after frame.

In order to complete the flow representation, snapshots of the vorticity field layered by the heat release for RANS 1 and LES 3 simulations alongside the experimental images are shown in Fig. 6.44. The heat release allows to visualize the flame front while the vorticity shows the turbulent structures of the flow. The snapshots have been taken at the same (shifted) moment as the experimental images.

Until the fourth frame, both simulations are quite similar as well in Fig. 6.43 as in Fig. 6.44. Afterwards, LES 3 accelerates more than RANS 1 as shown from the fifth frame to seventh of Fig. 6.43. Indeed, for the same period of time, the flame front of LES 3 has traveled a greater distance than RANS 1 flame front. However, the flame front obtained with the RANS approach is faster between the last obstacle and the chamber exit than the LES flame front. Therefore, the RANS approach with Goulier (2015) seems to be particularly faster at the end of the transient (as shown also below in Fig. 6.46).

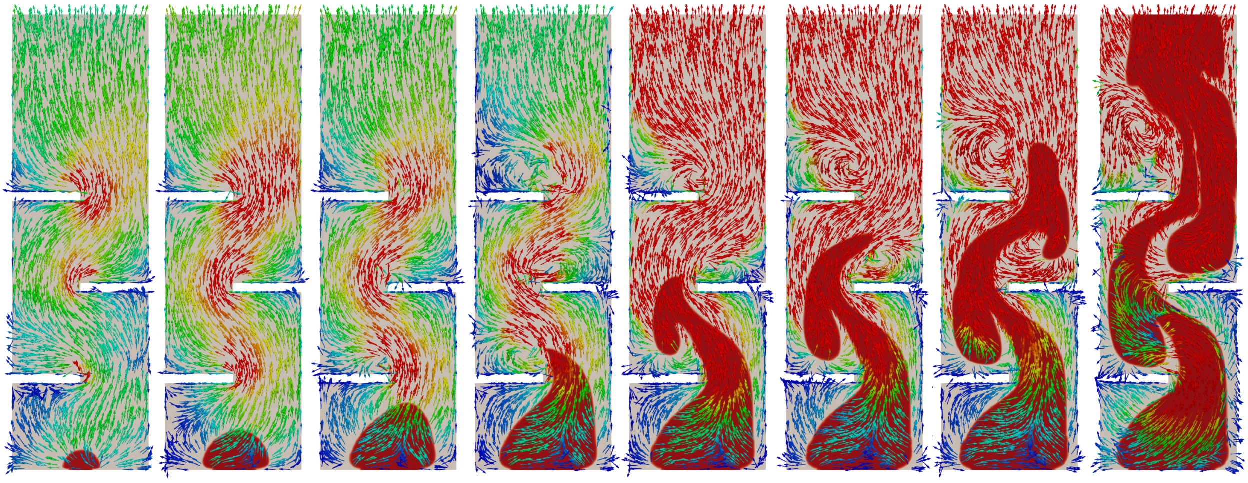

(a) Snapshots of the temperature field and velocity vectors of RANS 1

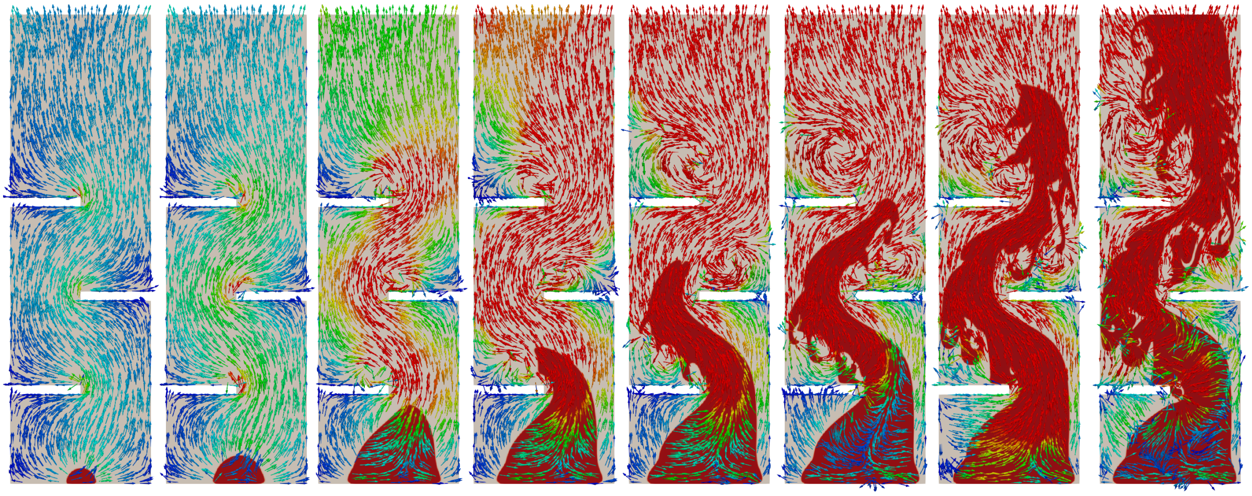

(b) Snapshots of the temperature field and velocity vectors of LES 3

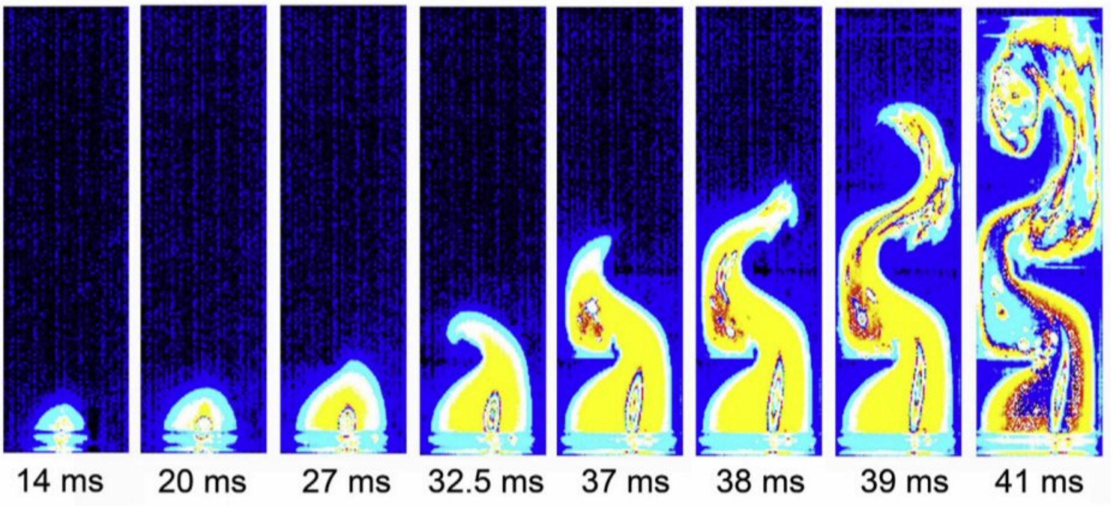

(c) Sequential images

Figure 6.43: (a) Snapshots of the RANS 1, (b) LES 3 and (c) experimental images showing a deflagration flame propagation in configuration 3 from Wen et al. (2013).

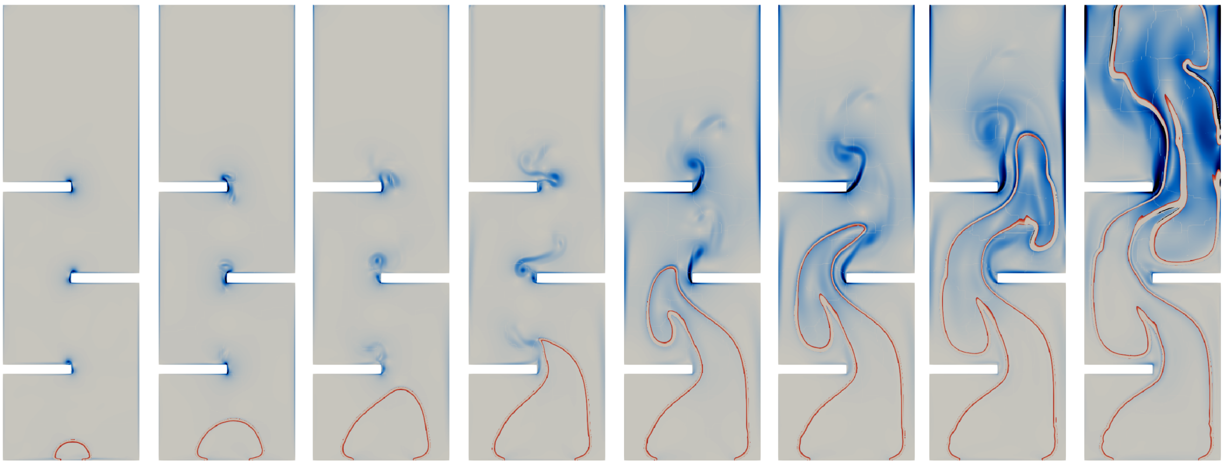

(a) Snapshots of the heat release and the flow vorticity of RANS 1

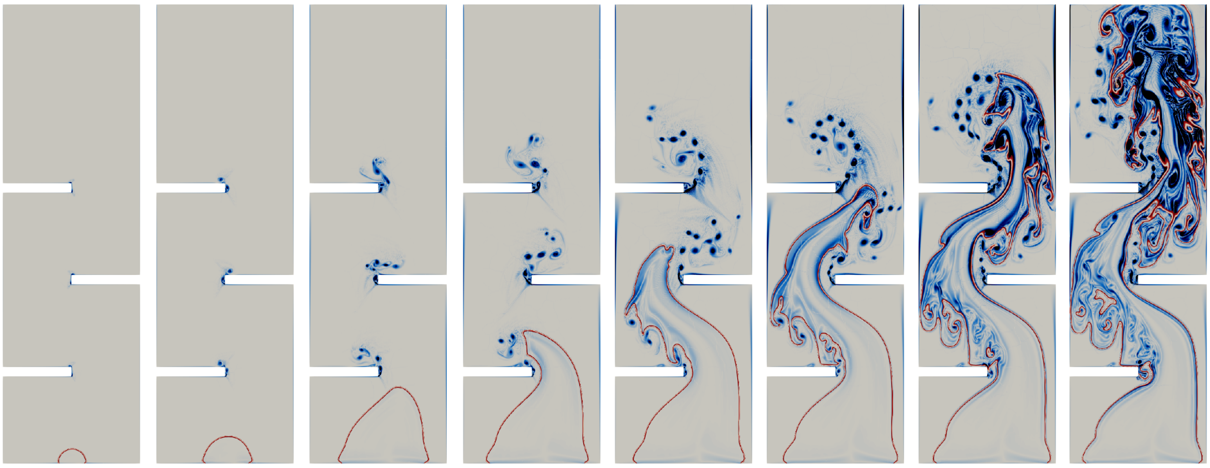

(b) Snapshots of the heat release and the flow vorticity of LES 3

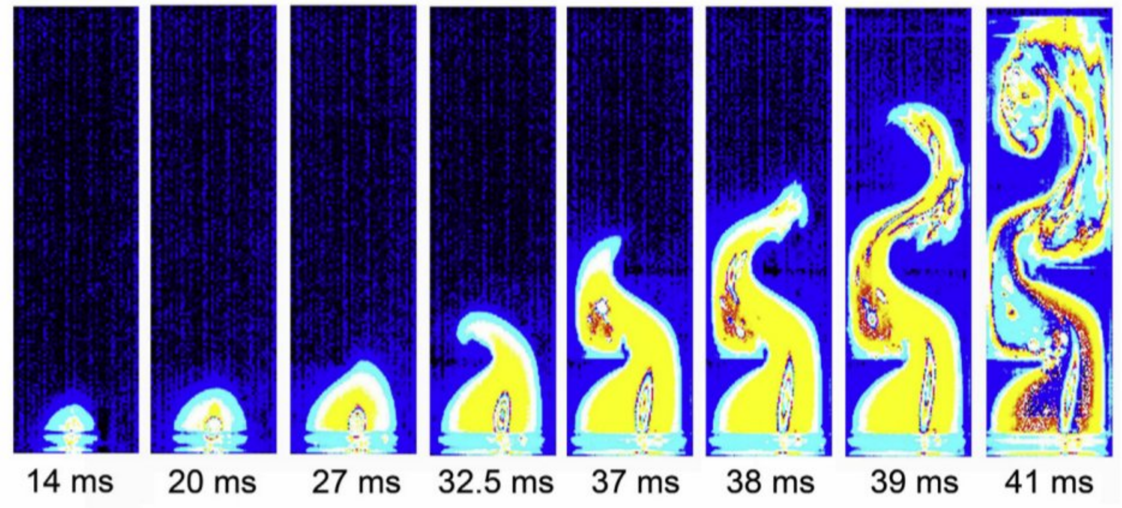

(c) Sequential images

Figure 6.44: (a) Snapshots of the RANS 1, (b) LES 3 and (c) experimental images showing a deflagration flame propagation in configuration 3 from Wen et al. (2013).

The flame fronts have the same global shapes. However, the flame is more wrinkled in the LES approach leading to small flame curls following the turbulent eddies. The flame front obtained with RANS simulation is globally smooth and is the convex envelop of the flame front obtained with the LES approach (as seen on the temperature fields in Fig. 6.43). This is expected from the averaged approach as the small fluctuations (small eddies) are not captured by the RANS approach leading to a less wrinkled flame front. This is highlighted by the vorticity fields. Indeed, only the large turbulent structures are observed in Fig. 6.44a while the small eddies are recovered with the LES approach as shown in Fig. 6.44b.

Flame front position and speed

The flame front positions obtained with RANS and LES approaches are compared in Fig. 6.45 to experimental data for configuration 3 (Wen et al., 2013). A derivative as a function of time of the numerical results has been performed in order to plot the flame front speed in Fig. 6.46.

RANS and LES computations are very similar in the early stage of the transient. RANS approach reaches the first obstacle at the same time as the LES approach (shown in Fig. 6.45 and on the third frame of Fig. 6.44).

Until the second obstacle, both simulations have relatively close flame front speed as seen in Fig. 6.46. However, after the first obstacle and until $y \approx 170\,\mathrm{mm}$ the flame front speed obtained with the LES approach is slightly superior. As a consequence, the LES flame front position slightly exceeds the RANS flame front position.

RANS models, mainly developed under homogeneous isotropic turbulence assumptions, generally are not able to reproduce laminar to turbulent transition. However, in our specific case, the turbulent flame speed correlation used seems to reproduce this situation. This could be due to the factor $(r/L_t)^{0.333}$ of Goulier (2015) turbulent flame speed correlation defined in equation (6.12) which according to Gostintsev et al. (1988) allows to describe this transition.

Between the second and the third obstacle, the slopes of both RANS and LES simulations are in agreement with the experimental one. Both approaches give a similar flame front speed (as shown in Fig. 6.46).

However, after the third obstacle, the flame front accelerates strongly. The RANS approach seems to have some difficulties with sudden raise or decrease of turbulent intensity. After the second obstacle and until the end, LES 3 flame position matches well the experimental data. However, RANS 1 overestimates the flame speed, and predicts a flame front speed higher than the LES one, as shown in Fig. 6.46. This may be due to the factor $(r/L_t)^{0.333}$, which is useful at the beginning of transient but can induce an overestimation of the flame speed as r increases throughout the simulation.

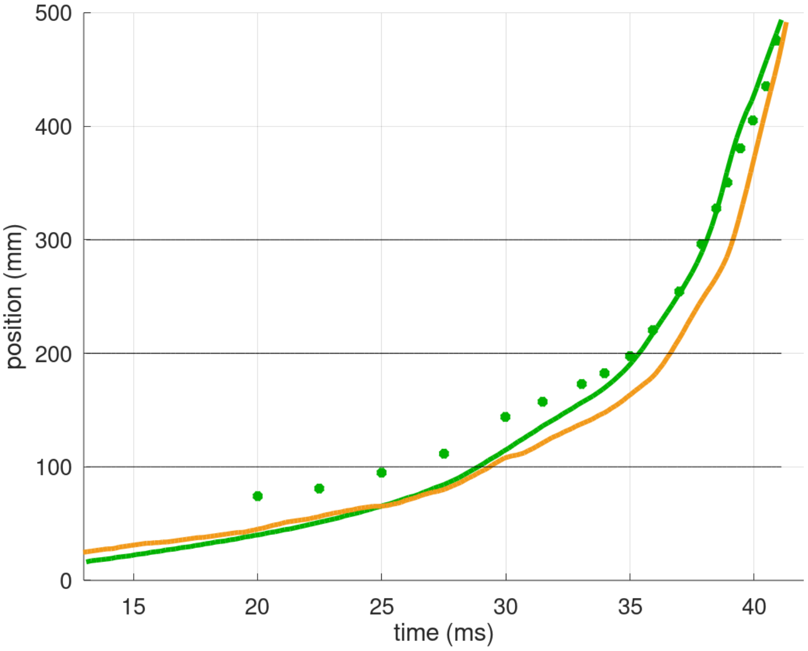

Figure 6.45: Flame front position for LES 3 and RANS 1. (—): LES 3; (●): experimental data of configuration 3; (—): RANS 1 and (—): obstacles locations.

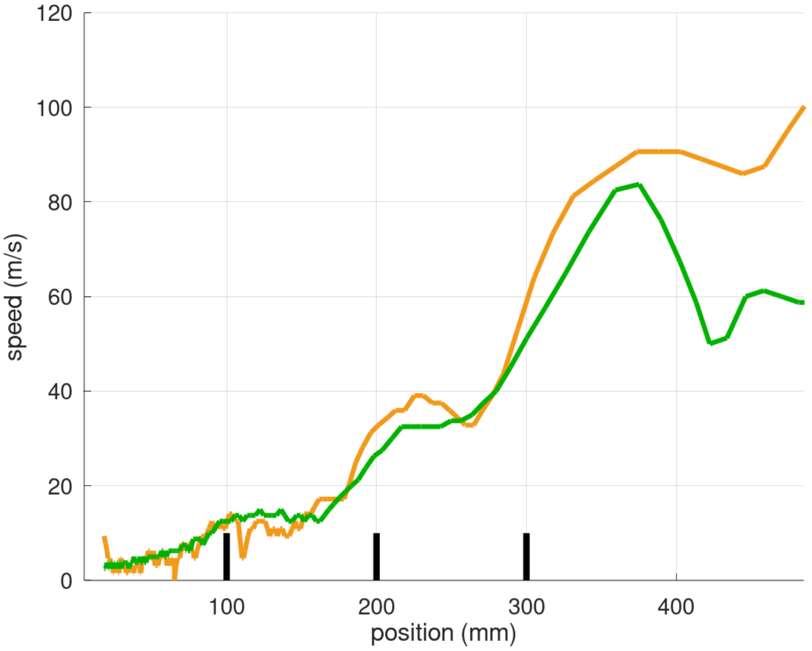

Figure 6.46: Flame front speed for RANS 1 and LES 3. (—): RANS 1; (—): LES 3 and (▬): obstacles locations.

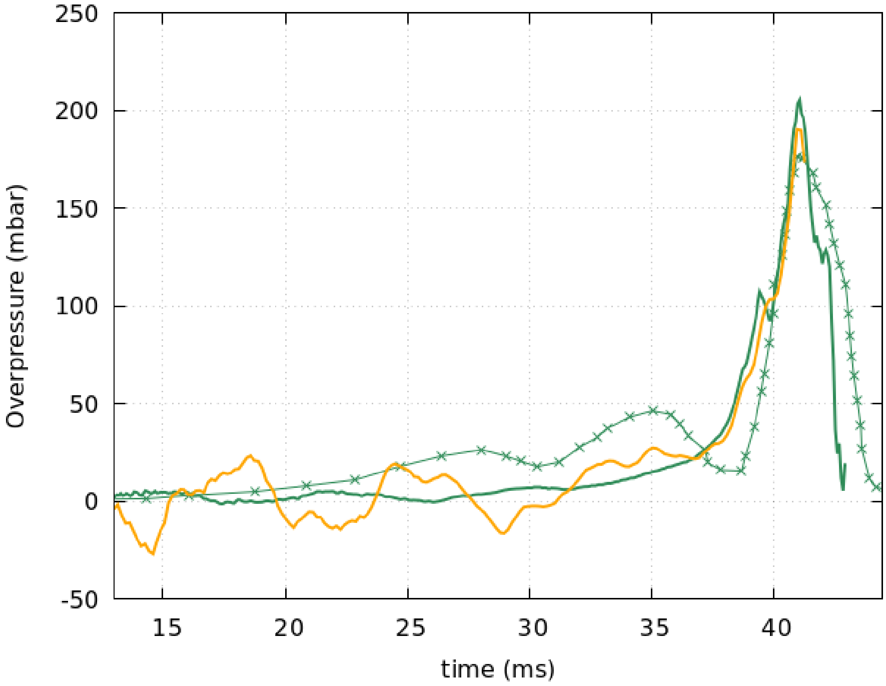

Figure 6.47: Overpressure evolution for RANS 1 and LES 3. (—): LES 3; (✳): Experimental data of configuration 3; (—): RANS 1.

Overpressure dynamics

In Fig. 6.47, the computed overpressure evolution with both RANS and LES approaches are compared to the experimental data (Wen et al., 2013).

Some fluctuations appear at the beginning of the simulation RANS 1 due to pressure waves reflections on the walls and on the obstacles. In LES, these fluctuations are almost not noticeable as their amplitude is approximately 3 mbar, yet the wave amplitude is more important with the RANS approach as its amplitude reaches almost 17 mbar. The peak obtained with the RANS approach appear at the same moment as in LES 3, after the flame exits. The same phenomenon in both cases seems to generate this pressure growth. As explained earlier, the flame seems to obstruct the way next the first obstacle leading to the overpressure peak. The RANS overpressure peak is relatively close to the LES overpressure peak.

Heat release

The heat release $\dot{\omega}_T$ (expression (4.13)) is integrated and compared to the heat release obtained with the large eddy simulation in Fig. 6.48.

The heat release profiles matches the flame speed behavior. Indeed, the flame front tip position represented in Fig. 6.45 shows that the flame front obtained with the RANS approach is slower than the LES flame front from the beginning to approximately the second obstacle. Then, both simulations have almost the same flame speed and then, at midway between the last obstacle and the chamber exit, the RANS flame speed exceeds the LES flame speed.

Fig. 6.48 shows the same behavior where the heat released by the RANS flame is inferior than the heat released by the LES flame and at midway between the third obstacle and the chamber exit, the heat released by the RANS approach is superior than the LES heat release.

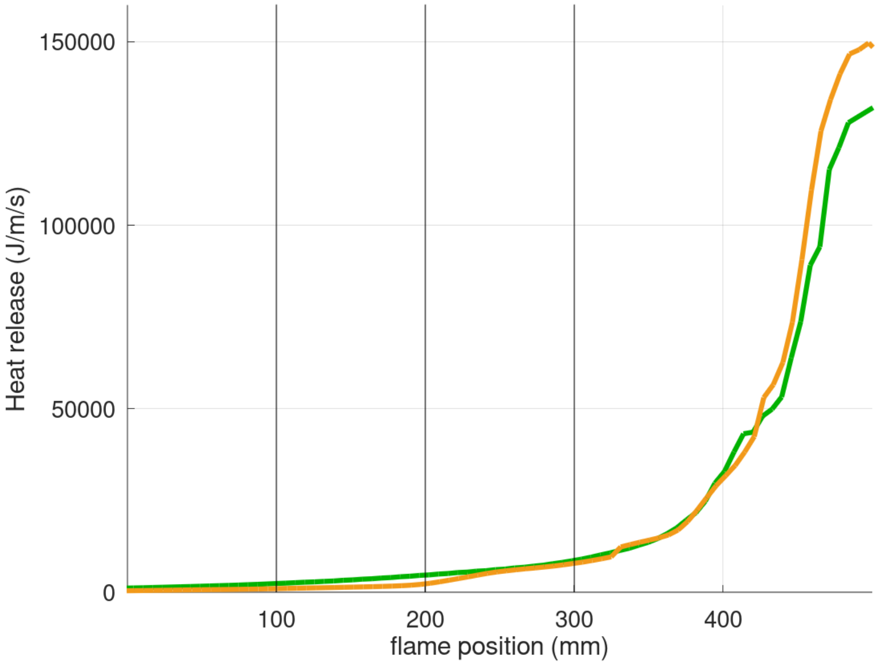

Figure 6.48: Heat release of LES 3 and RANS 1. (—): LES 3; (—): RANS 1 and (—): obstacles locations.

6.6.4 Comparison between RANS simulation and three-dimensional LES simulations

The two-dimensional RANS numerical results computed with the Goulier (2015) turbulent flame speed correlation and denoted by RANS 1 in Table 6.7 are compared to the three-dimensional ones obtained with the LES approach denoted by LES 3D.

Flame front structure

Fig. 6.49 aims to compare the flame front structure between the flames obtained with RANS 1 and LES 3D. In this figure, a time shift of 10 ms is applied to RANS 1 and of 11.4 ms to LES 3D. The snapshots have been taken at the same (shifted) moment as the experimental images.

The flame fronts have the same global shapes. However, the flame is more wrinkled in LES 3D leading to small flame curls following the turbulent eddies. The flame front obtained with RANS 1 is globally smooth and is the convex envelop of the flame front obtained with the LES approach. This is expected from the averaged approach as the small fluctuations (small eddies) are not captured by the RANS approach leading to a less wrinkled flame front.

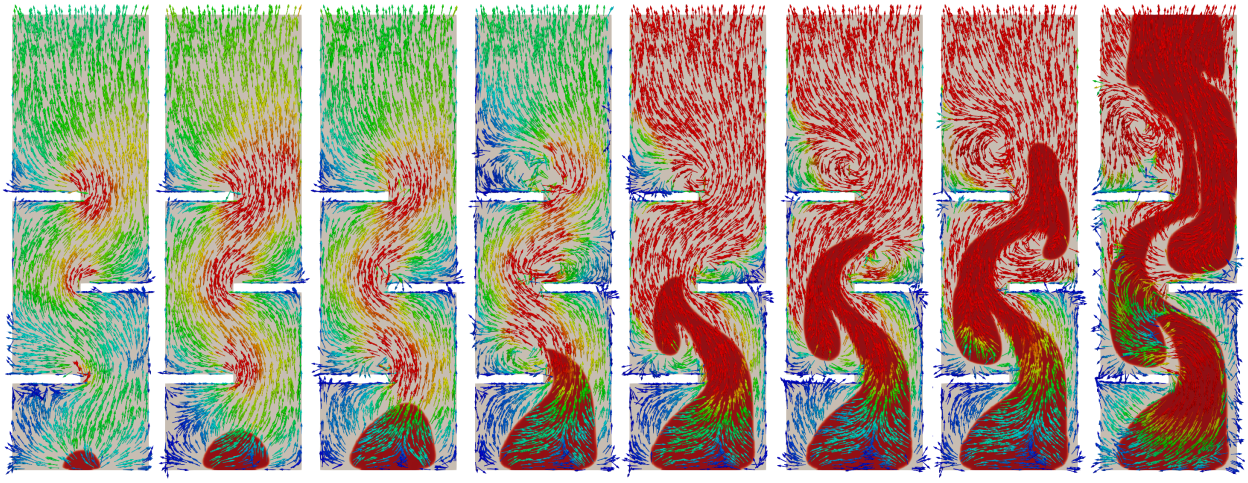

(a) Snapshots of the temperature field and velocity vectors of RANS 1

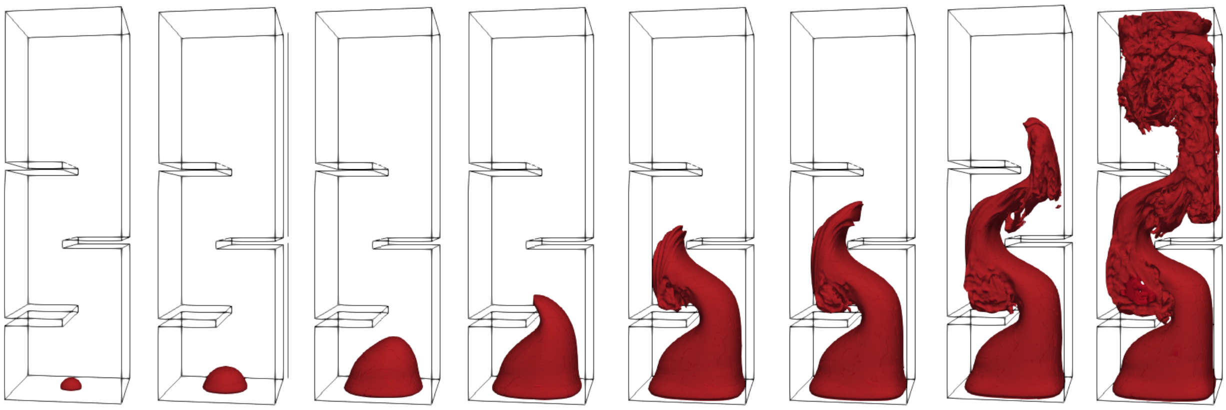

(b) Snapshots of the resolved progress variable contour ($\tilde{c} = 0.5$) of LES 3D

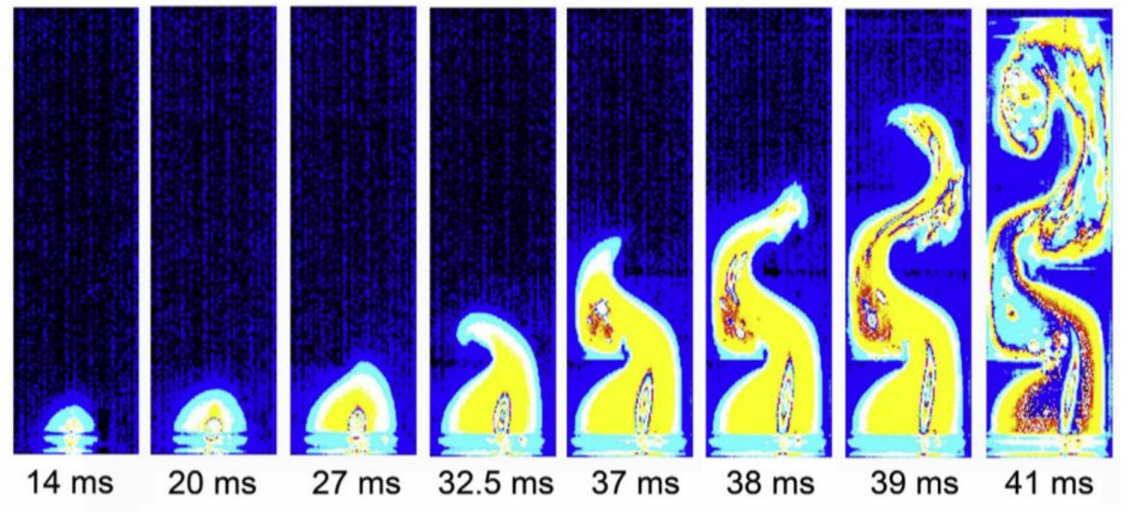

(c) Sequential images

Figure 6.49: (a) Snapshots of the RANS 1, (b) LES 3D and (c) experimental images showing a deflagration flame propagation in configuration 3 from Wen et al. (2013).

Globally, the flame fronts seem to reach the same position in RANS 1 and LES 3D in all frames of Fig. 6.49. However, both simulations seem to be late at first (from the beginning until seventh) compared to the experimental flame. Yet, at the end, in the last two snapshots the simulated flame fronts seem to catch up with the experimental flame.

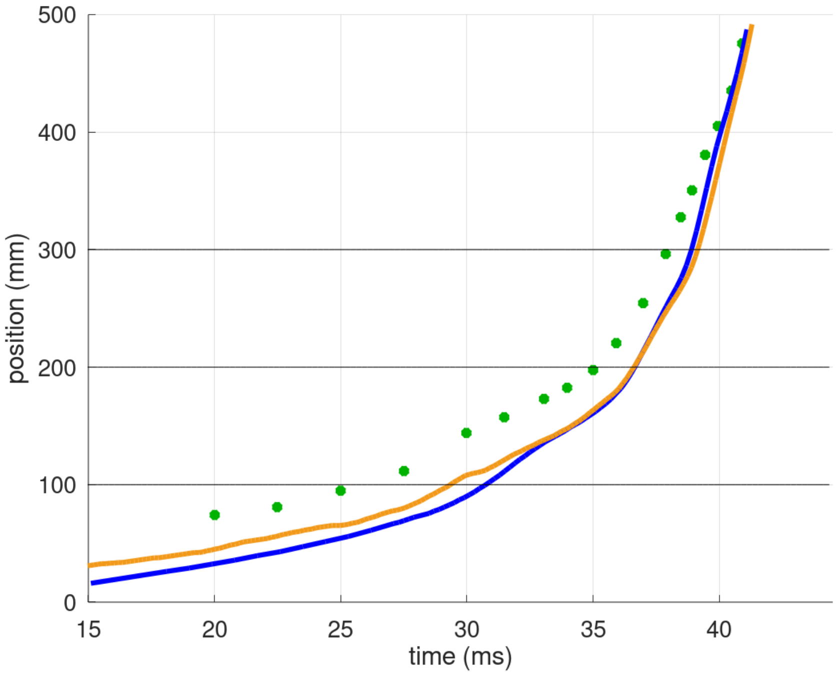

Figure 6.50: Flame front position for LES 3D and RANS 1. (—): LES 3D; (—): RANS 1 ; (●): experimental data of configuration 3; and (—): obstacles locations.

Flame front position and speed

Fig. 6.50 plots the time shifted flame front tip positions. The flame front speed, computed as the derivative over the time of the numerical flame front poition, is plotted in Fig. 6.51.

Fig. 6.50 and Fig. 6.51 show that both LES 3D and RANS 1 simulations predict similar flame front positions and speeds. As said earlier for the flame front structure, both simulations underestimates the flame front position with respect to experimental data. Yet, the accelerating numerical flames catch up with the experimental position at the end. After $y = 400\,\mathrm{mm}$, the flame front speed computed with RANS simulations keep increasing unlike the one computed by LES 3D.

Even if both simulations have globally the same flame front positions, RANS 1 is slightly ahead in the laminar phase. This may be explained by the ignition method. Indeed, for RANS 1, the surface covered by the initial flame kernel is slightly superior than the surface of LES 3D initial flame kernel leading to a higher reaction rate at the ignition.

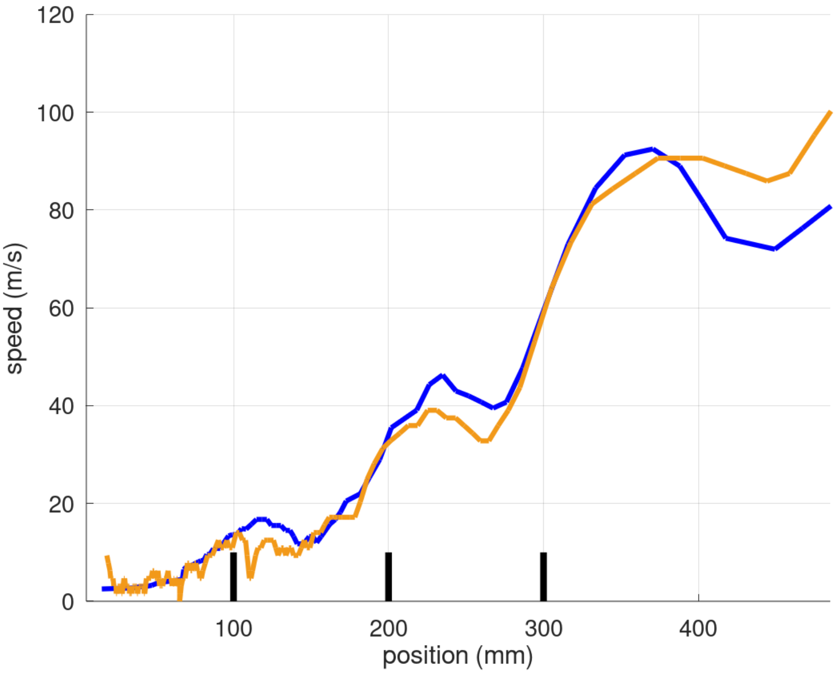

Figure 6.51: Flame front speed for RANS 1 and LES 3D. (—): RANS 1; (—): LES 3D and (▬): obstacles locations.

Overpressure

The time shifted overpressure evolutions obtained with RANS 1 and LES 3D simulations are represented in Fig. 6.52 and compared to experimental data.

Some fluctuations appear at the beginning of the RANS1 simulation due to pressure waves reflections on the walls and on the obstacles. The amplitude of these fluctuations amplitude reaches almost 17 mbar while no fluctuations are observed during LES 3D simulations.

RANS 1 overpressure peak matches almost the experimental peak while LES 3D overpressure peak is 23% below the experimental peak. The same phenomenon in both cases seems to generate this pressure growth. As explained earlier, the flame seems to obstruct the way next the first obstacle leading to the overpressure peak.

The difference between the overpressure peaks may be explained by the different ignition between the 2D and the 3D approaches. We have also keep in mind that RANS simulations have been performed on a 2D computational domain, thus avoiding the flame front propagation in the z-direction. Another computations with the RANS approach with a three dimensional computational domain will be mandatory.

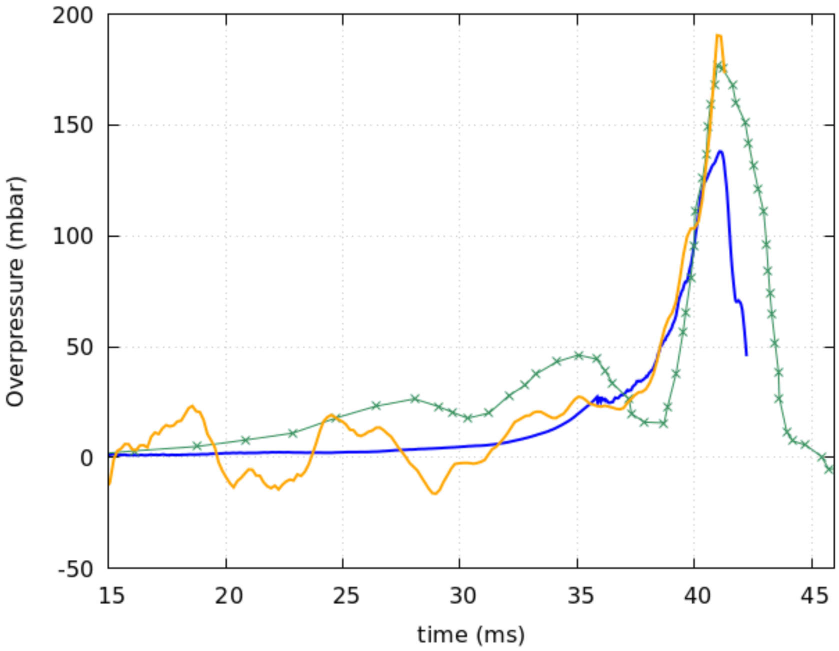

Figure 6.52: Overpressure evolution for RANS 1 and LES 3D. (—): LES 3D; (∗): Experimental data of configuration 3; (—): RANS 1.

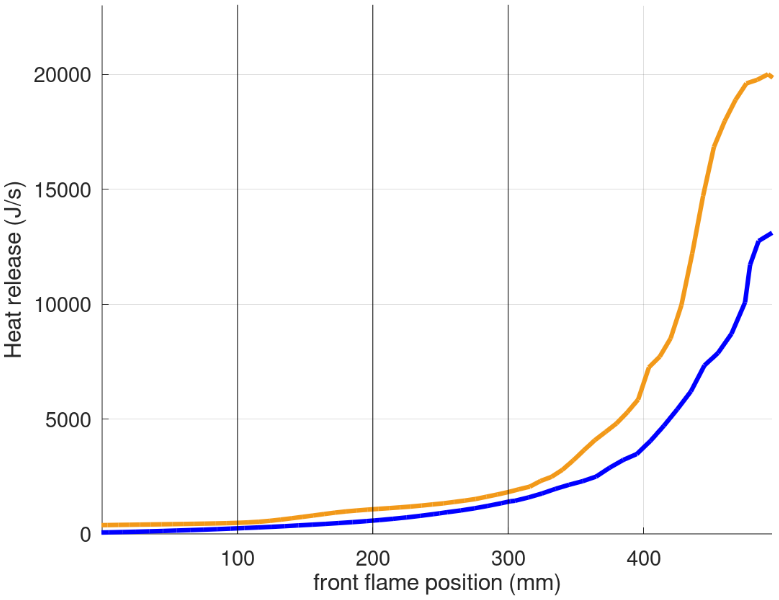

Figure 6.53: Heat release for RANS 1 and LES 3D. (—): RANS 1; (—): LES 3D and (—): obstacles locations.

Heat release

The integrated heat release over the chamber volume $\dot{\omega}_T$ (expression (4.13)) obtained with LES 3D is compared to the one computed with RANS 1 simulation (after multiplying the profile by the chamber depth) and plotted in Fig. 6.53.

Right after ignition, the flame kernel is cylindrical in RANS 1 (due to the two-dimensional surface conversion) and spherical in LES 3D. Thus, the flame surface is larger in the converted RANS 1 simulation than the LES 3D surface leading to a more important integrated reaction rate (*i.e.* integrated heat release) as shown in Fig. 6.42. Globally, the converted RANS 1 heat release is superior than the LES 3D heat release, especially after $y = 400\,\text{mm}$.

6.6.5 Turbulent flame speed correlation impact

Here, turbulent flame speed correlations introduced earlier are compared. Goulier (2015), Bray (1990) and Zimont (2000) are used to close the set of equations. The simulation parameters are reminded in Table 6.8. The overpressure, the flame front position and speed profiles are studied in the following.

Name	Configuration	$\mathcal{F}$	n	Δ_x in the chamber	Number of cells	δ_c	Unresolved flame speed
RANS 1	3	$\varnothing$	$\varnothing$	0.5 mm	409 066	G-equation	Goulier (2015)
RANS 2	3	$\varnothing$	$\varnothing$	0.5 mm	409 066	G-equation	Bray (1990)
RANS 3	3	$\varnothing$	$\varnothing$	0.5 mm	409 066	G-equation	Zimont (2000)

Table 6.8: Numerical parameters of RANS 1, 2 and 3.

Flame front position and speed

In Fig. 6.54, the flame front positions are plotted for the three RANS simulations. In this figure the RANS 1 time shift (10 ms) has been applied to the three simulations. In Fig. 6.55, a backward time shift for each simulation is applied to numerical results to match the experimental overpressure peak (10 ms for RANS 1, 6.1 ms for RANS 2 and 5 ms for RANS 3) and the flame front positions are plotted once again. Figure 6.56 represents the flame front velocity (derivation of the unshifted simulated flame front position). The experimental velocity is not represented along the simulation results as the experimental speed computation method has not been detailed by the authors Wen et al. (2013).

RANS 2 flame speed is more important than the two others during the laminar phase leading to an incorrect front position for this phase as seen in Fig. 6.54. This is probably due to the fact that this correlation is designed for situations where turbulence is fully developed. However, before the second obstacle, RANS 2 recovers approximately the same flame speed as RANS 1 (Fig. 6.56) leading to a similar flame front propagation and thus, to a similar position of the flame front after $y \approx 150\,\text{mm}$ (Fig. 6.55).

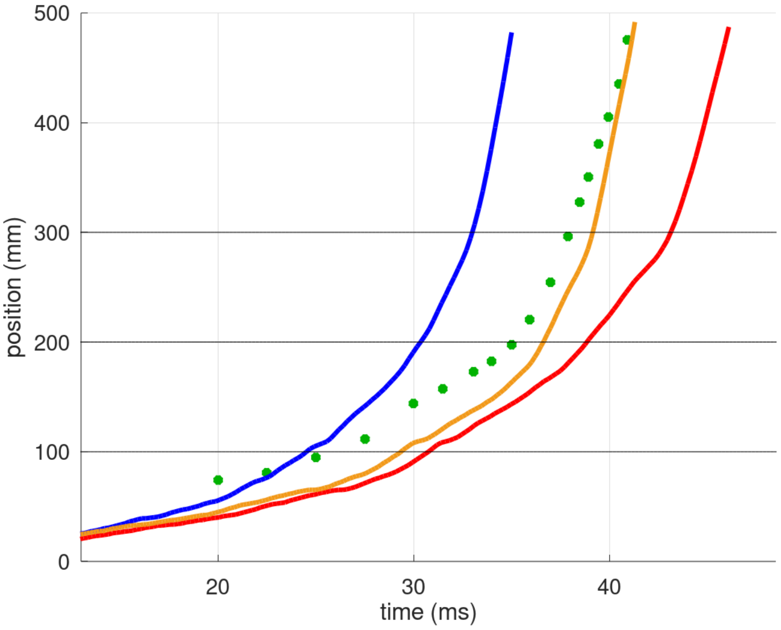

Figure 6.54: Flame front position obtained with the RANS approach and three different turbulent flame speed correlations with the same time shift. (🟧): RANS 1; (🟦): RANS 2; (🟥): RANS 3 and (●): experimental data.

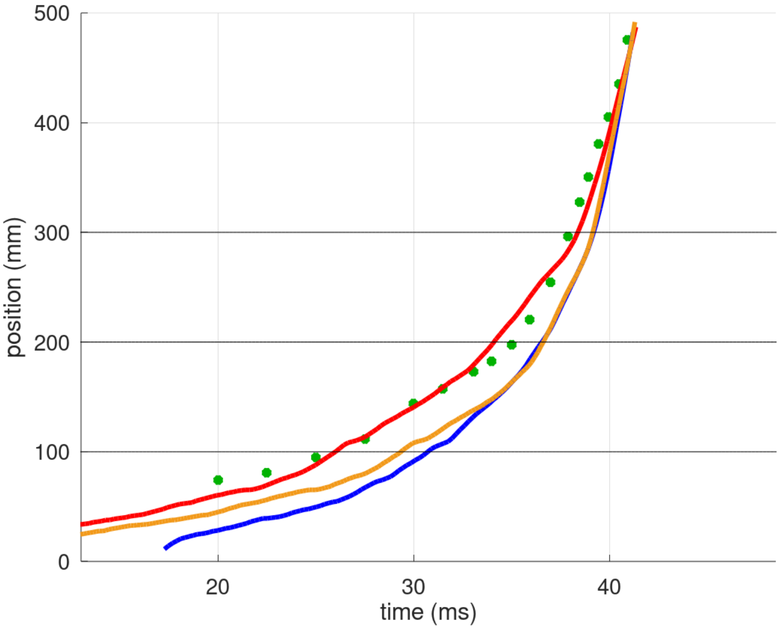

Figure 6.55: Flame front position obtained with the RANS approach and three different turbulent flame speed correlations with different time shifts. (🟧): RANS 1; (🟦): RANS 2; (🟥): RANS 3 and (●): experimental data.

RANS 1 and 3 seem to have approximately the same flame front speed before the first obstacle. Zimont (2000) correlation recovers the beginning of transient (*i.e.* the laminar to turbulent flame transition) and thus matches well the experimental position (Fig. 6.55).

After the first obstacle, RANS 1 is faster than RANS 3 as shown in Fig. 6.56. However, the flame front position predicted by RANS 3 seems to be closer to the experimental one than RANS 1, as reported in Fig. 6.55.

Goulier (2015) and Zimont (2000) correlations predict the closest flame front position to the experimental data compared to Bray (1990) correlation. A further investigation is needed, by comparing the turbulent characteristics of the flow obtained with the three RANS simulations as well as with LES simulations in order to understand this dispersion of numerical results.

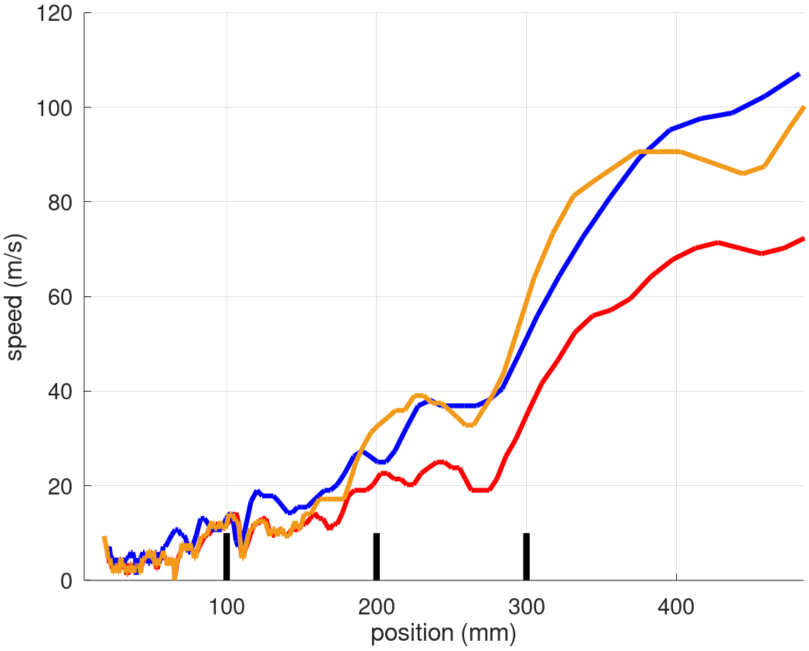

Figure 6.56: Flame front spreed for RANS 1, 2 and 3. (—): RANS 1; (—): RANS 2; (—): RANS 3 and (▬): obstacles locations.

Overpressure dynamics

In Fig. 6.57 are plotted the overpressure evolutions for the simulations performed with the RANS approach. Likewise the flame front position figure (Fig. 6.54), RANS 1 time shift has been applied for all simulations.

The same overpressure behavior is observed in Fig. 6.57 from the start to approximately 25 ms for the three simulations. The pressure waves bouncing back on the walls and on the obstacles lead to pressure fluctuations of the same amplitude and frequency for the three simulations.

The major overpressure peak is observed for the three RANS simulations when the flame front is outside the chamber. The reason of this peak are the same than for LES simulations:

the flame seems to obstruct the way next to the first obstacle leading to this overpressure peak. The peak is reached by RANS 3 simulation at 46.2 ms and has an amplitude of 118 mbar. RANS 3 predicts a lower flame speed (as shown in Fig. 6.56), thus the predicted overpressure peak is lower than the experimental one and occurs later than RANS1 and RANS 2. RANS 2 slightly overestimates the overpressure peak which occurs at 35.3 ms (that is before RANS 1 and RANS 3) and reaches an amplitude of 204 mbar. RANS 1 simulation obtained with the Goulier (2015) correlation matches best the experimental overpressure with an amplitude of 195 mbar.

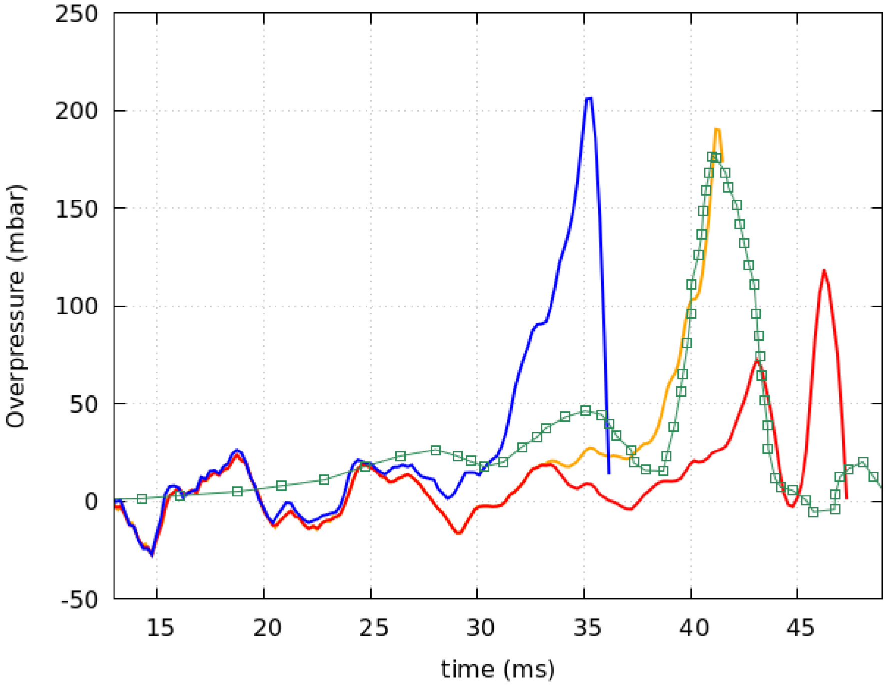

Figure 6.57: Overpressure evolution obtained with the RANS approach and three different turbulent flame speed correlations. (—): RANS 1; (—): RANS 2; (—): RANS 3 and (✳): experimental data.

6.7 Conclusion

Accelerated deflagration by obstructions in the experimental open chamber of Wen et al. (2013) has been simulated with two different approaches for the turbulent deflagration modelling with the in-house software CALIF^{3}S - P^{2}REMICS. In the first one, a large eddy simulation (LES) approach is used for turbulence. The combustion is modelled using a virtually thickened flame formalism (TFLES) combined with a dynamical determination of the subgrid scale flame wrinkling factors to handle unresolved contributions. In the second one, the turbulence is modelled by a Reynolds-averaged Navier-Stokes (RANS) approach and the combustion model relies on a *turbulent flame-speed closure.*

First, LES simulations have been performed on a two-dimensional domain to validate, investigate and calibrate the combustion model.

The dynamic fractal-like model has been validated on a range of test-filter sizes in order to check the good model behavior. The minimum number of grid points in the thickened front has been investigated and set to $n = 5$. The impact of the thickening factor value with a fixed number of points in the front has been discussed. Deflagration features are still well recovered even with a high thickening flame factor ($\mathcal{F} = 12$). The dynamic fractal-like model capacity of capturing the laminar and the turbulent regimes, as well as their transition is highlighted by comparing the dynamical approach to the constant value approach for the wrinkling factor exponent. The results show that the dynamical model is essential to capture transient phenomena such as deflagrations. Flame front interactions are then discussed by comparing the results with and without a correction for the nonphysical values induced by flame front interactions (Mouriaux et al., 2016). Without the wrinkling factor exponent correction for front interactions, the overpressure was overestimated and numerical instabilities could be generated by nonphysical high β values. Finally, the influence of the obstacle locations on the flame propagation has been studied by simulating the three different configurations of the Wen et al. (2013) experimental set-up.

The analysis made on the virtually thickened flame formalism parameters on a two-dimensional domain allowed to simulate the configuration with the more important overpressure peak of Wen et al. (2013) in a three-dimensional domain with the TFLES approach. Three-dimensional results have been confronted to the experimental data and the model behavior has been discussed. Comparison with the two-dimensional results have also been performed. In order to limit the CPU time while avoiding too thick flame fronts, the thickening flame factor has been set to $\mathcal{F} = 6$ and the number points for the flame front description has been set to $n = 5$. The numerical results are in good agreement with experimental data, but the overpressure peak is underestimated. Probably, better results will be obtained with a finer description of the flame front.

Finally, the last step was to compare the LES approach with the RANS one on the most turbulent obstacle configuration. The combustion model used in this latest approach is closed by a turbulent flame speed correlation. Simulations with several turbulent flame speed correlations have been made in order to check the reliability of this method. The numerical results have been compared with experimental data and with the numerical results obtained with the LES approach on two and three-dimensional computational domain. Goulier (2015) and Zimont (2000) turbulent flame speed correlations have shown the most accurate flame front position and overpressure profiles. However, the results are highly dependent on the correlation used. In addition, the RANS approach is less accurate in sudden acceleration of the flame front. We have also keep in mind that RANS simulations have been performed on a 2D computational domain, thus avoiding the flame front propagation in the z-direction. Another computations with the RANS approach with a three dimensional computational domain will be useful.

Appendix

6.A Validation of the wrinkling factor behavior

The wrinkling factor model main assumption is the fractal assumption based on the fractal theory (Mandelbrot, 1975, 1977, 1983; Sreenivasan and Meneveau, 1986). This theory has been then applied to premixed flames which have reacted with a fractal behavior in numerical and experimental analyses (Peters, 1986; Gouldin, 1987; Gouldin et al., 1989; Gülder, 1991; Gülder and Smallwood, 1995; Smallwood et al., 1995).

Resolved flame surfaces at filter S_r and test-filter $(\widehat{S_r})$ scales are related through the conservation of the total flame surface:

$$\Xi_\Delta S_r = \Xi_{\gamma\Delta}\,\widehat{S_r}, \tag{6.17}$$

where S_r and $\widehat{S_r}$ are given by:

$$S_r(t) = \int_{\mathcal{V}} |\nabla\tilde{c}| d\mathcal{V}, \quad \widehat{S_r}(t) = \int_{\mathcal{V}} |\nabla\,\widehat{\tilde{c}}\,| d\mathcal{V}, \tag{6.18}$$

with $\mathcal{V}$ a volume set by the user (this volume is discussed later in this section). By using the definition of Ξ_Δ and $\Xi_{\gamma\Delta}$ (relation (6.3)) in Equation (6.17), yields:

$$\frac{\widehat{S_r}}{S_r} = \frac{\Xi_\Delta}{\Xi_{\gamma\Delta}} = \left(\frac{\gamma\Delta}{\Delta}\right)^{-\beta} = \gamma^{-\beta}. \tag{6.19}$$

The ratio $\widehat{S_r}/S_r$ is thus supposed to follow a line of slope $-\beta$ when displayed as a function of γ in a log-scale. Here, the aim is to validate the linear behavior in a log scale of expression (6.19).

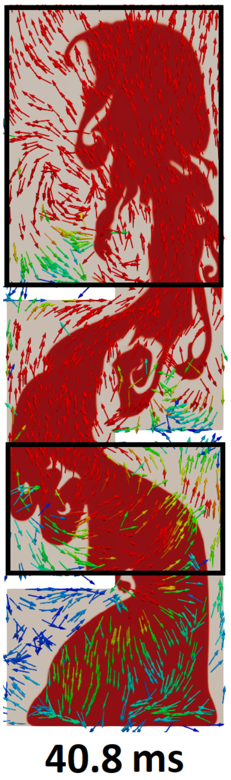

Figure 6.A.1: Last snapshot of LES 3.

The LES 3 simulation has been used for the validation test (see Table 6.1 for more details). The simulation has been run until 40.8 ms leading to a flame front tip located right before the chamber exit (shown in Fig 6.A.1). The test-filter size was varied on a range of 1.5 Δ to 8.5 Δ, with Δ the combustion filter width. The purpose is to compute the value of $S_r(t)$ and $\widehat{S_r}(t)$ for each test-filter size at a given time. To do so, two control volumes are selected for the integration in Equations (6.18). These volumes are represented by the two rectangles plotted in Fig. 6.A.1. The first one corresponds to the area between the first and second obstacle ($105\,\text{mm} < y < 195\,\text{mm}$) . The second one corresponds to the area between the third obstacle and the exit ($305\,\text{mm} < y < 500\,\text{mm}$). Afterwards, the ratio in Equation (6.19) is computed and plotted with respect to γ. Also plotted in Fig. 6.A.2, the line of slope $-\beta$ being the tangent of the orange curve. The results generated using the first rectangle are plotted on the left side of Fig. 6.A.2 and the results from the second rectangle are plotted on the right side of the same figure.

In the area between the first and second obstacle, the flame front is partially turbulent with weak values of β. The left plot in Fig. 6.A.2 shows that the curve has a linear behavior until a maximum value of γ which is $\gamma^{max} = 6$ corresponding to approximately $\widehat{\Delta}^{max} = 5.9\Delta$ (according to the definition of γ). The slope of the curve in this zone corresponds to $\beta = 0.14$.

After the third obstacle, the flame front is fully turbulent with relatively high values of β. The right plot in Fig. 6.A.2 shows that the curve has a linear behavior until a maximum value of γ which is $\gamma^{max} = 4$ corresponding to approximately $\widehat{\Delta}^{max} = 3.9\Delta$. The slope of the curve in this area corresponds to $\beta = 0.51$. $\widehat{\Delta}^{max}$ is a threshold value for the test-filter size, above this one, the test-filter captures adjacent flame fronts, thus, equation (6.19) does not hold anymore. The threshold value is lower for higher turbulent intensity (as shown in the right hand side of Fig. 6.A.2). Considering that the most turbulent region (between the third obstacle and the exit) in the most turbulent configuration (configuration 3) have a maximum value for the test-filter size of 3.9Δ, and that all simulations have been run with a test-filter size equal to $\widehat{\Delta} = 1.5\Delta$, the fractal assumption holds for all simulations presented in this manuscript.

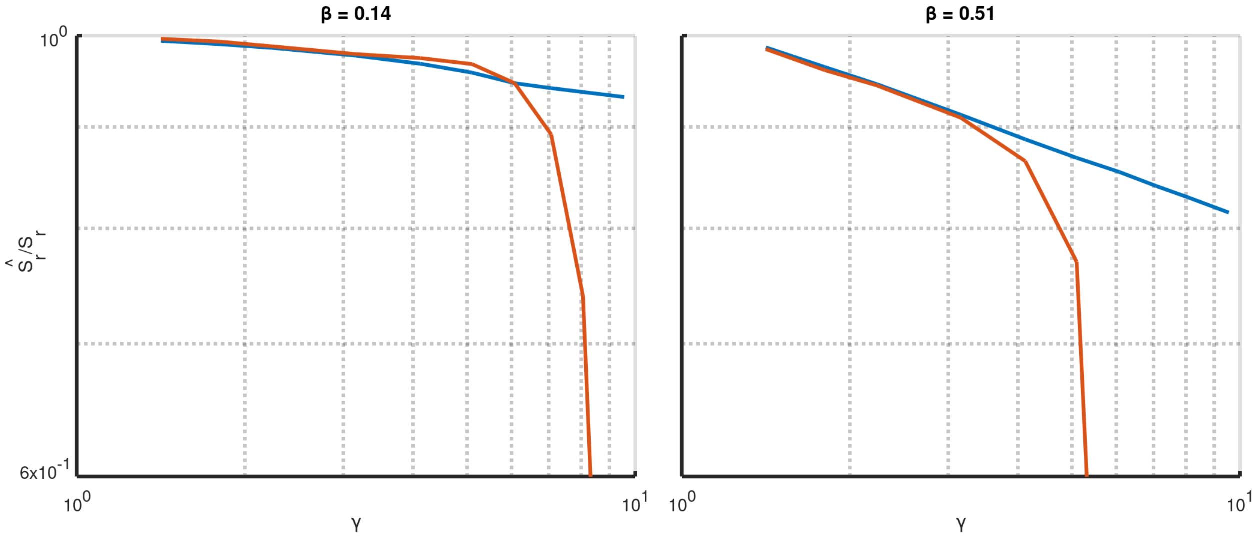

Figure 6.A.2: Normalized filtered surface flame as a function of the ratio of test and combustion filter sizes in log-scale. (▬): normalized filtered surface flame and (▬): linear slope $-\beta$.

Conclusion and perspectives

Conclusion

This work is part of the simulation of turbulent deflagrations encountered in safety studies for nuclear power plants or industrial plants. The aim of this thesis is to develop Large Eddy Simulation approach for deflagration and a numerical scheme as non-dissipative as possible for the resolution of the filtered equations in stake.

First, a formally second order scheme dedicated to the numerical simulation of the filtered Navier-Stokes equations for compressible non-reactive flow is proposed. The space discretization is staggered, using the Marker-And-Cell (MAC) scheme for structured grids (Harlow and Amsden, 1971; Harlow and Welch, 1965): the scalar variables are approximated at the cell centers and the velocity components at the face centers. Time-stepping is performed with a second order Runge-Kutta scheme, called the Heun scheme. Balance equations are solved successively, and each step is explicit, in the sense that, apart from the time-derivative, all terms involve only known quantities at this stage and thus do not require any linear system solver. The equation solved is the so-called sensible energy balance instead of the total energy conservation equation. This choice avoids building an approximation of the total energy which, for staggered discretizations, is a “composite” variable combining quantities discretized on the cells and at the faces. This difficulty may be overstepped by adding, as in Herbin et al. (2014), a corrective term in the discrete sensible energy balance equation. A high-order (MUSCL-type) positivity-preserving convection operator is used for the mass balance equation and for the sensible energy balance equation.

The scheme enjoys some stability properties: the density is shown to be non-negative at the discrete level under a CFL condition by an easy adaptation of the technique developed in Gastaldo et al. (2018). To obtain the positivity of the internal energy, the following two arguments are combined:

- first, to extend the proof of Gastaldo et al. (2018) to cope with a heat diffusion term (with an adaptation of the CFL condition),
- second, to implement a discretization of the momentum diffusion which yields a positive dissipation term. To this purpose, we use an idea proposed in Grapsas et al. (2016), which consists in recasting the MAC scheme under a weak form, so that we may closely mimick the continuous expression of the dissipation: *in fine*, the cell dissipation is computed as the integral over the considered cell of the inner product of the stress and strain tensors, linked *a.e.* by the usual (continuous) relation (hence the non-negativity).

Then we turn to the kinetic energy preservation property. Considering the Heun scheme as a three-steps scheme, with two prediction steps and a final average, we show that the solution of the first two steps obeys a kinetic energy balance with numerical production terms (*i.e.* non-negative residual terms when put at the right-hand side), while the last step is dissipative; finally, we are able to derive a local kinetic energy balance for the algorithm with remainder terms, which we show to be of second order in time. Numerical experiments show that these remainder terms take in fact very low values: the compensation operated by the final averaging is almost exact, in the sense that the final residual is more than one thousand times smaller than the residuals associated to the first two steps of the algorithm (which are nothing more than the first-order Euler forward scheme). Finally, we establish a total energy balance for the scheme, which may be made conservative by adding corrective terms to the sensible energy balance, for instance if one wants to compute shock solutions. Since we address here essentially viscous flows, we do not follow this line; however, we numerically check that the scheme correctly captures the viscous perturbation of mild shocks (similar for instance to the strongest ones which may be generated by deflagrations) even with coarse meshes. On the opposite, for strong shocks (typical of detonations), correcting the discrete sensible energy balance seems to be preferable.

In order to deal with reactive compressible flows such those encountered during an explosion, the filtered Navier-Stokes equations are complemented with chemical species balance equations and the reactive terms needed are added in the sensible energy balance. The virtually thickened flame model has been chosen for combustion modelling. The wrinkling model of Veynante and Moureau (2015) is used for the subgrid model incorporating the Mouriaux et al. (2016) correction for front/front interactions and front/wall interactions.

The numerical scheme developed in the first part of this work in the non-reactive case is then extended to the reactive case. A Strang splitting method is used for the resolution of the chemical species. One explicit half-step of homogeneous transport for the chemical species is first performed, then an implicit step deals with the reaction terms. Finally, a second explicit half-step of transport for the chemical species is performed. The associated reaction energy is introduced into the energy balance of Navier-Stokes equations, solved in a second time.

The positivity of the density is ensured by construction of the discrete mass balance equation, *i.e.* by the use of a second order MUSCL scheme. In addition, the positivity of the mass fractions are preserved thanks to the following (rather standard) argument: first, building a discrete convection operator which vanishes when the convected unknown is constant thanks to the discrete mass balance equation ensures a positivity-preservation property (Larrouturou, 1991), under a CFL condition; second, the discretization of the chemical reaction rate ensures either that it vanishes when the unknown of the equation vanishes (for fuel and oxidizer mass fractions), or that it is non-negative (for product mass fractions). Consequently, mass fractions are non-negative. Moreover, with a suitable choice of the coefficients involved in the MUSCL discretization of the chemical species convection terms, the sum of the chemical species is equal to 1. Thus, they are also bounded by 1.

The positivity of the sensible energy stems from the same essential arguments used in the non-reactive case: the consistency of the discrete convection operator and the mass balance and the positivity of the dissipation term in the momentum balance. This holds provided that the equation is exothermic. Moreover, as in the non-reactive case, the solutions of the scheme satisfy a discrete total energy balance up to reminder terms. This balance may be made conservative by adding corrective terms to the sensible energy balance, for instance if one wants to compute shock solutions.

The numerical schemes and the models developed have been implemented in the in-house CFD software CALIF^{3}S - P^{2}REMICS. The LES approach for deflagration has been first validated on a laminar one-dimensional flame. The numerical simulation recovered well the methane/air laminar flame features. The one-dimensional flame has been artificially thickened and a minimum number of points in the front for the well behavior of the simulation of $n = 5$ is found out. This test case may be considered as a prerequisite before applications to more realistic turbulent reactive problems.

Afterwards, a case of interest for IRSN has been simulated. The accelerated deflagration in an obstructed semi-confined chamber with different configurations for the obstacle locations has been investigated (Wen et al., 2013). Two-dimensional simulations have been first run in order to realise a parametric study of the TFLES parameters and validate the fractal assumption on a range of test-filter sizes in order to check the model good behavior (validity of the flame surface expression in our range of use). The minimum mesh grid number in the thickened front has been studied and found to be the same as the one-dimensional case with $n = 5$. The dynamical formalism is confronted to the constant exponent formalism in order to highlight the importance of a dynamic expression to capture the transition from laminar to fully turbulent regimes. The numerical results show that the dynamical formalism is unavoidable in order to have a good description of the flame front propagation. The influence of the location of obstacles on the flame propagation is well captured by LES approach.

The analysis made on the virtually thickened flame formalism parameters on a two-dimensional domain allowed to simulate the obstacle configuration of Wen et al. (2013) leading to the highest overpressure peak in a three-dimensional domain. The simulation has been performed on the supercomputer Topaze at the Research and Technology Computing Center (CCRT) showing the efficiency of the CALIF^{3}S - P^{2}REMICS software. The numerical results are in good agreement with experimental data, but the overpressure peak is underestimated. The mesh grid size has been limited by the available computation capacity. For further investigations, a finer three-dimensional simulation should be run. A comparison of the three-dimensional results with the converted two-dimensional data has shown that the two-dimensional simulations were relatively accurate and recovers results of the same order of magnitude.

An approach based on a RANS description of turbulence and a *turbulent flame-speed closure* combustion model (Lipatnikov and Chomiak, 2002; Peters, 2000) is also available for the turbulent deflagration modelling in the CALIF^{3}S -P^{2}REMICS software. The flame brush location is determined, solving the so-called level set G-equation. To handle partially premixed situations, the species mass balances are solved, but reaction rates are expressed from the level-set function. The model is closed by a turbulent flame speed correlation (Peters, 2000; Bradley et al., 1992b; Bray, 1990; Zimont, 2000; Goulier, 2015). The obstacle configuration with the highest overpressure peak of Wen et al. (2013) has been simulated with this approach. The results computed with different turbulent flame speed closure are compared. Zimont (2000) and Goulier (2015) turbulent flame speed correlation has shown the most accurate flame front position and overpressure profiles respectively. However, these results are highly dependent on the correlation used. In addition, the RANS approach is less accurate in sudden acceleration of the flame front simulation.

To conclude on the comparison between LES and RANS, a three-dimensional simulation with the RANS approach should be run. However, one should keep in mind the drawbacks of the RANS approach (*i.e.* high dependence on the turbulent flame speed correlation used and lack of predictability). In the other hand, the LES approach combined with the virtually thickened flame and dynamic subgrid scale model formalism developed during this thesis in CALIF^{3}S - P^{2}REMICS is an accurate and reliable approach capable of reproducing transiting phenomena such as deflagrations.

Perspectives

The investigations made during this thesis unlock many possibilities for future studies:

- Additional validation of the approach developed in this thesis is needed. Indeed, in this work, feasibility of LES 3D simulations has been carried out on only one case. An indepth parametric study should be carried out: number of grid points in the flame front, wall boundary conditions (adiabatic or not, no slip or wall law), etc... Moreover, the numerical results obtained have shown a lack of description of the beginning of the transient. In order to improve initial moments description and correct the delay between simulation and experiment, two techniques could be studied:
  - use of an ignition zone sufficiently refined in order to afford a low thickening factor, and thus, a smaller flame kernel. However, such solution may be costly CPU wise and would generate the need of a change of mesh grid after ignition;
  - instead of initialising with a burnt gases volume, igniting the mixture with a local energy source (additional source term in the sensible energy balance equation) to mimic the spark effect.

  Finally, the validation of the LES approach must be complemented with other test cases: accelerated deflagrations on large-scale combustion chambers (Kent et al., 2005b) or on confined chamber (Johansen and Ciccarelli, 2013), self-accelerated flames (Kanzleiter and Langer, 2010), etc..

- The aim of this work was to use the developed LES approach in order to better understand the physical phenomena involved during a deflagration and improve the RANS model more adapted to industrial purpose. Here, only a brief comparison between the two approaches has been made, showing the unreliability of the RANS approach. An indepth investigation of the turbulent characteristics of the flow computed during LES simulations must be made (root mean square velocity, turbulent viscosity) and compared to the results obtained with the RANS approach. A more reliable turbulent flame speed correlation for the RANS approach might be developed using the LES results.

- A global single-step reaction is chosen in this work to model chemistry but a more complex method (two or three-steps reactions, or simplified schemes or even the recently developed analytical mechanisms) could also be retained. This may allow a more accurate description of the flame front propagation. Another improvement in order to take into account non unitary Lewis numbers and different values of the diffusion coefficients could also be helpful (Volpiani, 2017). The numerical scheme developed in this work should thus be extended in order to be able to keep the chemical species in their physical bounds at the discrete level, even with a non constant diffusion coefficient. These improvements may be useful for the simulation of premixed flames of hydrogen/carbon monoxide/air as encountered during a severe accident in a nuclear power plant in case of failure of in-vessel corium retention (Nicolàs-Pérez et al., 2020).

- Given the constraints (in scale and Reynolds number) of industrial applications, turbulence modeling is most often done by one-point statistical models (RANS). Large eddy simulation, which is more predictive but more costly in computing time, most often comes in support, for purposes of understanding physical phenomena and interpreting state of experiences. A third category of so-called "hybrid" models, integrating in the same system of balance equations RANS and LES approaches, emerged for non-reactive flows (Spalart and Allmaras, 1992, 1994; Sagaut et al., 2006; Chaouat, 2017). However, few works of this type exist in the literature for premixed combustion (Hasse et al., 2009; Sainte-Rose et al., 2009; Hasse et al., 2010; Mansouri et al., 2016). The work done during this thesis could serve as starting point for the development of an hybrid approach for deflagration. The semi-implicit variants of the numerical scheme presented here, already available in CALIF^{3}S -P^{2}REMICS, may be useful to implement a solver buiding a bridge from Large Eddy Simulation models to statistical models, by hybrid approaches. However, an extension of the semi-implicit scheme to higher orders in space by a MUSCL-like technique is needed.

Appendix

Synthèse du manuscrit

Ce travail s'inscrit dans le cadre de la simulation des déflagrations turbulentes telles que celles rencontrées dans les études de sûreté pour les installations nucléaires ou civiles. Nous y développons une approche par simulation des grandes échelles permettant une description fine de l'écoulement. L'outil de simulation ainsi construit est utilisé dans l'étude de transitoires expérimentaux à petite et moyenne échelle. La première étape de la thèse a porté sur le développement et l'analyse d'un schéma numérique pour les équations de Navier-Stokes pour les écoulements compressibles non réactifs. Le schéma est explicite et basé sur une discrétisation en temps du second ordre (schéma d'Heun). La discrétisation enespace est de type mailles décalées. Elle se base sur une formulation en énergie interne. Une discrétisation des opérateurs de convection via une technique de montée en ordre de type MUSCL permet alors de garantir la positivité des variables scalaires (densité, énergie interne et pression) sous condition de CFL. De plus, le schéma est peu dissipatif numériquement, ce qui est primordial dans le contexte de la simulation des grandes échelles.

Ce schéma est étendu au cas réactif par une technique de pas fractionnaires. L'équation de conservation des espèces chimiques est résolue dans un premier temps par un algorithme de Strang découplant convection et réaction. L'énergie de réaction associée est introduite dans le bilan d'énergie des équations de Navier Stokes, traitées dans un second temps.

Nous développons ensuite un modèle de combustion et l'appliquons à l'étude d'écoulements d'intérêt. La combustion est traitée par un modèle de flamme artificiellement épaissie. Un modèle de sous-maille permet d'ajuster de façon dynamique le plissement de sous-maille, qui disparaît dans l'opération d'épaississement, à partir de la connaissance des champs résolus. Trois configurations expérimentales de déflagrations accélérées par des obstacles en chambre semi-confinée ont été étudiées. Ces configurations diffèrent par la disposition des obstacles qui génèrent la turbulence au passage de l'écoulement induit par l'expansion thermique et promeuvent l'accélération de la flamme. Ces cas ont permis d'analyser le comportement du modèle de combustion et valider ses résultats à partir des données expérimentales. L'étude a également mis en évidence la supériorité de la formulation dynamique du modèle par rapport à l'utilisation d'un paramètre de plissement constant. Des simulations de type RANS (résolution des équations de Navier-Stokes moyennées) où la combustion est décrite par une formulation de type « G-equation » ont également été réalisées et confortent l'utilisation de la simulation aux grandes échelles.

Les études réalisées lors de cette thèse ont ouvert plusieurs axes de recherche pour l'avenir :

- L'approche développé a besoin d'avantage de simulation afin de la valider. En effet, là LES 3D a été réalisé uniquement sur un cas. Une étude paramétrique devrait être mené sur : le nombre de maille dans le front, les conditions aux limites... De plus, les simulations ont montré un manque de précision au début de la transition de laminaire à turbulent. Afin d'améliorer les résultats, deux technique peuvent être explorées :

  - Raffiner la zone initiale d'allumage afin d'avoir un coefficient d'épaississement plus faible.
  - Utiliser un terme source dans l'équation de l'énergie afin d'initialisé la combustion.

  Enfin, d'autres cas expérimentaux doivent être simulé avec des volumes plus importants

- Faire un calcul 3D avec l'approche RANS.
- Réaliser une étude approfondie sur la turbulence afin de mieux comprendre le phénomène et observer les caractéristiques de l'écoulement turbulent (vitesse RMS, viscosité turbulente...) dans l'objectif de développer une corrélation de vitesse de flamme turbulente pour l'approche RANS.
- Utiliser un modèle plus détaillé pour la chimie afin de mieux décrire la propagation du front de flamme.
- Une approche hybride RANS - LES est aussi un axe de recherche intéressant au vu des contrainte industriel (temps de calcul et nombre de Reynolds élevé) permettant d'allier les points forts des deux approches.

Bibliography

R. Abdel-Gayed, D. Bradley, and M. Lawes. Turbulent burning velocities : a general correlation in terms of straining rates. *Proceedings of the Royal Society of London A*, 414: 389–413, 1987. 202

C. Angelberger, D. Veynante, F. Egolfopoulos, and T. Poinsot. Large eddy simulations of combustion instabilities in premixed flames. In *Proceedings of the summer program*, volume 159, pages 61–82, 1998. 54

A. Avdić, G. Kuenne, F. di Mare, and J. Janicka. LES combustion modeling using the Eulerian stochastic field method coupled with tabulated chemistry. *Combustion and Flame*, 175:201–219, 2017. doi: https://doi.org/10.1016/j.combustflame.2016.06.015. 54

M. Bauerheim, T. Jaravel, L. Esclapez, E. Riber, L. Gicquel, B. Cuenot, M. Cazalens, S. Bourgois, and M. Rullaud. Multiphase flow les study of the fuel split effects on combustion instabilities in an ultra low-nox annular combustor. *American Society of Mechanical Engineers*, 1:67–81, 2015. 49

C. Bauwens, J. Chaffee, and S. Dorofeev. Effect of ignition location, vent size, and obstacles on vented explosion overpressures in propane-air mixtures. *Combustion Science and Technology*, 182(11-12):1915–1932, 2010. 157

A. Bentaib, N. Meynet, and A. Bleyer. ISP-49 on Hydrogen Combustion. *NEA/CSNI/R(2011)*, 9, 2011. 17

A. Bentaib, N. Meynet, and A. Bleyer. Overview on hydrogen risk research and development activities: Methodology and open issues. *Nuclear Engineering and Technology*, 47:26–32, 2015. 17

A. Bentaib, N. Meynet, and A. Bleyer. Research and development with regard to severe accidents in pressurised water reactors: Summary and outlook, 2017. 15, 17

R. Bird, W. Stewart, and E. Lightfoot. Transport phenomena. *John Wiley and Sons*, page 15, 1960. 24

D. J. Bodony and S. K. Lele. On using large-eddy simulation for the prediction of noise from cold and heated turbulent jets. *Physics of Fluids*, 17(085103), 2005. 34

M. Boger and D. Veynante. Large eddy simulation of a turbulent premixed v-shaped flame. *Advanced in Turbulence*, VIII:449–452, 2000. 52

M. Boger, D. Veynante, H. Boughanem, and A. Trouvé. Direct Numerical Simulation analysis of flame surface density concept for Large Eddy Simulation of turbulent premixed combustion. *27th International Symposiom on Combustion*, pages 917–927, 1998. 52

P. Boivin, A. Jiménez, A. Sànchez, and F. Williams. An explicit reduced mechanism for H2–air combustion. *Proceedings of the Combustion Institute*, 33:517–523, 2011. 49

R. Borghi. On the structure and morphology of turbulent premixed flames. *Recent advances in the Aerospace Sciences*, pages 117–138, 1985. 46

R. Borghi and M. Destriau. Chemical and physical principles. *Combustion and flame*, pages 23–24, 1998. 46, 51

S. Bougrine, S. Richard, O. Colin, and D. Veynante. Fuel Composition Effects on Flame Stretch in Turbulent Premixed Combustion: Numerical Analysis of Flame-Vortex Interaction and Formulation of a New Efficiency Function. *Flow Turbulence Combustion*, 93: 259–281, 2014. doi: https://doi.org/10.1007/s10494-014-9546-4. 56

J. Boussinesq. *Essai sur la théorie des eaux courantes*, volume 23. Mémoires présentés par différents savants à l'Académie Royale des Sciences de l'Institut de France, Académie Royale des Sciences, 1877. 35, 114

F. Boyer, F. Dardalhon, C. Lapuerta, and J.-C. Latché. A Low Degree Non-Conforming Approximation of the Steady Stokes Problem with an Eddy Viscosity. In *Finite Volumes for Complex Applications VI*, 2011. 75

A. Bradley, C. Lau, and M. Lawes. Flame stretch rate as a determinant of turbulent burning velocity. *Philosophical Transactions of the Royal Society of London. Series A: Physical and Engineering Sciences*, 338(1650):359–387, 1992a. 48, 52

D. Bradley and A. Mitcheson. The venting of gaseous explosions in spherical vessels. i–theory. *Combustion and Flame*, 32:221–236, 1978. 157

D. Bradley, A. K. C. Lau, and M. Lawes. Flame stretch rate as a determinant of turbulent burning velocity. *Philosophical Transactions of the Royal Society of London A: Mathematical, Physical and Engineering Sciences*, 338(1650):359–387, 1992b. URL `http://rsta.royalsocietypublishing.org/content/338/1650/359.abstract`. 158, 202, 224

M. Braun. The fukushima daiichi incident. *Areva*, 2017. 15

K. Bray, M. Champion, and P. Libby. The interaction between turbulence and chemistry in premixed turbulent flames. *Turbulent Reactive Flows*, 40:541–563, 1989. 51

K. N. C. Bray. Studies of the Turbulent Burning Velocity. *Proceedings of the Royal Society of London A: Mathematical, Physical and Engineering Sciences*, 431(1882):315–335, 1990. URL `http://rspa.royalsocietypublishing.org/content/431/1882/315.abstract`. 52, 158, 202, 204, 215, 217, 224

T. Butler and P. O'Rourke. A numerical method for two dimensional unsteady reacting flows. *Symp. (Int.) Combustion.*, 16:1503–1515, 1977. 19, 53, 62, 112, 114, 143, 146, 157

V. Bykov and U. Maas. The extension of the ILDM concept to reaction-diffusion manifolds. *Combustion Theory and Modelling*, 11:839–862, 2007. 50

CALIF^{3}S. A software components library for the computation of fluid flows, 2021. URL `https://gforge.irsn.fr/gf/project/calif3s`. 65, 85

E. D. D. CALIF^{3}S-P^{2}REMICS. CALIF3S-P2REMICS V2 : Physical modelling. Rapport Technique N Pléiade : Rapport IRSN / 2020 000676, SA2I/LIE, sep 2020. 143, 157, 201

S. M. Candel and T. Poinsot. Flame stretch and the balance equation for the flame surface area. *Combustion Science and Technology*, 70:1–15, 1990. 44

CCRT. Atos livre le supercalculateur topaze au cea et ses partenaires de recherche. *L'Usine nouvelle*, 2021. 187

X. Chai and K. Mahesh. Dynamic k-equation model for large-eddy simulation of compressible flows. *Journal of Fluid Mechanics*, 699:385–413, 2012. 94, 99, 100

J. Chao, C. Bauwens, and S. Dorofeev. An analysis of peak overpressures in vented gaseous explosions. *Proceedings of the Combustion Institute*, 2010. 157

B. Chaouat. The State of the Art of Hybrid RANS/LES Modeling for the Simulation of Turbulent Flows. *Flow Turbulence Combust*, 99:279–327, 2017. 226

F. Charlette, C. Meneveau, and D. Veynante. A power-law flame wrinkling model for LES of premixed turbulent combustion part I: non-dynamic formulation and initial tests. *Combustion and Flame*, 131:159–180, 2002a. 55, 56, 57, 58, 59, 114

F. Charlette, C. Meneveau, and D. Veynante. A power-law flame wrinkling model for LES of premixed turbulent combustion Part II: dynamic formulation. *Combustion and Flame*, 131(1):181–197, 2002b. ISSN 0010-2180. doi: https://doi.org/10.1016/S0010-2180(02)00401-7. URL `https://www.sciencedirect.com/science/article/pii/S0010218002004017`. 57, 62, 114

Y. C. Chen, N. Peters, G. A. Schneemann, N. Wruck, U. Renz, and M. S. Mansour. The detailed flame structure of highly stretched turbulent premixed methane-air flames. *Combustion and Flame*, 107:223–244, 1996. 49

H. Choi and P. Moin. Grid-point requirements for large eddy simulation: Chapman's estimates revisited. *Physics of Fluids*, 24(011702):1–5, 2012. 18

S. Chung and C. Law. An invariant derivation of flame stretch. *Combustion and flame*, 55: 123–125, 1984. 44

P. Clavin and G. Joulin. Premixed flames in large scale and high intensity flow. *Journal de Physique et Lettres*, 44(1):1–12, 1983. 44

O. Colin, F. Ducros, D. Veynante, and T. Poinsot. A thickened flame model for large eddy simulation of turbulent premixed combustion. *Physics of Fluids*, 12:1843–1863, 2000. 53, 54, 55, 56, 114, 143, 146, 157

A. Cook and J. Riley. A subgrid model for equilibrium chemistry in turbulent flows. *Physics of Fluids*, 6(8):2868–2870, 1994. 51

M. Crouzeix and P.-A. Raviart. Conforming and Nonconforming Finite Element Methods for Solving the Stationary Stokes Equations i. *R.A.I.R.O. Analyse Numérique*, R-3(7):33–76, dec 1973. 109

P. Dagaut, M. Reuillon, J.-C. Boettner, and M. Cathonnet. Kerosene combustion at pressures up to 40 atm: Experimental study and detailed chemical kinetic modeling. *In Symposium (International) on Combustion*, 25:919–926, 1994. 48

G. Damköhler. Effects of Reynolds number on the flame speed. *Elektrochem*, 1940. 48

J. Daubech, J. Hébrard, S. Jallais, E. Vyazmina, D. Jamois, and F. Verbecke. Un-ignited and ignited high pressure hydrogen releases : concentration - turbulence mapping and overpressure effects. *Journal of Prevention in the Process Industries*, 36:439–446, 2015. 15

V. Di Sarli, A. Di Benedetto, and G. Russo. Using large eddy simulation for understanding vented gas explosions in the presence of obstacles. *Journal of hazardous materials*, 169(1): 435–442, 2009a. 157

V. Di Sarli, A. Di Benedetto, G. Russo, S. Jarvis, E. Long, and G. Hargrave. Large eddy simulation and piv measurements of unsteady premixed flames accelerated by obstacles. *Flow, turbulence and combustion*, 83(2):227–250, 2009b. 157

V. Di Sarli, A. Di Benedetto, and G. Russo. Sub-grid scale combustion models for large eddy simulation of unsteady premixed flame propagation around obstacles. *Journal of hazardous materials*, 180(1):71–78, 2010. 157

S. Dorofeev. Flame acceleration and explosion safety applications. *Proceedings of the Combustion Institute*, 33(2):2161–2175, 2011. 157

J. Driscoll. Turbulent premixed combustion: Flamelet structure and its effect on turbulent burning velocities. *Progress in Energy and Combustion Science*, 34(1):91–134, 2008. 9, 48

M. Düsing, A. Sadiki, and J. Janicka. Towards a classification of models for the numerical simulation of premixed combustion based on a generalized regime diagram. *Combustion Theory and Modelling*, 10(1):105–132, 2006. doi: 10.1080/13647830500293768. URL `https://doi.org/10.1080/13647830500293768`. 50

M. Elshimy, S. Ibrahim, and W. Malalasekera. LES – DFSD modelling of vented hydrogen explosions in a small-scale combustion chamber. *Journal of Loss Prevention in the Process Industries*, 72:104580, 2021. 157

A. Ern and V. Giovangigli. Multicomponent Transport Algorithms. *Springer Verlag, Heidelberg*, 1994. 24

R. Eymard, T. Gallouet, and R. Herbin. The finite volume method. In *Handbook for Numerical Analysis*. Ciarlet, P. and Lions, J.L., 2000. 73, 123

M. Fairweather, G. Hargrave, S. Ibrahim, and D. Walker. Studies of premixed flame propagation in explosion tubes. *Progress in Energy and Combustion Science*, 116(4):504–518, 1999. 157

F. L. S. Filho, N. Speelman, J. A. van Oijen, L. P. H. de Goey, A. Sadiki, and J. Janicka. Numerical analyses of laminar flames propagating in droplet mists using detailed and tabulated chemistry. *Combustion Theory and Modelling*, 22(5):998–1032, 2018. doi: 10.1080/13647830.2018.1470332. URL `https://doi.org/10.1080/13647830.2018.1470332`. 54

B. Fiorina, O. Gicquel, L. Verveish, S. Carpentier, and N. Darabiha. Premixed turbulent combustion modeling using tabulated detailed chemistry and PDF. *Proceedings of the Combustion Institute*, 30(1):867–874, 2005. 50

B. Fiorina, R. Vicquelin, P. Auzillon, N. Darabiha, O. Gicquel, and D. Veynante. A filtered tabulated chemistry model for LES of premixed combustion. *Combustion and Flame*, 157(3):465–475, 2010. 51

P. Flohr and H. Pitsch. A turbulent flame speed closure model for LES of industrial burner flows. In *Proceedings of the summer program 2000 - center of turbulence research*, pages 169–179, 2000. 52

B. Franzelli, E. Riber, S. M., and T. Poinsot. A two-step chemical scheme for kerosene–air premixed flames. *Combustion and Flame*, 157(7):1364–1373, 2010. 49

B. Franzelli, E. Riber, and B. Cuenot. Impact of the chemical description on a large eddy simulation of a lean partially premixed swirled flame. *Comptes Rendus Mécanique*, 341(1): 247–256, 2013. 49

J. C. H. Fung, J. C. R. Hunt, N. A. Malik, and R. J. Perkins. Kinematic simulation of homogeneous turbulence by unsteady random Fourier modes. *Journal of Fluid Mechanics*, 236:281–318, 1992. doi: 10.1017/S0022112092001423. 93

C. Fureby. *A Comparison of Flamelet LES Models for Premixed Turbulent Combustion*, chapter 44th, page 1. AIAA Aerospace Sciences Meeting and Exhibit, 2006. doi: 10.2514/6.2006-155. URL `https://arc.aiaa.org/doi/abs/10.2514/6.2006-155`. 50

J. Galpin, O. Angelberger, A. Naudin, and L. Verveish. Large-eddy simulation of H2–air auto-ignition using tabulated detailed chemistry. *Journal of Turbulence*, 9(13):1–21, 2008. 50

E. Garnier, N. Adams, and P. Sagaut. *Large Eddy Simulation for Compressible Flows*. Scientific Computation. Springer-Verlag Berlin Heidelberg, 2009. 22, 32, 34, 36, 39, 54

L. Gastaldo, F. Babik, F. Duval, C. Lapuerta, and J.-C. Latché. Simulation of Accelerated Deflagration Using the P^{2}REMICS Software. In N. Organization, editor, *International Topical Meeting on Nuclear Reactor Thermal Hydraulics*, volume 17, 2017. 18, 202

L. Gastaldo, R. Herbin, J.-C. Latché, and N. Therme. A MUSCL-type segregated-explicit staggered scheme for the Euler equations. *Computers & Fluids*, 175:91–110, 2018. 65, 66, 73, 74, 76, 77, 108, 222

M. Germano, U. Piomelli, P. Moin, and W. Cabot. A dynamic subgrid-scale eddy viscosity model. *Physics of Fluids*, A 3:1760–1765, 1991. 38, 39, 57, 118

S. Ghosal. Analysis and control of errors in the numerical simulation of turbulence. *Fluid Mechanics and its Application*, 66:101–110, 2004. 33

S. Ghosal and P. Moin. The Basic Equations for the Large Eddy Simulation of Turbulent Flows in Complex Geometry. *Journal of Computational Physics*, 118:24–37, 1995. 33

L. Y. Gicquel, G. Staffelbach, and T. Poinsot. Large eddy simulations of gaseous flames in gas turbine combustion chambers. *Progress in Energy and Combustion Science*, 38(6): 782–817, 2012. 157

O. Gicquel, N. Darabiha, and D. Thévenin. Laminar premixed hydrogen/air counterflow flame simulations using flame prolongation of ILDM with differential diffusion. *Proceedings of the Combustion Institute*, 28 (2):1901–1908, 2000. 50

V. Giovangigli. Multicomponent Flow Modeling. *Modeling and simulation in science, engineering and technology*, 1999. 24, 26

Y. A. Gostintsev, A. G. Istratov, and Y. V. Shulenin. Self-similar propagation of a free turbulent flame in mixed gas mixtures. *Combustion, Explosion and Shock Waves*, 24: 563–569, 1988. 201, 207

F. Gouldin. An application of fractals to modeling premixed turbulent flames. *Combustion and Flame*, 68(3):249–266, 1987. 220

F. Gouldin, K. Bray, and J.-Y. Chen. Chemical closure model for fractal flamelets. *Combustion and Flame*, 77(3):241–259, 1989. 220

J. Goulier. *Comportements aux limites de flammes de prémélange hydrogène/air. Etude de la transition flamme laminaire-flamme turbulente*. Energétique, Université d'Orléans, 2015. 47, 158, 201, 202, 204, 207, 210, 215, 217, 218, 219, 224

V. Granet, O. Vermorel, C. Lacour, B. Enaux, V. Dugue, and T. Poinsot. Large eddy simulation and experimental study of cycle-to-cycle variations of stable and unstable operating points in a spark ignition engine. *Combustion and Flame*, 159(4):1562–1575, 2012. 49

D. Grapsas. *Staggered fractional step numerical schemes for models for reactive flows*. Theses, Aix Marseille Université, Dec. 2017. URL `https://hal.archives-ouvertes.fr/tel-02091559`. 73, 103, 109, 110, 111

D. Grapsas, R. Herbin, W. Kheriji, and J.-C. Latché. An unconditionally stable staggered pressure correction scheme for the compressible Navier-Stokes equations. *SMAI Journal of Computational Mathematics, Société de Mathématiques Appliquées et Industrielles*, 2: 51–97, 2016. 65, 66, 90, 92, 102, 104, 109, 111, 125, 222

D. Grapsas, R. Herbin, J.-C. Latché, and Y. Nasseri. A staggered pressure correction numerical scheme to compute a travelling reactive interface in a partially premixed mixture. In *Recent Advances in Numerical Methods for Hyperbolic PDE Systems - SEMA SIMAI Springer series*, volume 28, pages 97–129, 2021. 85, 92, 202, 203

S. Gubba, S. Ibrahim, and W. Malalasekera. LES study of influence of obstacles on turbulent premixed flames in a small scale vented chamber. *6th Mediterranean Combustion Symposium*, 2009. 157

O. Gülder. Turbulent premixed combustion modelling using fractal geometry. *In Symposium (International) on Combustion*, 23:835–842, 1991. 220

O. Gülder and G. Smallwood. Inner cutoff scale of flame surface wrinkling in turbulent premixed flame. *Combustion and Flame*, 103:107–114, 1995. 62, 220

R. Hall, A. Masri, P. Yaroshchyk, and S. Ibrahim. Effects of position and frequency of obstacles on turbulent premixed propagating flames. *Combustion and Flame*, 156(2):439–446, 2009. 157

F. Harlow and A. Amsden. A numerical fluid dynamics calculation method for all flow speeds. *Journal of Computational Physics*, 8:197–213, 1971. 19, 64, 69, 101, 109, 113, 119, 222

F. Harlow and J. Welch. Numerical Calculations of Time-Dependent Viscous Incompressible Flow of Fluid with a Free Surface. *Physics of Fluids*, 8, 1965. 19, 64, 69, 101, 109, 113, 119, 222

C. Hasse, V. Sohm, and B. Durst. Detached eddy simulation of cyclic large scale fluctuations in a simplified engine setup. *International Journal of Heat and Fluid Flow*, 30:32–43, 2009. 226

C. Hasse, V. Sohm, and B. Durst. Numerical investigation of cyclic variations in gasoline engines using a hybrid URANS/LES modeling approach. *Computers & Fluids*, 39:25–48, 2010. 226

E. Hawkes and R. Cant. A flame surface density approach to large eddy simulation of premixed turbulent combustion. *Proceedings of the Combustion Institute*, 28 (1):51–58, 2000. 53

D. Haworth. Progress in probability density function methods for turbulent reacting flows. *Progress in Energy and Combustion Science*, 36(2):168–259, 2010. ISSN 0360-1285. doi: https://doi.org/10.1016/j.pecs.2009.09.003. 51

R. Herbin, W. Kheriji, and J.-C. Latché. On some implicit and semi-implicit staggered schemes for the shallow water and euler equations. *Mathematical Modelling and Numerical Analysis*, 48:1807–1857, 2014. 65, 90, 102, 109, 111, 222

R. Herbin, J.-C. Latché, and K. Saleh. Low mach number limit of some staggered schemes for compressible barotropic flows. *In preparation*, 2017. 65, 111

R. Herbin, J.-C. Latché, and T. Nguyen. Consistent segregated staggered schemes with explicit steps for the isentropic and full Euler equations. *Mathematical Modelling and Numerical Analysis*, 52:893–944, 2018. 65, 74, 91, 111

R. Herbin, J.-C. Latché, S. Minjeaud, and N. Therme. Conservativity and weak consistency of a class of staggered finite volume methods for the Euler equations. *Mathematics of Computation*, 90:1155–1177, 2021. 65, 85

R. Hilbert, F. Tap, H. El-Rabii, and D. Thévenin. Impact of detailed chemistry and transport models on turbulent combustion simulations. *Progress in Energy and Combustion Science*, 30:61–117, 2004. 25, 28

J. O. Hinze. *Turbulence.* McGraw-Hill, New-York, 1975. 45

J. Hirschfelder and C. Curtiss. Molecular theory of gases and liquids. *Wiley New York*, 26: 13, 15, 86, 118, 1954. 24

S. Ibrahim and A. Masri. The effects of obstructions on overpressure resulting from premixed flame deflagration. *Journal of Loss Prevention in the Process Industries*, 14(3):213–221, 2001. 157

S. Ibrahim, S. Gubba, A. Masri, and W. Malalasekera. Calculations of explosion deflagrating flames using a dynamic flame surface density model. *Journal of Loss Prevention in the Process Industries*, 22(3):258–264, 2009. 157

J. Janicka and A. Sadiki. Large eddy simulation for turbulent combustion systems. *Proceedings of the Combustion Institute*, 30(1):537–547, 2004. 51, 157

C. Johansen and G. Ciccarelli. Modeling the initial flame acceleration in an obstructed channel using large eddy simulation. *Journal of Loss Prevention in the Process Industries*, 26(4):571–585, 2013. 225

W. Jones and R. Lindstedt. Global reaction schemes for hydrocarbon combustion. *Combustion and Flame*, 73(3):233–249, 1988. 49

T. Kanzleiter and G. Langer. Hydrogen deflagration tests in the THAI test facility. Technical Report 150 1326-HD-2, Becker Technologies GmbH, 2010. 225

J. Kent, A. Masri, S. Starner, and S. Ibrahim. A new chamber to study premixed flame propagation past repeated obstacles. *In 5th Asia Pacific conference on combustion*, page 17–20, 2005a. 157

J. Kent, A. Masri, and S. Starner, S.H.and Ibrahim. A new chamber to study premixed flame propagation past repeated obstacles. In *5th Asia-Pacific Conference on Combustion, The University of Adelaide, Australia*, 2005b. 225

A. Kerstein, W. Ashurst, and F. Williams. Field equation for interface propagation in an unsteady homogeneous flow field. *Physical Review A*, 37(7):2728, 1988. 52, 201

W. Kim, S. Menon, and H. Mongia. Large-eddy simulation of a gas turbine combustor flow. *Combustion Science and Technology*, 143(16):25–62, 1999. 52

M. Kirkpatrick, S. Armfield, A. Masri, and S. Ibrahim. Large eddy simulation of a propagating turbulent premixed flame. *Flow, turbulence and combustion*, 70(1-4):1–19, 2003. 157

A. Klimenko. Examining the Cascade Hypothesis for Turbulent Premixed Combustion. *Combustion Science and Technology*, 139(1):15–40, 1998. doi: 10.1080/00102209808952079. URL `https://doi.org/10.1080/00102209808952079`. 56

R. Knikker, D. Veynante, and C. Meneveau. A priori testing of a similarity model for large eddy simulations of turbulent premixed combustion. *Proc. Combust. Inst.*, 29:2105–2111, 2002. 62

R. Knikker, D. Veynante, and C. Meneveau. A dynamic flame surface density model for large eddy simulation of turbulent premixed combustion. *Physics of Fluids*, 16:449–452, 2004. 52

E. Knudsen and H. Pitsch. A dynamic model for the turbulent burning velocity for large eddy simulation of premixed combustion. *Combustion and Flame*, 154:740–760, 2008. 52

A. Kolmogorov. The local structure of turbulence in incompressible viscous fluid for very large Reynolds numbers. *Doklady Akademii Nauk SSSR*, 30:299–303, 1941. 35, 45

R. H. Kraichnan. Diffusion by a Random Velocity Field. *The Physics of Fluids*, 13(1):22–31, 1970. doi: 10.1063/1.1692799. URL `https://aip.scitation.org/doi/abs/10.1063/1.1692799`. 93

K. Kuo. Principle of Combustion. *Wiley New York*, 1986. 24

B. Larrouturou. How to preserve the mass fractions positivity when computing compressible multi-component flows. *Journal of Computational Physics*, 95:59–84, 1991. 113, 120, 132, 133, 223

R. Li, W. Malalasekera, S. Ibrahim, and B. Liu. On the mechanism of pressure rise in vented explosions: A numerical study. *Process Safety and Environmental Protection*, 117: 551—-564, 2018. 157

S. C. Li, F. A. Williams, and K. Gebert. A simplified, fundamentally based method for calculating NOx emissions in lean premixed combustors. *Combustion and Flame*, 119: 367–373, 1999. 49

D. K. Lilly. A proposed modification of the Germano subgrid-scale closure method. *Physics of Fluids*, 4(3):633–635, 1992. 39

A. N. Lipatnikov and J. Chomiak. Turbulent flame speed and thickness : Phenomenology, evaluation, and application in multi-dimensional simulations. *Progress in Energy and Combustion Science*, 28:1–74, 2002. 52, 158, 201, 202, 224

T. Lovas, P. Amneus, F. Mauss, and E. Mastorakos. Comparison of automatic reduction procedures for ignition chemistry. *Proceedings of the Combustion Institute*, 29(1):1387–1393, 2002. 49

T. Lu and C. K. Law. A directed relation graph method for mechanism reduction. *Proceedings of the Combustion Institute*, 30(1):1333–1341, 2005. 49

T. Lu and C. K. Law. A criterion based on computational singular perturbation for the identification of quasi steady state species: a reduced mechanism for methane oxidation with NO chemistry. *Combustion and Flame*, 154:761–774, 2008. 49

U. Maas and S. Pope. Simplifying chemical kinetics: Intrinsic low-dimensional manifolds in composition space. *Combustion and Flame*, 88:239–264, 1992. 50

B. Mandelbrot. On the geometry of homogeneous turbulence, with stress on the fractal dimension of the iso-surfaces of scalars. *Journal of Fluid Mechanics*, 72 (03):401–416, 1975. 220

B. Mandelbrot. Fractals. *Wiley Online Library*, 1977. 220

B. Mandelbrot. The fractal geometry of nature. *Wiley Online Library*, 173, 1983. 220

Z. Mansouri, M. Aouissi, and T. Boushaki. Detached Eddy Simulation of High Turbulent Swirling Reacting Flow in a Premixed Model Burner. *Combustion Science and Technology*, 188:1777–1798, 2016. 226

P. Martin, U. Piomelli, and G. V. Candler. Subgrid-Scale Models for Compressible Large-Eddy Simulations. *Theoretical and Computational Fluid Dynamics*, 13:361–376, 2000. 36, 37

A. Masri, S. Ibrahim, N. Nehzat, and A. Green. Experimental study of premixed flame propagation over various solid obstructions. *Experimental Thermal and Fluid Science*, 21(1):109–116, 2000. 157

A. Masri, A. AlHarbi, S. Meares, and S. Ibrahim. A comparative study of turbulent premixed flames propagating past repeated obstacles. *Industrial & Engineering Chemistry Research*, 51(22):7690–7703, 2012. 157

A. Massias, D. Diamantis, E. Mastorakos, and D. Goussis. An algorithm for the construction of global reduced mechanisms with csp data. *Combustion and Flame*, 117(4):685–708, 1999. 49

M. Matalon and B. Matkowsky. Flames as gasdynamic discontinuities. *Fluid Mechanics*, 124: 239, 1982. 44

C. Meneveau and T. Poinsot. Stretching and quenching of flamelets in premixed turbulent combustion. *Combustion and Flame*, 86:311–332, 1991. 54

C. Meneveau, T. Lund, and W. Cabot. A Lagrangian dynamic subgrid-scale model of turbulence. *Journal of Fluid Mechanics*, 319:353–385, 1996. 39

F. R. Menter. Two-equation eddy-viscosity turbulence models for engineering applications. *AIAA Journal*, 32(8):1598–1605, August 1994. 201

F. R. Menter, M. Kuntz, and R. Langtry. Ten Years of Industrial Experience with the SST Turbulence Model. *Turbulence, Heat and Mass Transfer*, 4:625–632, 2003. 17, 201

J. Michel, O. Colin, and D. Veynante. Modeling ignition and chemical structure of partially premixed turbulent flames using tabulated chemistry. *Combustion and Flame*, 152(1-2): 80–99, 2008. 50

V. Moureau, G. Lartigue, Y. Sommerer, C. Angelberger, O. Colin, and T. Poinsot. Numerical methods for unsteady compressible multi-component reacting flows on fixed and moving grids. *Journal of Computational Physics*, 202:710–736, 2005. 33

V. Moureau, P. Domingo, and L. Vervisch. From large-eddy simulation to direct numerical simulation of a lean premixed swirl flame: filtered laminar flame-pdf modeling. *Combustion and Flame*, 158:1340–1357, 2011. 59, 118, 126, 141

S. Mouriaux. *Large Eddy simulation of the turbulent spark ignition and of the flame propagation in spark ignition engines.* Energétique, Université Paris-Saclay, 2016. 60

S. Mouriaux, O. Colin, and D. Veynante. Adaptation of a dynamic wrinkling model to an engine configuration. *Proceedings of the Combustion Institute*, pages 159–180, 2016. 9, 11, 60, 61, 62, 113, 118, 132, 157, 158, 161, 162, 184, 185, 187, 219, 223

S. Nagarajan and J. H. Lele, S. K.and Ferziger. A robust high-order compact method for large eddy simulation. *Journal of Computational Physics*, 191:392–419, 2003. URL `http://adsabs.harvard.edu/abs/2003JCoPh.191..392N`. 94, 95, 96, 97, 98, 101

K. Nerinckx, J. Vierendeels, and E. Dick. Mach-uniformity through the coupled pressure and temperature correction algorithm. *Journal of Computational Physics*, 206(2):597–623, jul 2005. 111

F. Nicolàs-Pérez, F. Velasco, J. Garcìa-Cascales, R. Otón-Martínez, A. Bentaib, and N. Chaumeix. Evaluation of different models for turbulent combustion of hydrogen-air mixtures. Large Eddy simulation of a LOVA sequence with hydrogen deflagration in ITER Vacuum Vessel. *Fusion Engineering and Design*, 161:111901, 2020. 226

F. Nicoud and F. Ducros. Sub-grid scale stress modelling based o the square of the velocity gradient tensor. *Flow, turbulence and Combustion*, 63 (3):183–200, 1999. 38

E. E. O'Brien. The Probability Density Function (pdf) Approach to Reacting Turbulent Flows. *Topics in Applied Physics, Academic Press London*, 1980. 51

OECD. The Safety of the Nuclear Fuel Cycle. Technical report, Nuclear Energy Agency Organisation for Economic Co-operation and Development, 2005. 15

E. Oran and V. Gamezo. Origins of the deflagration to detonation transition in gas-phase combustion. *Combustion and Flame*, 148(1):4–47, 2007. 157

T. Passot and A. Pouquet. Numerical simulation of compressible homogeneous flows in the turbulent regime. *Journal of Fluid Mechanics*, 181:441–466, 1987. doi: 10.1017/S0022112087002167. 93

S. Patel, S. Jarvis, S. Ibrahim, and G. Hargrave. An experimental and numerical investigation of premixed flame deflagration in a semiconfined explosion chamber. *Proceedings of the Combustion Institute*, 29(2):1849–1854, 2002a. 157

S. N. D. H. Patel, S. Jarvis, S. S. Ibrahim, and J. Hargrave. An experimental and numerical investigation of premixed flame deflagration in a semiconfined chamber. *Proceedings of the Combustion Institute*, pages 159–180, 2002b. 157

P. Pepiot-Desjardins and H. Pitsch. An efficient error-propagation-based reduction method for large chemical kinetic mechanisms. *Combustion and Flame*, 154(1):67–81, 2008. 49

N. Peters. Numerical and asymptotic analysis of systematically reduced reaction schemes for hydrocarbon flames. *Numerical simulation of combustion phenomena*, pages 90–109, 1985. 49

N. Peters. Laminar flamelet concepts in turbulent combustion. *International Symposium on Combustion*, 21:1231–1250, 1986. 46, 220

N. Peters. The turbulent burning velocity for large-scale and small-scale turbulence. *Journal of Fluid Mechanics*, pages 107–132, 1999. 46, 47, 62

N. Peters. *Turbulent Combustion.* Cambridge University Press, 2000. 112, 158, 202, 224

L. Piar, F. Babik, R. Herbin, and J.-C. Latché. A formally second order cell centered scheme for convection-diffusion equations on general grids. *International Journal for Numerical Methods in Fluids*, 71:873–890, 2013. 107, 108, 123, 134, 136, 137

H. Pitsch. Large eddy simulations of turbulent combustion. *Annual Review of Fluid Mechanics*, 38:453–482, 2006. 52, 157

H. Pitsch and H. Steiner. Large eddy simulation of a turbulent piloted methane/air diffusion flame (sandia flame d). *Physics of Fluids*, 12(10):2541–2554, 2000. 50

T. Poinsot and D. Veynante. *Theoretical and Numerical Combustion.* Edwards, 2012. 8, 9, 22, 23, 24, 25, 26, 31, 42, 43, 44, 45, 46, 53, 112, 147, 150, 157

S. Pope. Pdf methods for turbulent reactive flows. *Prog. Energy Comb. Sci.*, 19:119–192, 1985. 51

S. B. Pope. Computations of turbulent combustion: progress and challenges. In *23rd symposium (international) on combustion - the combustion institute*, pages 591–612, 1990. 51

S. B. Pope. Ten questions concerning the large-eddy simulation of turbulent flows. *New Journal of Physics*, 6(35), 2004. 18

F. Proch, P. Domingo, L. Vervisch, and A. M. Kempf. Flame resolved simulation of a turbulent premixed bluff-body burner experiment. part ii: A-priori and a-posteriori investigation of sub-grid scale wrinkling closures in the context of artificially thickened flame modeling. *Combustion and Flame*, 180:340–350, 2017. ISSN 0010-2180. doi: https://doi.org/10.1016/j.combustflame.2017.02.012. URL `https://www.sciencedirect.com/science/article/pii/S0010218017300433`. 62

P. Quillatre. *Simulation aux Grandes Echelles d'Explosions en Domaine Semi-Confiné.* Energetique, Institut National Polytechnique de Toulouse, 2014. 44, 47, 147, 157, 161, 187

R. Rannacher and S. Turek. Simple Nonconforming Quadrilateral Stokes Element. *Numerical Methods for Partial Differential Equations*, 8:97–111, 1992. 109

Z. Ren, S. B. Pope, A. Vladimirsky, and J. M. GuckenheimerBykov. The invariant constrained equilibrium edge preimage curve method for the dimension reduction of chemical kinetics. *The Journal of chemical physics*, 124:114111, 2006. 50

O. Reynolds. On the dynamical theory of incompressible viscous fluids and the determination of the criterion. *Philosophical Transactions of the Royal Society of London*, 186:123–164, 1895. 30

S. Richard, O. Colin, O. Vermol, A. Benkenida, C. Angelberger, and D. Veynante. Towards large eddy simulation of combustion in spark ignition engines. *Proceedings of the Combustion Institute*, 31(2):3059–3055, 2007. 53

P. Sagaut and R. Grohens. Discrete filters for large eddy simulation. *International Journal for Numerical Methods in Fluids*, 31(8):1195–1220, 1999. 34

P. Sagaut, S. Deck, and M. Terracol. *Multiscale and multiresolution approaches in turbulence*. Imperial College Press, 2006. 226

B. Sainte-Rose, N. Bertier, S. Deck, and F. Dupoirieux. A DES method applied to a Backward Facing Step reactive flow. *Combustion for aerospace propulsion*, 337:340–351, 2009. 226

A. L. Sànchez, A. Lépinette, M. Bollig, A. Liñàn, and B. Làzaro. The reduced kinetic description of lean premixed combustion. *Combustion and Flame*, 123:436–464, 2000. 49

T. Schmitt, M. Boileau, and D. Veynante. Flame wrinkling factor dynamic modeling for large eddy simulations of turbulent premixed combustion. *Flow Turbul. Combust.*, 94:199–217, 2015. 114, 118

K. Seshadri, X. S. Bai, and H. Pitsch. Asymptotic structure of rich methane-air flames. *Combustion and Flame*, 127:2265—2277, 2001. 49

J. Smagorinsky. General Circulation Experiments with the Primitive Equations: I. The basic experiment. *Monthly weather review*, 91:99–164, 1963. 37, 68, 114

G. J. Smallwood, O. Gulder, D. Snelling, B. Deschamps, and I. Gokalp. Characterization of flame front surfaces in turbulent premixed methane/air combustion. *Combustion and Flame*, 101 (4):461–470, 1995. 220

G. Smith, D. Golden, N. Frenklach, B. Eiteneer, M. Goldenberg, C. Bowman, R. Hanson, S. Song, and W. Gardiner Jr. GRImech, 2012. 48

P. Spalart and S. Allmaras. A one-equation turbulence model for aerodynamic flows. *AIAA Journal*, 0439:1–22, 1992. 226

P. Spalart and S. Allmaras. A one-equation turbulence model for aerodynamic flows. *La recherche Aérospatiale*, 94:5–21, 1994. 226

D. Spalding. Development of the eddy-break-up model of turbulent combustion. *In 16th Symposium (Int.) on Combustion*, 1:1657–1663, 1976. 50, 51

D. B. Spalding. Mixing and chemical reaction in steady confined turbulent flames. In *13th symposium (international) on combustion - the combustion institute*, pages 649–657, 1971. 50, 51

E. T. Spyropoulos and G. A. Blaisdell. Evaluation of the dynamic model for simulations of compressible decaying isotropic turbulence. *AIAA Journal*, 34(5):990–998, 1996. URL `https://doi.org/10.2514/3.13178`. 94, 95, 96, 97, 98, 99, 100

K. Sreenivasan and C. Meneveau. The fractal facets of turbulence. *Journal of Fluid Mechanics*, 173:357–386, 1986. 220

R. Sun and H. Xiao. Diffusion-based coarse graining in hybrid continuum–discrete solvers: Theoretical formulation and a priori tests. *International Journal of Multiphase Flow*, 77: 142–157, 2015. doi: https://doi.org/10.1016/j.ijmultiphaseflow.2015.08.014. 126, 140

F. Thiesset, G. Maurice, F. Halter, N. Mazellier, C. Chauveau, and I. Gökalp. Flame-vortex interaction: Effect of residence time and formulation of a new efficiency function. *Proceedings of the Combustion Institute*, 36(2):1843–1851, 2017. doi: https://doi.org/10.1016/j.proci.2016.06.172. 56

A. S. Tomlin, T. Turanyi, and M. J. Pilling. Mathematical tools for the construction, investigation and reduction of combustion mechanisms. *Comprehensive chemical kinetics*, 35: 293–437, 1997. 49

Q. H. Tran. Second-ordern slope limiters for the simultaneous linear advection of (not so) independent variables. *Communications in Mathematical Sciences*, 6(3):569–593, 2008. 136

T. Turanyi. Reduction of large reaction mechanisms. *New journal of chemistry*, 14(11): 795–803, 1990. 49

J. A. Van Oijen and L. P. H. De Goey. Modelling of premixed laminar flames using flamelet-generated manifolds. *Combustion Science and Technology*, 161:113–137, 2000. 50

J. A. Van Oijen, A. Donini, R. J. M. Bastiaans, J. H. M. Ten Thije Boonkkamp, and L. P. H. De Goey. State-of-the-art in premixed combustion modeling using flamelet generated manifolds. *Progress in Energy and Combustion Science*, 57:30–74, 2016. 50

A. Venetsanos, T. Huld, P. Adams, and J. Bartzis. Source, dispersion and combustion modelling of an accidental release of hydrogen in an urban environment. *Journal of Hazardous Materials*, 105:1–25, 2003. 16

D. Veynante. Investigation of flame surface density modeling for large eddy simulation of turbulent premixed flames by comparison with a prescribed reference solution. *Combustion and Flame*, page 111663, 2021. ISSN 0010-2180. doi: https://doi.org/10.1016/j.combustflame.2021.111663. URL `https://www.sciencedirect.com/science/article/pii/S0010218021004065`. 62

D. Veynante and V. Moureau. Analysis of dynamic models for large eddy simulations of turbulent premixed combustion. *Combustion and Flame*, 162:4622–4642, 2015. 19, 59, 60, 62, 112, 114, 115, 117, 118, 132, 157, 161, 223

D. Veynante and L. Vervisch. Turbulent combustion modeling. *Progress in energy and combustion science*, 28:20–92, 2002. 175

S. Volpiani. *Modèle de plissement dynamique pour la simulation aux grandes échelles de la combustion turbulente prémélangée.* Energétique, Université Paris-Saclay, 2017. 62, 117, 157, 161, 225

B. Vreman, B. Geurts, and H. Kuerten. Subgrid-Modelling in LES of Compressible Flow. *Applied Scientific Research*, 54:191–203, 1995. 37

G. Wang, M. Boileau, and D. Veynante. Implementation of a dynamic thickened flame model for large eddy simulations of turbulent premixed combustion. *Combustion and Flame*, 158 (11):2199–2213, 2011. 56, 58, 59, 62, 114

G. Wang, M. Boileau, D. Veynante, and K. Truffin. Large eddy simulation of a growing turbulent premixed flame kernel using a dynamic flame surface density model. *Combustion and Flame*, 159(8):2742–2754, 2012. 59, 62, 114, 174

X. Wen, M. Yu, Z. Liu, and W. Sun. Large eddy simulation of methane-air deflagration in an obstructed chamber using different combustion models. *Journal of Loss Prevention in the Process Industries*, 25:730–738, 2012. 157

X. Wen, M. Yu, Z. Liu, G. Li, W. Ji, and M. Xie. Effects of cross-wise obstacle position on methane air deflagration characteristics. *Journal of Loss Prevention in the Process Industries*, 26:1335–1340, 2013. 10, 11, 12, 20, 157, 158, 160, 163, 164, 165, 166, 167, 168, 169, 170, 186, 188, 189, 190, 191, 196, 197, 198, 201, 203, 205, 206, 207, 209, 211, 215, 218, 219, 224

D. C. Wilcox. Reassessment of the scale-determining equation for advanced turbulence models. *AIAA Journal*, 26(11):1299–1310, 1988. 201

F. A. Williams. *Combustion theory: the fundamental theory of chemically reacting flow systems.* Westview Press, 1985. 44, 53

C. Xu, L. Cong, Z. Yu, Z. Song, and M. Bi. Numerical simulation of premixed methane-air deflagration in a semi-confined obstructed chamber. *Journal of Loss Prevention in the Process Industries*, 34:218–224, 2015. 157

A. Yoshizawa. Statistical theory for compressible turbulent shear flows, with the application to subgrid modeling. *The Physics of Fluids*, 29:2152–2164, 1986. 34, 37

G. Yu, C. Law, and C. Wu. Laminar Flame Speeds of Hydrocarbon + Air Mixtures with Hydrogen Addition. *Combustion and Flame*, 63:339–347, 1986. 147, 150

Y. Zeldovich and D. Frank-Kamenetskii. A theory of thermal propagation of flame. *Zhurnal Fiziche skoi Khimii*, 12(1):100–105, 1938. 41, 45

Y. Zeldovich, G. Barenblatt, V. Librovich, and G. Makhviladze. *Mathematical theory of combustion and explosions.* Springer US, 1985. 9, 41

V. L. Zimont. Gas premixed combustion at high turbulence. Turbulent flame closure combustion model. *Experimental Thermal and Fluid Science*, 21(1-3):179–186, mar 2000. URL `http://www.sciencedirect.com/science/article/pii/S0894177799000692`. 48, 158, 202, 204, 215, 217, 219, 224